Hybrid electroactive morphing at real scale - application to Airbus A320 wings

Gurvan Jodin

THÈSE

En vue de l'obtention du

DOCTORAT DE L'UNIVERSITÉ DE TOULOUSE

Délivré par :

Institut National Polytechnique de Toulouse (INP Toulouse)

Discipline ou spécialité :

Génie Electrique

Présentée et soutenue par :

M. GURVAN JODIN

le mercredi 25 octobre 2017

Titre :

Hybrid electroactive morphing at real scale, application to Airbus A320 wings

---

Ecole doctorale :

Génie Electrique, Electronique, Télécommunications (GEET)

Unité de recherche :

Laboratoire Plasma et Conversion d'Energie (LAPLACE)

Directeur(s) de Thèse :

M. JEAN FRANCOIS ROUCHON

MME MARIANNA BRAZA

Rapporteurs :

M. JULIAN HUNT, UNIVERSITY COLLEGE LONDRES

M. LIONEL PETIT, INSA LYON

Membre(s) du jury :

M. LIONEL PETIT, INSA LYON, Président

M. FRANK THIELE, TECHNISCHE UNIVERSITAT BERLIN, Membre

M. JEAN FRANCOIS ROUCHON, INP TOULOUSE, Membre

M. JEAN-MICHEL SAUCRAY, AIRBUS FRANCE, Membre

Mme MARIANNA BRAZA, INP TOULOUSE, Membre

M. MICHAEL TRIANTAFYLLOU, MASSACHUSSETS INSTITUTE OF TECHNOLOGY, Membre

Acknowledgements

Before French acknowledgements, I would like to particularly thank the member of the jury for their devoted time and advice.

Je m'adresse maintenant en français pour remercier mes directeurs Jean-François et Marianna. Ils m'ont guidé et fait confiance en me donnant une autonomie dans ce projet. Je remercie également les ingénieurs d'Airbus avec qui nous avons travaillé et qui ont cru en ce projet : Christophe Cros, Alain Fontaine, Jean-Michel Saucray et Denis Descheemaeker.

Tout le travail que je présente n'aurait été possible sans une assistance scientifique et technique de haut niveau et très professionnelle par les personels du Laplace, de l'IMFT et de l'INP-ENSEEIHT : Dominique Harribey, Christophe Korbuly, Sébastien Cazin, Moïse Marshal, Pierre Elyakim, Robert Laroche, ...
Une pensée certaine aux personnels administratifs que j'ai bien embêté avec mes missions et commandes en tout genre, mais qui m'ont toujours aidé avec le sourire ! Pour leur conseils et leur présence, je tiens à remercier les membres des équipes GREM3 et EMT2.

Je n'oublie pas les stagiaires "gentiment exploités" avec qui j'ai eu plaisir à travailler. Pour toutes les parties de Haxball, les chocos, les verres, mais également les discussions scientifiques et professionnelles, un grand merci aux doctorants, postdoc et ingés qui m'ont supporté pendant ces trois années. Je souhaite transmettre des mots d'amours et des poulpis pour ma compagne et plus généralement toute ma famille pour leur support durant cette période importante pour moi.

Contents

Nomenclature

$\overline{u^2}$, $\overline{v^2}$ Time average of the stream-wise and crossflow component of the Reynolds tensor.

A, a^* HFVTE actuation amplitude (mm). $a^* = \frac{A}{c}$ is the dimensionless amplitude.

c chord length

D, $\overline{D}$, C_D Drag force, time average drag, drag coefficient $C_D = \frac{\overline{D}}{1/2 S \rho U_\infty^2}$. With ρ the air density, S the reference wing section.

F_a, f_a^* HFVTE actuation frequency (Hz), dimensionless actuation frequency $f_a^* = \frac{F_a c}{U_\infty}$

L, $\overline{L}$, C_L Lift force, time average lift, lift coefficient $C_L = \frac{\overline{L}}{1/2 S \rho U_\infty^2}$. With ρ the air density, S the reference wing section.

M Mach number: $M = U/v$ where U is the considered velocity and v the corresponding sound velocity.

St Strouhal number. $St = \frac{f \cdot c}{U_\infty}$, with f the frequency in Hz.

u, v Stream-wise ($\overline{u}$), respectively crossflow ($\overline{v}$) fluctuating component of the flow velocity normalized in relation with U_∞. $u = U - \overline{U}$, $v = V - \overline{V}$

U, V and $\overline{U}$, $\overline{V}$ Stream-wise (U), and crossflow (V) component of the flow velocity normalized in relation with U_∞. $\overline{U}$, $\overline{V}$ are the time averages of the components.

U_∞ free stream velocity (m/s)

CAD Computer Aided Design.

FEA Finite Element Analysis

HFVTE Higher Frequency Vibrating Trailing Edge

KH Kelvin-Helmholtz

MAV Micro Air Vehicle

MFC piezoelectric Macro-fiber Composite Patches.

POD Proper Orthogonal Decomposition.

PSD Power Spectral Density.

Re Reynolds number relative to the chord c. $Re = \frac{cU_\infty}{\nu}$ where ν is the kinematic viscosity of the air.

Sk Stokes number, $\mathrm{Sk} = \frac{\rho_\rho d_\rho^2 U_\infty}{18\mu\delta_c}$, where μ is the dynamic viscosity of the fluid, ρ_ρ is the density of the smoke particles, δ_c is the characteristic length i.e. the model chord and d_ρ is the diameter of the particles

SMA Shape Memory Alloy.

TNT Turbulent / Non Turbulent Interfaces

TRL Technology Readiness Level

VK Von Kármán

Introduction

Future aircrafts will be faster, safer, more silent, more comfortable, more environmental friendly and less expansive. This utopian objective has been evolving since the beginning of planes, in the very end of the 19th century. Firstly inspired from flying animals, the demand for carrying people and goods further and faster has led to large, rigid, fast and powerful aircrafts.

Nowadays aircrafts have fixed wing geometries. The unique airfoil profile results from an optimal compromise for some cruise flight states. Giving the ability of aircraft wings to change their shape – like birds do – improves their aerodynamic performance. The particular properties of bird feathers allow them to vibrate within the airflow. How does this interact with the flow turbulence? And can this be of help for improving future aircraft performance? Thus, the photomontage of Figure 0.1 illustrate our objective.

Within this context, the LAPLACE and the IMFT laboratories work together

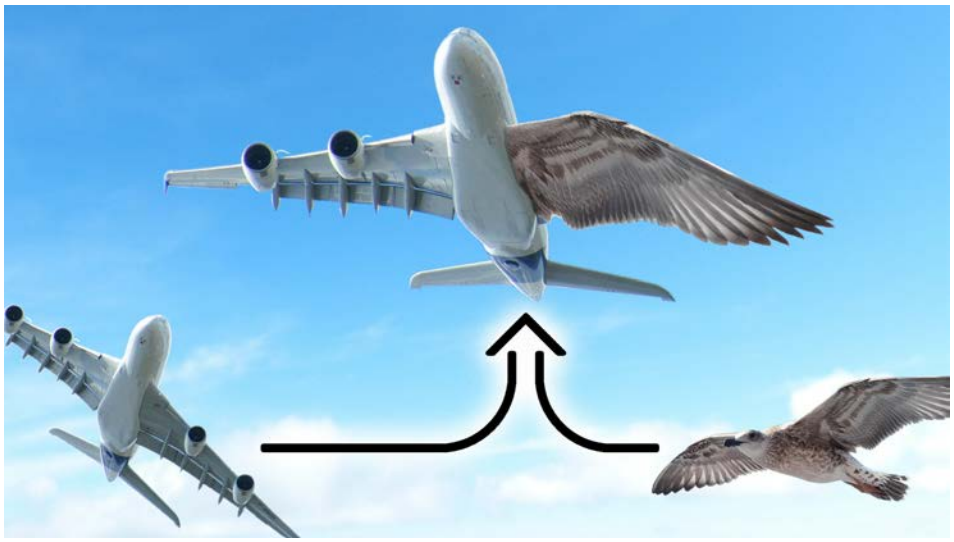

Figure 0.1: Photomontage made from Airbus A380 and seagull. MT180, a national scientific popularization competition, 2016.

on the research platform SMARTWING[1]. They have been supported by the Réseau thématique de recherche avancée (RTRA) – part of the Foundation STAE – and the Direction générale de l'armement (DGA). Efforts on electroactive morphing have been focused on micro- and nano-air-vehicles to improve their performance (Rouchon et al. [Rou+11]). Then an electroactive bending plate (Chinaud et al. [Chi+14]) and a small wing with electroactive vibrating trailing edge (Scheller et al. [Sch+15]) have been studied. Afterwards, a small electroactive wing with both camber control and vibrating trailing edge has been investigated, (Scheller et al. [Sch]). It has been the first hybrid electroactive wing prototype.

Based on this work, this thesis will focus on both aerodynamics and electromechanics. A multidisciplinary approach is proposed in order to understand further the hybrid electroactive morphing concept. Chapter 1 introduces a background on the different fields concerned by this thesis. Supported by Airbus, a hybrid electroactive wing is designed, made and characterized in Chapter 2. To investigate flow dynamics and quantify aerodynamic performance modifications, wind tunnel experiments are investigated in Chapter 3. Towards true aircraft scale, the design of a realistic morphing flap for an Airbus A320 is detailed in Chapter 4. Contributions and last elements are summed up in the conclusion 4.7.

Following the previous work of our research groups, this thesis is the continuation of the thesis of Johannes Scheller [Sch15]. Johannes made a proof of concept regarding hybrid electroactive morphing. The contributions of the present thesis is decomposed threefold:

- We propose design models for electroactive hybrid morphing wings. Starting from the material models, analytical and finite element models are proposed for both camber control and vibrating trailing edge. Models' achievements and limits are presented. The wing is built and instrumented for wind tunnel experiments. Impact of control laws on power consumption, electrodynamic characterization and sensor relevances are emphasized. The correlation between embedded pressure sensor measures and aerodynamic performance improvements is an original contribution.

- An experimental investigation of hybrid morphing in wind tunnel is performed. Reliability of the actuators is assessed. Wake dynamics is analyzed, and the impact of morphing is described. We propose a physical explanation based on Hunt's theory. For the first time, force measurements (i.e. lift and drag) modifications due to hybrid morphing are outlined.

- We propose a design process for a true scale morphing flap for A320, actuated with smart materials. The proposition consists in a camber control function

[1] www.smartwing.org

fulfilled by a macro actuator. This macro actuator – including internal actuators based on shape memory alloys – is designed through an optimization algorithm. Different technologies for skins and articulations are compared. The internal electroactive actuators are modeled. A mutli-objective genetic algorithm is used to find the best compromise between performance, weight, power consumption and cycle life.

CHAPTER 1

State of the art

"Nature is a library, read it instead of burning it."
"La nature est une bibliothèque, lisez-la au lieu de la brûler."
Idriss Aberkane

Abstract This manuscript describes a multidisciplinary work. This chapter relates a few examples from different scientific fields to give a background to the present work. The following path is observed: beginning with nature observation and bioinspiration, morphing is defined and industrial research projects on aircraft morphing are presented. Airflow physics around airfoils are mentioned to define actuators' aims. A specific attention is paid to electroactive smart materials before dealing with application of actuated structure.

1.1 From ornithology to aeronautics

1.1.1 Ornithology for bioinspiration

It is commonly believed that planes are inspired from birds. A famous example is the aircraft Éole of Clément Ader. This aircraft was inspired from flying foxes, which are bats. By the way, bats are mammals, not birds... Ornithology is the discipline that studies the birds. This section briefly introduces few researches on birds that can be useful to design future aircrafts.

Numerous birds' wings have alulae, which correspond to their thumbs. The alula has been studied in different ways. Different functions are attributed to the alulae and have their equivalent on aircrafts. Lee et. al. [Lee+15] performed PIV experiments on magpie wings. Performance of a wing with retracted alula is compared to a wing with extended alula. Figure 1.1 presents some of thier results. It has been shown that alula feathers create tip vortices that delay the detachment of the flow on the suction side of the wing. The complex structure of

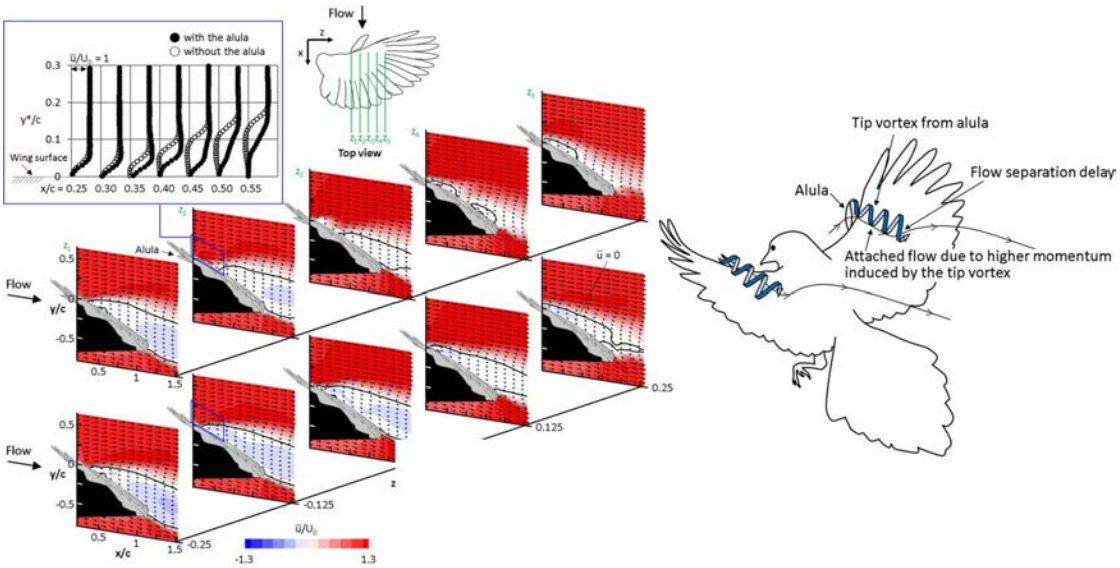

Figure 1.1: From Lee et. al. [Lee+15]. Velocity profiles with and without alula, time average streamwise velocity and artist's impression of the alula effect on the bird.

such 3D flow instabilities have been studied by Braza et al. [BFP01]. This allows the birds to flight at low speed with high angle of attack. It helps to land. This hyperlift function is analog to aircraft slats. The alula contains feathers that gives information on airflow. Brown et. al. [BF93] have looked at the neural signals coming from the wing nerves when the alula is exposed to airflow. They conclude that alula returns information on stall and wind velocity.

Belong their flat and esthetic look, feathers are complex and have multiple utilities. They are categorized by shape and function, [Orn13]. For example, the first remiges compose the wing and are hold on the bones, they carry aerodynamic loads. The secondary remiges can not hold the aerodynamic loads but gives the airfoil shape of the wings. The feathers are porous and can glide on each other to allow the bird to change its wing's shape. In section 4.4.2 of this manuscript, birds' feathers inspire an innovative concept of skin and feathers for aircraft. Feathers can provide low noise flight, like the well known owl hunting during the night. Studies have shown that the feathers of the owls are hairy, thus generating small vortices that change the flow dynamics of their wakes and then decrease their noise, Lilley et al. [Lil98]. The fact that birds have numerous feathers with different sizes prevent them from aeroelastic instabilities, like flutter. Clarke et. al. [CP15] measured flutter frequencies for different feathers. As the frequencies are spread, no resonance of the whole wing can occur and be dangerous.

More information on bird bioinspiration can be found in [Ald+16]. Morphology,

aerodynamics of wings, porous wings, passive and active flow control as well as structural characterization of structural stiffness and strengths are introduced.

1.1.2 Basis of flight physics and performance

Before focusing on aircraft performance enhancement, the basis of flight physics must be introduced. The book writen by Anderson [And10] is a succeeded introduction to aerodynamics. Figure 1.2 schematically represents the force balance of a flying aircraft. Notice the torques are not represented, as they are secondary for the following explanation. To stay at constant altitude, the weight W must be compensated by the lift L. A large part of the lift is due to the wing. The wing and the other component of the aircraft – with their shapes and sizes – generate the drag D. To flight at constant velocity, this drag is opposed by the thrust T. The thrust comes from the engines or propellers for aircrafts. For birds, the wing motion is in charge for both lift and thrust, but flapping motions are out of scope for this manuscript.

On one hand, considering a whole flight, the weight is not constant. Firstly depending on the variable boarded payload, aircrafts' weights decrease all along the flight as they literally burn the fuel. On the other hand, the wing aerodynamic performance are often characterized by the lift over drag ratio (LoD). Also called *aerodynamic finesse*, this criteria depends on flight conditions, angle of attack α, notably Mach number M and altitude a ($L/D = LoD(\alpha, M, a)$). The angle of attack control directly the lift, so that the LoD ratio is also expressed $L/D = LoD(L, M, a)$. Thus, as the expansive fuel consumption is directly linked to the

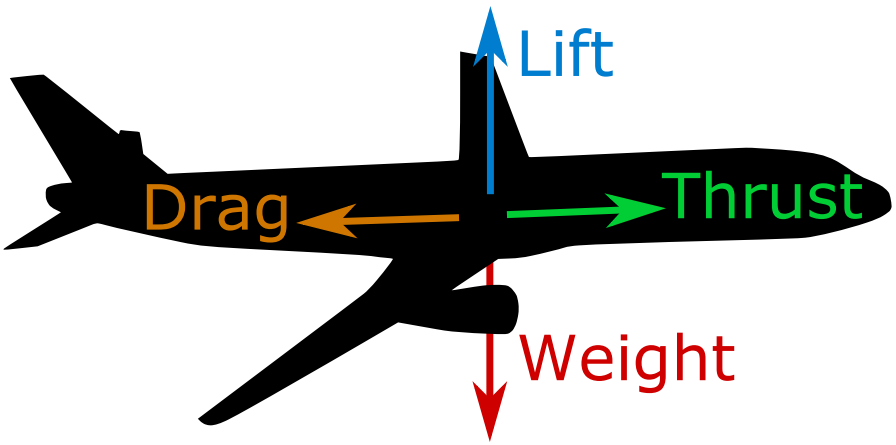

Figure 1.2: Illustration of the force balance of a flying aircraft along a steady without acceleration trajectory.

engines' thrust, equation 1.1 expresses the link between aerodynamic performance and fuel burnt.

$$\begin{aligned} \frac{L}{D} &= LoD(L, M, a) \\ L = W \quad D &= T \\ T &= \frac{W}{LoD(W, M, a)} \end{aligned} \tag{1.1}$$

This equation explains why it is so important to limit the weight. The power consumption of aircrafts is directly linked to aerodynamic performance. An improvement in aerodynamic performance can be achieved by decreasing the drag or increasing the lift at constant drag and angle of attack.

To go further on this analysis, nowadays aircraft wings "are designed for a compromise of good performance at a variety of flight conditions" as say Burdette et. al. [Bur+15]. It results that the aircrafts always fly at sub-optimal conditions, even during cruise.

The previously described elements concern the working principle of aircraft. It is also important to notice the way of flight control assessed by movable surfaces for planes, or morphing wings and tails of birds. Basically, the main control surfaces control the aircraft attitude (inclination). To introduce some vocabulary, ailerons are located close to the wing tips. They control the roll and can be assisted by spoilers. The elevators, located on the horizontal stabilizer, control the pitch; whereas the yaw is controlled by the rudder, mounted on the vertical stabilizer. *Flaps* and *slats* are secondary control surfaces. They fulfill *configuration control* function. This function consists in adapting the wings' areas and shapes to the flight conditions. As birds enlarge their wings and extend the alulae at low speed, aircrafts extend slats and flaps for take off and landing. Control trimming surfaces and other control surfaces like air brakes are not discussed here for brevity purpose.

Finally, a short attention is given to noise sources. It is known that aircraft noise is mainly due to landing gears and slats during landing, Dobrzynski et al. [Dob10]. Take off noise is dominated by engines. As silent birds hunt by night, a more silent aircraft will be allowed to fly during the night, with obvious commercial interest.

1.2 Industrial point of view on aircraft morphing projects

1.2.1 Definition of morphing

The definition of aircraft morphing can be quite subjective. An articulated structure can be understood as a morphing structure for some people, whereas the deformation has to be smooth and seamless from the point of view of other researchers...
In 2010, the NASA defined that "Aircraft morphing is:

- large shape change,
- smooth, seamless shape change,
- reconfigurable aircraft,
- reconfigurable aircraft using unconventional control surfaces,
- adaptive wings,
- real-time, seamless wing shape control,
- smart structures embedded in wings for passive or active shape control,
- any kind of wing adaptation,
- a crazy idea. "

Additionally, Steffen BAUSS from Airbus defines in 2013 that "Aircraft morphing is real-time adaptation to enable mutli-point optimized performance in air vehicles". Then morphing aims four objectives:

1 Improve aircraft performance to expand the flight envelope (mission segment optimization, noise reduction);
2 Replace conventional control surfaces for improved flight control and performance;
3 Drag reduction for increased range, fuel economy;
4 Flutter control, vibration control, passenger comfort, safety, structural health.

From an aircraft manufacturer point of view, the distinction between the critical maneuver functions and the configuration functions is important as they require different actuation frequencies and amplitudes. Figure 1.3 represents the different control surfaces as a function of deformation velocities and amplitude. This chart is not exhaustive, new functions can be added. For instance, dynamic flow / turbulence control can require small amplitudes at low or high frequency.

Finally, the most important about morphing definition is that *"The ultimate goal of morphing in an aircraft is to transform the airflow. Not the structure"* (Steffen BAUSS). Actually, beyond the engineering, the science, the environmental impacts linked to morphing, there are commercial reasons. Due to competition between aircraft manufacturers, aircrafts have to be more and more efficient. This

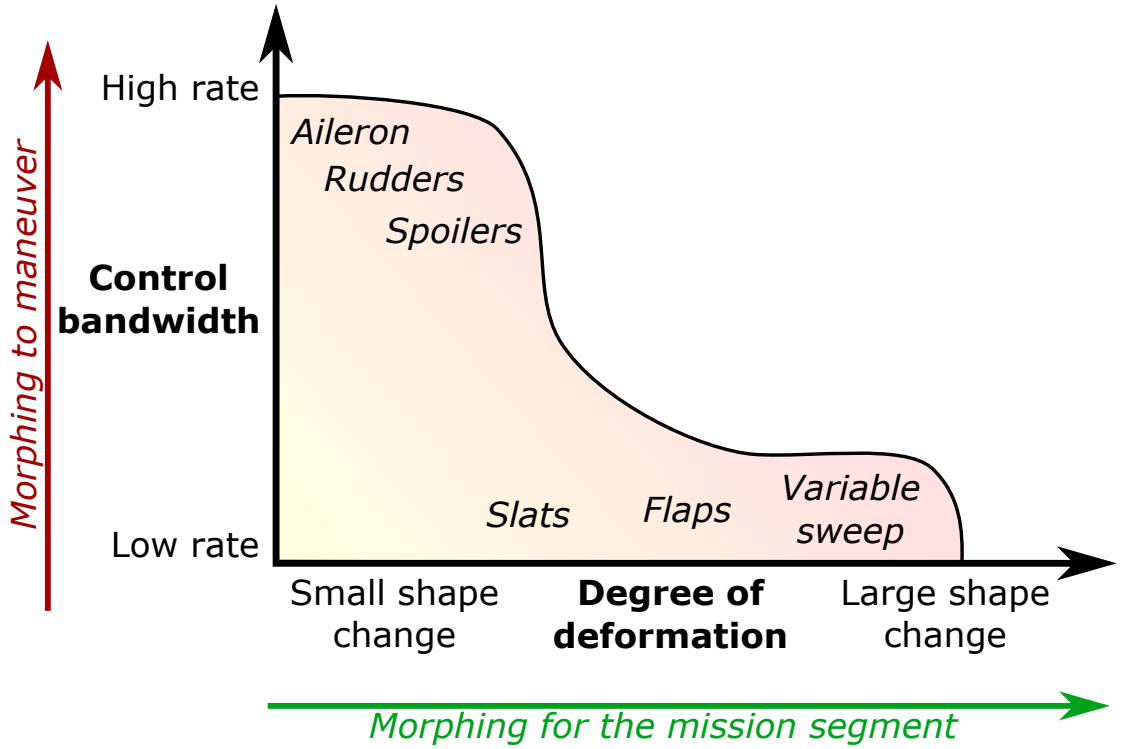

Figure 1.3: Representation of aircraft functions in the degree of deformation-deformation rate plane. From Steffen BAUSS (Airbus) presentation in 2013.

effectiveness is partially due to aerodynamic improvements. The potential of morphing has to be assessed by fluid dynamic studies. But to make it happen, all the work relies on the structure and the actuators.

1.2.2 Thorough research projects on morphing

Large research projects with industrials have addressed aircraft morphing. These projects with substantial funds deal with conventional and new technologies to develop credible solutions – i.e. at high Technology Readiness Levels (TRL). Industrial constraints like failure management, maintenance are dealt. Complete aerodynamic studies linked to aircraft design are proceeded. The gains are evaluated for a whole aircraft – i.e. they are not limited to a 2D airfoil aerodynamic performance improvement – so that the suitability of the technology can be evaluated.

1.2.2.1 SARISTU

The European research program SARISTU[1] focuses on operating cost reductions as well as on improving the aerodynamic performance. Three work packages are linked to morphing, embedded in the demonstrator visible in Figure 1.4.

One work package of SARISTU deals with a morphing wing trailing edge. Lead by CIRA – The Italian Aerospace Research Centre – the adaptive camber wing aims to stay at minimal drag, as the best configuration changes with reference to actual flight mission and during the flight. The device is based on servomotors driving an articulated structure, [Dim+16]. Elastomeric joints with foam have been designed to have smooth deformed shapes.

DLR is in charged of the enhanced adaptive droop nose for a morphing wing. This active leading edge is based on the work done during the previous European project SADE. This work package states that a feasible solution to enhance performance could be the laminar wing to reduce drag during take-off, cruise and landing. Therefore a morphing and gapless droop nose device is needed to provide laminar flow. Such a device would additionally decrease the overall noise emission. Aeronautic constraints concerning the design like bird strikes, failure analysis, deicing devices and lightning protection are developed. As presented in [Kin+16], the system relies on a servomotor driving a torque shaft which is linked to a simple optimized internal mechanism. This mechanism deforms the specifically studied morphing skin. The total mass of this system is evaluated to 14 kg, where 50% belongs to the motor. Having a localized actuator concentrates the mass, the distribution of the actuation can be a possible way to reduce mass.

The third morphing device corresponds to a Wingtip Active Trailing-Edge – WATE – directed by EADS Innovation Work. It consists in a control surface on the wingtip with specific flexible elastomeric joints. This allows the wingtip shape to be smooth and continuous despite the rotation of the control surface. This study demonstrates the ability of specific elastomer to work at low temperature, [Nag+16].

Michael X. Meyer from Airbus, announced [2] that morphing in SARISTU finally exhibits no gain. Indeed some aerodynamic enhancements are true but the global gain is null (with commercial factors and the added mass and systems).

1.2.2.2 Variable Camber Continuous Trailing Edge Flap

The VCCTEF concept has been developed in 2010 by NASA. This concept consists in replacing the wing trailing edge by a morphing trailing edge all along the

[1] http://www.saristu.eu

[2] Keynote at 52nd International Conference on Applied Aerodynamics, Lyon, France, 2017

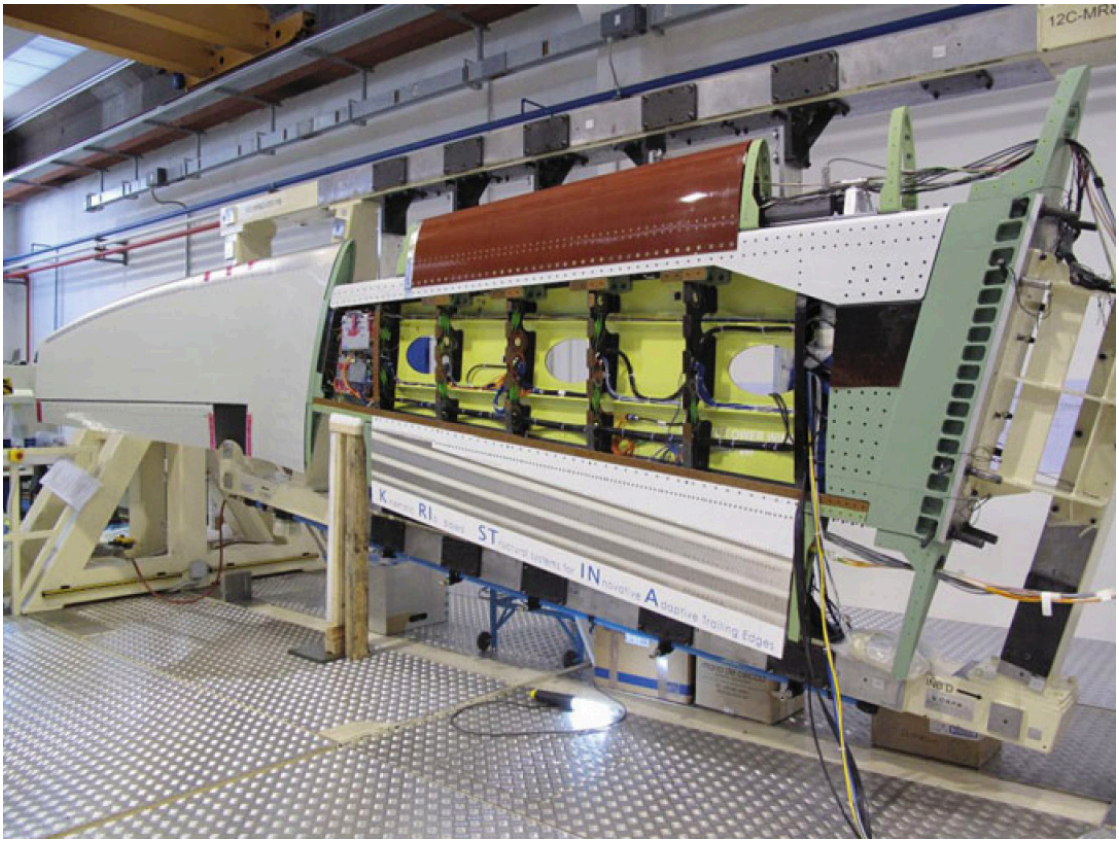

Figure 1.4: Picture of the SARISTU wing prototype from [Nag+16]. It embeds the different demonstrators of the assessed technologies of the project.

span. The camber can be adapted to different spanwise values. Different numerical [KN14] and experimental [PML14] studies on aerodynamics or actuators have taken placed. Control strategies also have been studied. The concept has different implementation: an articulated trailing edge with 3 hinges [PML14] or a continuous chordwise deformation [KH08]. This last solution – implemented by the firm Flexsys – relies on a gliding pressure skin to stand the skins' length changes. An optimized truss structure is made inside the flap. This truss is actuated thanks to a conventional hydraulic or electric actuator. A flap based on this last technology has been tested during flight test campaigns by NASA and Flexsys on a business jet, as visible in Figure 1.5, [KFC16] [Cum+16].

1.2.2.3 Realistic shape memory alloy actuator

Topic of smart material is covered latter in the section 1.4. Smart materials are not limited to academic laboratories. For example, industrials are interested in

Figure 1.5: Picture of the Gulfstream III SubsoniC Research Aircraft Testbed, with the morphing flap prototype from [Mil+16]

.

shape memory alloy (SMA) actuators.

As a first instance, the SAMPSON Smart Inlet is a full scale demonstrator of F-15 fighter aircraft inlet tested in a realistic environment. Funded by DARPA, the main objective is to replace the current hydraulic actuator used to rotated the cowl, changing the inlet geometry. Sixty Ni-Ti wires are bundled together to provide 90,000 N axial force output. This system has been tested in a NASA transonic wind tunnel, [PDW02].

Another interesting example regarding commercial aircraft is introduced by the Boeing Company [CM16]. This project consists in a SMA actuator that extends a miniature plain flap on the wing trailing edge, after the aileron. The purpose of such small flap was noise reduction with mixed results, but the design process to develop SMA actuator with a high TRL is very interesting. A hydraulic bake and redundant system is designed to assist the SMA torsion rod. This rod is made of an alloy specifically developed for the application, taking ageing issue into account.

These two examples draw the following conclusion: new actuator technologies are welcome to industrial application if the gains are true. The lack of knowledge concerning failure cases and ageing, the adaptation of the existing systems have to be addressed first. A system approach is needed to estimate the true gains, one cannot simply replace an existing actuator by a new one based on innovative technology. The More Electric Aircraft was promising, but as the failure cases are

different compared to existing hydraulic actuators for instance, a simple upgrade is not possible and the functions must be re-engineered.

1.3 Airflow physics around an airfoil and its control

1.3.1 Flow dynamics around an airfoil

For centuries, fluid mechanics have been intensively studied and some mysteries are still unsolved. A popular example is Clay Mathematics Institute that offers a 1 million dollar award for an analytic solution of the Navier-Stokes equation. One very developed field of fluid mechanics is aerodynamics with application to aircrafts. Anderson [And10] introduces the design of aircraft and the modeling of airflow around airfoils.

1.3.1.1 Flow around an airfoil

It is explained that boundary layers – close to the wing surface – is dominated by viscous effects. The flow is rotational, i.e. the rotational of the flow velocity field is not null. On the opposite, flow far from the surface is dominated by inviscid effects, non-rotational. The interaction and interface between these two behaviors is characterized by turbulent/laminar flow, attached/detached flow. One can note that a detached flow is not mandatory turbulent as well as an attached boundary layer is possibly turbulent. These phenomena can be associated to ranges of dimensionless numbers like Reynolds number (Re) or Mach number (M_∞). Their definitions are reminded in equation 1.2. c is the airfoil chord, U_∞ is the free flow velocity (far upstream of the wing), ν is the kinematic viscosity of the air and U_{sound} is the sound velocity in the wing environment.

$$\begin{aligned} Re &= \frac{c \cdot U_\infty}{\nu} \\ M_\infty &= \frac{U_\infty}{U_{sound}} \end{aligned} \tag{1.2}$$

Figure 1.6 schematically describes different flow behaviors for different shapes and Reynold numbers. Drag forces are represented with a distinguish between skin friction – coming from the integration shear forces on the skin – and pressure drag – i.e. the streamwise component of the skin pressure integral. After the separation point, the flow is detached and the wake is enlarging. Basically, a large and thick

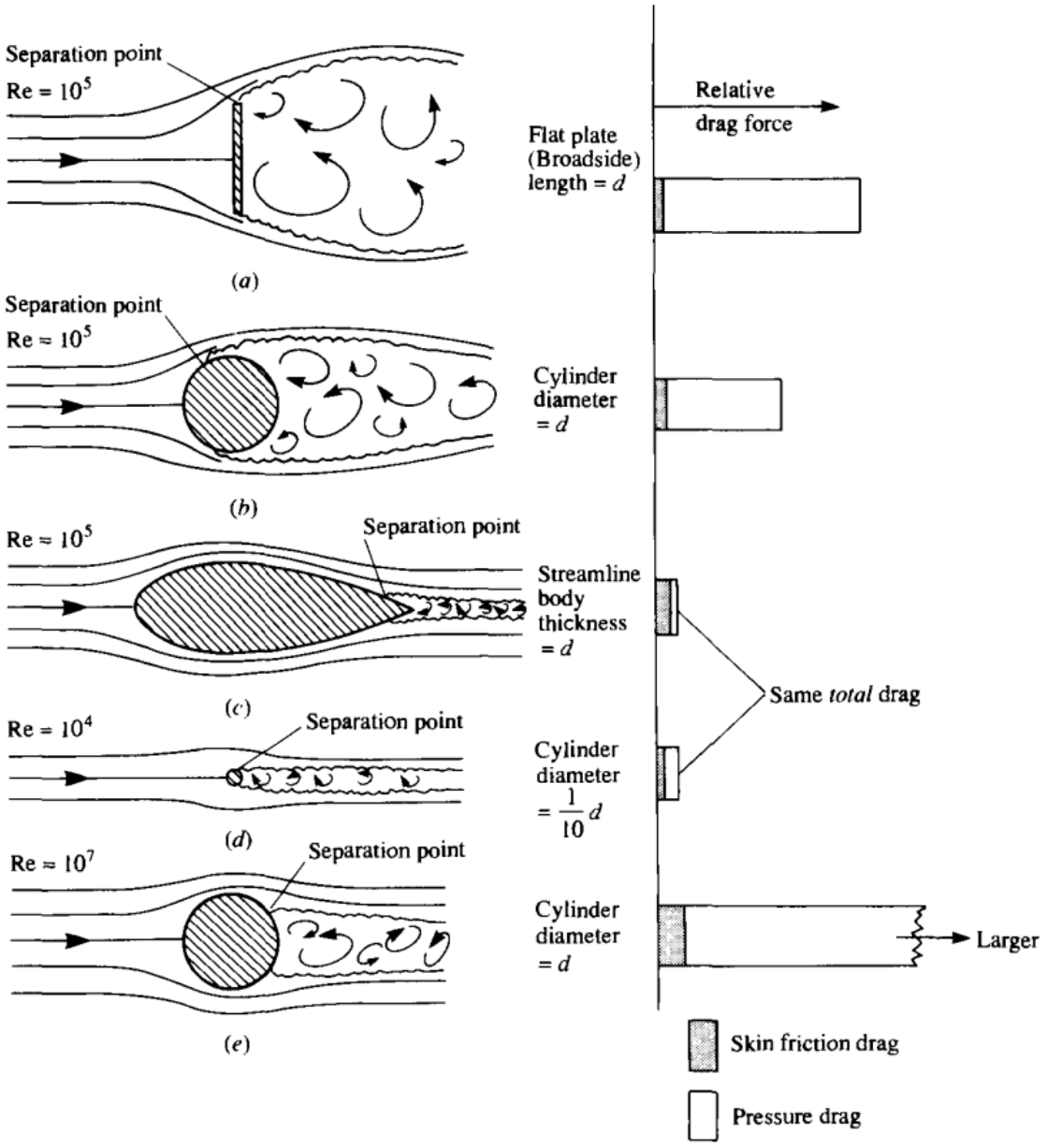

Figure 1.6: Reynolds and shape effects on wings and bluff bodies, from Anderson [And10]

wake is responsible for a large pressure drag. Increasing the velocity (i.e. Reynolds number) increases the drag, but the distribution between pressure and friction drag also changes. For example, increasing the Reynolds number around the cylinder Figure 1.6b to the case in Figure 1.6e change the drag distribution: the separation point goes further by increasing the Reynolds number to so called super-critic regimes. A thorough analysis of the forces related to the wake dynamics can be found in [BCM86] and [PB98].

Mach number is also a relevant dimensionless number that characterize airflows. This ratio quantifies the importance of compressibility effects. As presented in Figure 1.7, shockwaves occurs at high Mach flows. Subsonic flows 1.7a, does not exhibit shockwaves. Their physics are different from transonic flows 1.7b. Current jet airliners cruise at Mach numbers around $M_\infty \approx 0.8$. Locally on suction side – and sometimes on pressure side – a shockwave appears. This shockwave can oscillate, thus drastically affecting the wake dynamics, as investigated by Szubert et al. [Szu+16]. Figure 1.7c informs that the physics can be very different with a small change in Mach number in transonic conditions.

1.3.1.2 Wake dynamics

As represented by circular arrows in Figure 1.6, the wake presents vortices. At first sight, these vortices appear purely random and chaotic. But intensive research demonstrated that coherent vortices can be identified by statistic characteristics within a chaotic wake. The two most representative vortices present in the wake of a wing are named after famous scientists: the Von Kármán (VK) and the Kelvin-Helmholtz (KH) vortices.

The KH vortices looks like breaking waves in the sea. They occurs in presence of velocity shear. They are characterized by vortices rotating in the same direction. The VK vortex street consists in a repeating of alternative vortices. They come from the unsteady separation of flow around the airfoil. These two vortices are periodic and their sizes, shedding frequencies and locations have been studied. For instance, Yaru et al. [YSK06] have experimentally studied the boundary layer and wake dynamics of a NACA0025 airfoil at different Reynolds number (up to $Re \approx 150,000$). Another example is the numerical study of Hoarau et al. [Hoa+03]. The unsteady computation of airflow around a NACA0012 airfoil has been performed in 3D.

In order to improve simulation accuracy, Hunt et al. [Hun+16] proposed an explanation and model for the fluctuating interfaces between turbulent-non turbulent flow. These interfaces are present in a wing wake, the link between the vortices' energies and the growing or decrease in the wake width are explained This work suggests ways to control this turbulence to enhance aerodynamic per-

(a) Subsonic flow

(b) Transonic flow with $M_\infty < 1$

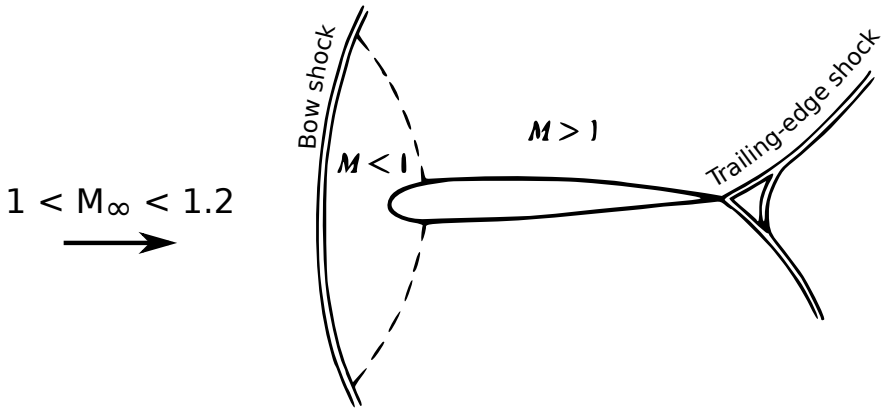

(c) Transonic flow with $M_\infty > 1$

Figure 1.7: Compressibility effects on wings, from Anderson [And10].

formance. More details are reported in section 3.4.

1.3.2 Flow control and turbulence control

1.3.2.1 Definitions

Based on the previously described flow dynamics, it is easily comprehensible that flow instabilities cause noise, vibrations and participates in the average forces on the structures. A fluid mechanics' field called *flow control* attempts to limit the unwanted phenomena. Because of the non-linearity of the fluid dynamics, a small action can have important effects. This can be an important advantage so that Professor Israel J. Wygnanski defines flow control as a small energy introduction in the flow, to expect a large change in flow behavior.

Therefore, flow control consists in implementing one or several actuators/de-

vices at a relevant position. Activating this actuator in the right conditions, at given aerodynamic conditions produces the wanted effect: shear layer turbulent energy reduction, preventing dynamic stall, noise reduction, drag reduction, ... The device can be a passive device on the surface (i.e. vortex generator, laminar skin) or actuators that locally change the shape, heat, impose velocity (by blowing or sucking, by vibrating, with plasma actuators, ...).

Considering the proposed approach of this manuscript, a distinction is made between the flow control strategies and the turbulence control proposed here. Previous studies of IMFT and LAPLACE laboratories – like Szubert [Szu15] and Scheller [Sch15] – prioritize an approach close to the vortex physics. This philosophy consists in discriminating the vortices responsible for the unwanted phenomena and attempt to eliminate them, for the benefit of more profitable vortices. This methodology can lead to also use actuators related to flow control, but the introduction can be lower as the aim is to manipulate the small vortices that will cause the expected flow modifications.

1.3.3 Research examples

The airfoil performance is very sensitive to its shape. A morphing aileron consisting in a smooth and continuous deformation of the airfoil to increase the camber is much more efficient than an articulated aileron. The boundary layer dynamics of a smooth morphing shape has been studied by Koreanshi et al. [K+14]. The influence on lift and drag is also observed in different experiments, with advantage for the continuous morphing shape, as related by Ohanian et al. [Oha+12].

Considering flow control, a few examples are discussed. Firstly, passive flow control. A passive flow control consists in a device with a specific shape that is added to the existing one to increase performance. A first example is the addition of hairs on a cylinder. Inspired from hairy plants, the hairs interacts with the wake and reduces the instability, as studied by Kunze et al. [KB12] Another example is the vortex generator located on wings' flaps to increase the lift and/or delay the dynamic stall by preventing the detachment. Lin [Lin02] draws a review on these small aerodynamics appendages located on the suction side of flaps. The main advantage of these devices is their easy implementation and robustness; but the main drawback is the lack of adaptability: the optimal shape depends on aerodynamic conditions and can degrade performance during other flight states as they correspond to off-design conditions.

Secondly, active flow control. The textbook case is a flow induced cavity resonance, as depicted in Figure 1.8. A review written by Cattafesta et al. [Cat+03] presents different ways to suppress the cavity oscillations. For subsonic and supersonic conditions, blowing actuators have been used based on electro-magneto-

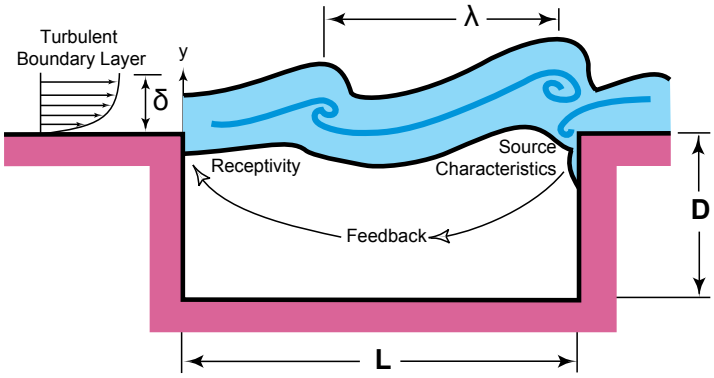

Figure 1.8: Active flow control flow induced cavity resonance, from Cattafesta et al. [Cat+03].

mechanical, piezoelectric devices or fluidic oscillating jets. Active oscillating flaps and plasma actuators can also be used. Applying high voltage between two electrodes on the wing ionize the surrounding air that becomes a plasma attracted by the electrodes. A large number of studies are related to flow control applied to aircraft. To give just one example of active flow control on an airfoil, Inaoka et al. [Ina+15] investigates in wind tunnel the effect of active vortex generators mounted close to the leading edge of a NACA0012 airfoil. For different Reynolds number, the actuated vibration frequency of the vortex generators was selected close to the vortex shedding frequency. An active control was set to activate these active devices to prevent the stall. The main advantage of the active devices is if the implementation is not too much invasive, they can be switched off during off-design conditions. If the phenomena are well understood, the actuation can be adapted to the flow condition to extend the aerodynamic range where gains can be expected. But the main drawback is the require power to supply the actuators. If the aim of such active control is to decrease drag, the power consumption have to be much lower than the saved energy due to the drag reduction. This balance is not obvious.

1.4 Electroactive smart material for actuators

1.4.1 Smart materials and electrocative materials

Wikipedia efficiently defines smart materials in one sentence: They are designed materials that have one or more properties that can be significantly changed in a controlled fashion by external stimuli, such as stress, temperature, moisture, pH, electric or magnetic fields. According to Ferreira et al. [FNM16], the smart materials are stimuli responsive materials belonging to the larger family of the multi-functional material systems. This large family contains designed materials with different scales and hierarchies, including composites and materials assessing different functions (sensing, actuating, self-healing, self-assembling, energy harvesting, ...).

Amongst the smart materials, this manuscript focuses on electroactive materials. Electroactive materials are here broadly defined as materials that convert a mechanical solicitation to an electrical solicitation and/or vice versa. This means that a material actuated by temperature encapsulated with a resistive electric wire, a material activated by magnetic field inside a coil or an electric-field responsive material with electrodes are considered as electroactive materials.

1.4.1.1 Review of some electroactive materials

This section draws a short review of electroactive materials. The following notations are used to compare the materials: ϵ_{act}, σ_{act} correspond respectively to the maximum strain and stress due to actuation. W_{act}/P_{act} stand for an order of magnitude of mass-specific output energy/power. E_{act} stands for applied electric field, H_{act} for magnetic field, T°_{act} for temperature, V_{act} for applied voltage. The letter ϕ precedes a short explanation of the physical principle of the smart material.

Dielectric elastomers

Common material: silicone based
Life cycle: $4 - 40$M cycles
Max. $\epsilon_{act} \approx 50\%$, $\sigma_{act} \approx 1$MPa
Electric field $E_{act} \approx 10 - 40$kV/mm
Actuator & sensor

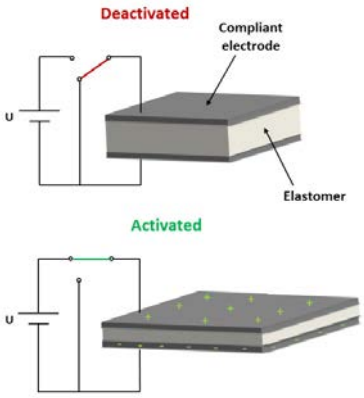

ϕ The applied electric field E_{act} between the electrodes generates a Maxwell pressure that crushes the elastomer. By Poisson effect, the edge lengths of the material grow.
A pre-stress is recommended for increase linearity.

Advantages:	**Drawbacks:**
- (low viscosity) high actuation frequency - low stress softening - large temperature range - no power consumption to maintain static position	- high voltage requirement - limited stress levels

Ref. Madsen et al. [Mad+16]

Ionic electroactive polymer (metal composite)

Common material: ionic polymer treated with ionic salt metal solution and chemically reduced
Max. $\epsilon_{act} \approx 5\%$, $\sigma_{act} \approx 10$MPa
Supply voltage $V_{act} \approx 4$V
$P_{act} \approx 40$W/kg
Actuator (≤ 5Hz) & sensor (≤ 100Hz)

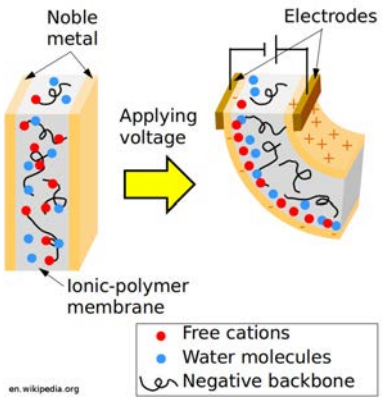

ϕ Hydrated cation from the ionic solution moves with the electric fields. The displacement of the water inside the porous polymer causes the motion.

Advantages:	**Drawbacks:**
- low voltage / low power consumption - performance comparable to biologic muscle	- stability (dry with time and loses properties) - limited stress levels - limited actuation frequency (becomes stiffer with actuation frequency)

Ref. Shahinpoor et al. [SK01], Bar-Cohen [Bar04]

Twist polymer coils

Common materials: Twist polyamide (nylon) or polyethylene fibers (fishing lines)
Life cycle: $>$ 1M cycles
Max. $\epsilon_{act} \approx 30\%$, $\sigma_{act} < 50$MPa
Actuation temperature $Ambiant < T^{\circ}_{act} < 120°$C
$P_{act} \approx 5$kW/kg
Actuator ($\leq$ 1Hz) only

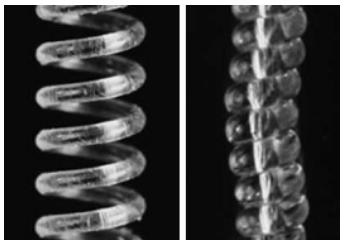

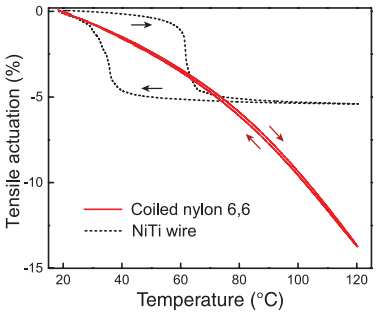

ϕ These elastomeric fibers exhibit small negative thermal expansion which is amplified by twisting the fibers until obtaining coils.
After thermo-mechanical training, the wires respond to thermal stimuli.
For instance, conductive paint can be applied on the fibers to be heated by joule losses.

Advantages:	**Drawbacks:**
- high strain	- sensitivity to high temperature
- low cost	- no reversible / efficiency
- stability	- limited actuation frequency (thermal time constant)

Ref. Haines et al. [Hai+14]

Ferrofluid

Common materials: Colloidal suspension of ferromagnetic particles in an insulating fluid
Controllable fluids

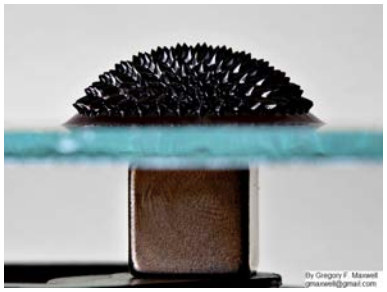

ϕ Analog to magneto-reheological fluids but the suspension is homogeneous.
The whole fluid has a ferromagnetic behavior.
An application is low friction dynamic sealing.

Advantages:	**Drawbacks:**
- reliable solution	- require bulky coils for active solution

Ref. Braz et al. [SF05]

Electro- / Magneto- rheological fluid

Common materials: Non-colloidal suspension of dielectric/ferromagnetic particles in an insulating fluid
Max. shear stress $\sigma_{yElectro} \approx 5$kPa / $\sigma_{yMagneto} \approx 100$kPa
Actuation fields $E_{actElectro} \leq 5$kV/mm / $H_{actElectro} \approx 250$kA/m
Controllable fluids

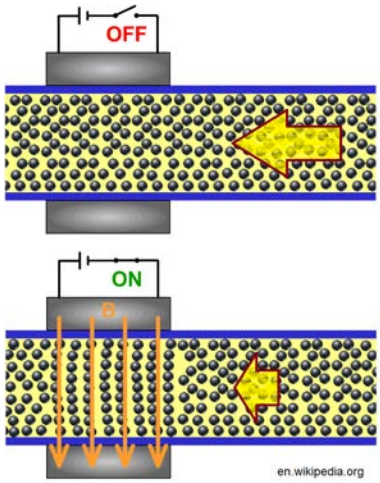

ϕ The interaction between the exciting electric/-magnetic field and the particles change the rheological properties. A shear stress plateau appears with fluid motion.
An application is active dampers.

Advantages:	**Drawbacks:**
- robustness - fine damping control	- power consumption of coils for magneto fluid

Ref. Carlson et al. [CCS96]

Electrostatic adhesion

Common materials: Sandwich composite material, two electrodes glides on a dielectric layer.
Max. shear stress $\sigma_y \approx 40$kPa / Normal adherence stress $\sigma_n \approx 100$kPa
Actuation fields $E_{act} \approx 60$kV/mm
Stiffness control

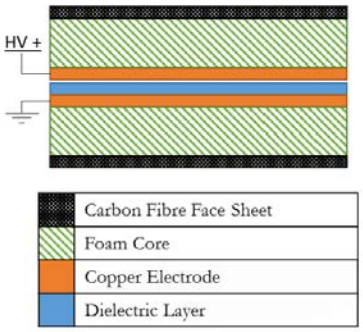

ϕ The electric field between the electrodes produces Maxwell pressure. This contact pressure control the friction between the electrodes.
Application are brakes and stiffness tunable structures.

Advantages:	**Drawbacks:**
- embedded solution - low power consumption	- very low maximum shear stress level

Ref. Heath et al. [HBP16]

Piezoelectric ceramics

Common materials: Lead Zirconium Titanium (LZT or PZT)
Max. $\epsilon_{act} \leq 0.2\%$ / $\sigma_{act} \approx 40$MPa
Actuation electric field $E_{act} \approx 100 - 2000$kV/m
Frequency $F_{act} < 1$MHz
Efficiency $> 90\%$
Actuator & sensor

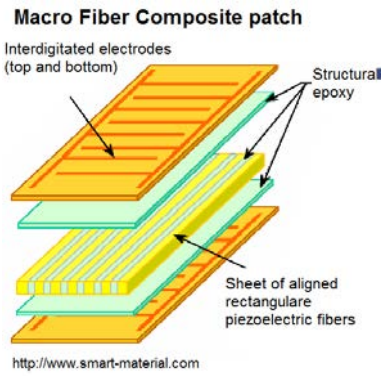

ϕ The electric field causes changes in crystalline structure due to microscopic magnetic dipole motions.

Advantages:	**Drawbacks:**
- suitable from low to very high frequencies	- limited temperature range (< 200°C for LZT)
- efficiency	- small displacement
- easy integration with electrodes	- brittle

Ref. Brissaud [Bri07], Ballas [Bal07]

Piezoelectric polymers

Common material: Polyvinylidene fluoride (PVDF)
Max. $\epsilon_{act} \leq 1\%$ / $\sigma_{act} \approx 1$MPa
Actuation electric field $E_{act} \approx 5 - 100$MV/m
Frequency $F_{act} < 1$MHz
Actuator & sensor

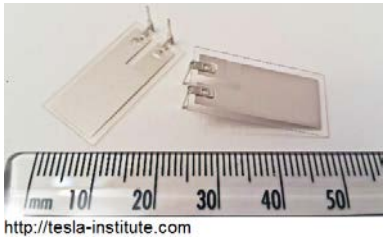

ϕ The PVDF is a semi-crystalline polymer. This structure interact like piezoelectric ceramics.

Advantages:	**Drawbacks:**
- easy integration due to flexibility	- lower electromechanical coupling than piezoelectric ceramics
- often too flexible for actuator application	- limited temperature range (< 90°C)
	- pyro-electric effect disturbs PVDF sensors

Ref. Ramadan et al. [RSE14]

Shape memory polymers

Material examples: Copolymer with polyurethanes and polyetheresters
Max. $\epsilon_{act} \approx 200\%$ / $\sigma_{act} \leq 3$MPa
Actuation temperature (for thermal induced effects) $T^{\circ}_{act} \approx 40 - 55°$C
Actuation frequency $F_{act} \leq 0.2$Hz
Actuator

ϕ The copolymer includes molecular switches sensitive to the stimuli. The material is trained by repetitively applying deformations and stimuli.

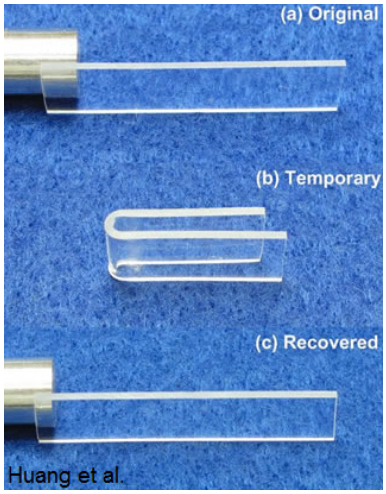

Advantages:	**Drawbacks:**
- large deformations	- limited frequency
- several shapes can be programmed	- sensitive to moisture and time
	- low stress levels

Ref. Behl et al. [BL07]

Magnetic shape memory alloys

Material example: NiMnGa
Life cycle: $\approx 10^9$ cycles
Max. $\epsilon_{act} \leq 10\%$ / $\sigma_{act} \leq 4$MPa
Actuation magnetic field $H_{act} \approx 700 - 10^3$kA/m
Actuation frequency $F_{act} \approx 1$kHz
$W_{act} \approx 50$J/kg
Actuator

ϕ A magnetic stimuli causes a change in ferromagnetic crystalline phase variants composing the metal alloy.
These variants are trained to have different shapes.

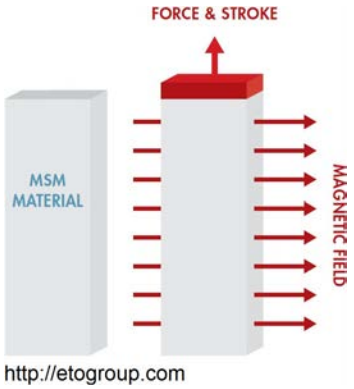

Advantages:	**Drawbacks:**
- quite large actuation frequency	- the high magnetic field levels require heavy coils or magnets
- large strain	- limited temperature range ($\leq 45°$)
- good fatigue life	- limited stress

Ref. Gabdullin et al. [GK15]

Shape memory alloys
Common materials: Nickel Titanium alloys (NiTi) Max. $\epsilon_{act} \leq 8\%$ / $\sigma_{act} \leq 600$MPa Actuation temperature tailorable within $T^{\circ}_{act} \approx -60 - 200°$C Actuation frequency $F_{act} \leq 1$Hz $W_{act} \approx 5$kJ/kg Actuator
ϕ A thermal stimuli causes a change in crystalline phases composing the metal alloy. These phases have different mechanical properties.

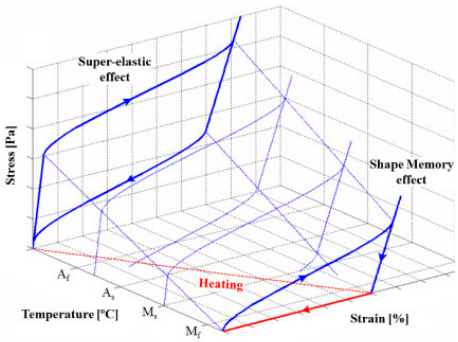

Barbarino et al.

Advantages:	**Drawbacks:**
- large specific actuation energy - large strain and stress	- strain and stress have to be limited for large number of actuation cycles - limited frequency - low efficiency

Ref. Lexcellent [Lex13]

Magnetostrictive materials
Common materials: Terfenol-D Max. $\epsilon act \leq 0.2\%/0.4\%$ (static/dynamic) / $\sigma_{act} > 100$MPa Actuation magnetic field $H_{act} \approx 50 - 200$kA/m Controllable fluids
ϕ The magnetic field interacts with the microcrystalline structure; this leads to macroscopic dimension changes.

Advantages:	**Drawbacks:**
- high frequency abilities - fine control	- power consumption - small displacement

Ref. Claeyssen et al. [CLM03]

These previous tables show an overview of electro-active materials suitable

for actuators. Amongst the large choice, the application with its environment determines the choice of the active material. Nevertheless, these short tables are simple and does not present inherent specificities of the materials corresponding to the making, the training, the assembly and the use.

Concerning the behavioral models, they can be summed up for the materials as a conservation law with constitutive laws. The conservation law is a linear expression of the energy where therms are related to the constitutive law. The constitutive laws can be simplified as linear or quadratic coupling between stimuli and mechanic variables. For more accurate models, non linearity like hysteresis, threshold and saturation. Dependence to parameters can also be taken into account like properties depending on temperature, stress, strain, ...

1.4.1.2 Electroactive material comparison

The previous section presents an overview of electroactive materials. The selection of the material the most suitable for a given application is done by comparing the different materials. Huber et al. [HFA97] propose a comparison based on graphics. Therefore, it is possible to compare the different actuator technologies (including electroactive materials, conventional magnetic actuators and natural muscle) on a same diagram, for instance stress VS strain in Figure 1.9a or power output VS frequency in Figure 1.9b. Depending on the application (static, dynamic, damping, ...) figures of merits are calculated and a new digram representing the materials

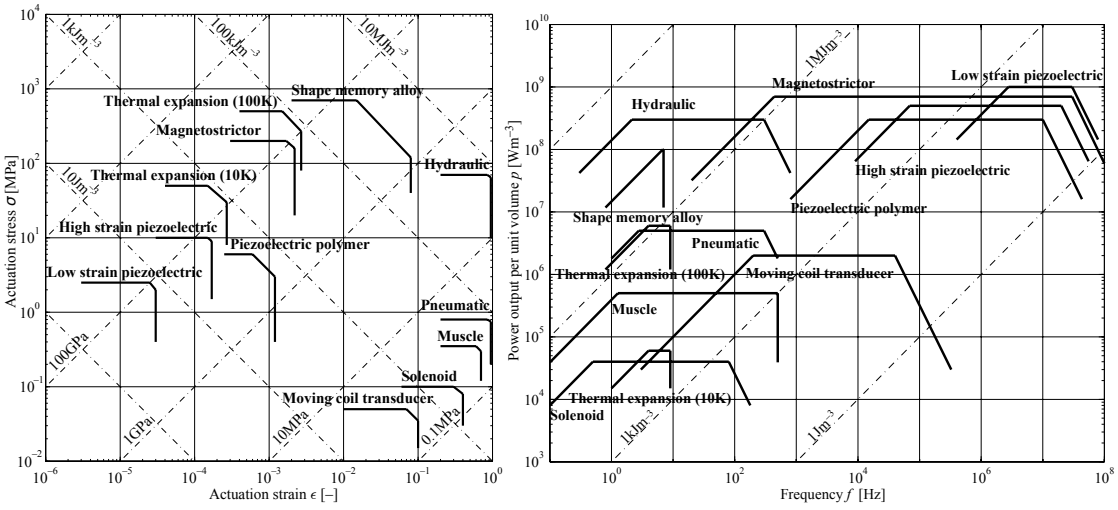

Figure 1.9: Representation of actuator technologies in stress VS strain diagram (a) and power output VS frequency diagram (b). From Huber et al. [HFA97].

as a function of the figures of merits. By the way, this approach developed by M. F. Ashby is also compatible with passive structure to find the best material.

A limit clearly announced of the previous comparisons is that the order of magnitudes of mass and volumes does not take auxiliary devices (casing, power supplies, valves/switches, ...) into account. For example magnetostrictive materials have a large output power density, but adding the mandatory coils and iron cores to made the actuator spoiled the total power density.

Only few research gives elements on true actuators as it depends on the application. Generally, applications requiring magnetic fields are much penalized; hydraulic actuators are penalized by the compressor and hydraulic network but the penalty is lower for a large number of hydraulic cylinders connected to one network.

Finally, this comparison does not imply the choice of one material for a given application. The disadvantages of one material can be compensated by another. For instance, the low frequency response of SMA and the limited deformations of piezo-ceramics has been compensated by the use of both these materials, by Pankonien et al. [PFI15]. Their synergistic smart morphing aileron includes a SMA actuated hinge plus a bending trailing edge. The piezo-actuator is used for quick response whereas the SMA are used for large deformations. Another example of material combination is applied to vibration energy harvesting to supply small autonomous electronic devices. Dielectric polymers can efficiently harvest mechanical energy with high strain but requires a power supply, whereas piezo-ceramic harvesters are autonomous but brittle. Cornogolub et al. [CCP16] associated both the two materials in one harvesting system: a first "piezo-harvester" generates the require electric source for the dielectric polymer harvester. The coupling topology has been optimized and a prototype is realized for experimental validation.

1.4.2 Actuators for morphing

1.4.2.1 Conventional aircraft actuators

The two following paragraphs present conventional aircraft actuator technologies to highlight the industrial philosophy on this topic. Firstly manual, the increase of aircraft size requires more force on control surfaces. Beginning with hydraulic assistance actuators, recent aircrafts are now "fly-by-wire", an electronic interface exchange informations between the pilot and the actuators. Conventional aircraft actuators consist in cylinder like actuators. Two ball joint anchors link the movable surface and the wing to the cylinder rod and case. The distance between the anchors controls the movable surface angle. Different technologies exist to apply forces and displacement to the rod from hydraulic to electro-mechanic.

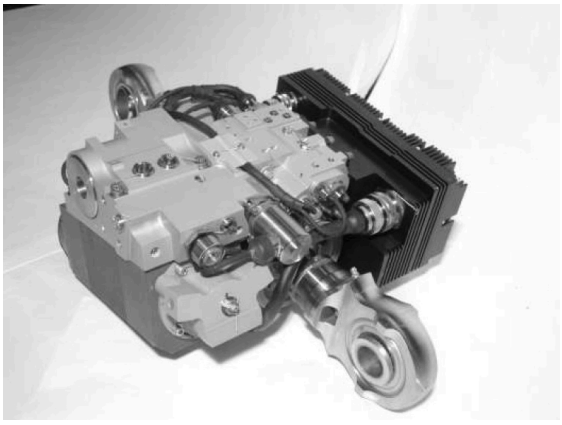

Figure 1.10: Picture of an Electro-Hydrostatic Actuator for A380 aileron, 2007

Hydraulic Actuators rely on a global hydraulic system, powered by the aircraft engines. Despite its high reliability, the complex and wide hydraulic network is heavy and costly to maintain. A next approach is the use of a local hydraulic circuit, power by an electric pump – Figure 1.10 presents a A380 aileron's Electro-Hydrostatic Actuator. The Electro-Hydrostatic Actuators are based on this principle and are compatible with a redundant fully hydraulic system. One main advantage of hydraulics are the behavior during failure cases. Indeed, in case of actuator failure, the movable surface goes to neutral position due to aerodynamic loading and the moving oil in the cylinder provides enough damping to prevent any fluid-structure dynamic instability. The most recent actuators are named Electro-Mechanical Actuators. They use no hydraulic power. These components are generally composed of a high speed rotating electric motor, a dropbox and a ball screw to transform the rotation to the translation of the cylinder rod. The advantages are the reduced mass and easier maintenance, but thermal management has to be seriously dealt. The main drawback is that the failure cases are very different from the hydraulic actuators. A mechanical failure can lock the control surface at a given position, which is not tolerable for critical functions. The implementation of Electro-Mechanical Actuators everywhere on an aircraft requires a system approach and to re-define functions.

1.4.2.2 Smart material actuators

The following paragraphs focus on shape memory alloy and piezoelectric actuators.

Shape Memory Alloy (SMA) actuators

Methods for designing SMA actuators have been studied. W. Kim [Kim16] details a design framework for SMA wire actuators. The wires can be embedded in

composite structures. For instance, bending beams with embedded SMA wires are detailed by Ma et al. [MSL04].

The use of designed SMA actuators require control. Despites their non linearities, the control of SMA actuators is mastered. Based on state space theory, the control of a SMA wire at contant tension with perturbation is assessed bu Jayender et al. [Jay+08]. Control of a agonist/antagonist actuator with several crossing SMA stages has been achieved by Grant et al. [GH97]. A feedback controller with different states is used. Additionally, feedback control based on artificial intelligence has also been investigated. Song et al. [SCB03] propose a neural network controller for SMA wire with counter spring.

Concerning SMA actuator, the research projects SAMPSON or the flap actuator of Boeing described in 1.2.2.3 are good examples.

To illustrate other industry application, General Motors developed a SMA actuator commercialized on the Corvette 2014[3], [Jan+14]. This actuator consists in silently opening an event to ease the door closing.

Piezoelectric actuators

The main applications of piezoelectric materials are piezoelectric ceramic stacks (piezo-stacks) and Macro Fiber Composite (MFC). The MFC are composite materials embedded LZT fiber with electrode within an epoxy structure.

One application of piezoelectric materials is electroactive lubricant. This is performed by introducing vibrations at the contacts between two mechanical parts. This can be used to realize high torque/low velocity motors based on quasi-static motion of piezo-stack actuators, as done by Rouchon et al. [Rou+13].

Piezoelectric materials have limited actuation strain. One way to increase the piezo-actuator stroke is the use of non-linear structural instability like buckling. Neal et al. [NA09] assembled two piezo-stacks and a spring to control bucking of a structure. Such control can also be more integrated: Giddings et al. [Gid+11] work on bistable plates made of carbon fiber composite with MFC embedded that allow for an active control of the shape. Such plates exhibit two different stable shapes, the actuation of embedded MFC is used to switch from a shape to another.

Next section focuses on these actuators' potential for aircraft morphing.

1.5 Smart and active structures for morphing aircrafts

One reason justifying why there are so many different research about morphing structures is the following paradox: the structure has to be flexible enough to

[3] https://www.youtube.com/watch?v=gdNvsZNk2PI

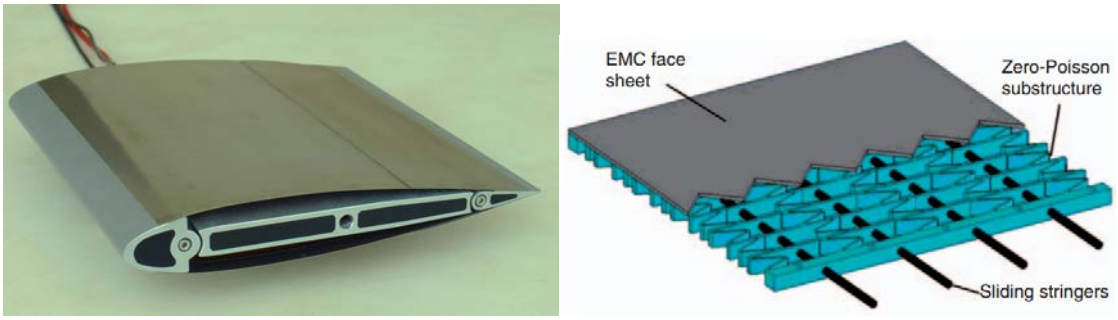

(a) (b)

Figure 1.11: (a) MFC actuated wing from Debiasi et al. [Deb+13]. (b) morphing skin from Bubert et al. [Bub+10].

be deformed, but stiff enough to carry the aerodynamic forces without being deformed.

Structures and skins

Nowadays, different propositions solve this paradox. A first bio-inspired example is the fish bone active camber morphing concept, created by Woods et al. [WBF14]. This concept relies on a bending beam spine with stringers. An elastic skin is taut over this structure and the whole is controlled by a servomotor driving tendons attached on the spine.

Another approach is the use of a bending upper skin with flexible truss elements inside the wing. Wu et al. [Wu+17] propose a configuration where the lower skin is cut and the different parts glide one upon the others. The whole is plane to be actuated by linear ultrasonic motors (based on piezoelectric materials). But the realized prototype was actuated by servomotor pulling wires linked to the truss elements.

Ramrakhyani et al. [Ram+05] propose a morphing structure based on tendons embedded in a compliant cellular truss. This work based on optimization does not propose skin solution to realize a demonstrator.

Michael X. Meyer from Airbus[4] says that morphing most important limitation is skin technologies. Indeed, even if the internal structure can be deformed whilst carrying the forces, the skin which provides the interface with the airflow has also to exhibit the same behavior. Towards the design of a skin with low elongation resistance, but with high out-of-plan stiffness and zero poisson ratio, Bubert et al. [Bub+10] proposed an anisotropic structure with an elastomer cover. The concept is visible in Figure 1.11b. This skin can be easily stretched but carry the forces with limited bending.

[4]Keynote at 52nb International Conference on Applied Aerodynamics, Lyon, France, 2017

Structures with SMA actuators
What about adding SMA actuators in an Airbus A380 wing to control the twist ? G. Duval [Duv05] worked on this question and answer that this can be achieved by approximately adding 50kg of SMA to the existent structures. This amount can be optimized if the structure can be adapted. Concerning more academic research, Rediniotis et al. [Red+02] have worked on a biomimetic hydrofoil. By assembling SMA actuated hinges in series, they have studied the swimming of their robot.

The idea of SMA morphing wings have raised a lot of studies regarding low scale and low velocity wings with a SMA actuated camber control. Different or similar topologies are used. Papers resulting from these studies states an innovative control system that improve aerodynamics of the wing. A few examples follows: [KBR14], [ESW03], [Mus01] or [SLY08].

Structures with piezoelectric actuators
The small deformations provided by the piezoelectric materials do not restrict them for reduced scale applications. Janker et al. [Jan+06] draw a review of piezoelectric actuator applications for aircraft. For instance, amplified piezo-stack actuator allows for controlling an aileron on rotative wings of rotorcraft. The aileron is actuated at the rotation frequency ($\approx$ 50Hz). Another example is piezoelectric active dampers for passenger comfort or protecting sensitive payloads.

Piezoelectric benders have been investigated by Li et al. [Li+15] to passively control the flutter instability. Their work has been based on numerical simulations.

Micro Air Vehicles (MAVs) with piezoelectric actuators have been designed and build. LaCroix et al. [LI14] have developed a twist control thanks to MFC. This allows to control the roll without conventional aileron. Another MAV – developed by Ohanian [Oha+12] – has been updated from conventional ailerons actuated by servomotor to flexible wings actuated by MFC. It has been shown that the aerodynamic performance and controllability are increased but actuators are 70% heavier in the worst design case.

Another interesting application of the MFC is proposed by Debiasi et al. [Deb+13]. MFC glued on both pressure and suction sides of a small airfoil, as visible in Figure 1.11a. The actuation cause a change in the shape with a good dynamic. Performance improvements have been validated by wind tunnel experiments.

Finally, the work of O. Bigen [Bil+10; Bil05] investigates the use of MFC for energy harvesting and actuators for MAV purpose. Power electronics and aerodynamic performances have been investigated.

1.6 Conclusion and originality of the proposed work

This chapter draws a non exhaustive state of the art regarding electroactive morphing and associated fields: ornithology, flight physics, industrial development around morphing topic, fluid mechanics and turbulence, flow control, electroactive materials. It appears that small scale electroactive morphing is well represented. Also flow control (without morphing) is a current research topic. Academic research aims are different from industrial requirements. System approaches that attempt to solve structural, actuation and aerodynamic issues are rare. Only a few research focuses on morphing application at realistic scales regarding commercial passenger aircraft.

The proposed multidisciplinary approach of this manuscript therefore seems original. It consists in the development of a complete wing that investigates electroactive morphing through turbulence control. Discussions with Airbus results in industrial specifications used to design a true scale electroactive morphing wing part.

Furthermore, the European research project SMS[5] "Smart Morphing and Sensing for aeronautical configurations", started on 2017/05/01. It focuses hybrid morphing effects developed in the present manuscript. The present state of the art has presented the background of this project.

[5] http://smartwing.org/SMS

CHAPTER 2

An electroactive hybrid morphing wing at reduced scale for wind tunnel experiments

"Those who don't build must burn."
Ray Bradbury

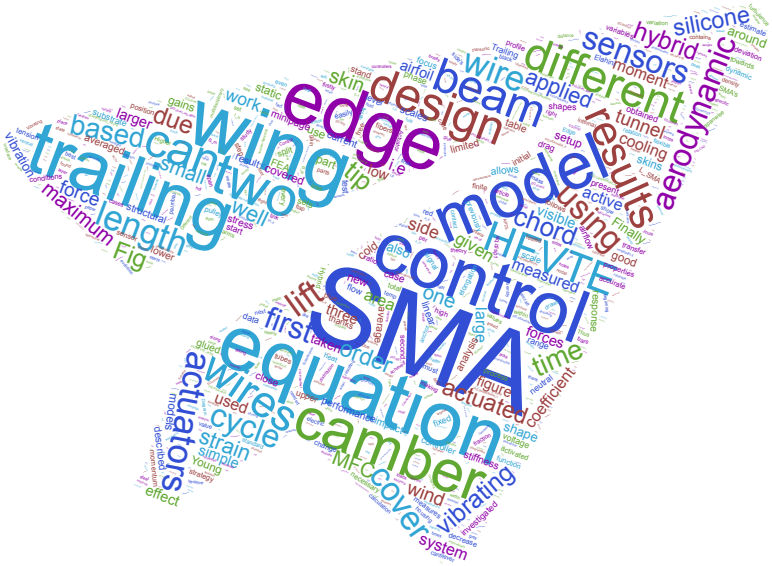

Figure 2.1: Word cloud of this chapter content (`www.wordclouds.com`).

This chapter is written from different publications. Sections 2.2, 2.3 are translated from "Congrès Français de Mécanique 2015", but subsection 2.2.4 is from a paper published in Solid State Phenomena in 2017: "An experimental platform for surace embedded SMAs in morphing applications". Section 2.5 is from a published proceeding in IEEE Xplore: "On the multidisciplinarity control and sensing of a smart hybrid morphing wing".

Abstract Within the context of hybrid morphing of LAPLACE and IMFT laboratories, a new morphing wing model equipped with embedded sensors. This model is a precursor to a larger scale one that will be designed for commercial aircraft application. This paper presents the design of the small-scale demonstrator. The camber control system activated by shape memory alloys and the vibrating trailing edge actuated by piezoelectric materials are modeled both in analytical and numerical ways. This smart wing is a mechatronic system that contains embedded sensors to measure the surrounding flow and control the actuators. The wing is then made and electrodynamic characterization is performed. A particular attention is paid to the shape memory alloy control strategy and to the measures pressure signals.

2.1 Introduction

2.1.1 Context

Following the work of Scheller et al. [Sch15], a collaborative project involving Airbus and the two laboratories Laplace and IMFT has taken place. Scheller et al. firstly developed a small wing prototype based on NACA4412 airfoil. This hybrid morphing wing both embeds SMAs and trailing edge piezoelectric fiber actuators [Sch+16]. This allowed both large deformations ($\approx$ 10% of the chord) at limited frequency ($\leq$ 1 Hz) and small deformations (several mm) at higher frequencies ($\leq$ 100 Hz). As a proof of concept, it has been shown that the trailing edge vibration interacts with the shear layer. The wing's wake energy has been reduced, leading to an improvement in aerodynamic performance. The purpose of the present chapter is the development of design tools for both vibration actuators and quasi-static camber control actuator. The design and the making of a small hybrid electroactive morphing wing is detailed. This wing features a A320 airfoil and aims electro-dynamic characterization and wind tunnel experiments.

2.1.2 Hybrid morphing

Hybrid morphing is the main concept discussed in the manuscript. As the aim of morphing is to control the airflow, the explanation of this multi-disciplinary approach starts with an observation of the airflow around a wing. Different time-space scales can be observed. We can focus on two main time-space scales: the first one is the global flow around the airfoil. This flow exhibits large fluid displacement associated with large slow vortical structures. The wake dynamics is smaller, characterized by shear layers composed of smaller vortices at higher frequencies. Then two different actuators are selected to interact with these two space-time flow scales. It has been shown by Ursache et al. in [Urs+07] that SMAs are very interesting smart materials for large deformations at low actuation rates. Piezoelectric ceramics and composites are commonly used for morphing purpose as well as to control structure dynamics, [Bar+11]. Bilgen et al. [Bil+10] also demonstrates that piezoelectric composite patches – like MFC – are suitable for small wing morphing. Finally, SMA are used to design a large amplitude quasi static actuator to control the wing camber. A Higher Frequency Vibrating Trailing Edge (HFVTE) is design thanks to MFC. Figure 2.2 sums up the approach.

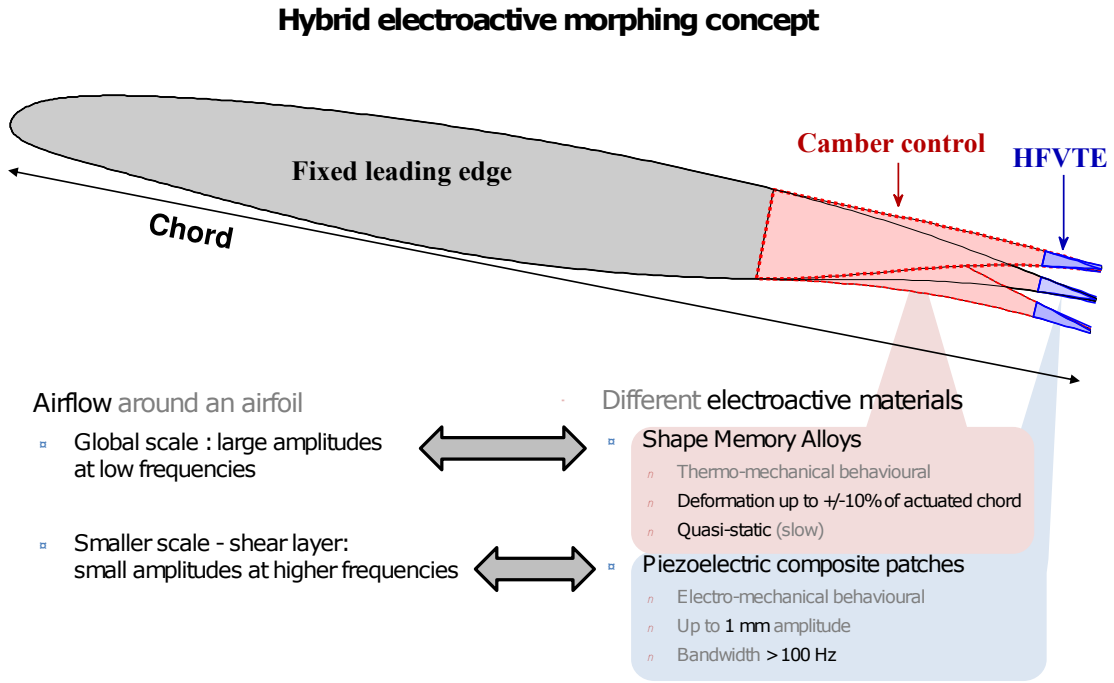

Figure 2.2: Concept of the hybrid morphing, using electroactive materials.

2.1.3 Specifications

Previous studies – like Scheller thesis [Sch15] – demonstrates the capability of hybrid morphing to impact the airflow through turbulence control. The camber can tailor the lift or the lift over drag ratio to the best value at a given flight step. Trailing edge vibrations have the potential to enhance the noise and/or the lift and drag at different flight steps.

Nevertheless, optimal actuation frequencies as well as corresponding optimal actuation amplitudes of the HFVTE are not known precisely. Also the coupling between the camber changes and the trailing edge vibrations has not been studied. Among the three investigated actuation frequencies, 60Hz has been found to be the best actuation frequency for a 0.42m chord wing section with NACA 4412 airfoil and free stream velocity of 7m/s. The dimensionless actuation frequency in this previous work is evaluated as $f_a^* = 3.7$. The vibration amplitude is about a few millimeters. The studied HFVTE actuators consist in vibrating bending beams within the wing wake, past the trailing edge. Then the airfoil profile is modified by the actuators.

The specifications of the new wing model's HFVTE are the following ones:

- quasi-static maximum displacement in two ways: $+/-10\%$ of the actuated chord
- first resonance mode above 100 Hz
- the trailing edge must respect the airfoil profile when no actuated
- the trailing edge deformations must be smooth
- the HFVTE actuated length is fixed to 5% of the wing chord

A distributed camber control of a wing has proved its efficiency, for example studies supervised by Martins [LM15] present gains of several percents of fuel burn thank to camber control (the actuator to perform the deformations is not taken into account). The order of magnitude of trailing edge displacement is about 5% of the chord, corresponding to approximately 10% of the flap chord. The effects of distributed wing twist and camber control for an aircraft can be estimated for a whole 3D wing. The small scale prototype here is designed as a wing section. Additionally, to assess the SMA actuation capabilities, the actuation specifications of the new wing aims large deformations, for research purpose. The stiffness of the solution is also addressed, the deflection under a pressure loading is limited by design. The stiffness of the morphing part is specified as a maximum trailing edge tip displacement with no actuation, whilst carrying representative loads of transonic conditions. These transonic conditions are not encounter during

the subsonic experiments but this indicates the possibilities of the electro-active morphing of stiff structures.

The specifications of the new wing model's camber control actuator are the following ones:

- quasi-static maximum peak to peak displacement: 1 mm
- actuated chord corresponds to a A320 flap length: $\approx 30\%$ of the wing chord
- stiffness: maximum 4% chord tip displacement under transonic case loading
- the trailing edge deformations must be smooth and airtight

This prototype must also embeds specific sensors: pressure transducers on the rear part of the suction side for investigation of flow dynamics, strain gauges and temperature sensors for actuator control, aerodynamic balance to measure lift and drag.

The geometry of such actuator positions is visible on Figure 2.2. This prototype is an evolution compared to the previous work. Based on design models to achieve the specifications, as well as a particular attention to sensors, this hybrid electro-active morphing wing materializes a technology transfer towards higher morphing scales. Both fluid dynamics investigation in wind tunnel as well as electro-mechanical characterization are performed.

Therefore, this chapter firstly focus on the modeling, the design and the characterization of the camber control actuator. Then the vibrating trailing edge design is discussed. Thirdly, manufacturing issues are addressed. Finally, the in situ characterization of the wing prototype is described with remarks regarding the following work.

2.2 Camber control actuator

The first 3 following sections come from a translation of a conference article "Dimensionnement d'une maquette pour l'investigation du morphing électroactif hybride en soufflerie subsonique", presented to 22ème Congrès Français de Mécanique, Lyon, 2015.

2.2.1 Actuator description

The proposed actuator deforms the last 30% of wing profile chord length. Aerodynamic forces are taken into account. The working principle relies on distributed and structure embedded actuation: SMA wires are spread under the upper and lower aluminum skins of the wing. These wires are encapsulated inside silicone tubes. These tubes wind through the anchors and pulleys that are glued under the skins. The actuation of the upper wires (suction side) causes bending of the trailing edge towards higher cambered shapes. Antagonistically, the actuation of SMA wires under the pressure side skin causes a decrease in camber.

SMA wires properties are activated by a change in temperature. They are heated thanks to electric current through themselves, and they are cooled down by forced air in the silicone tubes. The used alloy is based on Nickel and Titanium (grade SM495 from the firm NDC). These materials have been studied for decades, Lexcellent provides an accurate SMA handbook [Lex13]. Research concerning SMA is still evolving, but the physical principle is understood. The SMAs have an austenitic crystalline phase – stable at high temperature – and two martensitic phases – stable at low temperature. These alloys are mainly characterized by a austenetic phase stiffer than the martensitic one, the austenitic super-elastic behavior and the shape memory effect of the martensite. According to the targeted application, the choice of this grade is justified by its affordable price, a recoverable strain about 8%, a maximum stress around 600 MPa and a correct fatigue life. Figure 2.3 presents tensile tests of 1 mm diameter SMA wire. These measures have been performed at different temperatures. The area defined by the two extreme temperature curves corresponds to the working area. Thus, to size the actuator, these two extreme curves are used to compute the minimum and maximum wing deformations.

2.2.2 Analytical modeling

As a first approach, an analytic model based on material strength theory highlights the influence of sizing parameters. The Figure 2.4a presents the modeled part of the wing. The camber control trailing edge is modeled by two cantilever beams

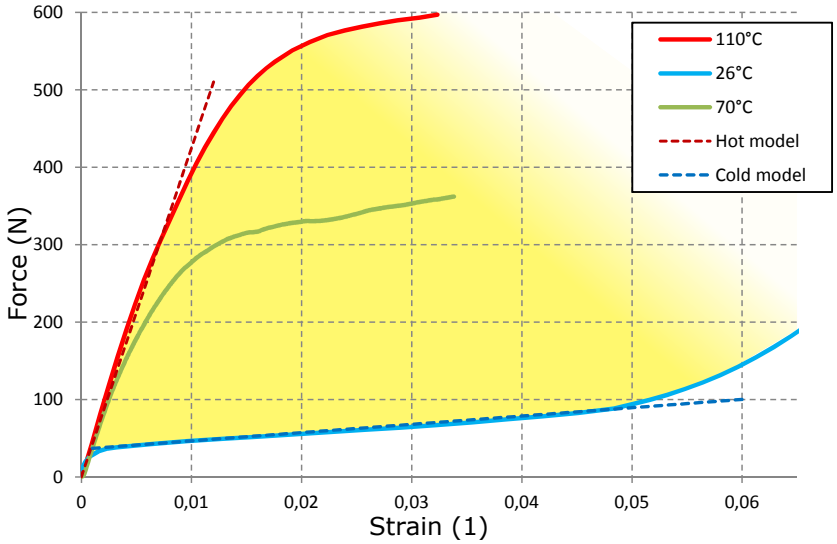

Figure 2.3: Tensile test of 1 mm diameter SMA wire at different temperatures.

that touch each other at the tip. As the slopes of the beams are relatively small, we assume the beams to be parallel, as drawn in Figure 2.4b. Concerning the SMA wires, it is assumed that the wires are parallel to the beams and follows the deformations of the structure.

As a consequence, the beam bending results from the sum of three solicitations: aerodynamic pressure loading, bending moment from the SMA wires, and the reaction force between the two beams. Pressure is here simplified as a constant value, chosen as equal to the average pressure around the trailing edge skins. The SMA forces are modeled by affine functions of strain, as presented by dash lines in Figure 2.3.

The parametrized models of the two beams are reported in Figure 2.4c. Where F_{Ru} and F_{Rd} are the reaction forces, $F_{SMA\ u}$ and $F_{SMA\ d}$ are the SMA wire tension forces, e_u and e_d represent the lever arms between the wires and the beams' neutral fibers. x_u and x_d are the tip displacement of the beams and ultimately P_u and P_d are the applied pressure. The tip displacement of the suction side skin is related in equation 2.1, where L is the beam length, $\mathbb{E}$ is the Young modulus of the material and I_u is the second moment of area of the beam cross section. The equation corresponding to the pressure side skin is similar to equation 2.1, with $._d$ indexes.

$$X_u = \frac{F_{Ru} \cdot L^3}{3 \cdot \mathbb{E} \cdot I_u} - \frac{P_u \cdot B \cdot L^4}{8 \cdot \mathbb{E} \cdot I_u} - \frac{F_{SMA\ u} \cdot e_u \cdot L^2}{2 \cdot \mathbb{E} \cdot I_u} \tag{2.1}$$

The calculation of the reaction forces F_{Ru} and F_{Rd} is solved by the equality between X_u and X_d, as the two skins are in contact. The calculation of the SMA

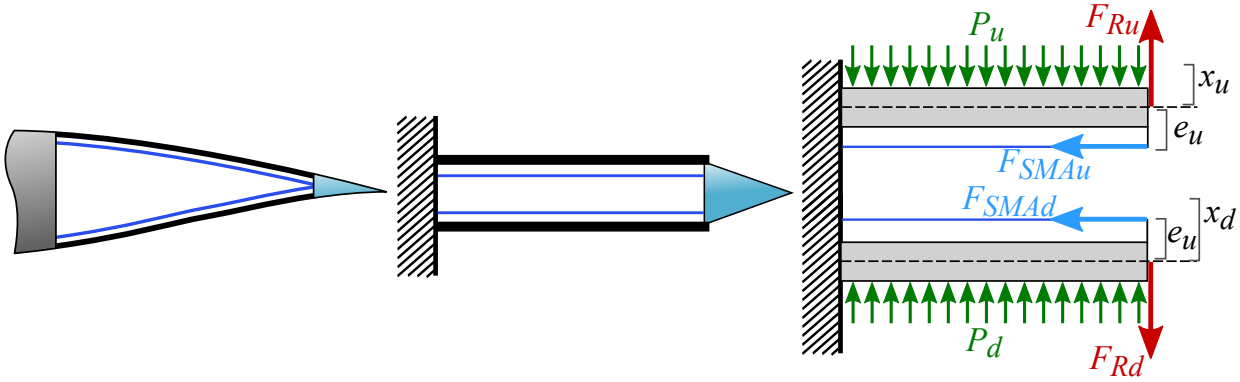

Figure 2.4: (a) Scheme of the camber controlled wing section. The SMA wires appear in blue. (b) Equivalent modeled trailing edge. (c) Parametrized model of the two beams.

wire tensions required the calculation of the wire strains $\epsilon_{SMA\ u}$ and $\epsilon_{SMA\ d}$. This is done in equation 2.2, where $\theta(L)$ is the tip beam rotation angle, $L_{SMA\ 0}$ is the initial wire length and $\epsilon_{SMA\ 0}$ the wire pre-strain.

$$\begin{aligned} \epsilon_{SMA\ u} = \frac{L_{SMA\ u}}{L_{SMA\ 0}} + \epsilon_{SMA\ 0} &= \frac{L_{SMA\ 0} + \int e \cdot \frac{\mathrm{d}^2 y}{\mathrm{d}x^2}}{L_{SMA\ 0}} + \epsilon_{SMA\ 0} \\ &= \frac{L_{SMA\ 0} + e_u \cdot \theta(L)}{L_{SMA\ 0}} + \epsilon_{SMA\ 0} \end{aligned} \tag{2.2}$$

These equations allow the calculation of the trailing edge deformations due to camber control. Different cases are investigated: with or without aerodynamic pressure, the influence of the pre-strain on the non actuated shape and the maximum reachable deformed shapes. A noticeable result is the drawing of the surface total mass VS actuation energy VS structure stiffness. All the points of this surface correspond to designs that satisfy a specified maximum actuated deformation under aerodynamic loading. The computation process follows: equations 2.1 and 2.2 are solved using the specified maximum actuated deformation. It results in a relation between the design parameters (skin thicknesses, lever arms and the spanwise spacing of the SMA wires). This relation allows different parameter sets that respect the specifications. For each set, the total mass, the actuation energy (proportional to the amount of SMA) as well as displacement due to aerodynamic loading (i.e. represents the structure stiffness) are evaluated.

Figure 2.5 presents this plan for the following conditions: trailing edge tip

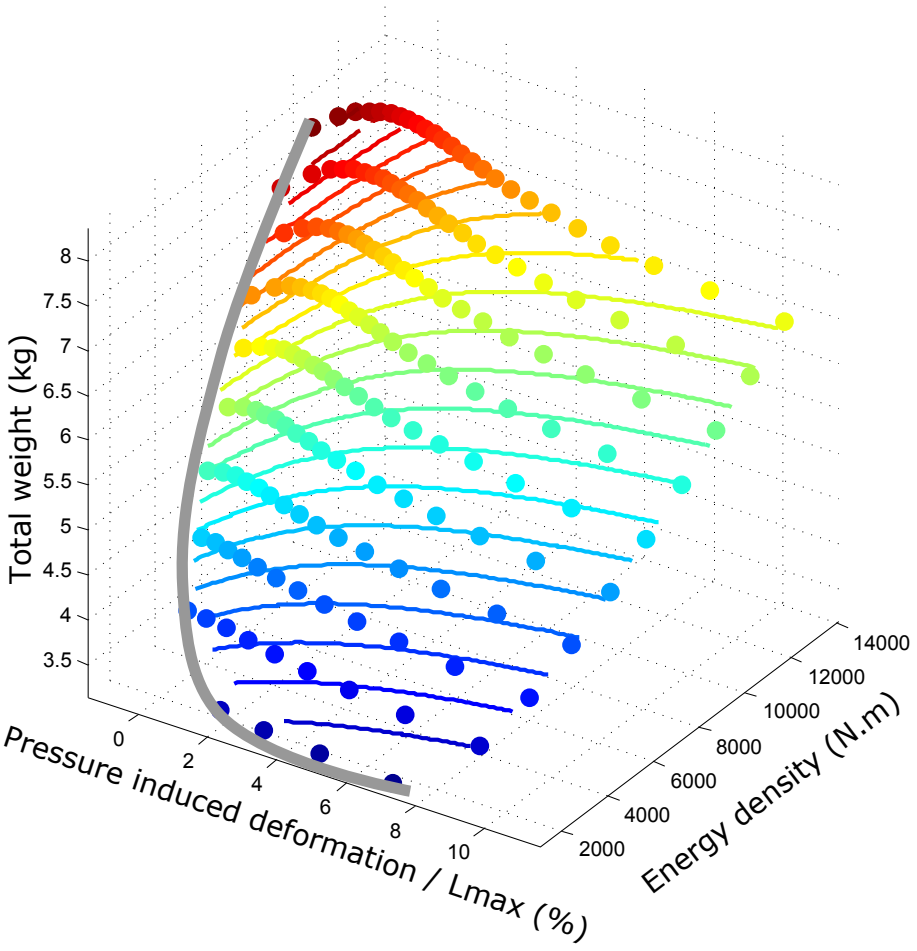

Figure 2.5: Influence of the parameter sets on the energy, the stiffness and the weight.

deviation of 10% of actuated chord, aluminum skins, actuated chord of 0.9 m, for a span section of 0.14 m, and aerodynamic pressure of 15 kPa representative of conditions of real aircraft flight.

Qualitatively, the stiffest solutions are the heaviest and request for more energy. On the opposite, the lighter the design, the more flexible. But a bad choice in design parameter may result in heavy, very flexible and high energy consumption solution (the designs located on the top right corner). The border depicted by grey line represents parameter sets that are at the limit of the specifications. There is no parameter set above this border that respects the displacement specification. Thus the best solution appears to be a compromise between flexibility, actuation energy and total weight. A good compromise can be located at the bottom left corner of the figure.

Finally, assuming small deformations and a simple geometry is questionable. The first results give indications towards the feasibility of a camber control wing, but a more detailed finite element model is developed in the following to complement this analytical model.

2.2.3 Finite element model

2.2.3.1 Model

In order to refine the results from the analytical model, and in order to model the contact between the upper and lower skin, mechanical finite element analysis (FEA) have been performed thank to ANSYS Mecahnical APDL software. The numerical computation software Mathworks MATLAB is coupled with ANSYS. Parameter sets are defined in a MATLAB code that writes an APDL source code. Then this source code is processed by ANSYS that performs the FEA computations. The nodal results are post-processed by the MATLAB code. This topology allows to try different configurations related to different parameter sets and contact places.

The FEA model is based on a 2D geometry presented in Figure 2.6a. Different elements are used to model the structure, the SMA wires, the contact and the links. The spanwise direction is taken into account with a out of plan thickness equal to the distance between two consecutive SMA wires. The skins are modeled by beam elements (BEAM188); the trailing edge is supposed rigid thank to solid beams (PMC184). The two SMA wires – one under the suction side, the other one under the pressure side – are modeled by taut wires; they are modeled by elements applying constant force between each anchor (COMBIN14). Contact between pressure and suction sides and the rigid trailing edge are modeled by beams (CONTA175) and targets (TARGE169). The two skin beams are clamped on the spar.

In reality, the SMAs are gliding in the anchors. The proposed model of the SMA does not consider the gliding link but the result is realistic because of the following analysis: every anchor behaves like a pulley/wire joint.

Figure 2.6b illustrates an anchor where F_{W1} and F_{W2} are the wire tensions, $F_{P/W}$ is the force from the pulley applied on the wire and $F_{P/S}$ is the force of the pulley applied on the skin. By isolating the elements {pulley + small amount of SMA wire around the pulley}, the relation between the forces describing the pulley and wire is analog to a system with wires fixed on anchor – as modeled in the FEA. The tension force of the elements corresponding to the SMA wires is computed as a function of the wire elongation. The length of a SMA wire is calculated as the addition of the wires' element lengths plus additional length

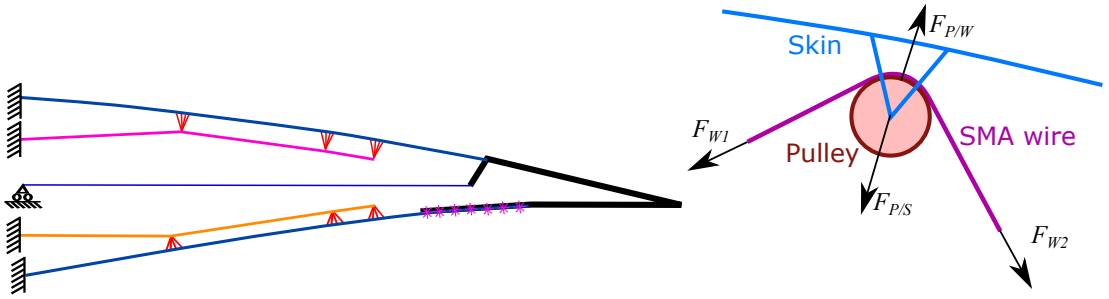

Figure 2.6: (a) Geometry of the finite element model. (b) Illustration of the pulley/wire link.

within the start and stop of the wire – not modeled in the simulation. Then an iterative algorithm coded in APDL finds the working point. If the wire is activated (respectively non activated), the wire is hot (cold) and its behavior corresponds to the force/elongation curve at 110° (26°) of Figure 2.3. The iterative routine proceeds as follows: for an applied wire's tension, a simulation is performed, then the wire length is evaluated. The elongation of the wire is therefore calculated. The force corresponding to this elongation is estimated by the SMA wire behavior of Figure 2.3. The difference between the applied force and the physical force corresponding to the resulting elongation is the convergence criteria. A new applied wires' tension is calculated from this criteria and the previous applied tension. A new simulation is performed and so on... This algorithm stops when the criteria is low. This means that the applied force matches the material behavior for the computed elongation.

2.2.3.2 Model validation

Before using the developed FEA model to design the new prototype, it has been validated using experimental results from a previous study. Scheller et al. [Sch15] have built a 40 cm chord morphing wing. Based on NACA4412 profile, the last 50% of the chord length embeds the same SMA wire implementation as investigated in the chapter. Figure 2.7a shows the prototype on its stand, ready for the Royal Society Summer Exhibition 2014[1]. Figure 2.7b presents a picture of the a actuated up-bending trailing edge, with superimposed simulation. The white lines present the initial shape, whereas the colored profile is the simulation result, where color-shades relates the nodal vertical displacement.

[1] http://sse.royalsociety.org/2014/

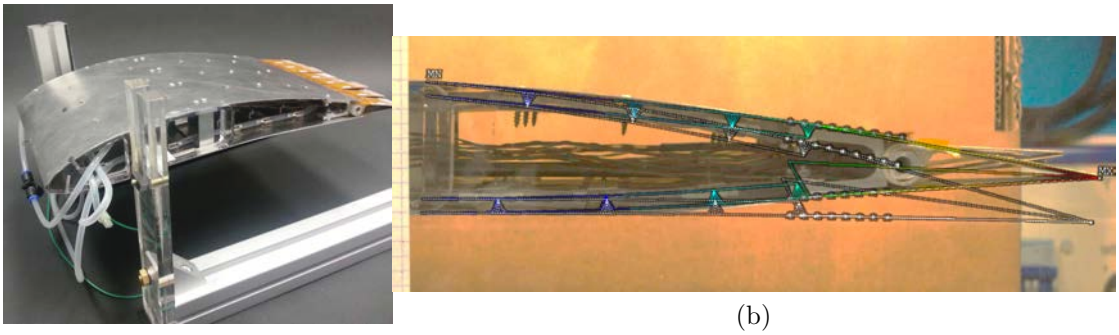

(a) (b)

Figure 2.7: (a) Picture of the RS1 prototype on its stand. (b) Actuated trailing edge with superimposed simulated deformed shape. [Sch15]

The experiment and the simulation match. This test bench has highlighted the design parameter sensitivity. A change in lever arm or in SMA wires' pre-strain has significant impact on the resulting deformation. The first one is due to a difference between the model and the experiment: the lever arm is fixed in simulation but experimentally the wires go through tubes. Depending on the movement, the wires touch one side of the internal diameter. This detail is easily fixed on the simulation by taking into account the internal diameter as an offset on the lever arms. The other source of difference is the accuracy of the pre-straining. Experimentally, an uncertainty of 0.5 mm during pre-straining a 20 cm wire cause a change in maximum force by hundreds of MPa. As a conclusion, the pre-strain has to be precisely adjusted for the experiment. A screw with locknut is integrated to adjust the pre-strain after the assembly.

2.2.3.3 Design of the new prototype

Approximately 70 sets of parameters have been simulated with different mechanical links at the solid trailing edge (i.e. gliding link or gliding contacts). The results of the final choice are visible on Figure 2.8. The 20 cm actuated section uses 1.5 mm thick aluminum foils for the two skins. SMA wires are distributed every 30 mm with 3% pre-strain. Anchors' lever arms are 5 mm for the suction side skin, and 4 mm for the pressure side skin.

Four different actuation and loading cases are computed. Figure 2.8a corresponds to the deformation due to the pre-strain cold SMA without aerodynamic loading. Figure 2.8b presents the deformation due to the pre-strain cold SMA with aerodynamic loading. Upwards actuation without aerodynamic loading (pressure side's SMAs are hot, suction side's SMAs are cold) is visible on Figure 2.8c. Finally, downwards bending under aerodynamic loading (pressure side's SMAs are

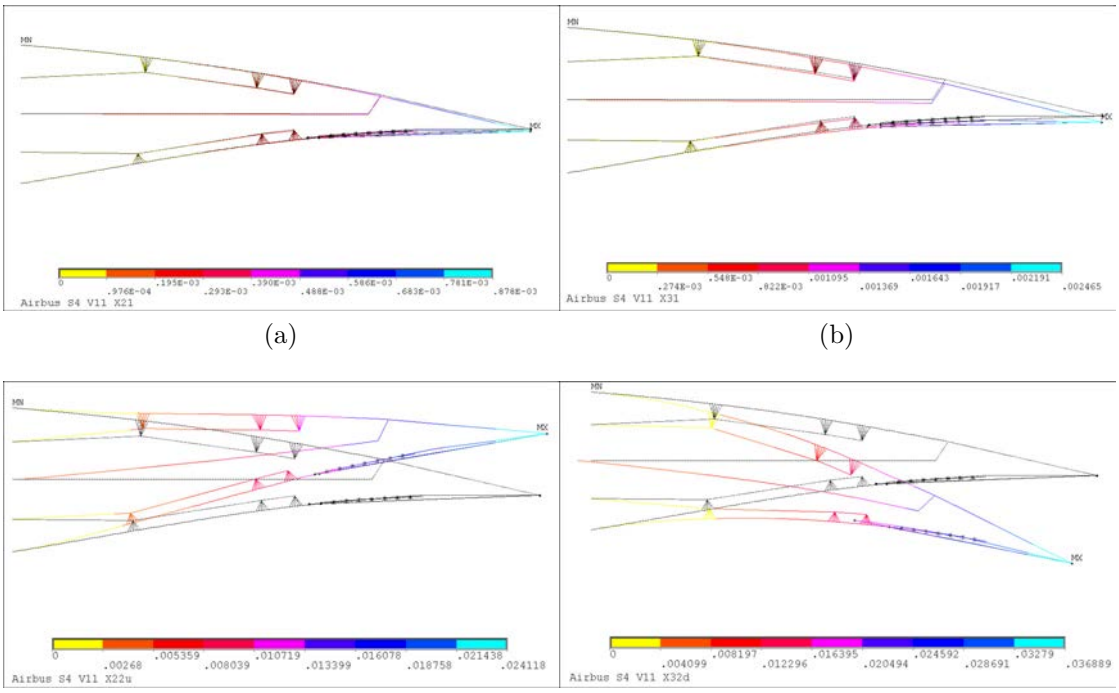

(a) (b)

(c) (d)

Figure 2.8: Simulation results for the selected parameter set. Color shades represent the nodal displacement amplitude.

cold, suction side's SMAs are hot) is presented on Figure 2.8d. The trailing edge deviations of all the cases respect the specifications introduced in 2.1.3.

2.2.4 An experimental platform for surface embedded SMAs

This section comes from the article G. Jodin, J. Scheller, E. Duhayon, J. F. Rouchon, M. Triantafyllou, M. Braza. "An Experimental Platform for Surface Embedded SMAs in Morphing Applications", *Solid State Phenomena*, Volume 260, pages 69-76, 2017, doi.org/10.4028/www.scientific.net/SSP.260.69.

A cantilever beam featuring the currently discussed technologies has been realized. This prototype helps in the design of the morphing wing prototype. Indeed, the purpose of such a prototype is the test of sensors and the development of control loops. The same sensors and control loops are implemented on the morphing wing. An electro-thermo-mechanical model of the system is developed and validated using this bending beam.

This work is developed as follows: in a first part the experimental setup is described, then an analytical model based on the works of Elahini [Ela04] is introduced to estimate the achievable deflection of the system. The experimental results are then shown and compared to the analytical model. Finally the results are discussed and a short conclusion is drawn.

2.2.4.1 Experimental setup

The experimental setup is illustrated in Figure 2.9a and the actual experiment is shown in Figure 2.9b. The SMA actuators which are embedded on the surface of the aluminum substrate are activated at different current intensities using a Delta SM 400-AR-8 Power Supply Unit (PSU). The Pulse-Width Modulated (PWM) control signal for both the PSU and the solenoid valve controlling the forced convection is generated using an Arduino Mega 2560 which also collects the strain gauge and temperature measurements. In order to channel the forced convection the embedded SMAs are encapsulated inside of a silicone tube which was selected due to its high temperature resistance and large flexibility.

The overall displacement is measured using a Mitutoyo linear gage. The measurement synchronization is done using a control PC running Matlab. The strain, voltage and current measurements are acquired at an acquisition frequency of 8 Hz, the temperature measurements are acquired at 1 Hz. Due to the limited temporal dynamics of the SMA actuators this low acquisition frequency was estimated to be sufficient. The temperature data was re-sampled using a linear approximation algorithm in order to adapt the measurements to the acquisition frequency of the Arduino.

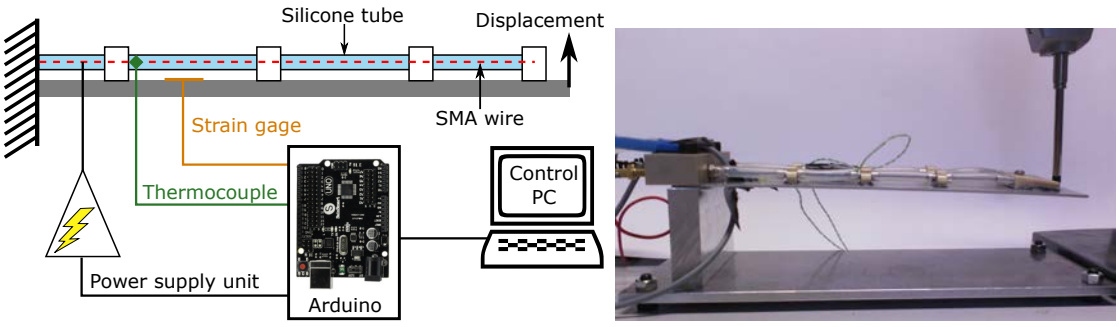

(a) (b)

Figure 2.9: (a) Experimental setup. (b) Picture of the experiment.

2.2.4.2 Analytical model

As previously mentioned, the derived actuator model is based on the phenomenological SMA model developed by Elahini [Ela04]. Due to the fact that phenomenological models are based on easily measured engineering quantities they are favored in engineering applications. In these models the phase-transformation dynamics are described by means of internal variables and the interdependence of these variables is modeled using kinetic equations. The structural behavior can be estimated using the quasi-static Euler-Bernoulli beam theory modeling the contraction and extension of the SMA actuator as a moment applied at a distance r of the beam's neutral layer. In this case the deflection δ of the beam can be written as 2.3.

$$\delta = \frac{\sigma \cdot A \cdot r \cdot L^2}{2 \cdot E \cdot I_g} \tag{2.3}$$

where δ is the deflection at the linkage between the SMA and the aluminium substrate, σ is the stress in the SMA, A is the SMA's cross-sectional area, L is the length of the substrate from the fixation to the linkage and E and I_g are the substrate's Young Modulus and area moment of inertia respectively. This allows us to define an equivalent spring constant k_{eq} for the use in the simulation model.

To simulate the prototype's response due to the SMA's actuation the previously described structural model will be combined with the phenomenological

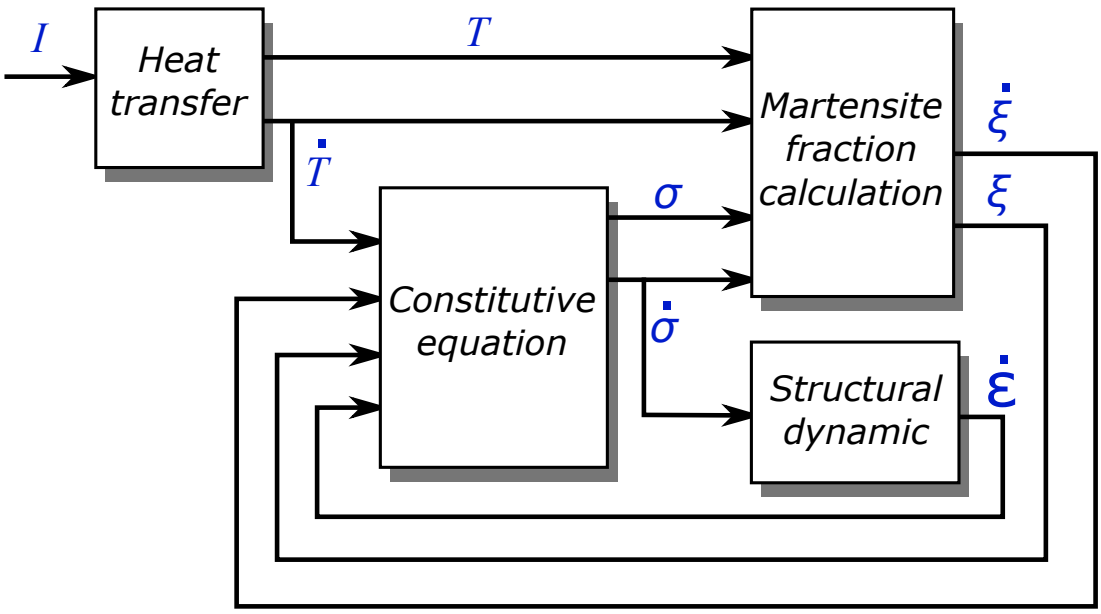

Figure 2.10: Block diagram of the combined SMA-structural model

Table 2.1: Simulation parameters

Parameter	Value		Parameter	Value
Radius r_{SMA}	$0.5 \cdot 10^{-3}$ m		SMA length cold	$227.5 \cdot 10^{-3}$ m
Density	6500 kg/m3		Heat capacity	320 J/kg°C
Convection coefficient	120 W/m^2 °C		Resistance	1.1 Ω
Initial/ambient Temperature	20 °C		Austenite Young modulus E_a	$75 \cdot 10^9$ Pa
Martensite Young modulus E_m	$28 \cdot 10^9$ Pa		Austenite start temp. A_s	30 °C
Austenite finish temp. A_f	75 °C		Martensite start temp. M_s	65 °C
Martensite finish temp. M_f	25 °C		Stress influence coefficient cA	10.3 Mpa/°C
Stress influence coefficient cM	10.3 Mpa/°C		Substrate thickness	$1.5 \cdot 10^{-3}$ m
Substrate width	$33 \cdot 10^{-3}$ m		Substrate length @ SMA interface	$165 \cdot 10^{-3}$ m
Substrate length total	$195 \cdot 10^{-3}$ m		Substrate Young Modulus E	$69 \cdot 10^9$ Pa
Distance SMA to neutral layer r	$2.5 \cdot 10^{-3}$ m			

SMA model as defined by Elahini [Ela04]. The simulation is created using the Matlab/Simulink platform. The block diagram of the combined SMA-structural model is shown in Figure 2.10. The model forms an algebraic loop as the SMA's behavior is dependent on both stress and temperature of the actuator. Hence, an iterative solution has to be conducted. The parameters were mainly taken from previous experiments as well as from the literature [Ela04], [Duv05] and can be seen in the table above. The equations describing the heat transfer, the phase transformation, the structural dynamics as well as the relationship between stress, strain and temperature in the SMA will only be briefly repeated below for a thorough explanation please refer to Elahini [Ela04].

Heat transfer. The SMAs are activated using Joule heating. The differential equation governing the SMA's heat transfer is given in the equation 2.4. It combines Joule heating with natural convection.

$$\dot{T} = \frac{1}{m_{SMA} \cdot c_p}(I^2 \cdot R - h_c \cdot A_c \cdot (T - T_\infty)) \tag{2.4}$$

In this Equation m_{SMA} is the mass per unit length of the SMA, A_c is the surface area of the wire, I is the current applied, c_p is the specific heat, T is the temperature of the SMA, T_∞ is the ambient temperature and h_c is the coefficient of heat convection. For the purpose of this simulation the resistance R of the wire is assumed constant.

Phase transformation. The phase transformation in the actuator is governed by the martensite fraction, which has to be known for each instant in time and can be calculated knowing the temperature, the stress and their derivatives. Due to the SMA's hysteretic nature the description of their phase transformation behavior depends on the previous state of the system. In case the system was previously in the austenite state and is being transformed into the martensite state the transformation is called the forward transformation (see equation 2.5). In the inverse case a so called reverse transformation is taking place as described by equation 2.6. In both cases the phase transformation is expressed in the form of the time derivative of the martensite fraction ξ.

$$\dot{\xi} = \frac{\xi_A - 1}{2}\sin(A_m \cdot (T - M_f + B_m \cdot \sigma) \cdot (A_m \cdot \dot{T} + B_m \cdot \dot{\sigma}) \tag{2.5}$$

$$\dot{\xi} = \frac{-\xi_M}{2}\sin(A_a \cdot (T - A_s + B_a \cdot \sigma) \cdot (A_a \cdot \dot{T} + B_a \cdot \dot{\sigma}) \tag{2.6}$$

The variables ξ_M and ξ_A represent the martensite fraction at the beginning of the A $\rightarrow$ M and M $\rightarrow$ A transformation respectively. A_a, A_m, B_a and B_m can be calculated via equation 2.7 knowing the material properties given in the table below. A_s, A_f are the start and finish temperature of austenite creation and respectively M_s, M_f are the start and finish temperature of martensite creation. Variations on temperature linked to stress are represented through c_m and c_a.

$$A_a = \frac{\pi}{A_s - A_f} \quad A_m = \frac{\pi}{M_s - M_f} \quad B_a = \frac{-A_a}{c_a} \quad B_m = \frac{-A_m}{c_m} \tag{2.7}$$

Constitutive equation. The relationship between the different variables governing the actuators behavior is given as equation 2.8, where $E(\xi)$ is the Young modulus, ϵ is the strain, θ is the thermoelastic tensor and $\Omega(\xi)$ the transformation tensor.

$$\dot{\sigma} = E(\xi) \cdot \dot{\epsilon} + \theta \cdot \dot{T} + \Omega(\xi) \cdot \dot{\xi} \tag{2.8}$$

It should be kept in mind however that the model assumes a fully detwinned martensite and hence does not model the detwinning process.

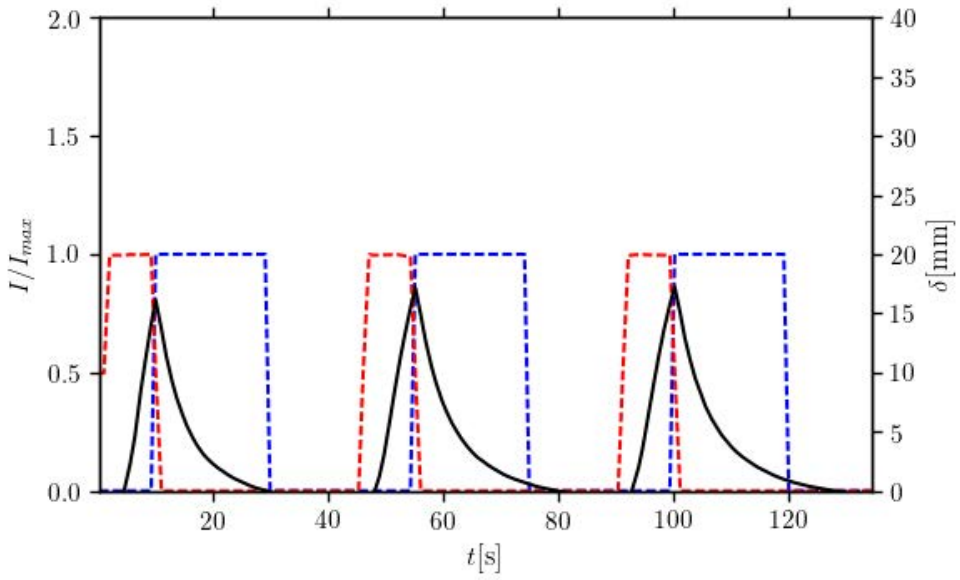

Figure 2.11: Measurement cycle at 4 A (black: tip displacement, blue cooling cycle (when active) and red heating cycle).

2.2.4.3 Results

After this very brief introduction to the analytical modeling procedure, the experimental results are focused. A measurement cycle is shown in Figure 2.11. The measurement cycle is repeated every 45 s. The SMAs are heated during 9.8 s at different current intensities and depending on whether cooling via forced convection is used or not a forced convection cooling cycle of 20 s follows the heating. These heating and cooling times are relevant with system dynamics because cooling is slower than heating. The remaining dead times allow the system stabilization over the cycles. In order to compare the different results the measurements are averaged over the active cycle from the beginning of the heating process to the end of the forced convection cooling. The results of this averaging process are shown in Figure 2.12a for the measurements without forced convection and in Figure 2.12b for the measurements with forced convection. Comparing these two graphs two things stick out: first as expected the forced convection significantly improves the cycle time allowing for faster actuation and second the measurements at higher current intensities have a significantly larger standard deviation and a lower maximum achievable deflection. Whereas this seems counterintuitive it is actually more due to the thermal characteristics of the system than due to the SMAs characteristics.

Taking a look at the measurement cycle at 6 A with and without forced convection (Figure 2.13) clearly show that even during the relatively long cycle time

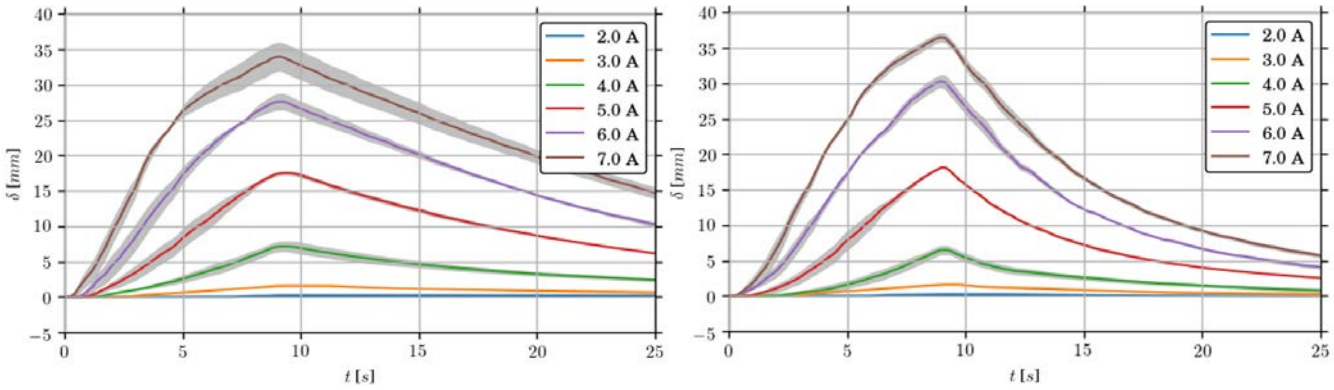

(a) (b)

Figure 2.12: (a) Averaged displacement VS time *without* forced convection. The grey envelope represents one-time the standard deviation averaged over three iterations. (b) Averaged displacement VS time *with* forced convection. The grey envelope represents one-time the standard deviation averaged over three iteration.

the SMA is not completely cooled down hence at the beginning of the subsequent cycle not the entire potential of the actuators can be realized. Furthermore, as mentioned in [Jay+05] the higher starting temperature might even be counterproductive due to the higher convection at higher temperatures. Hence, as the time dynamics depend largely on the initial temperature a control systems is necessary in order to implement this control an indicator of the trailing edge deflection is necessary. Whereas different publications either use a force-based [FT06] or a resistance/inductance [Kim+12], [MSL04] based approach, a strain-gage position feedback was selected in this paper due to the relative simplicity of implementation as well as the fact that the measured deformation is on the structure and the low cost of the sensors. Comparing the averaged measurement values to the averaged measured strain in mV we can see that this type of simple sensor is indeed capable to accurately represent the deformation achieved by the prototype. Figure 2.14a depicts the displacement VS strain response of the system for different current intensities. However, whereas a near liner response can be observed between the measured tip displacement and the measured voltage it also becomes evident that a saturation occurs once the displacement surpasses 20 mm. In order to avoid this kind of saturation an a-priori knowledge of the achievable displacement is necessary. Hence, the next paragraphs will briefly compare the achieved displacement during the measurements with the results obtained using the combination of the phenomenological model developed by Elahini [Ela04] and the structural behavior.

Result comparison. Figure 2.14b shows the comparison of the analytically obtained results and the experimental results with forced convection. A good cor-

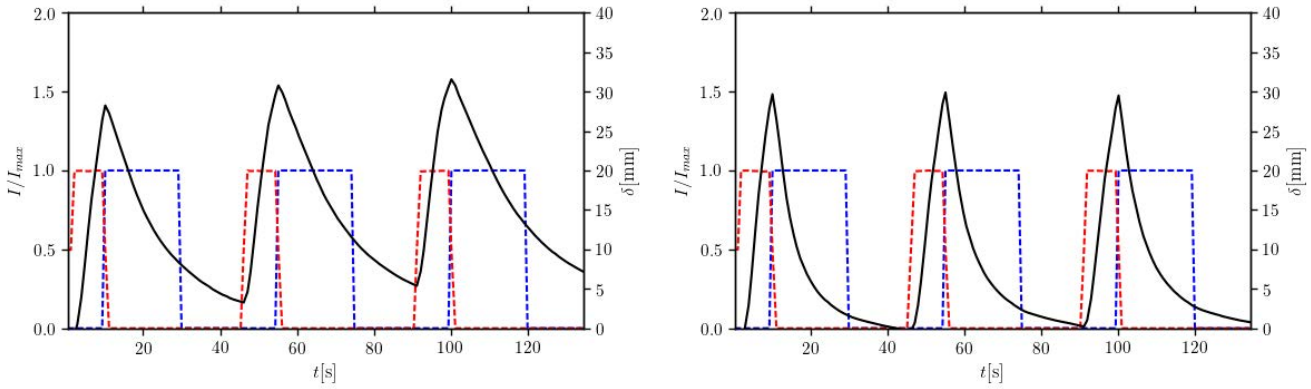

(a) (b)

Figure 2.13: (a) Measurement cycle at 6A without forced convection (black: tip displacement, blue cooling cycle (when active) and red heating cycle). (b) Measurement cycle at 6 A with forced convection (black: tip displacement, blue cooling cycle (when active) and red heating cycle).

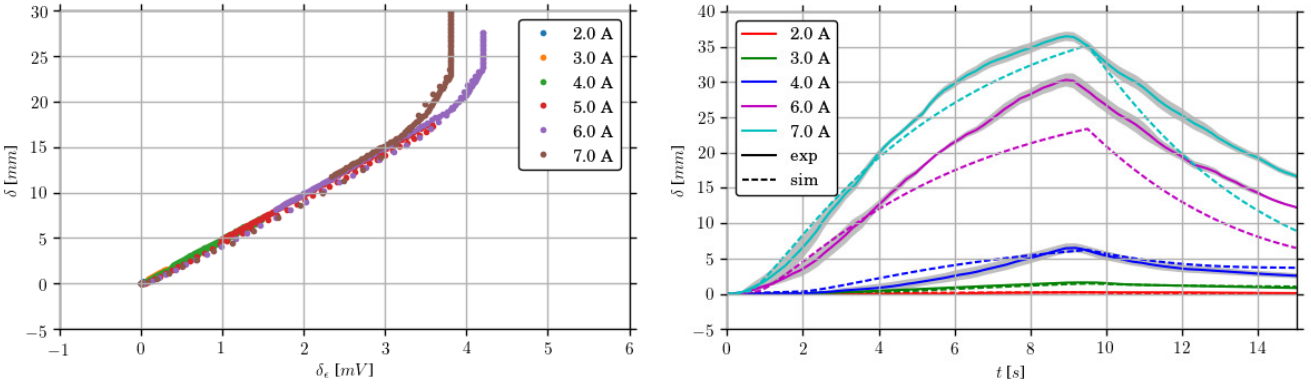

(a) Displacement vs. strain response of the actuated flat plate.

(b) Exerimental results VS analytical simulation.

respondence both quantitatively and qualitatively can be observed between the analytical and experimental results. However, whereas during the heating section the simulation results follow the trajectory of the experiment a larger difference can be observed during the cooling portion of the cycle. In order to account for this behavior a more thorough investigation of the temporal dynamics of the experimental setup is necessary especially regarding the heat exchange with or without forced convection in both a constraint and unconstrained environment. In other words the temperature exchange in the silicone tubes has to be more

deeply analyzed. Furthermore for a better understanding of the SMAs properties the variation of the SMA properties during repeated cycles should be taken into account. However, even though the simulation results show room for improvement it is notable that even using this simple simulation model as well as the SMAs properties obtained from previous experiments and the literature a good correspondence between simulation and measurement can be obtained.

2.2.4.4 Conclusion

This paper presented a simple experimental prototype for the analysis of the behavior or SMA actuators. The goal was to generate an extensible platform for characterization of surface embedded SMAs allowing to implement different control approaches as well as both forced and natural constraint convection cooling. It was shown that using forced convection the cycle time can be significantly reduced by up to 30%. Furthermore, due to temperature variation of the SMA during the cycle in the natural constraint convection case the use of forced convection also allows for smaller standard deviation and larger average temperature. Moreover, a simple low-cost position feedback was introduced in the experimental platform. The simplicity of the linear relationship between displacement and measured strain was highlighted. However, it was shown that care has to be taken as saturation can occur especially at larger values of deflection. Finally, in order to gain an a priori knowledge of the displacement, a combination of a phenomenological SMA model with a simplified structural model was introduced and it was shown that however simple this model a good quantitative and qualitative correspondence during the heating cycle can be obtained. However, it was also shown that due to the added complexity by thermally constraining the actuators a more in-depth analysis of the thermal behavior of the platform is necessary.

In summary this work showed a simple platform for evaluating different SMA control strategies characterized its deflection behavior both using forced and natural convection and also developed a mean to analyze the platform using a simulation model. This allows in a next step to create and validate different control approaches enabling potentially larger cycle times.

2.3 Higher Frequency Trailing Edge design

2.3.1 Actuator description

As specified in section 2.1.3, the purpose of the vibrating actuator is to displace the trailing edge tip by 1 mm amplitude with actuation frequencies over 100 Hz. The retained solution is composed of a metallic substrate sandwiched between two "Macro Fiber Composite" (MFC) piezoelectric patches, as described in Figure 2.14b. The whole is covered by a flexible molded silicon that gives the trailing edge shape. The MFC patches are LZT piezoelectric fibers and electrode networks encapsulated within epoxy. They are sold by the firm Smart Material GmbH. On the wing prototype, the actuator's active length is 35 mm. Figure 2.14a presents a small prototype of a composite piezoelectric beam inside its silicone cover (the picture prototype is 60 mm long). In the following, the sizing is decomposed twofold: the piezoelectric vibrating beam is firstly design without the cover. Then the silicone cover is designed in order to limit its impact on the actuator performances.

2.3.2 Actuator modeling

2.3.2.1 Active part modeling

In a first time, the silicone cover is not taken into account, for simplicity purpose. The design focuses on the vibrating composite piezoelectric beam. The proposed approach is based on the work of Ballas [Bal07], itself based on Euler-Bernoulli beam theory, on linear piezoelectricity, on linear elasticity and on thermodynamics.

Thus, an analytical model of the actuator has been developed to assess the

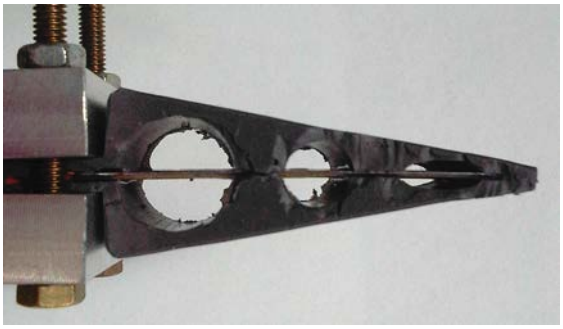

(a)

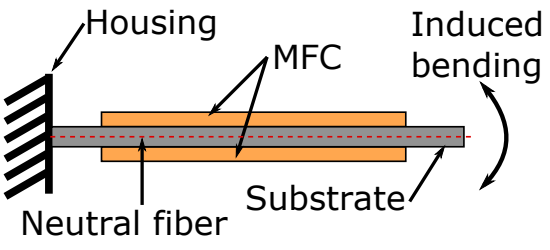

(b)

Figure 2.14: (a) Actuator prototype. (b) Diagram of vibrating piezoelectric composite beam.

performances. Assuming small deformations induced by the MFC, the actuator is modeled as an Euler-Bernouilli cantilever beam. Diagram in Figure 2.14a illustrate the model. In this case, the equation 2.9 depicts the displacement dynamics, and is given in [Ert+08]. M, u ρ, A and c_a respectively stand for the internal bending moment, the transverse deflection, the density, the cross section and the damping coefficient.

$$\frac{\partial^2 M(x,t)}{\partial x^2} + \rho \cdot A \cdot \frac{\partial^2 u(x,t)}{\partial t^2} + c_a \cdot \frac{\partial u(x,t)}{\partial x} = 0 \tag{2.9}$$

Using the piezoelectricity equations proposed in IEEE standards [88], the bending moment is expressed in equation 2.10, where Y is the Young modulus of the materials, I is the second moment area of the cross section, $V(t)$ is the voltage applied to the MFC and Γ the piezoelectric coupling constant given by equation 2.11.

$$M(x,t) = Y \cdot I \frac{\partial^2 u(x,t)}{\partial x^2} + \Gamma \cdot V(t) \tag{2.10}$$

$$\Gamma = -\frac{d_{33} \cdot Y_{MFC} \cdot w_{fiber} \cdot n_{fibers}}{2 \cdot \Delta_{el}} \cdot (z_2^2 - z_1^2) \tag{2.11}$$

These expressions correspond to only one piezoelectric actuator. In equation 2.11, Y_{MFC} is the equivalent Young modulus of the MFC, n_{fibers} the amount of fibers, w_{fiber} the fibers' width. z_1 (respectively z_2) is the distance between the neutral fiber and the bottom (respectively the top) of the piezoelectric fibers. Δ_{el} is the effective length between the electrodes. The transfer function in equation 2.12 is get by solving equation 2.9.

$$H_s(j \cdot \omega) = \frac{u(x,t)}{V(t)} = \sum_{i=1}^{N} \frac{\Gamma}{j \cdot \omega} \frac{W_i(x) \cdot \xi_i}{\frac{\rho \cdot A \cdot L^4}{Y \cdot I \lambda_i^4 \cdot j \cdot \omega} + j \cdot \omega + \frac{2 \cdot c_a \cdot \omega_i}{\rho \cdot A \cdot \omega_1}} \tag{2.12}$$

This equation is the sum of participations from N modes. The ξ_i coefficients represent the electric field distribution within the MFC (taking into account the non-uniform field distribution due to the electrode topology, [Ert+08]). The $W_i(x)$ are proper functions normalized to the mass. The expression of the $W_i(x)$ depends on eigenvalues λ_i and is reported in equation 2.13.

$$\begin{aligned} W_i(x) = \sqrt{\frac{1}{\rho \cdot A \cdot L}} \Bigg[& \cos(x \cdot \frac{\lambda_i}{L}) - \cosh(x \cdot \frac{\lambda_i}{L}) + \\ & \frac{\sin(\lambda_i) - \sinh(\lambda_i)}{\cos(\lambda_i) - \cosh(\lambda_i)} \cdot \left(\sin(x \cdot \frac{\lambda_i}{L}) - \sinh(x \cdot \frac{\lambda_i}{L}) \right) \Bigg] \\ & \lambda_i \text{ are solutions of } 0 = 1 + \cos(\lambda) \cdot \cosh(\lambda) \end{aligned} \tag{2.13}$$

In order to validate the model, a measurement campaign have been performed on different MFCs and substrates. The configurations are summed up in table 2.2. The actutators' tip volicities have been acquired by a Polytec Laser Vibrometer CLV-1000. The power supply is a high voltage amplifier PI HVPZT. A signal analyzer HP 3562 records the frequency responses. Experimental setup is presented in Figure 2.15a It can be ween that experimental results and analytical results are in good accordance up to approximately 100 Hz. Differences in amplitude are visible for the bi-morph configuration (i.e. two patches are glued on both sides of the metallic substrate. These differences can be attributed to a different damping value. Globally the simulations are accurate enough to estimate the first resonance frequency with the velocity amplitude. In conclusion, a 35 mm length actuator composed of a 0.30 mm thick substrate with two MFC patches reaches millimeter deformations up to the first resonance mode around 250 Hz.

2.3.2.2 Elastomeric cover design

Analytical remarks.
Now the sizing of the piezoelectric vibrating beam is designed, the silicone cover is designed. The decoupling of the active vibrating beam and the over simplifies the study. Consider a straight homogeneous beam with constant cross section. The product of its elasticity modulus by its second moment area is noted $E_p \cdot I_p$. e_p is its thickness. This beam is covered by a triangle silicone cover - i.e. the cover's thickness is a linear function of the abscissa x, as visible in Figure 2.16a. The product of elasticity modulus by second moment area of the cover at a given abscissa is noted $< E \cdot I >$ and is expressed in equation 2.14.

$$\begin{aligned} < E \cdot I > &= E_p \cdot I_p + E_s \cdot \left(\frac{b \cdot h(x)^3}{12} - \frac{b \cdot e_p^3}{12} \right) \\ &= E_p \cdot I_p + E_s \cdot \left(\frac{b \cdot (H \cdot (1 - \frac{x}{L}))^3}{12} - \frac{b \cdot e_p^3}{12} \right) \end{aligned} \tag{2.14}$$

$$\frac{\mathrm{d}^2 y(x)}{\mathrm{d}x^2} = \frac{M_{piezo}}{< E \cdot I >} \tag{2.15}$$

Table 2.2: Characteristics of the tested bending actuators.

Reference	Substrate	Substrate thickness	MFC type
4312 b 0.3	Stainless steel	0.30 mm	4312 (60 mm x 21 mm)
8514 u 0.25	Stainless steel	0.25 mm	8514 (101 mm x 20 mm)
8514 u 0.5	Stainless steel	0.50 mm	8514 (101 mm x 20 mm)

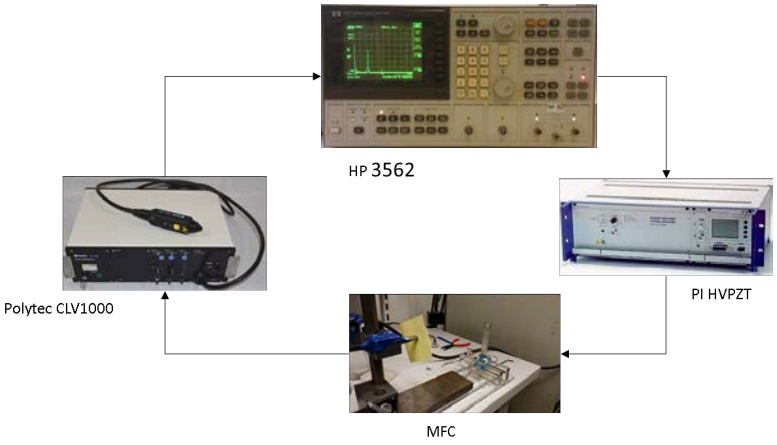

(a)

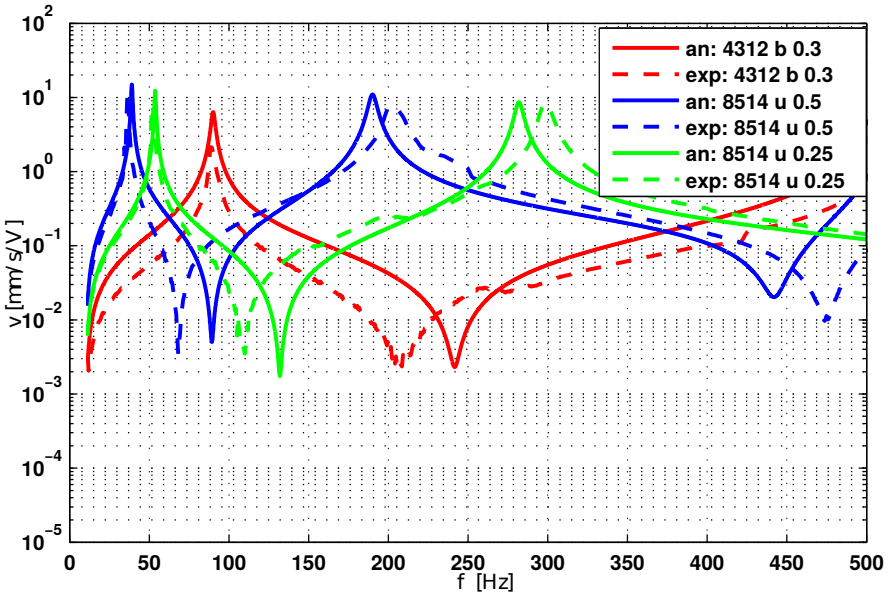

(b)

Figure 2.15: (a) HFVTE experimental setup. (b) Tip velocity frequency response of the different vibrating beams compared to the analytical models. Letters u stand for unimorph and letters b stand for bimorph.

The calculus of the deformed shape is then given by equation 2.15, where $y(x)$ is the transverse displacement along the neutral fiber and M_{piezo} is the bending moment due to the piezoelectric materials. Then it is possible to compare the deformation amplitude with and without the silicone cover. Figure 2.16b presents the values of $< E \cdot I >$ as well as the neutral fiber static displacement for different covers. The investigated covers start with 0% (no cover) to 100% silicone (fully

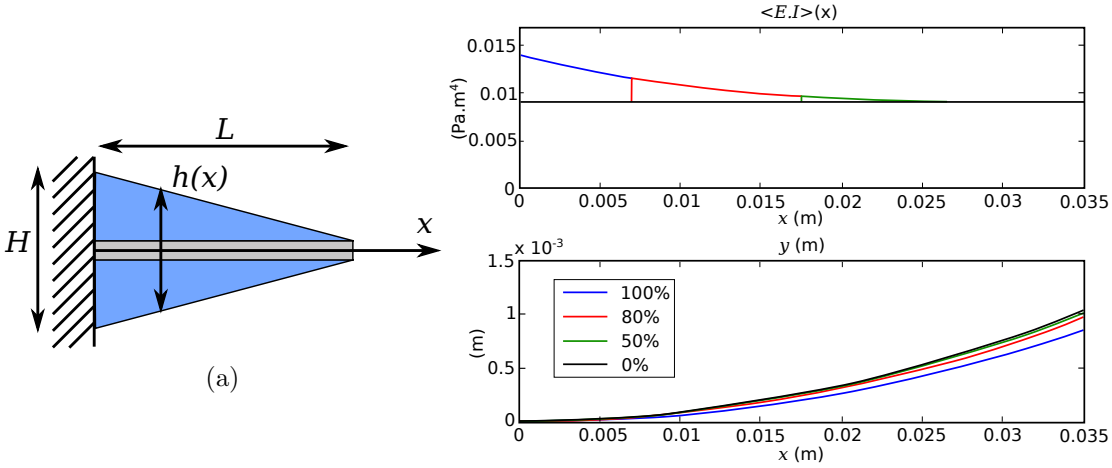

(a) (b)

Figure 2.16: (a) Covered actuator model. (b) Diagram of vibrating piezoelectric composite beam.

covered), where the percentage represents the position on the beam where the cover starts. It can be notice that a cantilever beam with the first 20% length free of cover increases the deflection by 13% compared to the fully covered one. Additionally, freeing the remaining 80% only increases the deflection by 5% more. Thus, matter close to the fixation of the beam slightly decreases the deformation amplitude.

The influence of matter close to the beam tip has also an important influence. If its effect is limited on the static deflection, its impact on the dynamic is important. Let assume the beam is vibrating under the first resonance, so in quasi-static regime. It can be assumed that the deformation is quadratic. The actuation energy from the patches is converted into momentum. As the actuation energy is limited by the active material capabilities, this energy requirement have to be limited by design to expect a good dynamic of the actuator. Then the amount of energy expressed in 2.16 represent the momentum, where y_0 is the vibration amplitude of the tip, ω is the vibration pulsation and $\rho(x)$ is the linear density.

$$k(t) = \int \frac{\mathrm{d}y}{\mathrm{d}t} \cdot \mathrm{d}m = \int_0^L y_0 \cdot \left(\frac{x}{L}\right)^2 \cdot \sin(\omega \cdot t) \cdot \rho(x) \cdot \mathrm{d}x \tag{2.16}$$

The calculus of the momentum of beams with different covered parts (this time, the cover starts from the housing and stop at a given percentage) is performed. It results that the matter close to the housing has a low influence on the dynamics, but uncovering of the 40% beam length closed to the tip allows a decrease in momentum by 30% at constant frequency and amplitude. This result is rele-

vant compare to the maximum 50% decrease in momentum if the cover is totally removed.

These two observations highlight that the cover must be hollowed close to the housing as well as close to the tip, as presented in Figure 2.14a. A finite element model is developed to further investigate hollowed shapes.

Finite element analysis of the cover.

The finite element model consists in a 2D analysis of a beam. This beam length and thickness give resonance frequencies close to the previously designed active vibrating beam. Here, no piezoelectric material is considered on the beam; the work is focused on the behavior of the silicone cover. For each investigated cover, two simulations are performed: a static one corresponding to simple bending with a transverse force applied on the tip, and the computation of the first resonance modes. Figure 2.17 introduces few results. The left column contains the first resonance mode for different covers, and the right column contains the corresponding static deformed shapes. The results are summed up in Figure 2.18. Configurations with one to three holes and with different span densities (i.e. the cover is repeatedly gutted along the span) are compared to the non-covered beam. The solution with three holes located at 15%, 40% and 64% of the beam length stating from the housing, and with a 20% spanwise density has the best static displacement with a bandwith over 100 Hz. This cover is selected as the definitive solution.

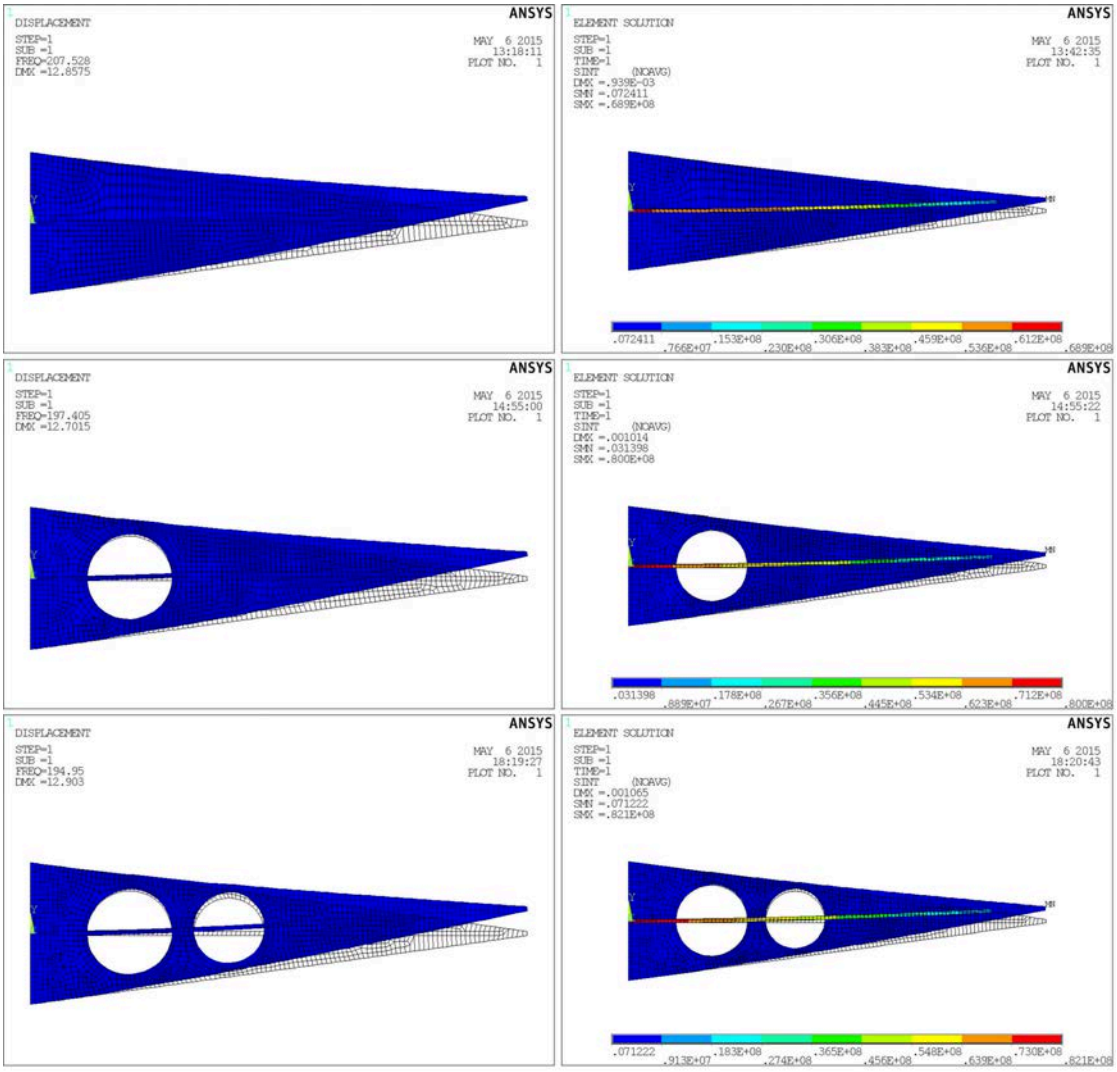

Figure 2.17: Some simulation results of the covered beams. Left column contains the first resonance mode and the right column contains the corresponding static response.

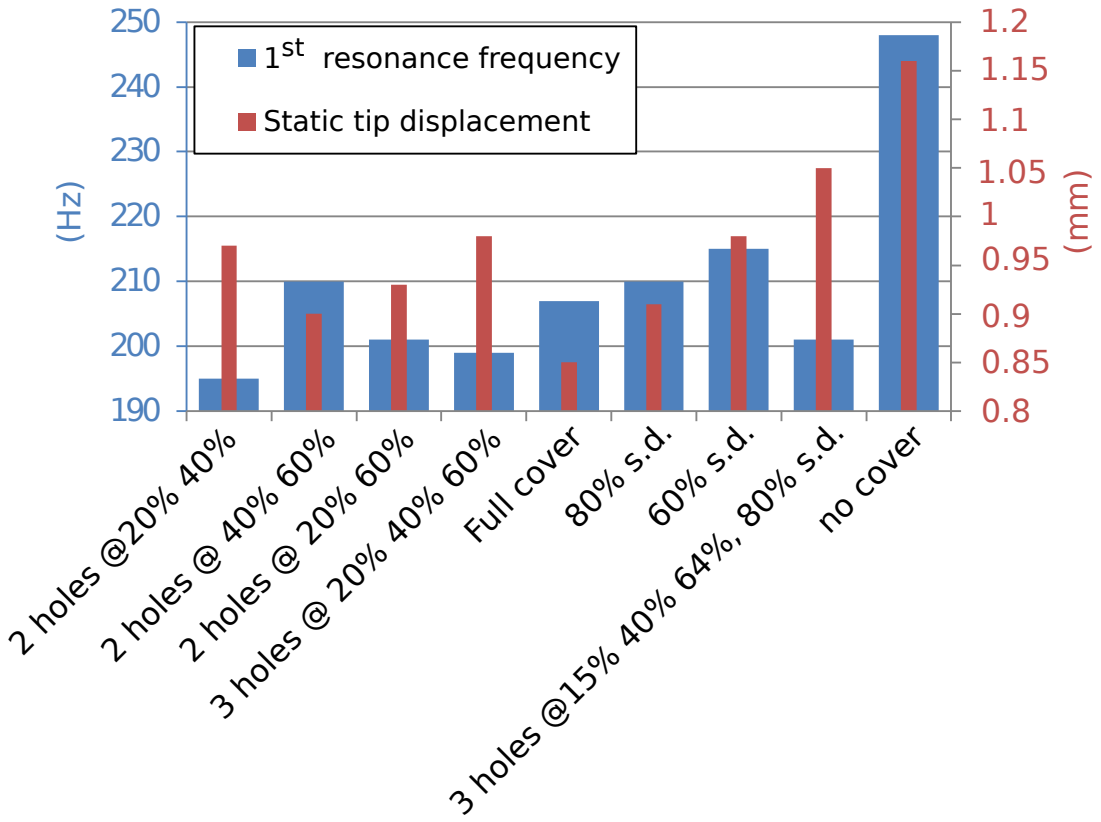

Figure 2.18: Summary of the simulation results: impact on first modal frequency and static displacement. The letters **s.d.** stands for spanwise density; holes' positions are indicated in total length fraction.

2.4 Features and making of the hybrid electroactive wing prototype

This section briefly describes the technological choices regarding the wing prototype. A CAD model has been developed, and a view is presented on Figure 2.19. The assembly counts approximately 500 parts. The fixed part is made from milled wood profiles that are glued together with aluminum stiffeners, as visible in Figure 2.20a. A door made of aluminum sheet allows the access to the wires and embedded electronic devices (visible in Figure 2.20a and Figure 2.20h. Milled aluminum – for strength – and plastic (PEEK) – for electric insulation – parts are assembled for the camber control actuator, as presented in Figure 2.20b. The 3D printed anchors (in Ultem^{TM} resin) are glued on the skins, using cured Epibond 420 A/B epoxy glue. Figure 2.20c depicts the assembly of one side of the camber actuator. Figures 2.20d, 2.20e and 2.20f describe the silicone cover, the wired MFC and an assembled HFVTE actuator. 50 MFC patchs are precisely glued and independently wired to 100 supply wires. All the wires from the patches have been braided for electromagnetic compatibility reasons. The hybrid morphing active parts – i.e. the trailing edge with the actuators – are assembled and tuned on a test bench presented in Figure 2.20g. The trailing edge is covered with an extra taut latex film to ensure the airtightness of the wing. Then the mock-up is finally closed with a final black cover for optical measurement purpose, as visible in Figure 2.20h. Figure 2.20i shows the SMA power supply rack with the Arduino based control card. Figure 2.21 presents the devices and interface that are used to calibrate and control the wing before and during the wind tunnel experiments.

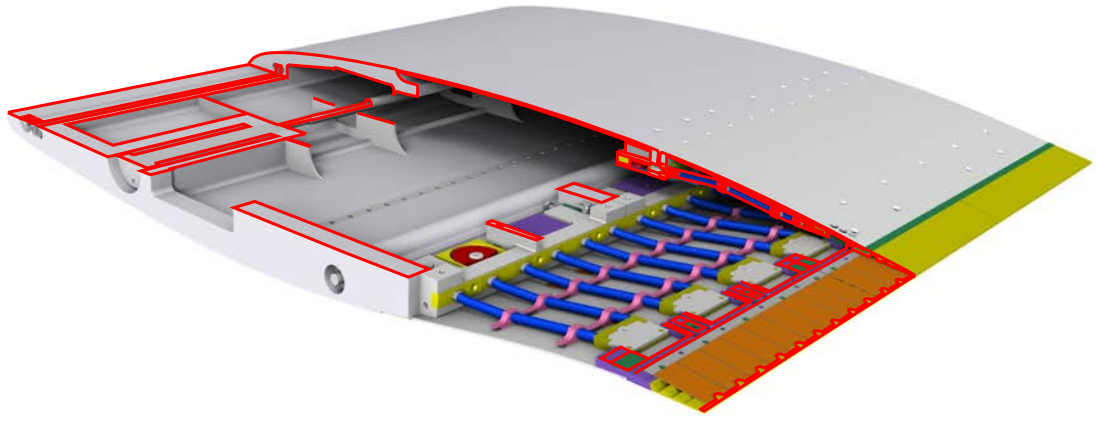

Figure 2.19: A CAD partial sectional view of the wing design. Screws, wires and sensors are not represented. Cut sections' edges are highlighted in red.

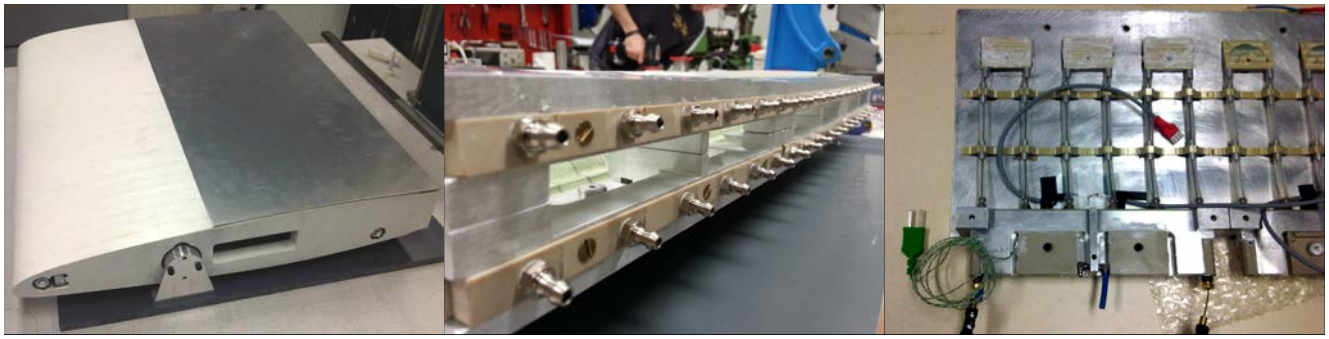

(a) Fixed hollow wood leading edge. (b) Fixed/morphing interface. (c) SMA actuator with sensors.

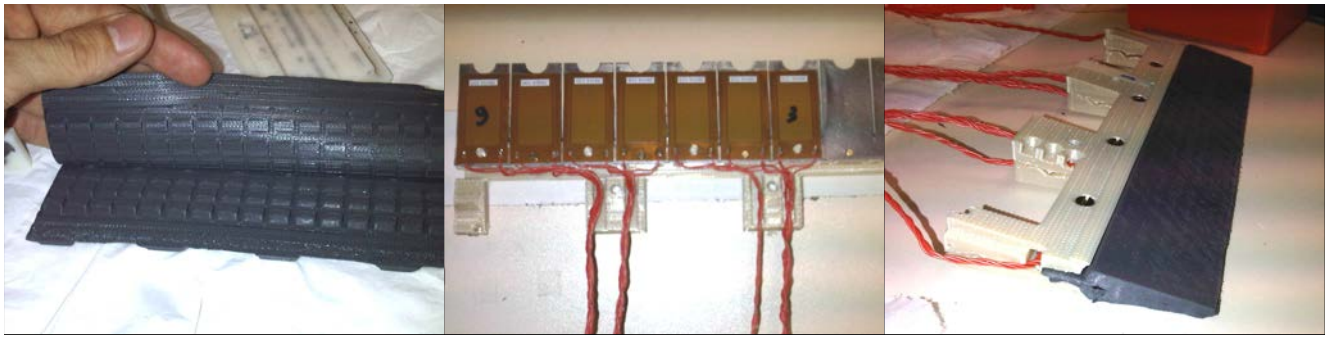

(d) Molded silicone cover. (e) Wired HFVTE actuator. (f) Assembled HFVTE actuator.

(g) Hybrid morphing test bench. (h) Assembled wing prototype. (i) SMA controler and power supply.

Figure 2.20: Making of the wing prototype.

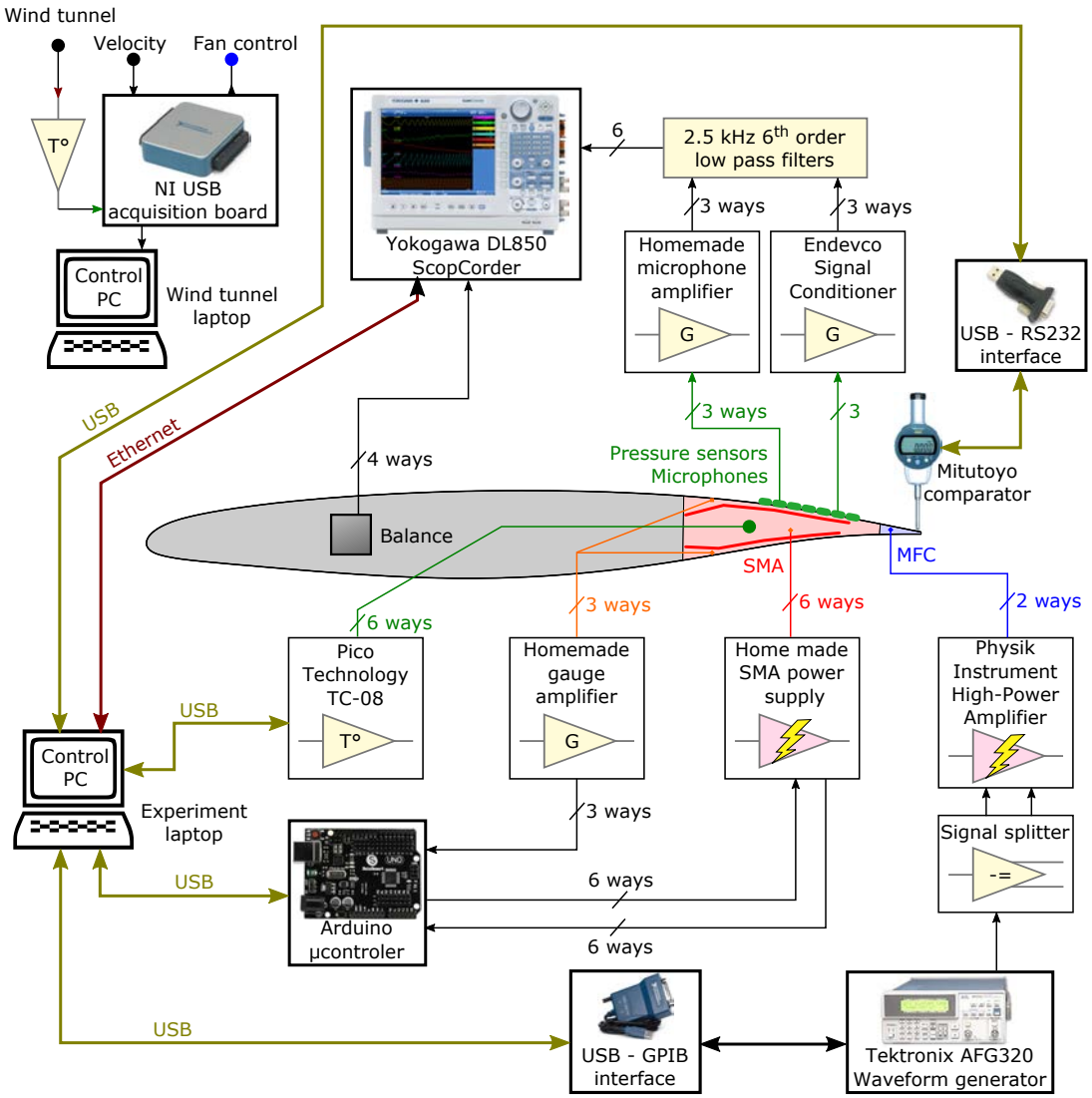

Figure 2.21: Schematic of the experimental set-up, control and interface point of view.

2.5 Electrodynamic characterization

This section comes from the conference proceeding: G. Jodin, J. Scheller, J.F. Rouchon, M. Braza. "On the multidisciplinary control and sensing of a smart hybrid morphing wing, *2017 IEEE International Workshop ofElectronics, Control, Measurement, Signals and their Application to Mechatronics (ECMSM)*, `https://doi.org/10.1109/ECMSM.2017.7945866`
This contribution has received the Best paper award.

To the authors' knowledge, the originality of the present work is the study of the links between camber control, vibrating trailing edge and the airflow dynamics. Previous work has primarily targeted the Micro Air Vehicle (MAV) scale; now the purpose of the present work is the up-scaling towards commercial passenger airliners. In cooperation with Airbus, a first step is a reduced scale wing with an innovative electroactive hybrid morphing flap design. This section firstly introduces the wing prototype. Secondly, a focus on the link between control law, power consumption and actuator design is provided. Thirdly, wind tunnel experimental results are presented; showing some answers on the use of embedded sensors to estimate morphing performances.

2.5.1 Electroactive hybrid morphing wing prototype

2.5.1.1 Hybrid morphing

The airflow around a wing can be decomposed in two space-time domains: a global time averaged effect - influenced by large wing shape deformation at low frequencies - and small amplitude higher frequency dynamics - influenced by small amplitude but higher frequency actuation. These two different effects justify the use of two actuators based on two different electroactive materials. The here presented morphing wing embeds both *camber control* and *Higher Frequency Vibrating Trailing Edge (HFVTE)* actuators. Figure 2.22 presents the hybrid morphing prototype. The chord length is 700 mm, the span is 590 mm.

2.5.1.2 Higher Frequency Vibrating Trailing Edge actuator

The HFVTE actuation system is based on piezoelectric Macro Fiber Composite (MFC) patches which expand in length when subject to an electric field. Piezoelectric patches are glued on both sides of a metallic substrates. By alternatingly applying a voltage to the patches, the patches generate a bending moment which results in actuator vibration. To respect the shape of the airfoil, the HFVTE actuators are placed at the trailing edge, covered by a specifically designed silicone shell.

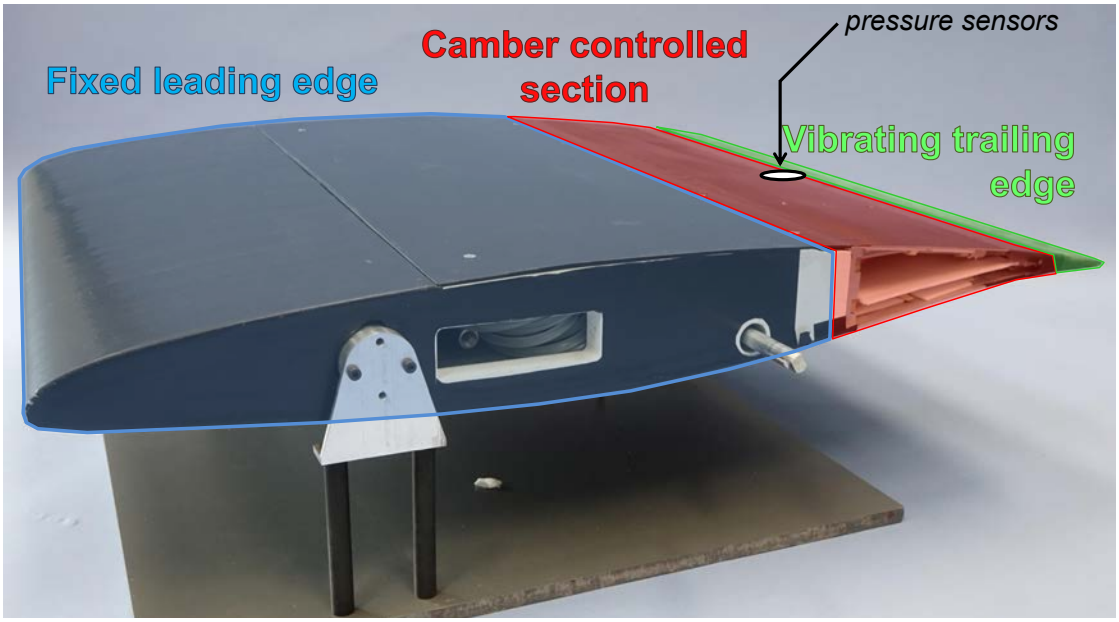

Figure 2.22: Picture of the hybrid wing model on its stand out of wind tunnel.

As presented in Figure 2.23, vibrations of 0.7 mm can be reached at frequencies up to 100 Hz. It can be noticed that an extra glue is applied on the silicone cover to fix an airtight latex foil over all the trailing edge. The glue thickness affects the actuator performances; this can explain that effective vibrations are lower than computed in section 2.3.

2.5.1.3 Camber control actuator

The camber actuation system is designed to bend the trailing edge structure while withstanding aerodynamic loads. The actuator is based on surface embedded SMAs. Three SMA wires are embedded under the upper skin and three other SMA wires are embedded on the lower skin, as shown in Figure 2.24. SMAs are characterized by a strongly non-linear thermomechanical coupling, which has been modeled and understood during the last decades [Lex13]. The actuator has been modeled in [Jod] and [Jod+17]; to sum up the principle, cold SMA are pseudo-plastic and can be easily stretched thanks to a low stress plateau. The SMAs are heated through Joule heating generating strong forces to recover their initial shapes. To easily design the mock-up and as cold SMA are very flexible, the SMA stiffness is neglected. This creates a sub-optimal design with a large amount of SMA, but the design solution is reliable and stiff regarding to aerodynamic loads. The maximum trailing edge deflection is about -25 mm to +20 mm. This

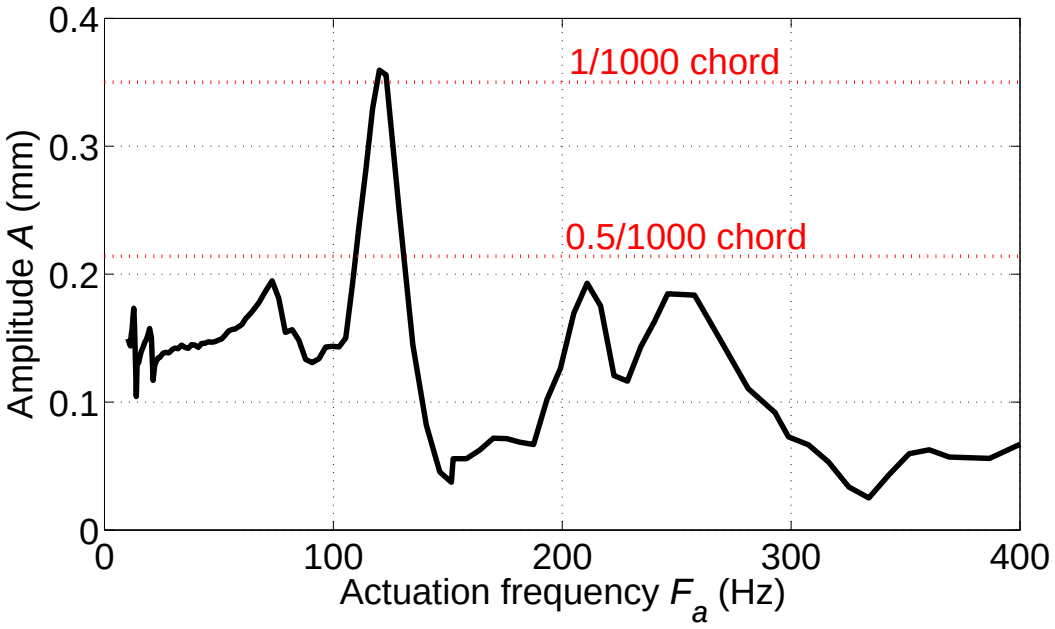

Figure 2.23: Measured amplitude displacement A of the trailing edge, depending on the actuation frequency F_a. This frequency response measurement of the actuator has been performed with 1 kV applied voltage on the MFC patches, using a high-speed camera.

corresponds to a controllable camber modification range of 22% (from -10% to +12%) of the actuated chord.

2.5.2 Camber control: control loop and performances

To precisely reach the desired deformations while controlling 6 independent SMA wires, temperature and deformation sensors are implemented. One thermocouple per SMA wire is used. One strain gauge bridge is implemented per up and down SMA pair, to reconstruct the trailing edge displacement. Two strain gauges are glued on the upper skin and the other two are on the lower skin. This atypical gauges distribution has been calibrated using an external displacement sensor that measured the trailing edge displacement. A polynomial interpolation ensures an accurate trailing edge displacement reconstruction from the bridge's signal. As shown in Figure 2.25, the average absolute error is under 0.4 mm for trailing edge displacements up to 10 mm. Over 10 mm, hysteresis decreases the accuracy to 1 mm.

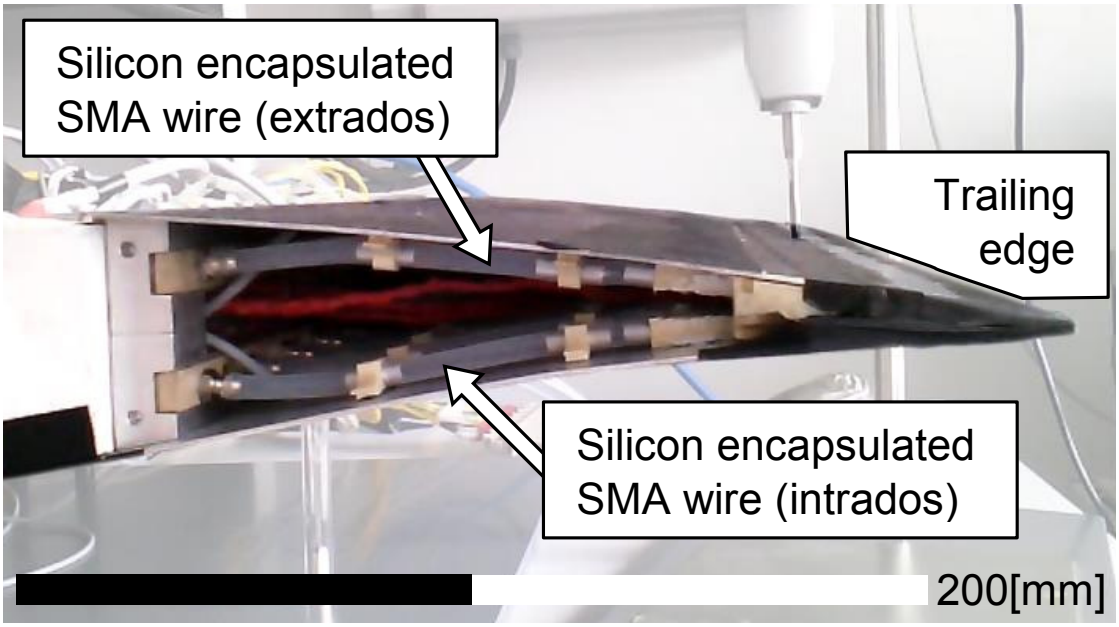

Figure 2.24: Trailing edge with surface embedded SMA actuators.

These sensors are used in two nested closed loops to control the camber. The reconstruct displacement is compared to a camber reference. Then a Proportional Integral (PI) controller send a SMA temperature reference to the temperature controllers. These controllers use temperature sensor information to provide heating and cooling commands via PI controllers. The control architecture is summed up in Figure 2.26. Temperature references are output from displacement controller, with limited slope, in order to ensure a uniform variation of every SMA actuator. The displacement controller has a custom anti-windup on the PI's integrator in order to avoid over integration during the temperature slopes.

The performance of the nested-loop control is visible Figure 2.27 for two displacement controller settings. A displacement step is applied on the controller. Rising the trailing edge displacement from 5 mm to 10 mm needs an increase of heating power to rise SMA temperature. The control strategy with displacement overshoot seems to be more efficient in steady power consumption than the strategy without overshoot. Overshoots in displacement lead the controller to decrease the final SMA temperature reaching the reference displacement. The overshoot effect is often seen as a control drawback; but due to the SMA activation temperature hysteresis, the final required temperature to obtain trailing edge position when decreasing the displacement is lower than the temperature needed to obtain the same position when increasing the displacement. This effect is clearly visible on Figure 2.28, where temperatures are drawn depending on displacement for the

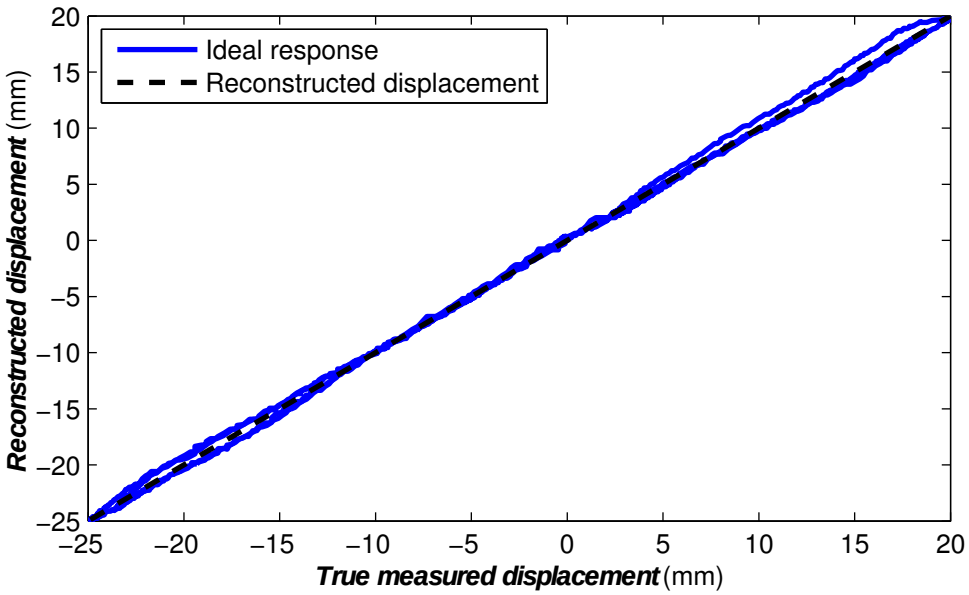

Figure 2.25: Characterization of the reconstructed displacement evaluated from embedded strain gauges.

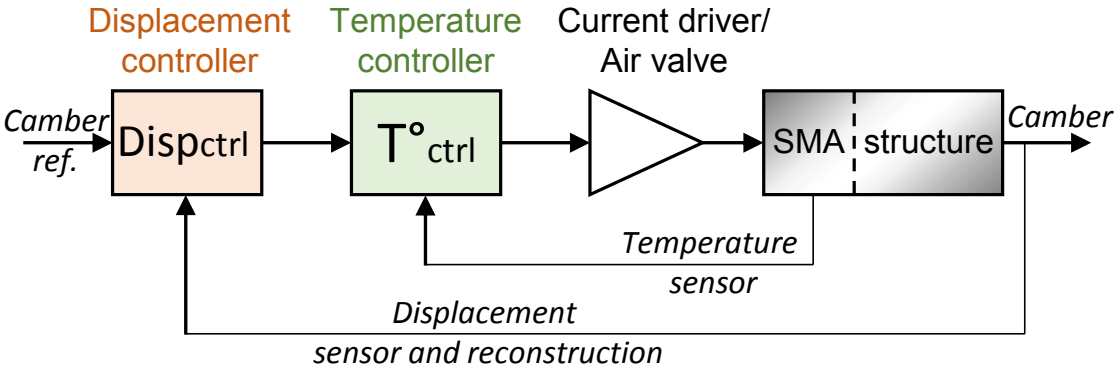

Figure 2.26: Nested control loop architecture of the camber control actuator.

same experiment as presented in Figure 2.27. The required SMA temperature difference between the two strategies is over 6°C. *Finally, a simple change in the control strategy leads to a reduction of more than 20% of required heating power to maintain the displacement.*

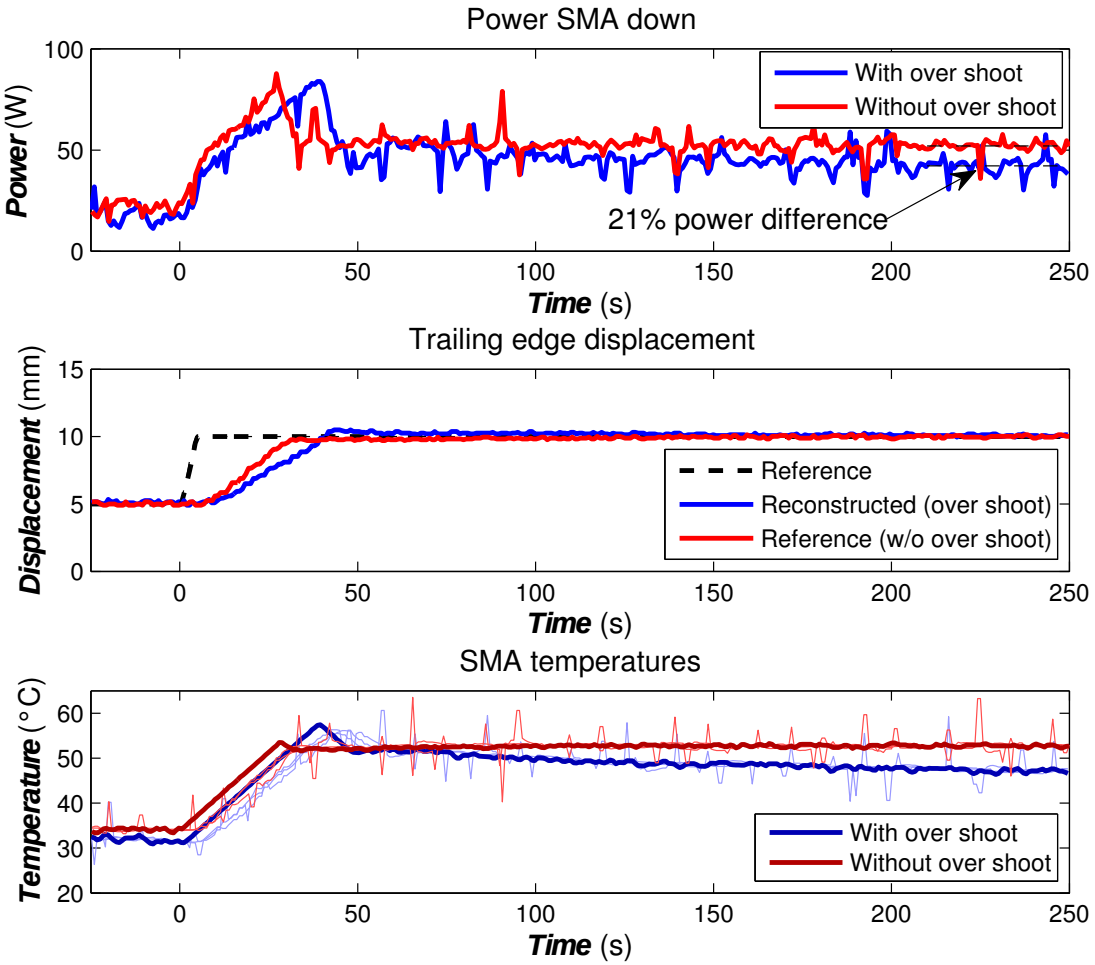

Figure 2.27: Control strategy influence of the camber control actuator. From top to bottom: instantaneous SMA power consumption, reconstructed displacement, SMA temperatures.

2.5.3 Wind tunnel experiments

2.5.3.1 Experimental set-up

The wing model is tested in a subsonic wind tunnel. The test section is 592 mm width per 712 mm high. The wing chord c is 700 mm as previously mentioned. The wing is mounted at a maximal incidence of 10°. As a result a blockage ratio of 18% is obtained. The blockage ratio effects are found to be acceptable in the present experiments which focus on the morphing effects. This is done by comparing a morphing configuration to the non-actuated case, both of which are subject to the same blockage ratio. The turbulence intensity of the inlet section is

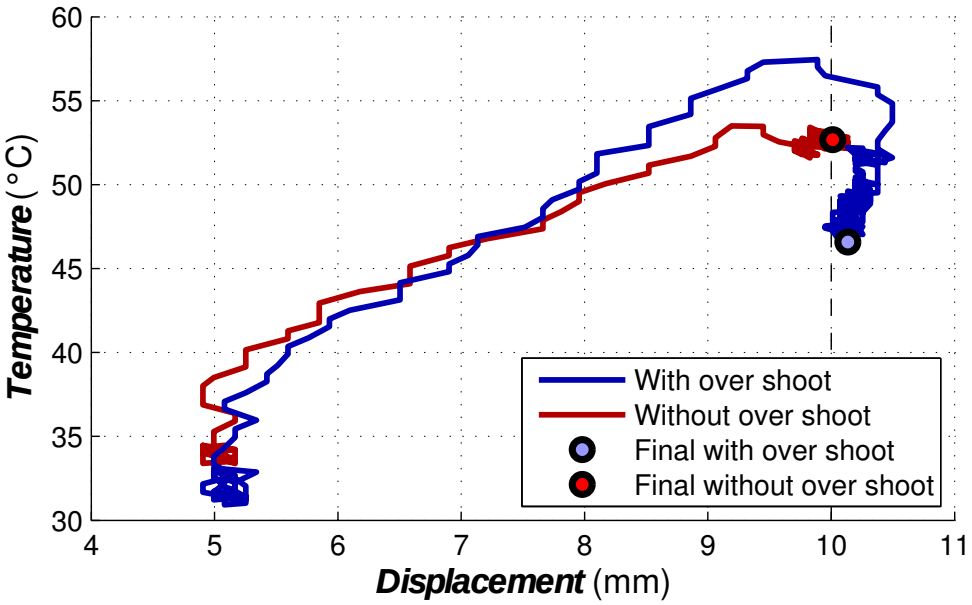

Figure 2.28: Control strategy influence of the camber control actuator. Temperature - displacement plane representation of the experiments.

about 0.1% of the free stream velocity. Measurements are performed at ambient temperature ($22°C$). Figure 2.29 presents the experimental wind tunnel set up. An aerodynamic balance based on strain gauges has been designed to measure lift and drag force on the wing. Precautions in design and mounting have been taken to ensure the quality of the measures despite the vibrations and the wires coming from the embedded sensors and actuators. Three dynamic pressure transducers (MEGGIT 8507C-1) are implemented on the suction surface (upper skin) of the prototype. They are lined up one behind the other. The respective locations of the sensor P1, P2 and P3 are closed to the trailing edge, i.e. respectively at 80%, 86% and 93% of the wing chord. An experimental campaign exploring the influence of free stream velocity, angle of attack, camber, HFVTE frequency and HFVTE amplitude is performed. Illustrations of the amplitude of deformations are given in Figure 2.29. For every experimental morphing experiment, forces, pressures, wind conditions and actuator information are recorded for 20 s. This record time has been found long enough to ensure a good statistical convergence.

2.5.3.2 Morphing effects

Hybrid morphing – Camber and HFVTE coupled effects The coupling between camber and vibrating trailing edge is presented in the next chapter, in

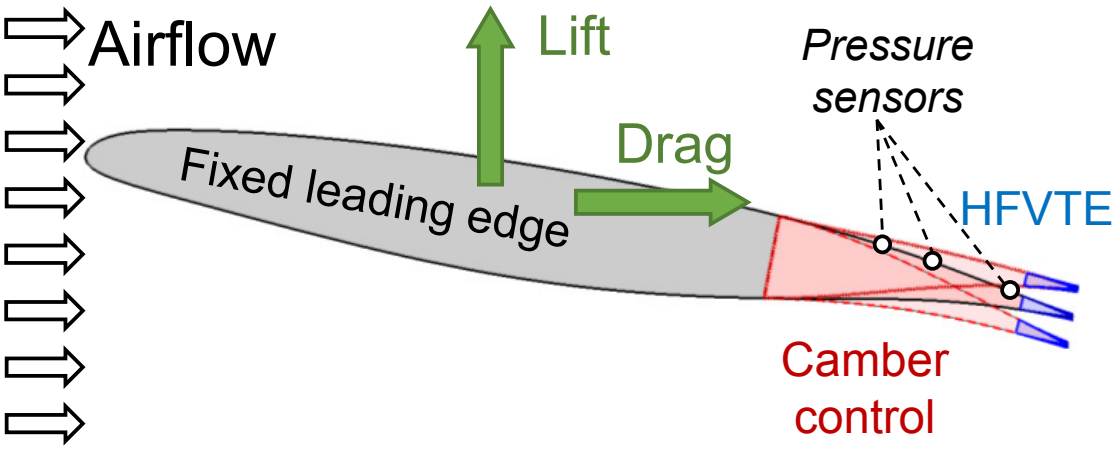

Figure 2.29: Scheme of the wind tunnel experiment.

section 3.3.

The focus is given here on the validation of embedded pressure transducers.

HFVTE effects at initial cambered airfoil

Dedicated experiments focus on the influence of the trailing edge vibrations on the flow, at fixed camber. For instance, Figure 2.30 presents the processed data from 500 experiments, each during 20 s. HFVTE frequency range is 12 Hz to

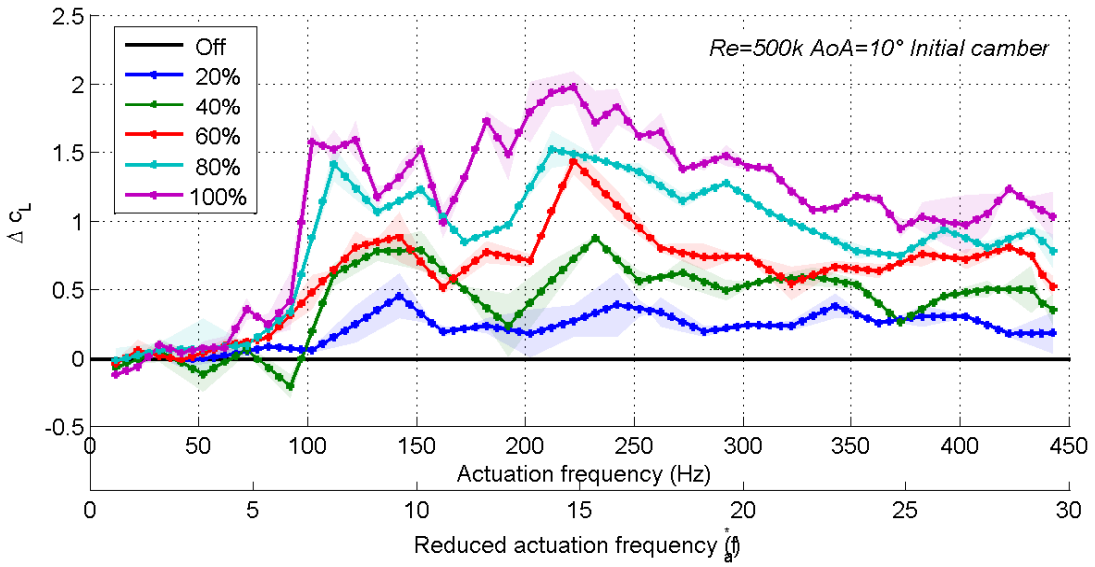

Figure 2.30: Impact of the HFVTE frequency and amplitude on the lift coefficient C_l. Reynolds number for this experiment is $Re = 5 \cdot 10^5$.

450 Hz (i.e. $f_a^* \in [0.8 \cdots 30]$); 5 amplitude levels are tested from 20% to 100% of the maximum amplitude of the actuators ; Reynolds number here is $Re = 10^5$. Particular attention has been payed to repeatability and accuracy of the measures. The order of the measures has been generated randomly, in order to prevent any memory or hysteresis effect from the sensors. Finally, one measure at a given HFVTE setting is compared to a previous and a following reference measure with no actuation.

Figure 2.30 shows the variation of the lift coefficient in relation with the actuation frequency. The different actuation amplitude are drawn in different colors. Pale areas described the variations of the measures between the two experiments whereas the darker lines are the average values. The experiments are repeatable with $+/-0.14\%$ lift difference. The first observation is the effect of the amplitude. Generally, the larger the HFVTE amplitude the larger the gain. This clearly indicates that if the actuator could vibrates at larger amplitudes, more gains can be achieved. But increasing amplitude over a certain limit would decreases the gains, as reported in [Col+04] for the forced active control of airflows. Secondly, a frequency threshold appears close to 100 Hz, separating low HFVTE effects area from higher gain area. This threshold is linked to the first resonance of the HFVTE actuator which can be seen by the 110 Hz peak in Figure 2.23. Complex structural vibrations are detected with accelerometer on the wing, but the understanding of the coupling between wing structural resonance modes and the effects on flow is the purpose of next work.

Finally, it is worth noting that for the two tested velocity – i.e. the two Reynolds numbers $Re = 10^6$ *or* $5 \cdot 10^5$ *– experimental gains above 2% have been identified, thanks to small vibrations of the trailing edge.*

2.5.3.3 Morphing and sensing

Experimental morphing performance enhancements are characterized using an aerodynamic balance. This instrumental device cannot easily be embedded on aircraft. Other embedded sensors are needed. The three dynamic pressure sensors P1, P2 and P3 are used to this purpose.

The recorded pressure signals are useful. For instance they contain vortex signature in their frequency spectra that could be analyzed. A simpler analyze that can be used as morphing efficiency estimator is the evolution of time average pressures presented in Figure 2.31. Indeed, an increase of the absolute value of the pressure increases the lift; as the lift is the vertical component of the resulting pressure forces. Notice that the measured pressures are strongly affected by the propagated vibrations in the structure, as the sensors are embedded into the structure. So the signal variance is more affected by the vibrations than the

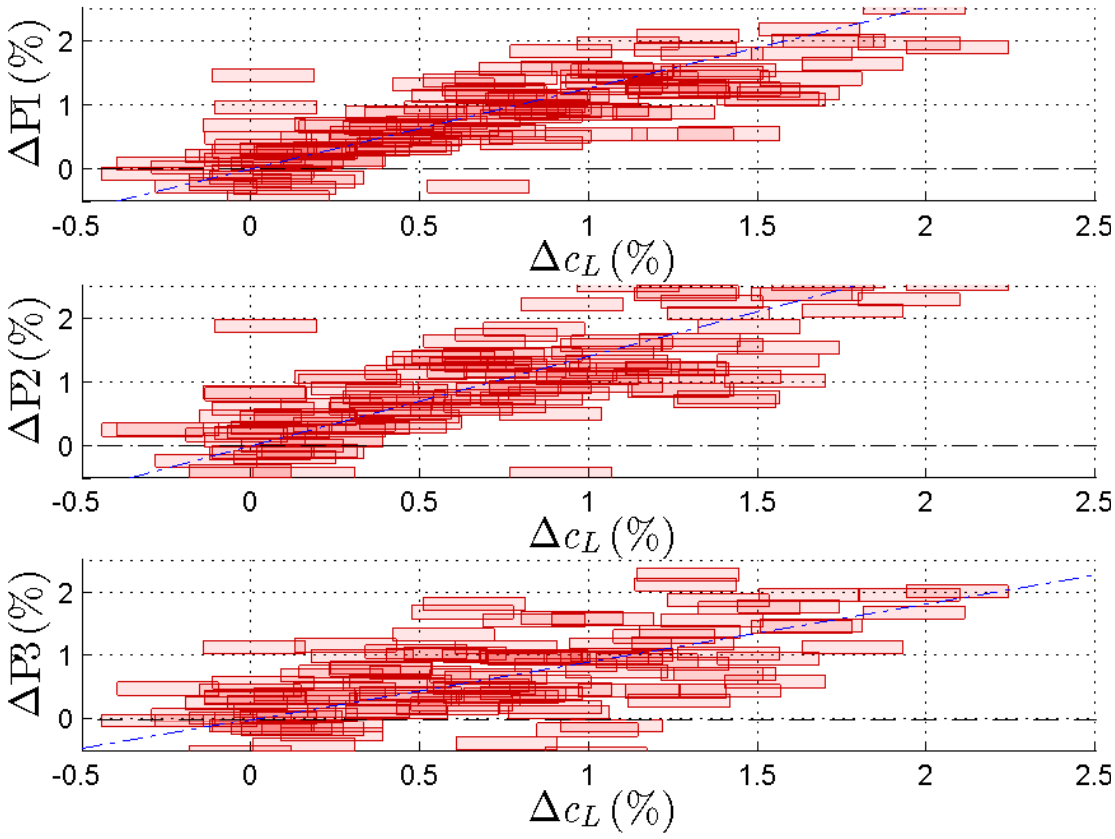

Figure 2.31: Lift coefficient evolution against time average pressure variations of the 3 transducers P1 to P3. The plotted data corresponds to all HFVTE actuated experiment at $Re = 5 \cdot 10^5$ at initial camber.

pressure variations. Nevertheless, the time average pressures of the three sensors in Figure 2.31 are correlated to the lift gain. Then these sensors demonstrate the suitability for the detection of aerodynamic performance enhancement thanks to HFVTE actuation. Next work has to focus on the signal processing to determine an accurate observer of the aerodynamic gains.

2.5.4 Conclusion

This section presented the multidisciplinary coupling between an innovative mechatronic hybrid morphing wing prototype and the aerodynamic forces. The different time scales of aerodynamic phenomena justify the use of two electroactive smart material based actuators. Integration of piezoelectric and shape memory alloy actuators in the prototype requires a multidisciplinary design approach to fulfill the

design target during the construction and to achieve accurate control of the innovative prototype, before moving towards the dedicated wind tunnel experiments. It has been shown that the control law of the SMAs can decrease the steady power consumption by more than 21%. Also, the aerodynamic performance enhancements are closely linked to the coupled actuator-structure dynamic behavior.

The camber modifications is able to change the lift by 23% and the drag by 35%, leading a lift over drag ratio enhancement of 16%. Additionally the actuated small vibrations of the trailing edge can increase the performances by 2% in addition to the camber gains. Embedded pressure sensors show the ability to estimate the morphing gains without needing external sensors.

The next step focuses on both the sensors and actuators. A better understanding of the fluid mechanism is needed to estimate in real time the gains with embedded sensors. A full scale flap demonstrator equipped with hybrid morphing actuator is currently under construction.

2.6 Chapter conclusion

Within the concept of hybrid electroactive morphing, a new prototype is designed and build. The design is based on both analytical and FEA models. The two actuators achieve deformations at two different time space scales, to affect the airflow and turbulence around the airfoil.

Firstly, the camber control design is based on the study of the SMA. Knowing their limits, an analytical model based on the bending beam theory is developed. This model gives basis data for a further FEA model. The parameter sensitivities return design and making instructions. The validation and the control laws have been developed on a simple SMA actuated plate. Secondly, the vibrating trailing edge is modeled. The active vibrating part is modeled then the impacts of the silicone cover are investigated thanks to analytical and FEA models. Thirdly, key points of the making as well as the experimental setup of the wing are introduced. The fourth part focuses on electrodynamic characterizations. Vibration performance and effects of the settings on the power consumption are highlighted. It is shown that sensor measure analysis provide information on the aerodynamic performance detection.

The design process requires the development and validation of models that are discussed in this chapter. Making processes have been made. Practical knowledge regarding the implementation and the use of smart materials has been learned. The sensors are suitable for wind tunnel measurements. The main outlook of this ready hybrid electroactive wing model is a further investigation in wind tunnel of the impact of morphing on aerodynamics. The mechanisms of creation and destruction of turbulence aided by morphing have to be understood to specify specific actuators at larger scales. The practical knowledge is helpful to design a larger scale.

The presented prototype – developed in collaboration with Airbus – is part of the "Reduced Scale" prototype for the European project SMS[2]*. It will serve for applying the control command laws in order to improve the aerodynamic performances in real time. More details are given in the outlooks of this manuscript 4.7.*

[2] `http://smartwing.org/SMS`

CHAPTER 3

Wake dynamics of the hybrid morphing wing prototype by TR-PIV and force measures

"It's not an experiment if you know it's going to work."
Jeff Bezos

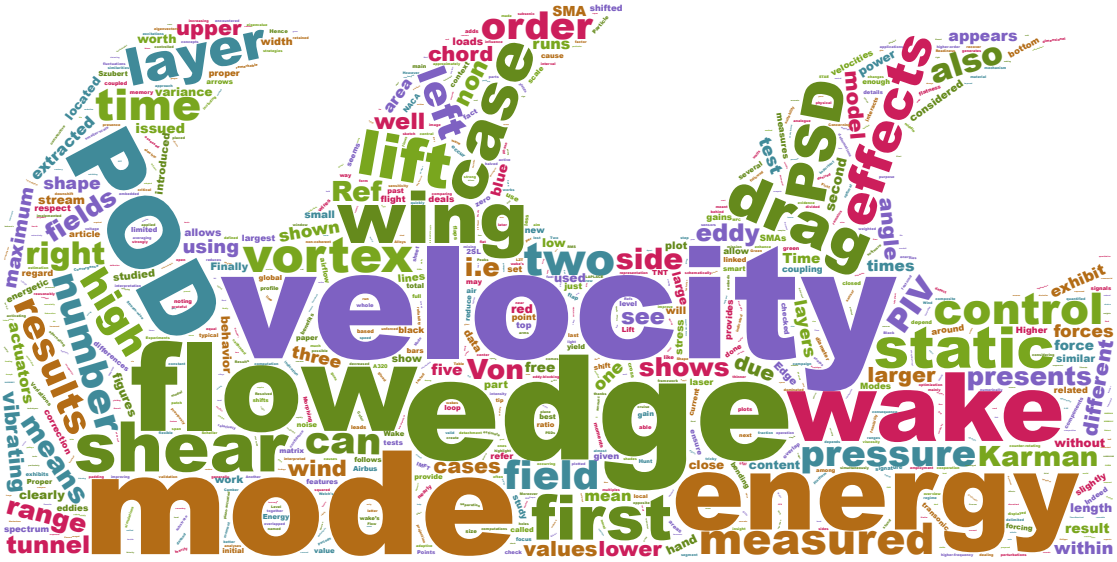

Figure 3.1: Word clood of this chapter content (`www.wordclouds.com`).

This comes from the published paper: G. Jodin, V. Motta, J. Scheller, E. Duhayon, C. Döll, J.F. Rouchon, M. Braza. "Dynamics of a hybrid morphing wing with active open loop vibrating trailing edge by Time-Resolved PIV and force measures", Journal of Fluid and Structures, 2017, doi.org/10.1016/j.jfluidstructs.2017.06.015

Abstract A quantitative characterization of the effects obtained by high frequency-low amplitude trailing edge actuation is presented. Particle image velocimetry, pressure and aerodynamic forces measurements are carried out on a wing prototype equipped with shape memory alloys and trailing edge piezoelectric-actuators, allowing simultaneously high deformations (bending) in low frequency and higher-frequency vibrations. The effects of this hybrid morphing on the forces have been quantified and an optimal actuation range has been identified, able to increase lift and decrease drag. The present study focuses more specifically on the effects of the higher-frequency vibrations of the trailing edge region. This actuation allows manipulation of the wake turbulent structures. It has been shown that specific frequency and amplitude ranges achieved by the piezoelectric actuators are able to produce a breakdown of larger coherent eddies by means of upscale energy transfer from smaller-scale eddies in the near wake. It results a thinning of the shear layers and the wake's width, associated to reduction of the form drag, as well as a reduction of predominant frequency peaks of the shear-layer instability. These effects have been shown by means of frequency domain analysis and Proper Orthogonal Decomposition.

3.1 Introduction

Limiting energy consumption has become a central concern for reducing aircraft operational costs. Improving aerodynamic performance is a way to reduce the fuel burn during flight.

Current airfoil shapes are generally optimized for only a few flight states, corresponding to nominal cruise conditions. During flight, the altitude, the weight and the speed are continuously changing. Hence this design is sub-optimal for the

whole aircraft mission. Traditional solutions to control and adapt the wing shape (like slats and flaps) exhibit limited performance ranges [Bar+11]. Changing the shape of the wing during a mission can save several percents of fuel for a regional passenger aircraft [LM15]. The concept of real time shape and vibrational behavior adaptation enabling multi-point optimization is called morphing. In the context of the studies carried out in the authors multi-disciplinary research platform involving the LAPLACE and IMFT French Laboratories [1], the morphing is achieved by means of electro-actuation and is called "electroactive morphing".

Within the framework of aircraft aerodynamic performance, it was demonstrated that camber control of the trailing edge of a wing is very efficient to improve aircraft performance [LM15]. With this regard relatively high Technology Readiness Level (TRL) projects, targeting current industrial airliners at true scale, were undertaken. The European research programs SARISTU[2] and CleanSky[3] have work packages dealing with morphing wing trailing edge devices, [Dim+16] [PAM16]. Another trailing edge morphing concept, called Adaptive Compliant Trailing Edge, was developed by NASA in cooperation with FlexSys Inc.[4]. This concept features an adjustable structure which can be actively deformed. Endurance flight tests for this concept were performed and described in Ref. [KFC16]. This solution was proved to yield aerodynamic benefits and its effectiveness and airworthiness are being ultimately assessed.

However these new adaptive structures are actuated through conventional actuators like servomotors. Recent advances in the field of smart materials show the potential to overcome difficulties to make a wing both stiff enough to withstand the loads, and flexible enough to be easily deformed [Bar+14]. The related research focuses mainly on low scale Micro Air Vehicles. Among electro-active materials, Shape Memory Alloys (SMAs) and piezoelectric materials are the most frequently used. SMAs are characterized by thermo-mechanical behaviors, and most applications use Joule heating to activate the SMAs. Different morphing concepts were developed, an overview of which is presented by Barbarino et al. in [Bar+11]. The electromechanical response of piezoelectric materials is activated via the application of an electric field [Bar+14]. The material commonly employed is Lead Zirconate Titanate (LZT or PZT) ceramic. Piezoelectric composites allow for a simple implementation. Piezoelectric composite patches glued on structure are often used as bending actuators to control the wing shape. The desired operation is generally accomplished using one specific smart material. A combination of both SMAs and LZT can enhance significantly the global performance. The

[1] www.smartwing.org/
[2] http://www.saristu.eu
[3] http://www.cleansky.eu/
[4] http://www.flxsys.com/

synergistic smart morphing aileron [PFI15] is the combination of a SMA actuated hinge followed by a flexible piezoelectric driven trailing edge.

The works mentioned above deal with global airflow control to improve macroscopic behavior i.e. lift, drag, aeroelastic response, or load alleviation by means of quasi static shape control. A dynamic flow control is also possible. For example Ref. [Gri] presents a wind tunnel model with shape adaptive upper side. Two SMA actuators control the airfoil thickness, whereas pressure sensors are used to estimate the location of the separation point. The work of Inaoka et al. in [Ina+15] deals with active vibrating flaps located on the leading edge. These flaps are actuated at a frequency corresponding to the vortex generation frequency of vortices in the separated area. This control allows for avoiding the flow separation when a decrease in free stream velocity occurs. Vibrating trailing edge concepts are also studied for rotorcraft applications. Large coherent flow instabilities have been modeled and then open and closed loop strategies have been investigated by Motta et al. in [MMD16]. It has been shown that vortex breakdown can occur by trailing edge vibrations.

Flow dynamics around airfoils has been studied for years and the complexity of the phenomenon makes it a current research topic. Ref. [YSK06] investigates the dynamics of the coherent vortices on the wake of a NACA 0025 at Re up to 150 000. More details on the dynamics of vortex shedding past an airfoil can be found in Ref. [FL95], Ref. [Hoa+03], Ref [Bou+08], Ref [Szu+15] and [Szu+16]. These experimental or numerical analyses characterize the size and the frequencies of coherent vortices from low to high Reynolds numbers, including also compressibility effects.

As part of collaborative effort from two laboratories (LAPLACE and IMFT) a SMA actuated plate was previously developed for wind tunnel purposes, in the context of the Foundation STAE ("Sciences et Technologies pour l'Aéronautique et l'Espace" [5]) research project EMMAV : Electroactive Morphing for Micro-Airvehicles [Chi+14]. Afterwards, a NACA 0012 wing prototype with a vibrating trailing edge was experimentally investigated by wind tunnel tests, in the context of the STAE research project DYNAMORPH: "Dynamic Regime Electroactive Morphing". It was shown that the trailing edge vibration interacts with the shear layer. The wing's wake energy was reduced, leading to an improvement in aerodynamic performance, according to Scheller et al. [Sch+15]. More recently, the same research platform focused on a NACA 4412 wing section featuring embedded SMA and trailing edge piezoelectric fiber actuators [Sch]. This actuation concept is called *hybrid electro-active morphing wing*. It was demonstrated that the flow dynamics are significantly affected by the trailing edge actuation. A significant reduction of the wake's width and spectral energy associated to drag and aerody-

[5] http://www.fondation-stae.net/

namic noise respectively was quantified by means of Particle Image Velocimetry (PIV) measurements.

In the context of these studies, the aim of the hybrid morphing concept is to *use the turbulence itself*, in order to manipulate part of the "harmful" eddies and to enhance the beneficial ones. The objective is to increase the aerodynamic performances and simultaneously decrease the noise sources generated from predominant instability modes. Hence at a given controlled camber, the vibrating trailing edge adds kinetic energy in the wake that fosters the suppression of coherent turbulent structures. This concept was first studied theoretically numerically by Szubert et al.in Ref. [Szu+15] for a transonic flow around a supercritical airfoil. Introducing a small amount of kinetic energy by means of Proper Orthogonal Decomposition (POD) provides an eddy blocking effect that reduces significantly the wake thickness. This concept has been experimentally put in evidence by Scheller et al. [Sch15].

Considering these previous analyses, the purpose of this paper is to enlighten in more detail the interaction of higher frequency-low amplitude actuation with the wake flow and to explain the modification of the turbulence structure and its link with the global effects (forces). In cooperation with Airbus, a first step is to size, design, build and test an intermediate-scale mock-up of a wing with an novel high-lift flap design. The wing section is an A320 profile. Targets like drag reduction, shape optimization and noise mitigation are addressed through hybrid electroactive morphing.

This chapter is structured as follows. Section 3.2 presents the hybrid electroactive morphing wind tunnel model. The experimental set-up is also described. Section 3.3 briefly discusses the results obtained with the employment of hybrid morphing. Section 3.4 introduces the flow dynamics and control strategy. The subsequent sections provide an insight into the flow response obtained with high frequency-low amplitude actuation only, i.e. without the employment of camber control. Section 3.5 deals with the Time Resolved PIV (TR-PIV) measurements. Several instantaneous fields are first presented and the differences between the actuated and the non actuated (in the following referred to as baseline) configuration are discussed. Then the time averaged fields, together with the velocity profiles in the wake region are presented. The proper orthogonal decomposition performed on the measured velocity fields is detailed in Section 3.6. The coherent structures detected on the flow for the baseline and for the actuated configurations are illustrated throughout. The frequency domain analysis of the measured velocity field is reported in section 3.7, to complement the results of the proper orthogonal decomposition. The effects of high frequency actuation on the wing loads are presented in section 3.8. Concluding remarks are given in section 3.9.

3.2 Wind tunnel model

3.2.1 Electroactive hybrid morphing wing

The morphing wing embeds both camber control and Higher Frequency Vibrating Trailing Edge (HFVTE) actuators. Figure 3.2 presents the three sections of the hybrid morphing prototype. The baseline airfoil is a wing section of an A320. The chord c is 700 mm and the span 590 mm. The actuators are sized, simulated and implemented on the last 30% of the chord, corresponding to usual flap positions. The hollow fixed leading edge contains electronics and tubing for all temperature, pressure and position transducers as well as actuator interfaces.

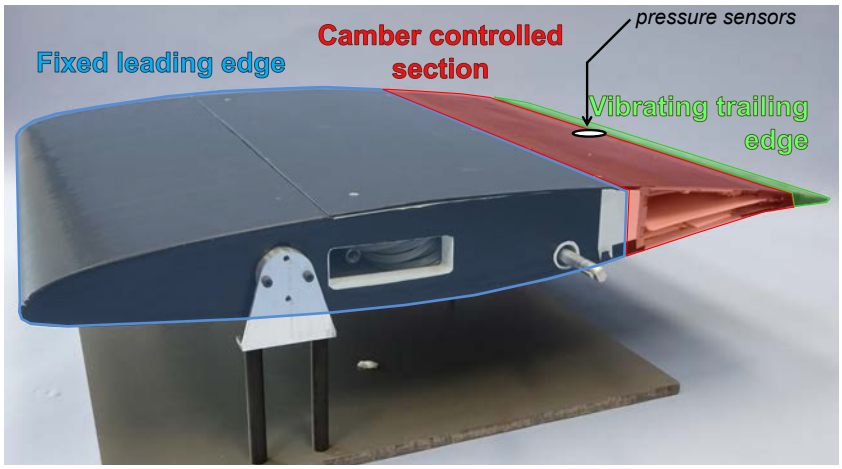

(a)

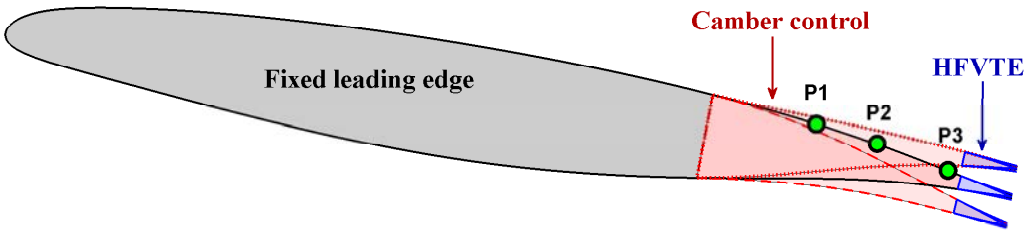

(b)

Figure 3.2: (a) Picture of the hybrid wing model on its stand out of wind tunnel stand. (b) illustration of the maximum deformed shapes of the airfoil. The red superimposed profiles depict the effect of the camber control, the blue parts represent the vibrating trailing edge. Green circles P1, P2 and P3 correspond to the location of the pressure taps.

The camber actuation system is designed to bend the trailing edge structure while supporting the aerodynamic loads. This actuator is based on surface embedded SMA. Six different SMA wires are pre-strained to +3% with respect to their initial length. When the wires are heated by electric current, a microscopic crystallographic change occurs. This internal change generates stress such that the SMA wires tend to recover their initial length. The generated forces create a bending moment that changes the camber of the actuated wing section. In order to cool down the SMAs and recover the initial wing camber a pressurized air network with a control-valve is provided.

The HFVTE is designed to reach millimeter vibration amplitudes up to $F_a =$ 200Hz , as shown in Figure 3.3. For higher frequencies, resonance modes can be exploited to allow larger deformations. To fulfill these requirements, piezoelectric composite patches are glued on both sides of a metallic substrate. The piezoelectric components are Macro Fiber Composites (MFC) which were fabricated by Smart Material GmbH. The MFC patches are alternatively activated to provide the desired two way trailing edge displacements. Due to the substrate thickness, the patch forces create an alternate bending moment that results in the actuator vibration. To respect the airfoil shape, the assembly is covered by a silicone shell that is specifically designed to limit its impact on the actuator performance. For more information about the electro-active hybrid morphing actuators, the reader might refer to Refs. [Jod; Sch+16].

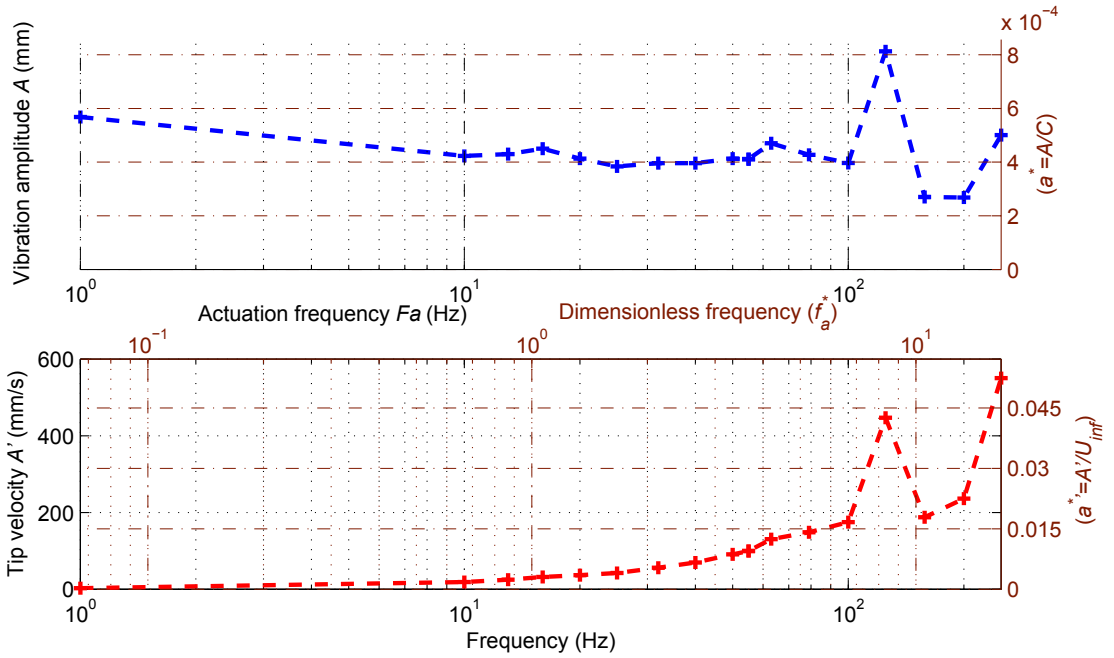

Figure 3.3: Vibration amplitude of the Higher Frequency Vibrating Trailing Edge at full voltage (1000 V). The top chart presents the displacement whereas the bottom one shows the tip velocities, depending on the actuation frequency.

3.2.2 Experimental set up

The wing model is tested in a subsonic wind tunnel. The test section is 592mm width per 712mm high. The wing is mounted with an incidence of 10°. As a result a blockage ratio of 18% is obtained. The blockage ratio effects are found to be acceptable in the present experiments which focus on the morphing effects. This is done by comparing a morphing configuration to the non-actuated case, both of which are subject to the same blockage ratio. Further explanations are introduced in A.3 The turbulence intensity of the inlet section is about 0.1% of the free stream velocity. Measurements are carried out at ambient temperature ($22°C$). Figure 3.4 presents a 3D view of the wind tunnel test section experimental set up.

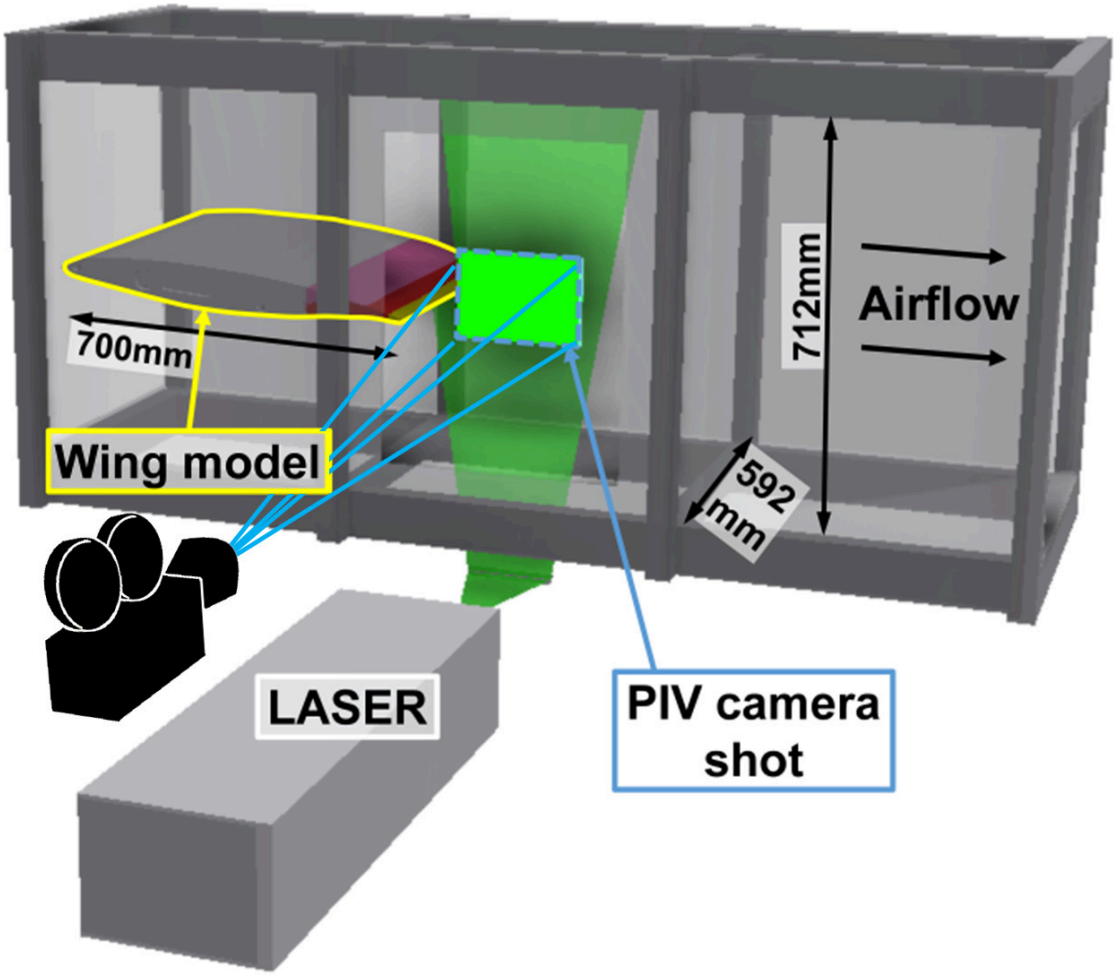

Figure 3.4: Wind tunnel test section CAD with hybrid wing model highlighted in yellow. The PIV plane is located at mid-span and is highlighted in green.

Smoke particles of 3.4 μm diameter are introduced in the airflow for the Time

Resolved PIV (TR-PIV) measurements. The depth of the field was focused on the stream-wise laser light sheet – in Figure 3.4 the green area corresponds to the laser sheet within the camera range. The laser pulsations are generated by a two cavity Nd:YLF (527nm) laser (Quantronix, Darwin Duo). The thickness of the laser sheet is $2.5mm$. Particle images are recorded during the experiment using the digital high-speed camera Phantom V1210. Each image is divided into interrogation windows. The interrogation window size is $16 \times 16\text{px}^2$ (px being Pixel), which corresponds to $3.4 \times 3.4\text{mm}^2$, with an overlap of 75%. The most probable displacement of the particles between consecutive images and for a given interrogation window is obtained from the cross-correlation plane of consecutive images; DAVIS8 commercial software as well as CPIV[6] are used for the computation. The displacement during the HFVTE movements reflects the resulting velocity according to the displaced trailing edge position, as the Stokes number $Sk = 5 \cdot 10^{-4}$ is much smaller than one. This, as suggested by Green [Gre95], indicates that the particles follow the motion of the fluid. During the 45 experiments the velocity variation was below 1.5%. The experimental benchmark also embeds an aerodynamic balance that measures lift and drag forces. This balance is composed of two arms with strain gauges. It is worth remarking that the quantification of the lift and drag is tricky, as the measurements are significantly affected by the trailing edge actuator vibrations. Therefore a specific balance design as well as a detailed characterization of the sensor is performed. The balance supports the model through holes in the left and right wind tunnel test section walls. These holes are also used for connecting the morphing systems and sensors. Two small 6mm diameter microphones and one dynamic pressure sensor (Kulite XCQ063) are implemented on the upper surface. Detailed studies have been carried out to establish the suitability of the experimental results provided in the following sections. Namely, the frequency responses of the pressure transducers are evaluated by means of calibrated white noise sound source. The characterization of the balance is carried out by evaluating the accuracy, the precision and the sensitivity to the HFVTE induced vibrations. The quality of the following statistical analysis is ensured as the time average convergence is checked, see A.1. The drag/lift coefficients of the current experiments are estimated within a $+/-1.1\%/+/-0.8\%$ accuracy range, with a statistical confidence interval of 95%. These accuracies concern Reynolds 10^6 ($U_\infty = 21\ m/s$) experiments. Moreover, force measurements at Reynolds $0.5 \cdot 10^6$ ($U_\infty = 10.5\ m/s$) have been carried out but do not exhibit the same accuracy and therefore are not discussed. Both Reynolds numbers experiments ensure sufficient convergence for the measurements, see A.2

[6] A software for massively parallel computations, developed at IMFT Laboratory by Pierre ELYAKIM.

3.3 Hybrid morphing experiment overview

An experimental campaign exploring the influence of free stream velocity, angle of attack, camber, HFVTE frequency and HFVTE amplitude is performed. Figure 3.2 introduces the shape control range of the hybrid morphing model. To give an order of magnitude of the actuation levels of the HFVTE, Figure 3.5 shows the change in effective angle of attack of the wing, due to the vibrations of the trailing edge. Such a small and localized amplitude deformation is able to slightly interact with global forces on the wing. To investigate the impact of all the controlled variables, more than 3000 runs are performed. For instance Figure 3.6 presents the results of 476 individual measurements for different cambers, vibrations amplitudes and frequencies , at incidence of 10° and Reynolds number $Re = 10^6$. Lift coefficients are computed from balance data time averaged on acquisitions of 20s for camber control that displaces the trailing edge from -10 to +10 mm (i.e. $+/-1.5\%c$) and trailing edge vibrations at frequencies from $F_a = 0 - 250$Hz (i.e. f_a^* =0 to 8.3). The lift coefficient surface is plotted as a function of camber and vibration frequency. Each experiment testing a HFVTE configuration is preceded by a reference measure with the same camber, the same velocity and the same incidence, but with no trailing edge vibration. This ensures the accuracy in capturing the high frequency-low amplitude actuation effects. At a given camber, the additional modifications due to the HFVTE are represented by vertical bars. The colors of these bars indicate if the HFVTE actuation increases the lift (green bars) or decreases the lift (red bars) compared to the experiment at same camber without HFVTE actuation.

A first result is the well known effect of the camber on the lift. Positively increasing the camber raises the lift, as the zero lift angle of attack shifts towards smaller values. On the one hand that up and down deformed shapes are different, leading to non-symmetrical lift effects for negative and positive cambers respectively. On the other hand characterizing the effects of trailing edge vibrations is somehow tricky. In fact, according to Figure 3.6, a frequency range from 100Hz to 250Hz ($f_a^* \in [3.3 \cdots 8.3]$) seems to be beneficial for the lift, especially for high cambers. On the other side, at low cambers the effect of the vibration on the lift is reduced and the frequency range is shifted.

The strong coupling between the camber and the vibrating trailing edge is complex and will be the purpose of future works. As the effects of camber have already been largely assessed (see for instance Ref. [Av49]), the present work focuses on the effect of the vibrating trailing edge on the baseline cambered airfoil. To provide an insight into the vortex breakdown effect of this high frequency–low amplitude actuation, control mechanisms are described in next section. Then PIV results are detailed in the following sections. Then the results obtained in terms of local and

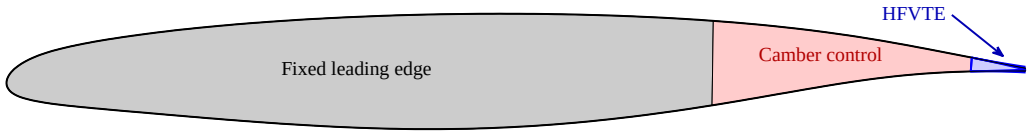

(a)

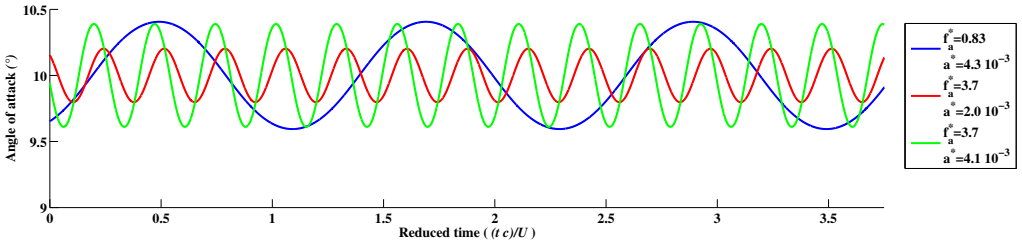

(b)

Figure 3.5: (a) a cross section of the wing is represented with the extreme positions of the vibrating trailing edge in blue. (b) the change in effective angle of attack of the whole wing is plotted as a function of the time for different actuation cases. The effective angle of attack is defined as the angle between the straight line passing by the leading edge and the trailing edge, and the stream-wise axes. This angle depends on the camber and on the position of the vibrating trailing edge at a given time.

resulting force measurements are discussed, in order to investigate the potential feasibility of a real-time on board closed loop control.

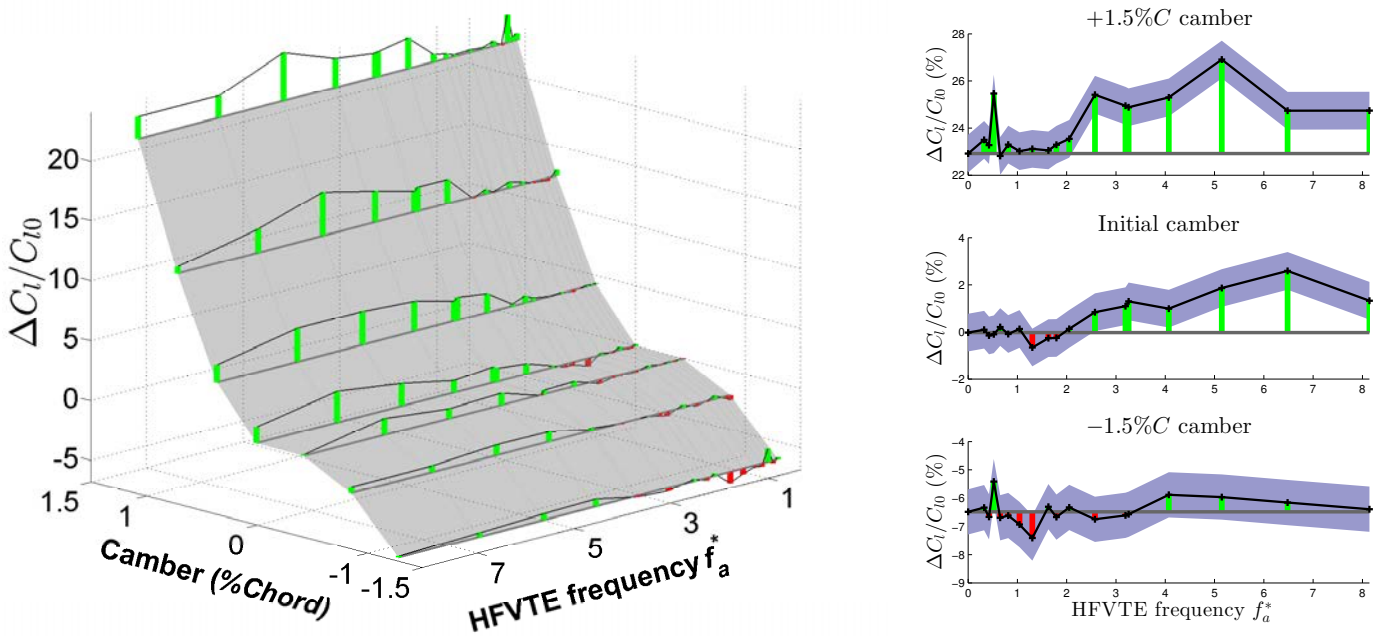

(a) (b)

Figure 3.6: (a) modification of the measured lift coefficient C_l as a function of the dimensionless camber and the dimensionless actuation frequency. The percentage lift modification is normalized to the measured lift coefficient without any morphing C_{l0}. (b) Corresponding 2D plots of three selected cambers. The blue areas around the data correspond to the 95% confidence level. Camber range is -10 to $+10$mm and frequency range is $0 - 250$Hz.

3.4 Wake dynamics and control mechanisms

The understanding of the operation of vortex shedding allows their control by means of morphing. The trailing edge vibration triggers eddy blocking effects that change the wake. Such changes in wake cause a vortex breakdown. The following subsections refer to results that are discussed later in this chapter.

3.4.1 Wake instability creation: Kelvin-Helmholtz instability

The sketch presented in Figure 3.7 describes the mechanisms of the wake dynamics. Numerical simulations[7] based on the same experimental conditions show that the detachment occurs at nearly 60% of the chord. Going downstream, this shear layer is turbulent and interacts with the Kelvin-Helmholtz vortex shedding coming from the pressure side shear layer – blue vortices in the figure. An interaction of the two shear layers coming from both sides of the wing is observed. This is also depicted by the instantaneous TR-PIV field of the non-actuated flow of Figure 3.8. The trailing edge is visible on the left of the figure; the flow goes from left to right, the figure is a blow up of the wake past the trailing edge. Color shades from blue to red highlight intense vorticity areas. We clearly see a thick shear layer coming from the suction side, characterized by negative vorticity. Coming from the pressure side, a typical Kelvin Helmholtz vortex shedding – red vortices in Figure 3.7 – with positive vorticity interacts and melts with the shear layer from the suction side.

Regarding the melting of the coherent structures, it will be shown in Section 3.6 that high energy POD modes are linked to this vortex shedding (the reader can refer to mode #2 of static baseline Figure 3.16). This POD mode temporal coefficient spectrum exhibits a peak at a frequency $St = 11.5$. Phase-averaged crossflow velocity component corresponding this frequency are presented in Figure 3.9. This clearly shows the time consistency of the vortices at this frequency over the time, as 20 periods are averaged in this figure. Finally, the spectra which will be introduced in Figure 3.28 are computed from the crossflow velocity of 8 points in the wake. The peaks corresponding to a Strouhal of 11.5 are present everywhere. But peaks on the points corresponding to the lower shear layer are more prominent (SL peaks) and the harmonic (2SL peaks) is also present. This indicates that the Kelvin-Helmholtz instability is more present in the lower shear layer. The spectra

[7] Private communication to Airbus, unpublished.

from the upper shear layer indicate that this area is more chaotic and is dominated by the Von Kármán instability.

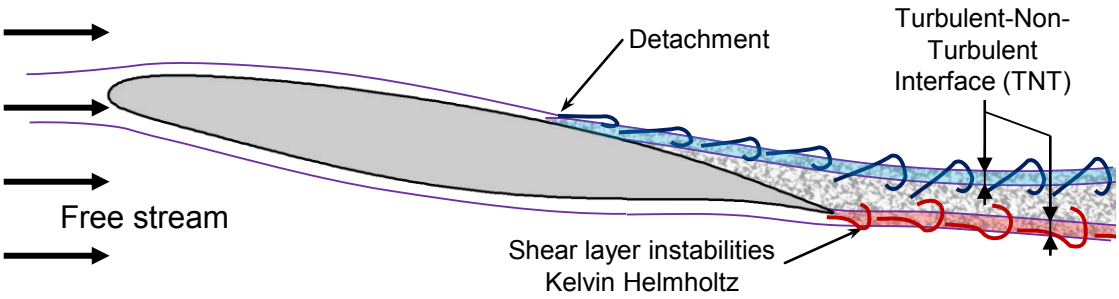

(a)

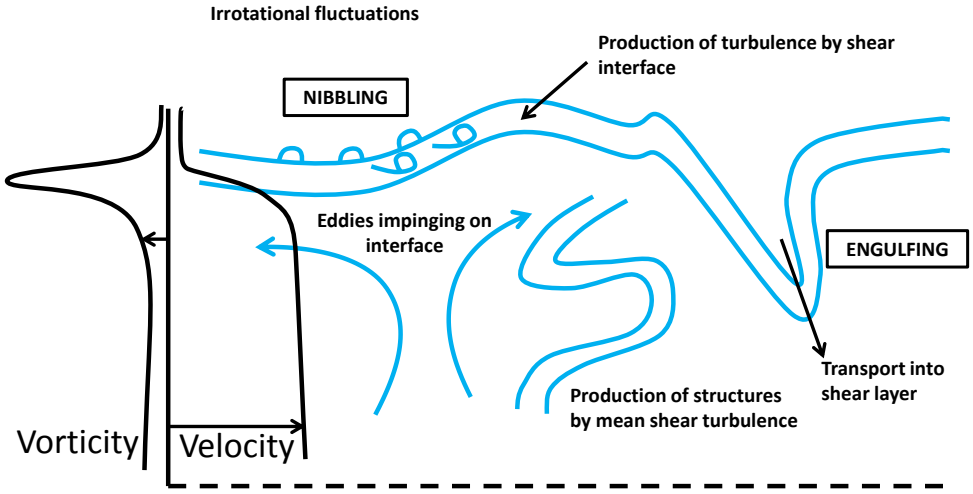

(b)

Figure 3.7: (a) Sketch of the wake dynamics. The detachment occurs at nearly 60% of the chord, shedding turbulences in the blue shear layer. Kelvin-Helmholtz instabilities appear just downstream the trailing edge; these vertical structures represented in red, coupled with those of the shear layers from the suction side, grow moving downstream. (b) Schematic representation of the eddy-blocking effect between TNT, Ref [Hun+16].

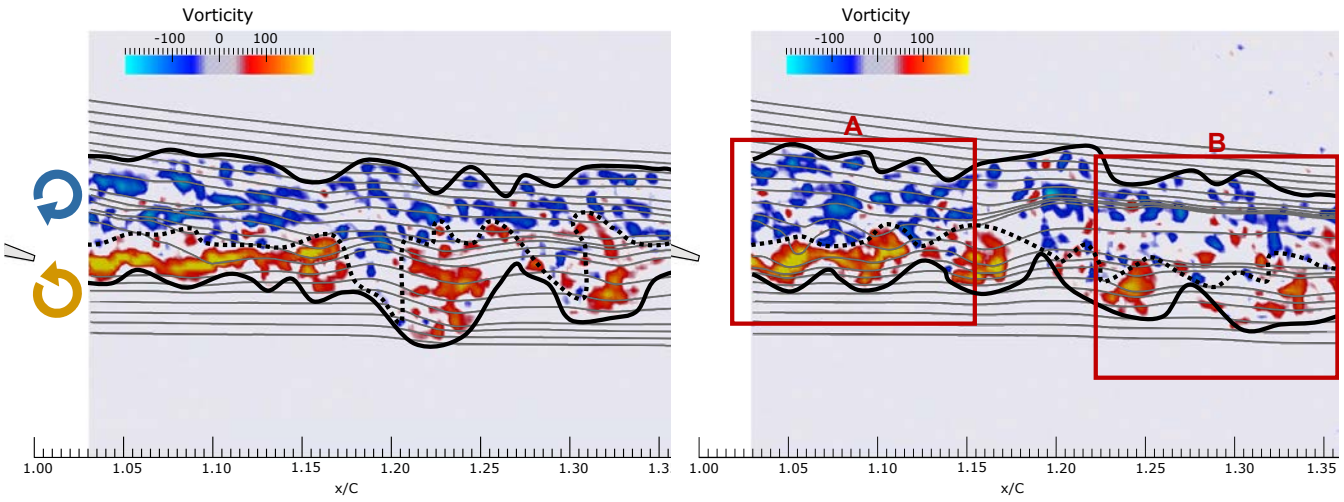

(a) (b)

Figure 3.8: Instantaneous PIV visualization of the static non actuated flow. The trailing edge is visible on the left of the figures; flow comes from left, the field focus on the wake just downstream the trailing edge. Color shades from blue to red highlight intense vorticity areas. (a) corresponds to the static case, (b) is for the actuation frequency $f_a^* = 3.7$ with an amplitude of $a^* = 0.04\%$ (55Hz, 0.3mm peak to peak). The black lines schematically indicate the wake s width. The mixing frontier corresponding to zero vorticity between the two shear layers (upper shear layer – blue and lower shear layer – red) is qualitatively shown by the dashed line.

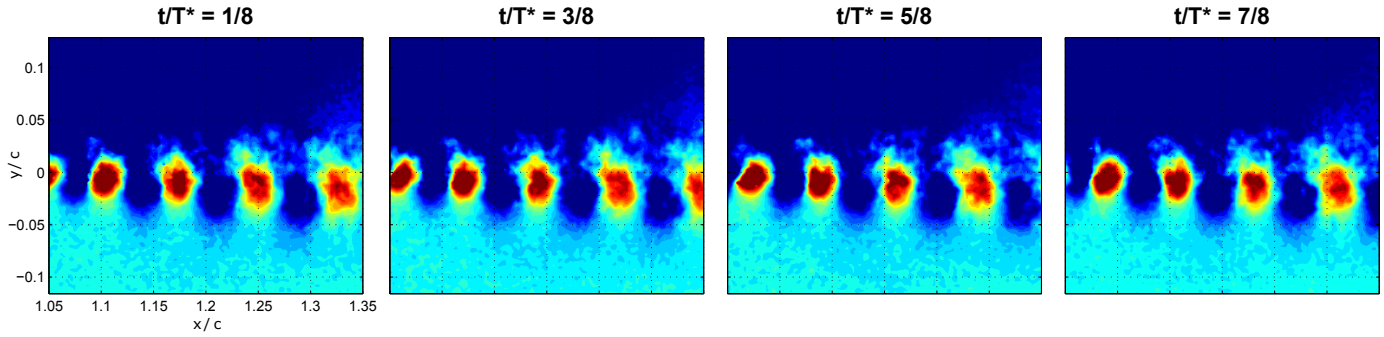

Figure 3.9: Four screenshots of crossflow component of the velocity phase average. The time period T* corresponds to the frequency 172 Hz ($St = 11.5$). Here is the average on 20 periods.

3.4.2 Wake instability creation: Von Kármán instability

In the present experimental conditions (angle of attack and velocity) the Von Kármán instability is not predominant; however the flow contains its signature and its effect. First, coherent peaks in velocity spectra from Figure 3.28 at a frequency $f = 46$Hz (St = 3.0) are present in the upper shear layer coming from the suction side. In the experimental study by Huang and Lin [HL95] the authors measured the Von Kármán Strouhal number (Figure 10 of the publication) as a function of angle of attack and Reynolds number. Regarding the condition of the present paper experiment, the Strouhal is expected in the range of 0.35 by taking as characteristic length the crossflow projection of the airfoil profile. In this study, 46Hz corresponds to a Strouhal number of 0.39 if we take the crossflow projection of the airfoil profile as characteristic length (which still corresponds to $St = 3.0$ when the characteristic length is the chord). This frequency is in the expected range; this is evidence of presence of the Von Kármán mode. The effect of this weak instability is described by its interaction with the Kelvin-Helmholtz previously introduced. This is explained later in the paper by the frequency named A, defined by the relation $St_A = St_{K-H} - St_{VK}$.

3.4.3 Control strategy: from eddy blocking effect to the vortex breakdown

The eddy blocking effect has been investigated in previous studies of our research group; for example, please refer to Hunt et al. [Hun+16]. This is qualitatively presented by the sketch in Figure 3.7. At a wake, a shear interface separates the turbulent region from the non-turbulent one; this interface is referred to as TNT (Turbulent-Non-Turbulent) in the following, as in the related article. The turbulent kinetic energy in the wake delimited between the two TNT interfaces is directly linked to the thickness of the shear layers, their movement and the wake s width, i.e. the expansion or contraction of the turbulent wake. It has been shown (Hunt et al. [HEW08], Szubert et al. [Szu+15]). that by activating smaller-scale structures of the inertial range in the turbulence energy spectrum in between the two shear layers, an upscale energy transfer is achieved towards the larger scale coherent eddies and a shear-sheltering mechanism leads to constriction of the turbulent-non-turbulent interfaces. This mechanism has been depicted in free shear layer flows (Hunt et al. [HEW08]). Thanks to this effect, the shear layers are thinned and the distance between them is reduced. By activating higher-range POD modes where energy is concentrated in the TNT, an effect of loss of coher-

ence on the low-range most energetic POD modes is achieved, as demonstrated by Szubert et al. [Szu+15]. Regarding the present experiment, the eddy blocking effect can be achieved by means of morphing: by the vibrations of the trailing edge, energy is introduced in the wake. A direct morphing-induced vortex breakdown may occur: small vortices clockwise and counter-clockwise are produced, interacting with the existing vortices of the upper and lower shear layer regions leading to pairing or breakdown of vortices depending on the sense of rotation, frequency and phase.

Figure 3.8 presents instantaneous PIV fields with qualitative delimitations of the shear layers. It is recalled that the left Figure 3.8a corresponds to the baseline static case, whereas the right one 3.8b corresponds to the actuation frequency $f_a^* = 3.7$ with an amplitude of $a^* = 0.04\%$ (55Hz, 0.3mm peak-to-peak). The turbulent wake is delimited by black lines. The interaction of two shear layers is schematically illustrated on the figures by black dashed lines. These two snapshots illustrate the eddy blocking effect: compared to the static baseline, the trailing edge actuation adds kinetic energy in the shear interface between the two shear layers (area A). Farther downstream, the eddy blocking effect occurs leading to a mixing and thinning of the shear layer and the wake s width (area B). This smoothing and thinning constrain the formation of large vortices, leading to a vortex breakdown effect. As the actuation is at the trailing edge, the most affected region is the shear layer coming from the bottom side of the wing, because the flow coming from the upper side is detached.

Finally, the eddy blocking effect that shrinks the wake leads to the collapse of the coherent vortices. This causes vortex breakdown. A difference is made between these two phenomena: the eddy blocking effect consists of increasing the energy of non coherent small structures, whereas the vortex breakdown describes a decrease in energy of large coherent vortical structures.

3.5 TR-PIV measurements and characterization of HFVTE effects on airflow

This section deals with TR-PIV of the wing wake, at $Re = 5.10^5$ ($U_\infty = 10.5$m/s). Results are provided and discussed for 4 test cases with baseline camber: no trailing edge vibration (static), vibrations at 55Hz ($f_a^* = 3.7$) at full amplitude (i.e. 1kV applied on actuators leading to $a^* = 0.06\%$) and half amplitude (i.e. 500V, $a^* = 0.03\%$)) respectively, and vibrations at 12.5Hz ($f_a^* = 0.83$) at full amplitude ($a^* = 0.09\%$). The reduced frequency $f_a^* = 3.7$ is selected as it corresponds to the best actuation from results of Ref. [Sch+15]. Indeed 60Hz has been found to be the best actuation frequency for a 0.42m chord wing section with NACA 4412 airfoil and free stream velocity of 7m/s. The dimensionless actuation frequency in this work is evaluated as $f_a^* = 3.7$. On the other hand 12.5Hz is selected as it is a low mechanical resonance of the actuator – which does not excite the whole wing structure. Therefore, this low actuation frequency with its harmonics provides magnitudes large enough to affect strongly the dynamics of the flow as will be shown in the following results.

This section focuses on experiments at Reynolds number of $5 \cdot 10^5$, whereas the force measurements presented in the last section are performed at Reynolds number of 10^6. This is due to technical limitations. Performing TR-PIV at high Reynolds numbers requires large acquisition frequencies. As the memory of the high speed camera is limited, experiment record durations are inversely proportional to Reynolds number. Specifically for Re $= 5 \cdot 10^5$ the acquisitions last more than 11s. On the other hand for $Re = 10^6$ experiment records are only 6.5s. The physical PIV interpretations provided in the following concern experiments at Reynolds number of $5 \cdot 10^5$.

Time averages of the velocity fields are computed from the TR-PIV for the different configurations. Figure 3.10 on left presents the contour plot of time average stream-wise velocity for the static experiment. Black and gray vertical lines represent cut lines corresponding to the superimposed velocity profiles of experiments. Namely velocity profiles are extracted for x/c equal to 1.05, 1.10, 1.15, 1.20, 1.25, 1.30 and 1.35. The values of each curve are normed so that the maximum value among each set of curves does not cross over the neighboring sets, i.e. within a +/-0.05 horizontal unit. This figure should allow the reader to compare the evolution of the wakes for the different test cases. The experimental results appear close to each other, so the velocity profiles at $x/c = 1.05$ corresponding to the black box on the left plot are represented on the right of the figure. Namely, for each

of the 4 test cases 3 acquisition runs are performed to check the repeatability of the measurements. The lines represent the average velocity profiles within envelopes of the same color tones corresponding to the maximum and minimum measurements. Compared to the static case, actuating at $f_a^* = 0.83$ (12.5Hz) increases the velocity defect. On the other hand forcing at $f_a^* = 3.7$ (55Hz) with amplitudes of both $a^* = 0.06\%$ (1000V) and $a^* = 0.03\%$ (500V) – slightly decreases the wake thickness, with consequent potential benefits in terms of drag reduction. These two actuations decrease the velocity defect by more than 3% in average, as visible in Figure 3.10b.

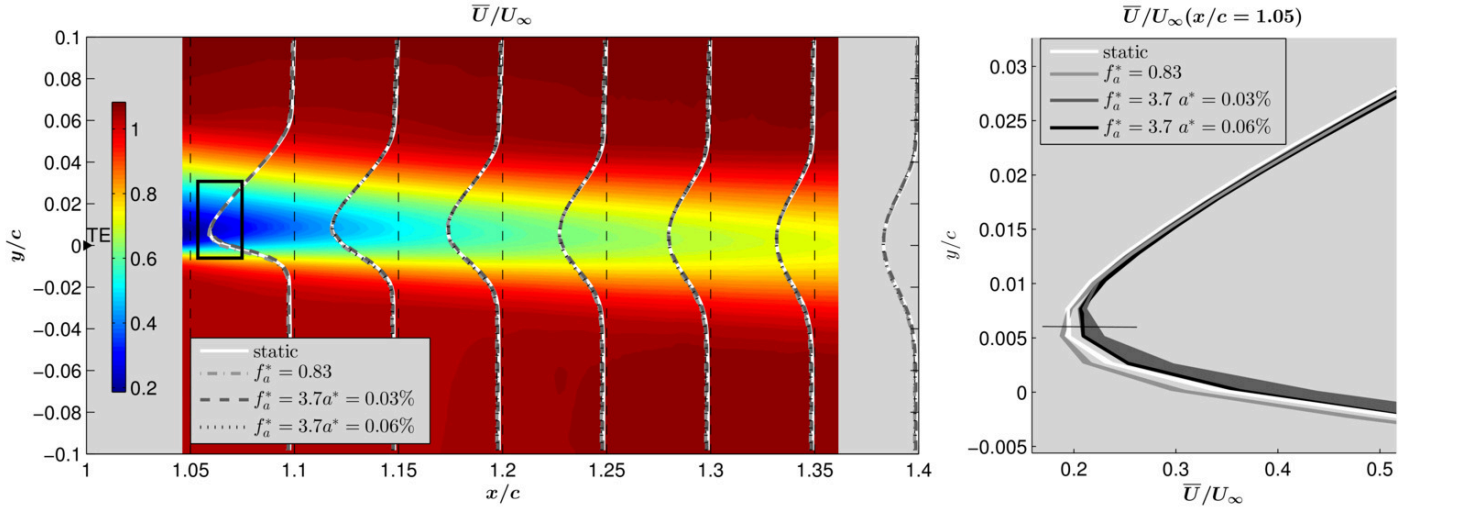

(a) (b)

Figure 3.10: Time average of the stream-wise velocity component for the static case and velocity profiles for the non-actuated and the actuated configurations; $\mathrm{Re} = 0.5 \cdot 10^6$. The thicknesses of the envelopes corresponds to minimum and maximum values calculated using the three acquisitions.

Differences between experiments are more clearly visible in Figure 3.11, which represents the energy of the fluctuating stream-wise component of Reynolds stress tensor $\overline{u^2}$. Consistently with Figure 3.10, the left plot displays the mean stress tensor field for the non actuated configuration. The $\overline{u^2}$ profiles corresponding to the different test cases are superimposed. The right plot is a zoom on $\overline{u^2}$ profiles at $x/c = 1.20$. The turbulent energy associated to the Reynolds stress $\overline{u^2}$ appears concentrated in two regions of the wake: the most energetic one is just past the trailing edge, whereas the second one is located above the trailing edge, coming from the wing suction side.

It appears that actuation concentrates the energy in the shear layer, leading to

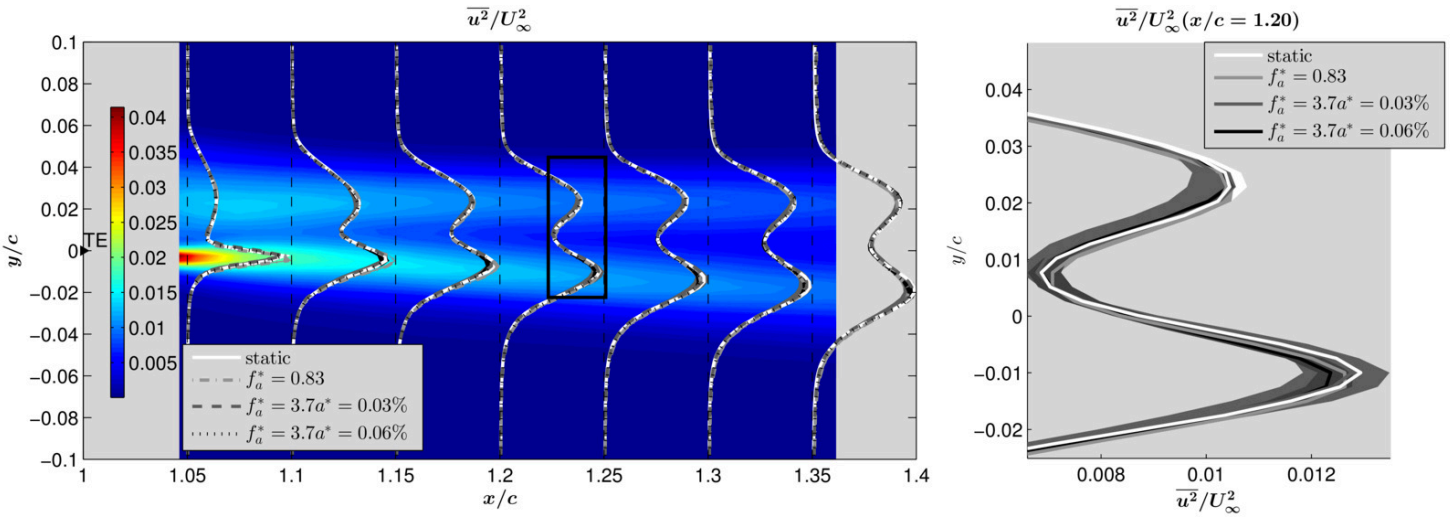

(a) (b)

Figure 3.11: Time average of the squared stream-wise perturbation velocity $\overline{u^2}$ for the static case and profiles for the non-actuated and the actuated configurations; Re $= 0.5 \cdot 10^6$. The thicknesses of the envelopes corresponds to minimum and maximum values calculated using the three acquisitions.

an increase of $\overline{u^2}$ in the lower region of the wake, whilst decreasing the energy of the upper area. Actuating at $f_a^* = 3.7, a^* = 0.03\%$ (55Hz, 500V) decreases $\overline{u^2}$ in both upper and the lower parts of the wake.

Figure 3.12 shows the $\overline{v^2}$ Reynolds stress. The effects of actuation on this component are more significant. The peaks of this quantity are located in the lower part of the shear layer. Namely actuation at $f_a^* = 0.83$ (12.5Hz) reduces by 12% the $\overline{v^2}$ peak, whereas actuation at $f_a^* = 3.7$ (55Hz) increases it by up to 10%. It also appears that all of the actuated configurations reduce the $\overline{v^2}$ stress component just behind the trailing edge (at $x/c = 1.05$).

Figure 3.13 displays the flow field and the profiles of the quantity $\overline{u^2} + \overline{v^2}$. Reasonably assuming the flow as incompressible, $\overline{u^2} + \overline{v^2}$ may be considered as a representation of the turbulent kinetic energy.

Actuating at $f_a^* = 3.7$ (55Hz) decreases the energy just past the trailing edge ($x/c = 1.05$). The opposite is obtained when actuating at $f_a^* = 0.83$ (12.5Hz). Moving downstream, the wake forced at $f_a^* = 0.83$ (12.5Hz) exhibits a significant decrease in kinetic energy on the lower area. On the other side a light decrease in kinetic energy is observed on the upper part of the wake (flow coming from the suction side). Actuating at 55Hz and 1000V slightly decreases the turbulent kinetic energy. On the contrary the actuation at 55Hz and 500V seems to increase

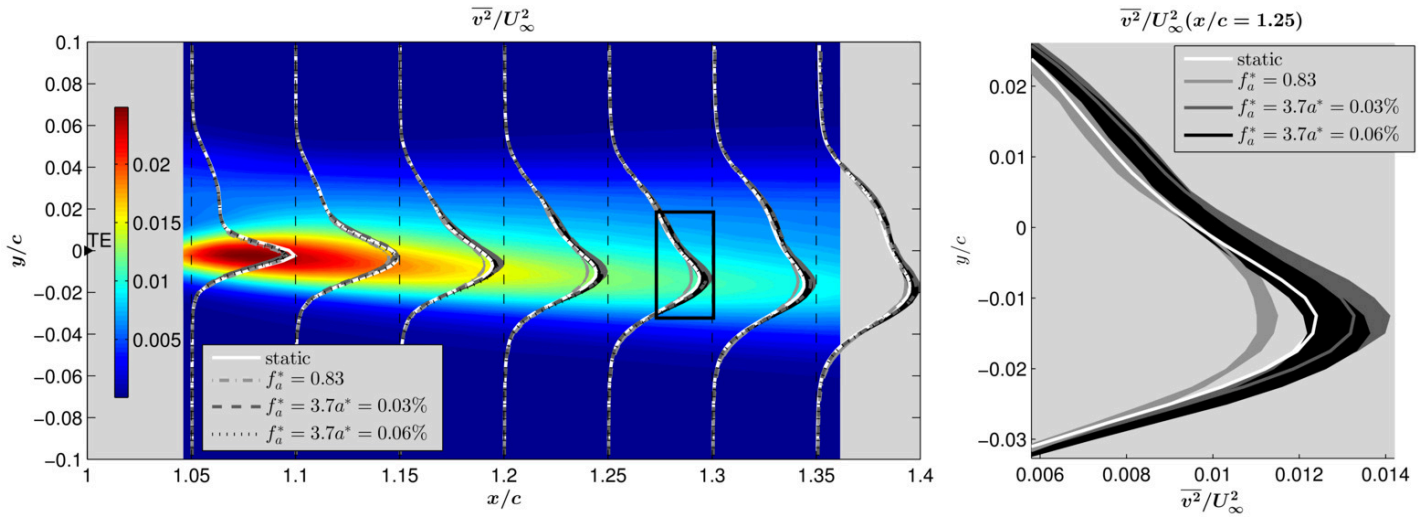

(a) (b)

Figure 3.12: Time average of the squared crossflow perturbation velocity $\overline{v^2}$ for the static case and profiles for the non-actuated and the actuated configurations; Re $= 0.5 \cdot 10^6$. The thicknesses of the envelopes corresponds to minimum and maximum values calculated using the three acquisitions.

the flow energy.

Overall the best actuation in terms of turbulent kinetic energy seems to be at a frequency of 12.5Hz. The energy is concentrated close to the trailing edge, and it quickly decreases moving downstream. Actuation at $f_a^* = 3.7$ $a^* = 0.06\%$ (55Hz 1000V) seems to have no significant effect on kinetic energy. Finally for $f_a^* = 3.7$ $a^* = 0.03\%$ (55Hz 500V) actuation appears to essentially increase the wake energy.

Beyond the present published article, recent PIV measurements have been performed to compare the static non-morphing baseline to the best actuation frequency for $Re = 5.10^5$ i.e. $F_a = 220$ Hz ($f_a^* = 14.7$ $a^* = 0.028\%$). This actuation causes an increase of 2% in lift. Figure 3.14 compares the streamwise velocity component in the wake and for the first time, over the suction side. Figure 3.14c presents the velocity profiles for different positions. The actuation significantly reduces the wake's width in the wake but also upstream the actuation, on the suction side.

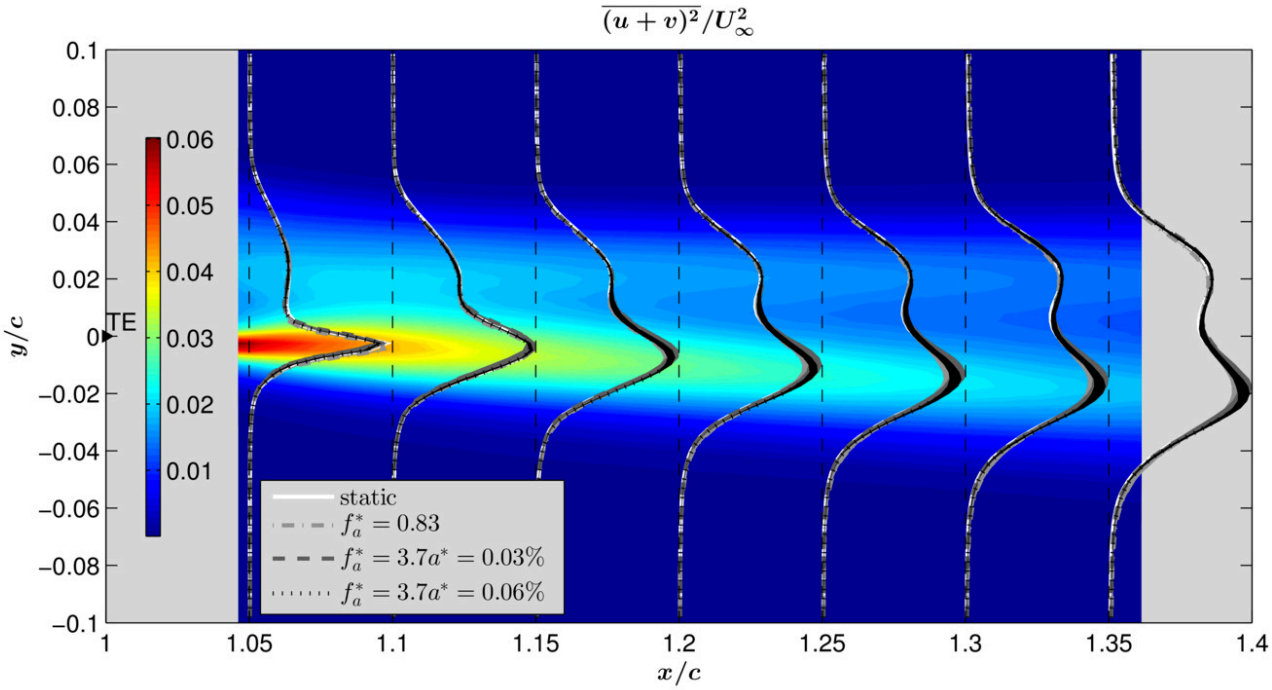

Figure 3.13: Time average of the turbulent kinetic energy $\overline{u^2} + \overline{v^2}$; Re $= 0.5 \cdot 10^6$. The thicknesses of the envelopes corresponds to minimum and maximum values calculated using the three acquisitions.

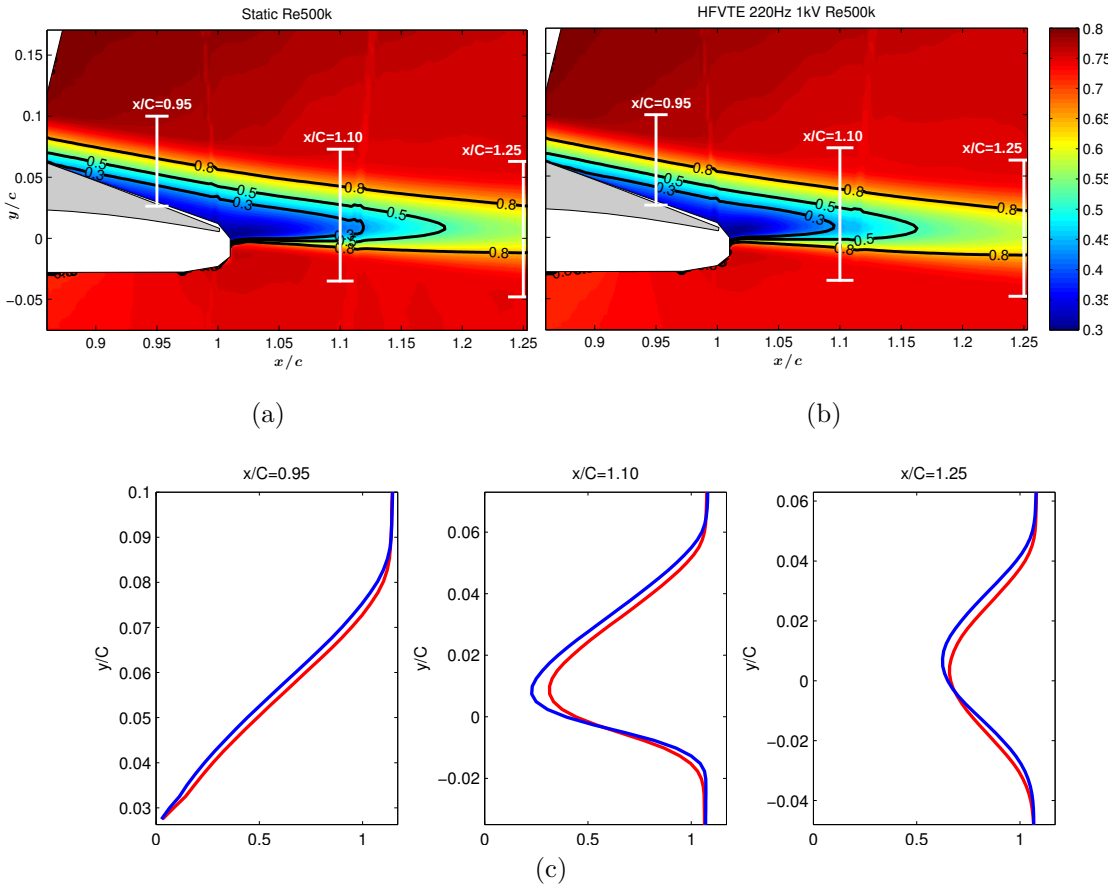

Figure 3.14: Complementary results. Comparison of TR-PIV measures at $Re = 500k$. The time average streamwise component of the velocity is represented in the wake region comprising the last 14% of the wing chord. (a) represent the non morphing case. (b) presents the wake for the best actuation frequency found after balance measures. (c) details the velocity profiles at three positions. It is noticeable that the 2% lift improvement measured by the balance corresponds to significant changes in the velocity profile.

3.6 Proper orthogonal decomposition of the wake flow

In order to have a better understanding of the flow behavior, a proper orthogonal decomposition (POD) is performed on the measured velocity field for the tests at $\mathrm{Re} = 0.5 \cdot 10^6$ and angle of attack of 10°. The POD has been computed on the entire PIV field. The vorticity of each mode is also computed. The POD allows for detecting the coherent structures featured by the flow field on the basis of their wake number and frequency. The POD is extensively used for the assessment of turbulent flow fields, when dealing with experimental data, or with numerical computations [Ber11].

The velocity field can be expressed as a composition of spatial and temporal modes as follows:

$$U'(x,t) = \sum_{i=1}^{n} \phi_i(x) a_i(t), \tag{3.1}$$

being $\phi_i(x)$ and $a_i(t)$ the i^{th} spatial and temporal modes, respectively. The method proposed in Ref. [Per05] is selected among the several techniques employed for the flow modal decomposition. This approach is particularly suitable for experimental data. As the field is discretized in N_x spatial samples for each N snapshots, PIV issues a matrix of data that can be written as:

$$M = \begin{bmatrix} u_1^1 & u_1^2 & u_1^{N-1} & u_1^N \\ u_2^1 & u_2^2 & u_2^{N-1} & u_2^N \\ u_{N_x}^1 & u_{N_x}^2 & u_{N_x}^{N-1} & u_{N_x}^N \\ v_1^1 & v_1^2 & v_1^{N-1} & v_1^N \\ v_2^1 & v_2^2 & v_2^{N-1} & v_2^N \\ v_{N_x}^1 & v_{N_x}^2 & v_{N_x}^{N-1} & v_{N_x}^N \end{bmatrix} \tag{3.2}$$

The correlation matrix required for the modal decomposition is computed as :

$$R = \frac{1}{N} M^T \cdot M, \tag{3.3}$$

and the corresponding eigenvalue problem writes

$$RA = \lambda A, \tag{3.4}$$

being λ the array of eigenvalues and A the matrix of eigenvectors. The computed eigenvalues are then rearranged in descending order as $\lambda_1 > \lambda_2 > ... > \lambda_N = 0$. The matrix of eigenvectors is employed to compute the spatial modes as follows:

$$\phi_i = \frac{\sum_{j=1}^{N} A_j^i u^j}{||\sum_{j=1}^{N} A_j^i u^j||}, \quad i = 1, 2, ...N \tag{3.5}$$

being ϕ_i the i^{th} spatial mode. The computation of the temporal modes is straightforward:

$$a_i = \phi_i M \tag{3.6}$$

Based on 15000 snapshots, the first 200 modes are retained from the POD. In the following only the first five modes and the higher order modes exhibiting the most significant vortical structures are displayed and discussed in a first time. Subsection 3.6.5 deals with higher POD modes to underline the control strategy. Namely, Von Kármán, Kelvin Helmholtz and two other coherent vortical structures have been detected within the wake. First the static configuration, i.e. with the trailing edge non-actuated, is discussed. Then PODs for the velocity fields obtained by trailing edge actuation at frequency $f_a^* = 3.7$ (55Hz) and amplitude $a^* = 0.03\%$ (500V) and $a^* = 0.06\%$ (1000V) respectively are illustrated. Finally the spatial and temporal modes for excitation at frequency $f_a^* = 0.83$ 12.5Hz and amplitude $a^* = 0.09\%$ (1000V) are described.

The Figures 3.16, 3.18, 3.20, 3.22, 3.23, 3.24a, 3.25, 3.26, 3.27c, 3.27b represent from left to right: i) the stream-wise component of the i^{th} spatial velocity mode; ii) the crossflow component of the i^{th} spatial velocity mode; iii) the vorticity computed for the corresponding i^{th} spatial velocity mode; iv) the power spectral density (PSD) of the temporal mode associated to the velocity magnitude. The velocity spatial modes are normalized by the free stream velocity. The black triangle on the left hand side of the flow fields represents the location of the wing trailing edge.

The PSDs are computed using the Welch's weighted overlapped segment averaging estimator [Wel67]. Periodogram estimations use 4 s Hamming windows with 64% overlap (minimum variance) and zero padding. The shedding frequencies are often provided in non dimensional form, using Strouhal number.

3.6.1 POD of the PIV measurements for the baseline configuration

Figure 3.16 displays the first five modes issued by the POD. The first mode (four plots on the top of the figure) corresponds to the time average of the flow field. The wake region is clearly visible both on the velocity and on the vorticity fields. In particular the two counter-rotating vorticity regions correlated to the flow from the upper and on the lower side of the wing section are clearly visible. The PSD of the temporal mode decays rapidly, as expected for the mean field. The energy content of mode #1 is equal to the 98.4% of the total energy, see Figure 3.15. An estimation of the energy featured by a specific mode is provided by the associated eigenvalue, or equivalently by the area subtended by the PSD of the temporal mode. Modes #2 and #3 exhibit shear layer vortical structures, detectable both on the velocity and on the vorticity fields. The peak at Strouhal St = 11.5 observed in the PSD confirms shedding phenomena typical of Kelvin Helmholtz instabilities. The shear layer instability frequency is consistent with the estimation provided in section 3.4, as well as with the findings of [Szu+15] for numerical simulations in transonic conditions. With this regard it's worth remarking that the flow beside the wake in Ref. [Szu+15] features local Reynolds number comparable to that of the experiments carried out in the present work. In fact the flow is substantially decelerated downstream the shock on the suction side. By considering at the velocity fields of modes #2 and #3, they are in space quadrature, and additionally they feature the same spectrum and the same energy content. Therefore a progressive wave of counter-rotating vortices occurs, alternately shed from the trailing edge, and convected downstream.

Modes #4 and #5 seem chaotic and are discussed in 3.6.5.

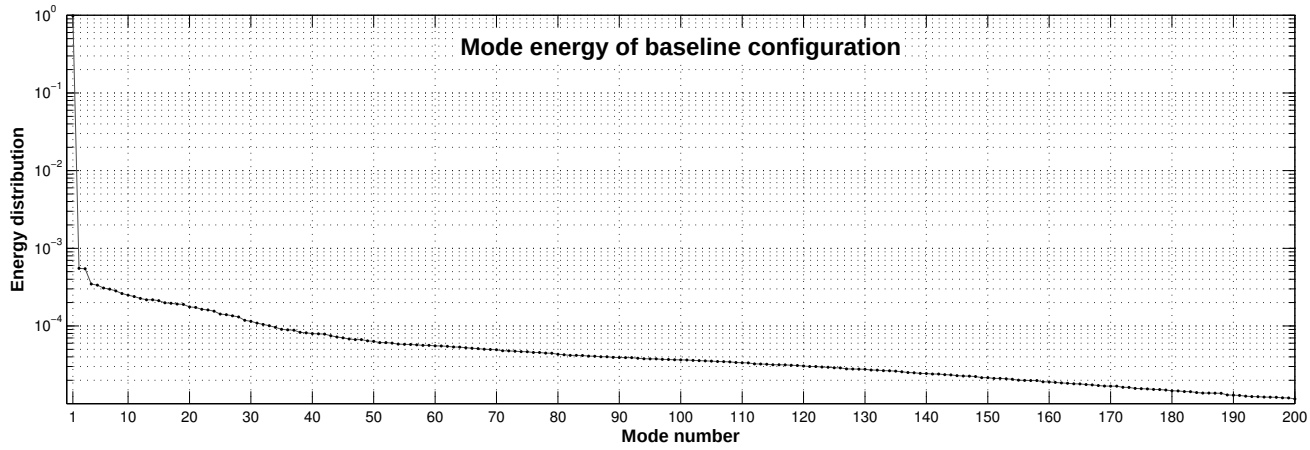

(a)

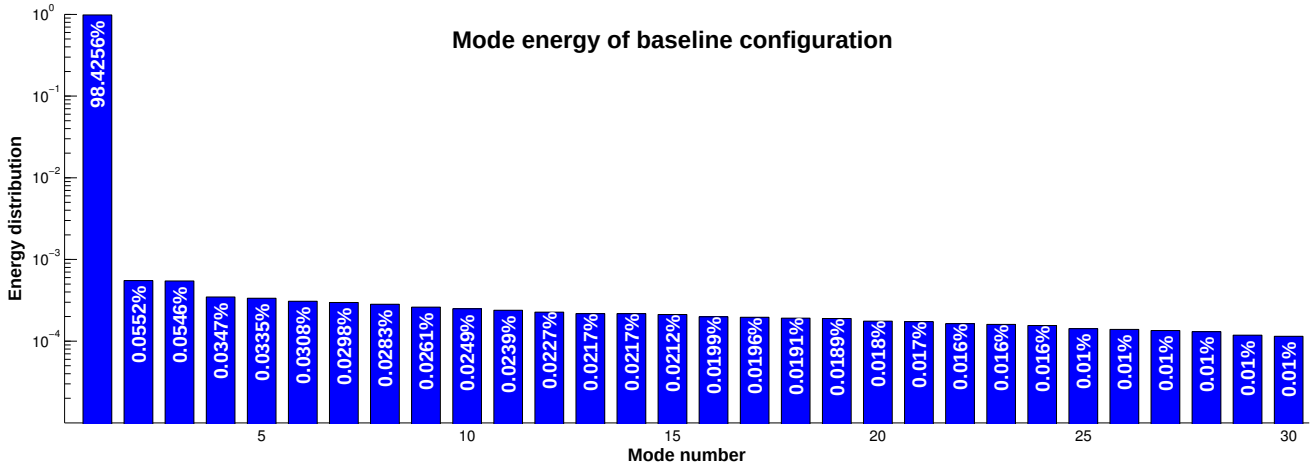

(b)

Figure 3.15: Energy distribution of the first modes issued from the POD for the baseline configuration. The first 200 are presented in (a), (b) focuses on the first 30.

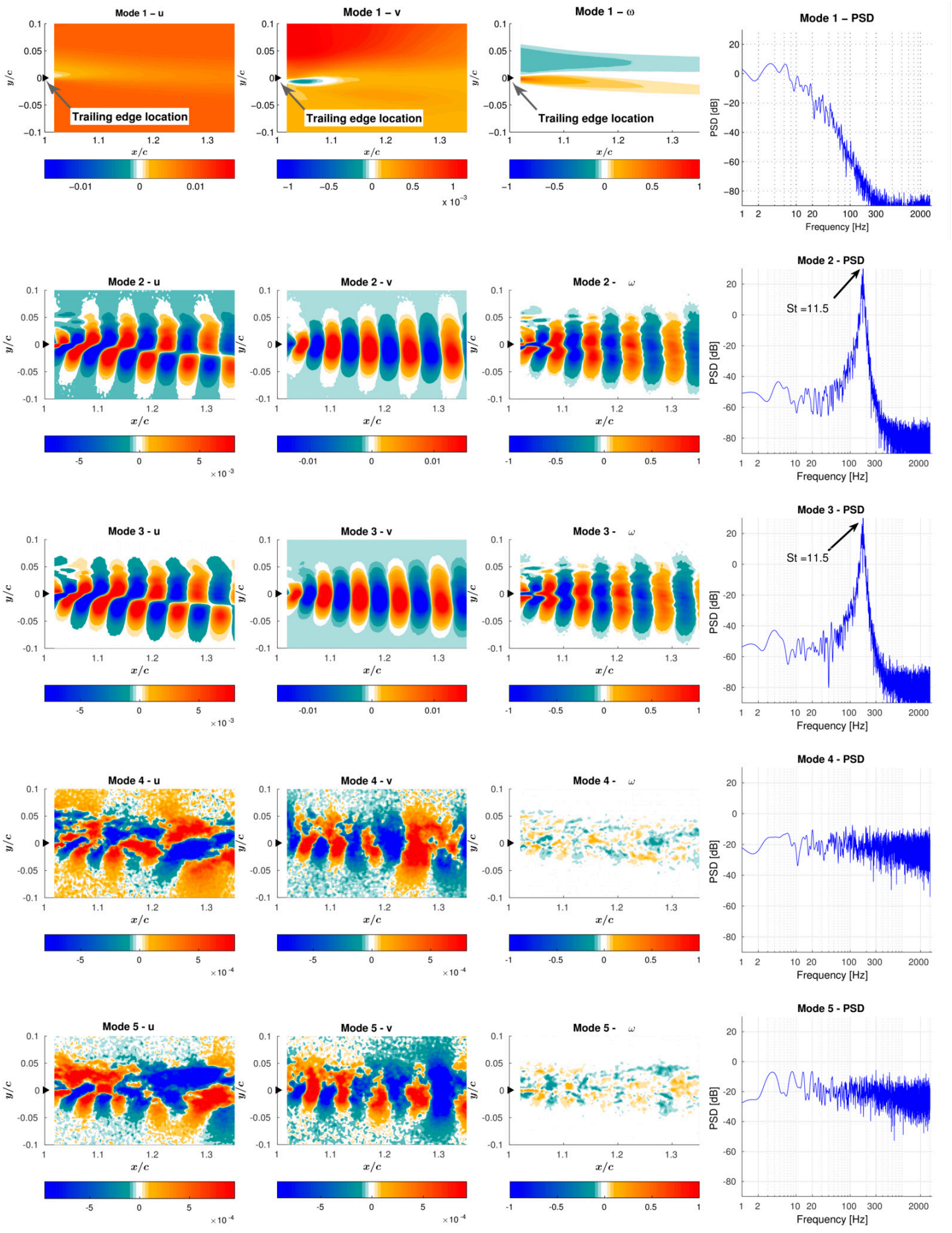

Figure 3.16: POD of the first five modes for the non actuated configuration. From left to right: stream-wise velocity component; crossflow velocity component; vorticity of the corresponding mode; PSD of the temporal coefficients of each POD mode.

3.6.2 POD of the PIV measurements for HFVTE at $f_a^* = 3.7\ a^* = 0.03\%$ (55Hz 500V)

Results of the POD performed for the velocity data measured with actuation at $f_a^* = 3.7\ a^* = 0.03\%$ (55Hz and amplitude 500V) are discussed here. The trailing edge tip cross flow peak to peak velocity imposed by the actuation corresponds to $1\%U_\infty$. The reader can refer to Figure 3.3 (performance of the HFVTE actuator), assuming in this actuation case the vibration amplitudes and velocities are halved, as the voltage is halved compared to the 1kV characterization in the figure (specifically, assuming linear piezoelectricity).

Figure 3.18 shows the first five spatial modes, together with the PSD of the corresponding temporal mode. The first row of figures from the top is the first mode, therefore it describes the mean behavior of the wake. The velocity and vorticity fields, as well as the PSD of the temporal mode, resemble the static counterpart. However in this case the energy associated to the first mode contains the 97.5% of the total energy, therefore it is smaller than the static analogue. As a consequence a larger fraction of energy is contained within the higher order modes, see Figure 3.17.

The second row of plots in Figure 3.18 displays the second mode of the POD. Mode #2 shows non-coherent vortices with almost flat and high amplitude PSD. Modes #3 and #4 exhibit Kelvin Helmholtz vortices. Their frequency shifts from $St = 11.5$ (173Hz) of the non-actuated case, to $St = 11$ (165Hz). The corresponding dimensional frequency of 165 Hz corresponds to three times the actuation frequency. Mechanisms of such change in flow due to morphing are explained in section 3.6.5.

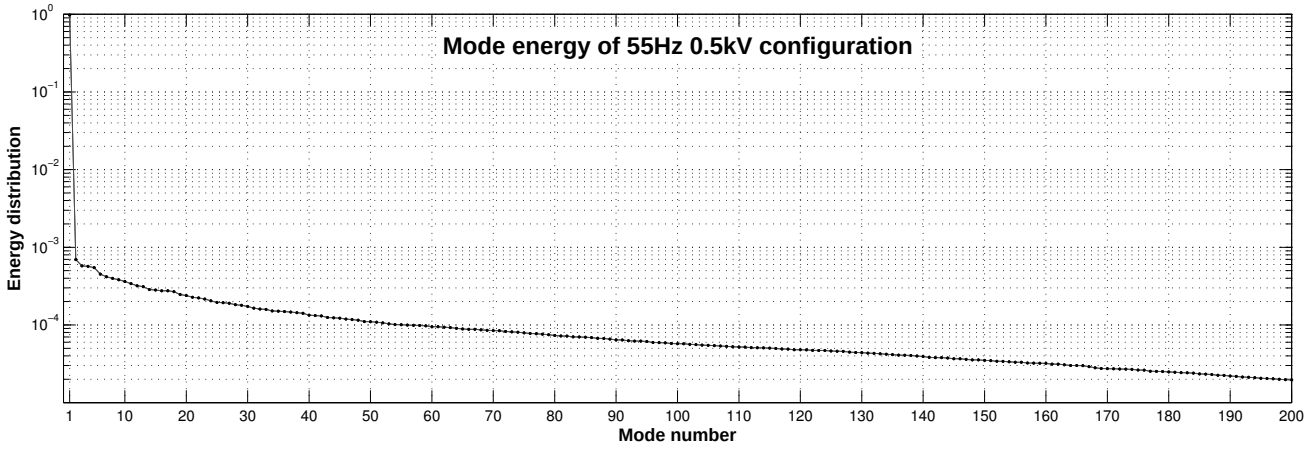

(a)

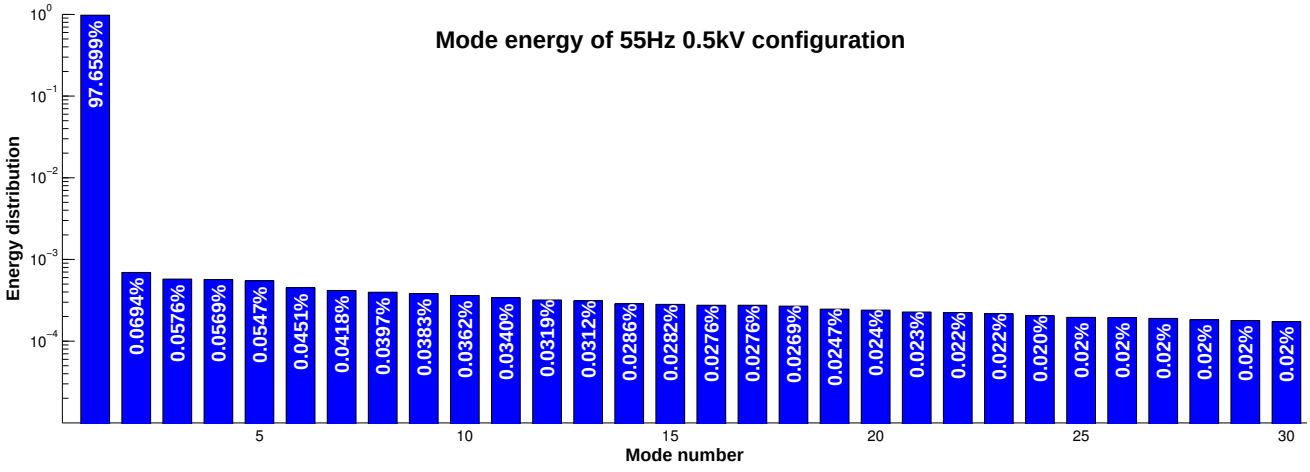

(b)

Figure 3.17: Energy distribution of the first modes issued from the POD with trailing edge harmonic actuation at $f_a^* = 3.7$ $a^* = 0.03\%$ (55Hz 500V). The first 200 are presented in (a), (b) focuses on the first 30.

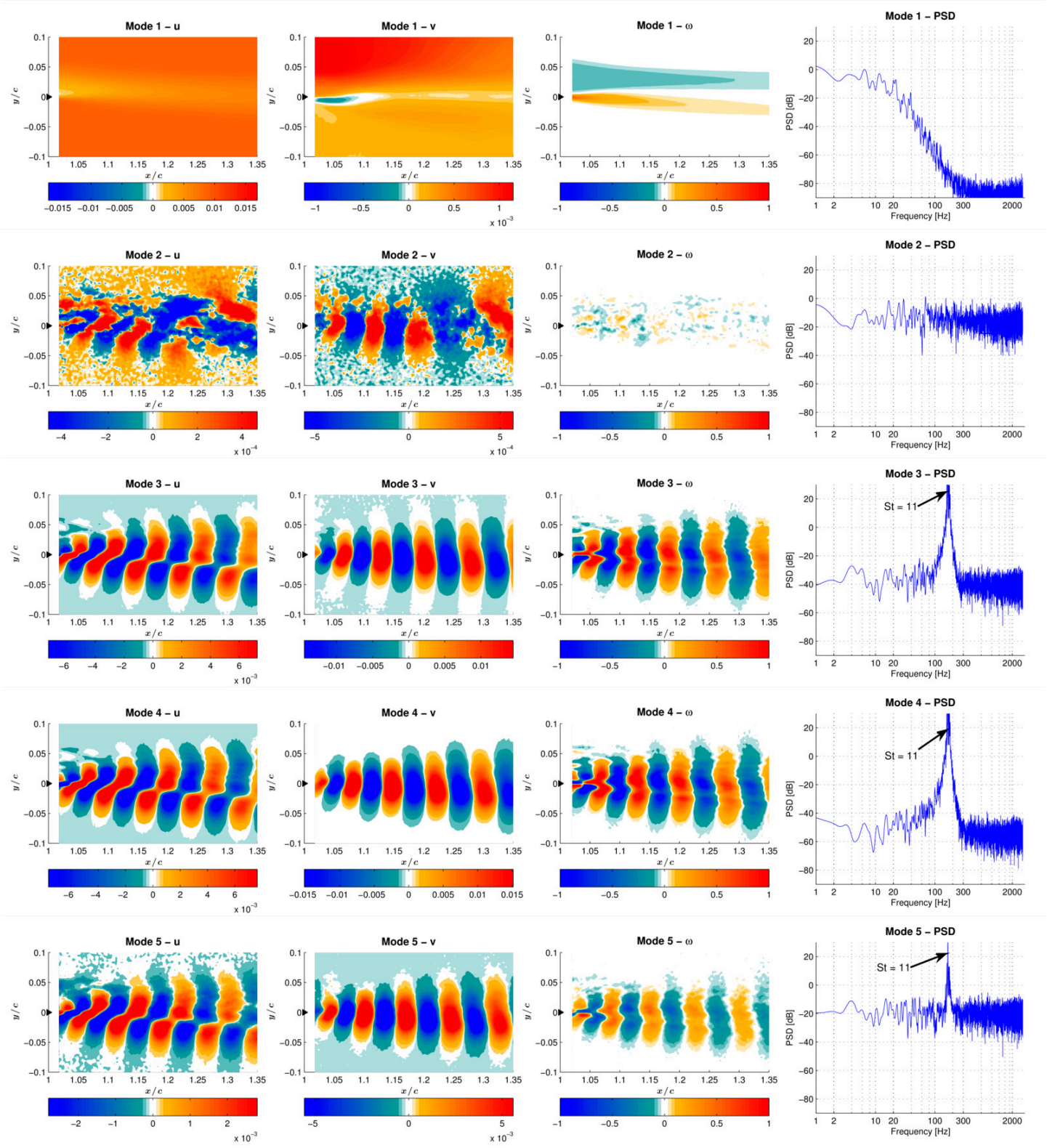

Figure 3.18: POD of the first five modes with trailing edge harmonic actuation at $f_a^* = 3.7$ $a^* = 0.03\%$ (55Hz 500V). From left to right: stream-wise velocity component; crossflow velocity component; vorticity of the corresponding mode; PSD of the temporal coefficients of each POD mode.

3.6.3 POD of the PIV measurements for HFVTE at $f_a^* = 3.7$ $a^* = 0.06\%$ (55Hz 1000V)

Figure 3.20 shows the first five POD modes extracted by the measured velocity field. The energy content of the first mode is 97.5% of the total energy, as for the actuation at 500V. Therefore the energy content of the mean flow remains unchanged when doubling the actuation amplitude, as shown in Figure 3.19. Mode #2 exhibits a tight peak in the PSD of the temporal mode at three times the actuation frequency, i.e., St = 11. This mode is associated with coherent vortical structures not observed within the non actuated configuration. The energy content of mode #2 is found to be larger compared to the static counterpart.

With regard to modes #3 and #4 similar effects to those obtained when actuating at 500V are observed. Namely Kelvin Helmholtz structures are shifted to St = 11 (165Hz), corresponding to three times the actuation frequency. The mechanisms of such change in flow due to morphing are explained in section 3.6.5.

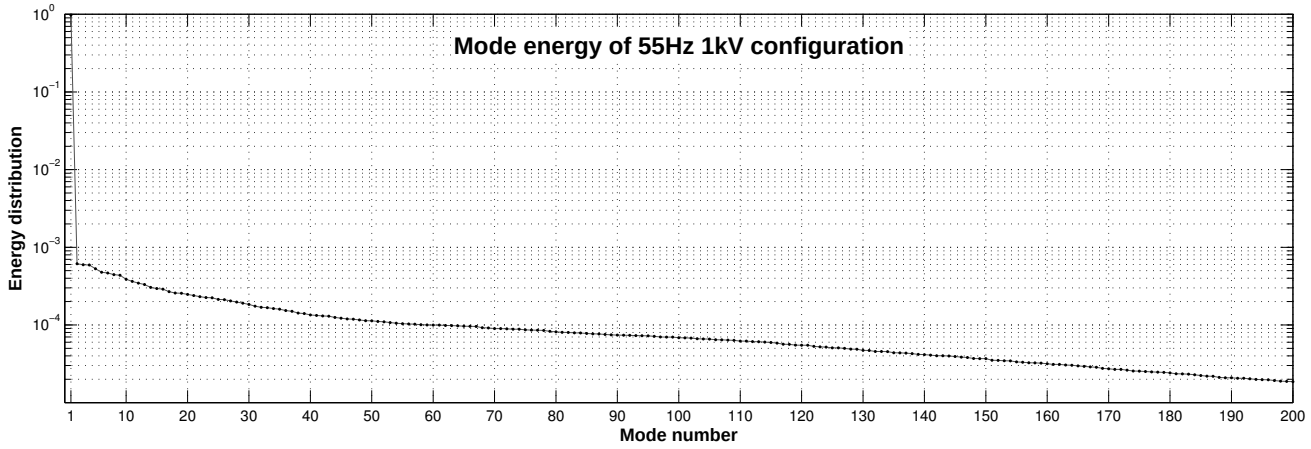

(a)

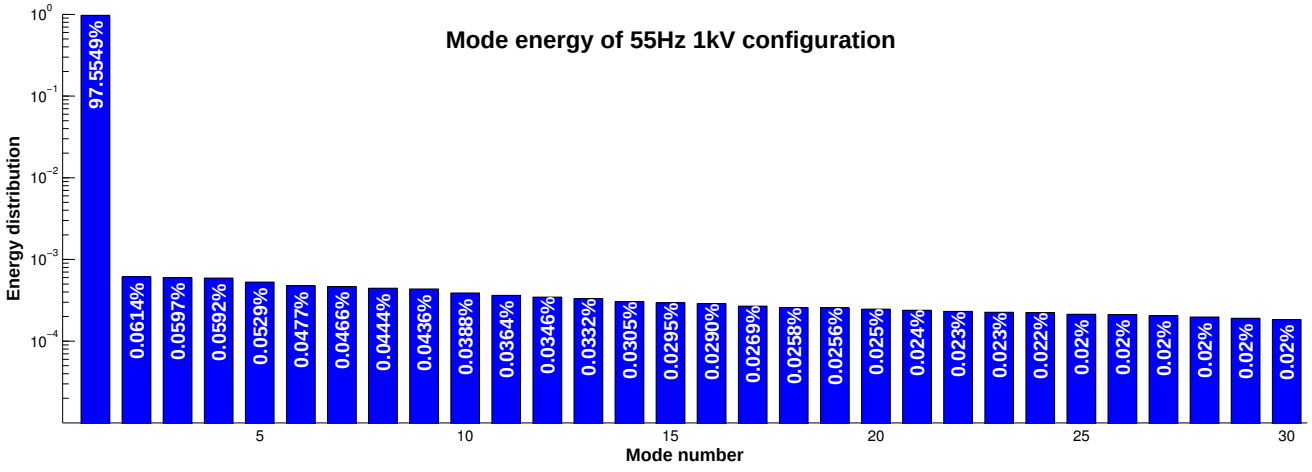

(b)

Figure 3.19: Energy distribution of the first modes issued from the POD with trailing edge harmonic actuation at $f_a^* = 3.7$ $a^* = 0.06\%$ (55Hz 1000V). The first 200 are presented in (a), (b) focuses on the first 30.

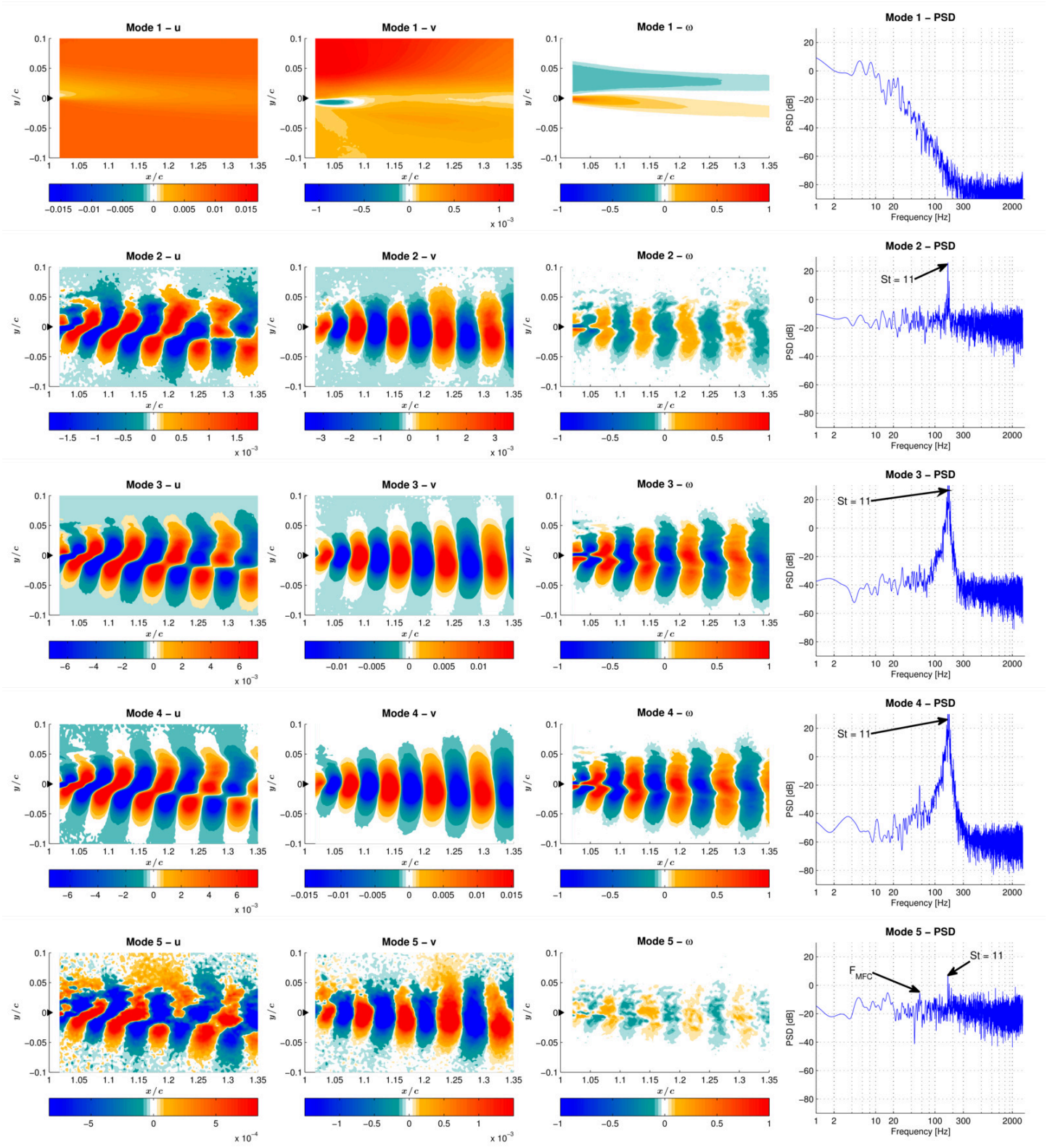

Figure 3.20: POD of the first five modes with trailing edge harmonic actuation at $f_a^* = 3.7$ $a^* = 0.06\%$ (55Hz 1000V). From left to right: stream-wise velocity component; crossflow velocity component; vorticity of the corresponding mode; PSD of the temporal coefficients of each POD mode.

3.6.4 POD of the PIV measurements for HFVTE at $f_a^* = 0.83$ $a^* = 0.09\%$ (12.5Hz 1000V)

The response of the flow to harmonic excitations at frequency $f_a^* = 0.83$ (12.5Hz) and amplitude $a^* = 0.09\%$ (1000V) is finally investigated by means of POD. The deflection velocity of the trailing edge tip is $0.45\%U_\infty$.

Figure 3.22 shows the first five modes issued by the POD of the measured velocity field. The first mode, corresponding to the time average of the velocity and of the resulting vorticity, features an energy content of 97.6%, not dissimilar to that of the static counterpart, see Figure 3.21.

The energy content of mode #2 contains the 0.06% of the total energy amount. The corresponding velocity and vorticity fields show non-coherent vortices with almost flat and high amplitude power spectral density. The flow energy of this mode appears to be significantly increased compared to the non-actuated case. A similar phenomenon as $f_a^* = 3.7$ $a^* = 0.06\%$ (55Hz 500V), i.e. a new chaotic second POD mode is found. Discussion is detailed in section 3.6.5.

The PSD of mode #3, #4 and #5 show peaks at 10 times the actuation frequency (St = 8.5), associated to very coherent structures and corresponding to Kelvin Helmholtz vortices. Moreover, a secondary energy peak is visible at St = 11.7 (175Hz), i.e., 14 times the actuation frequency.

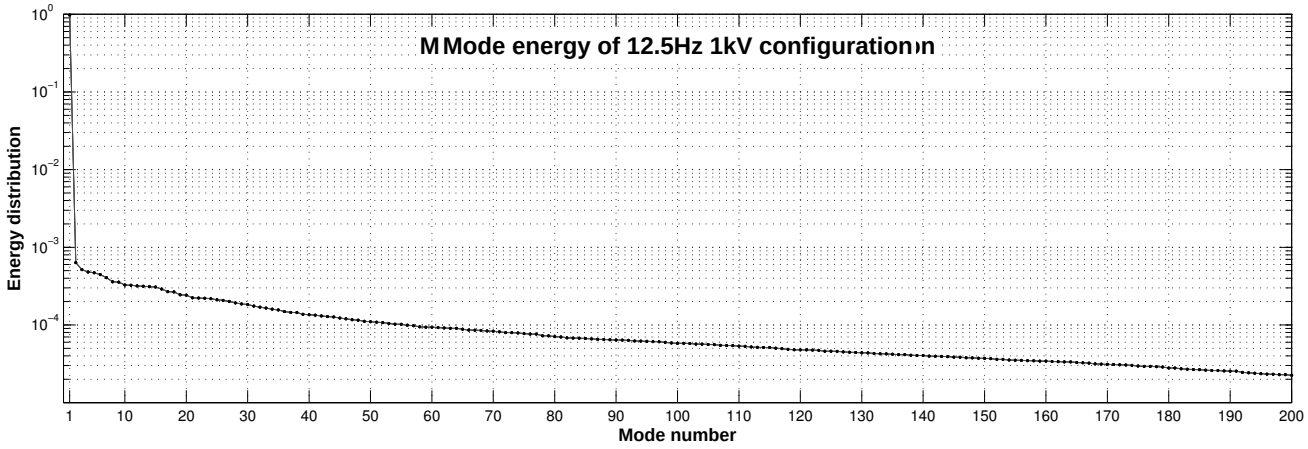

(a)

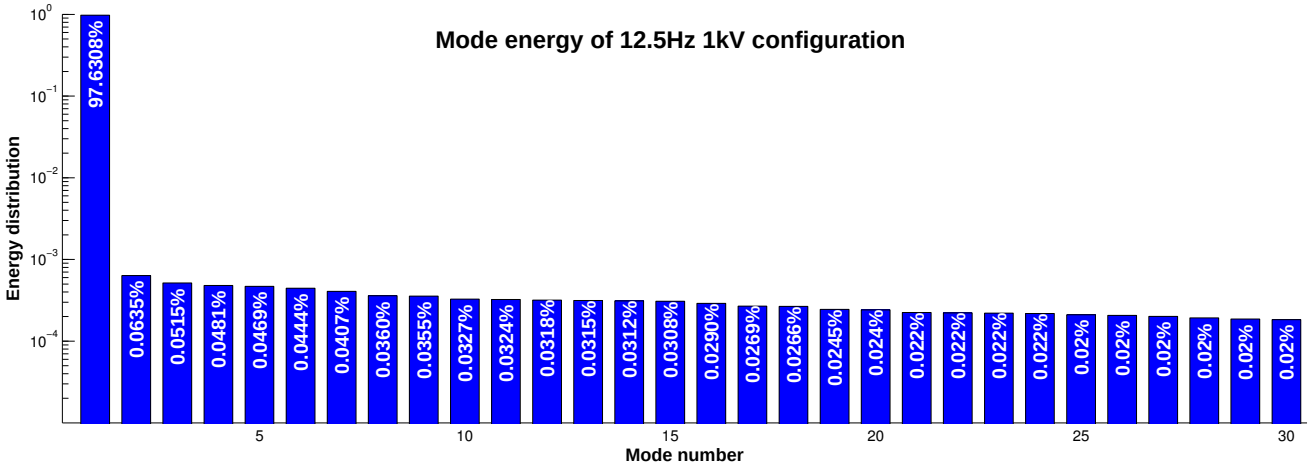

(b)

Figure 3.21: Energy distribution of the first modes issued from the POD with trailing edge harmonic actuation at $f_a^* = 0.83$ $a^* = 0.09\%$ (12.5Hz 1000V). The first 200 are presented in (a), (b) focuses on the first 30.

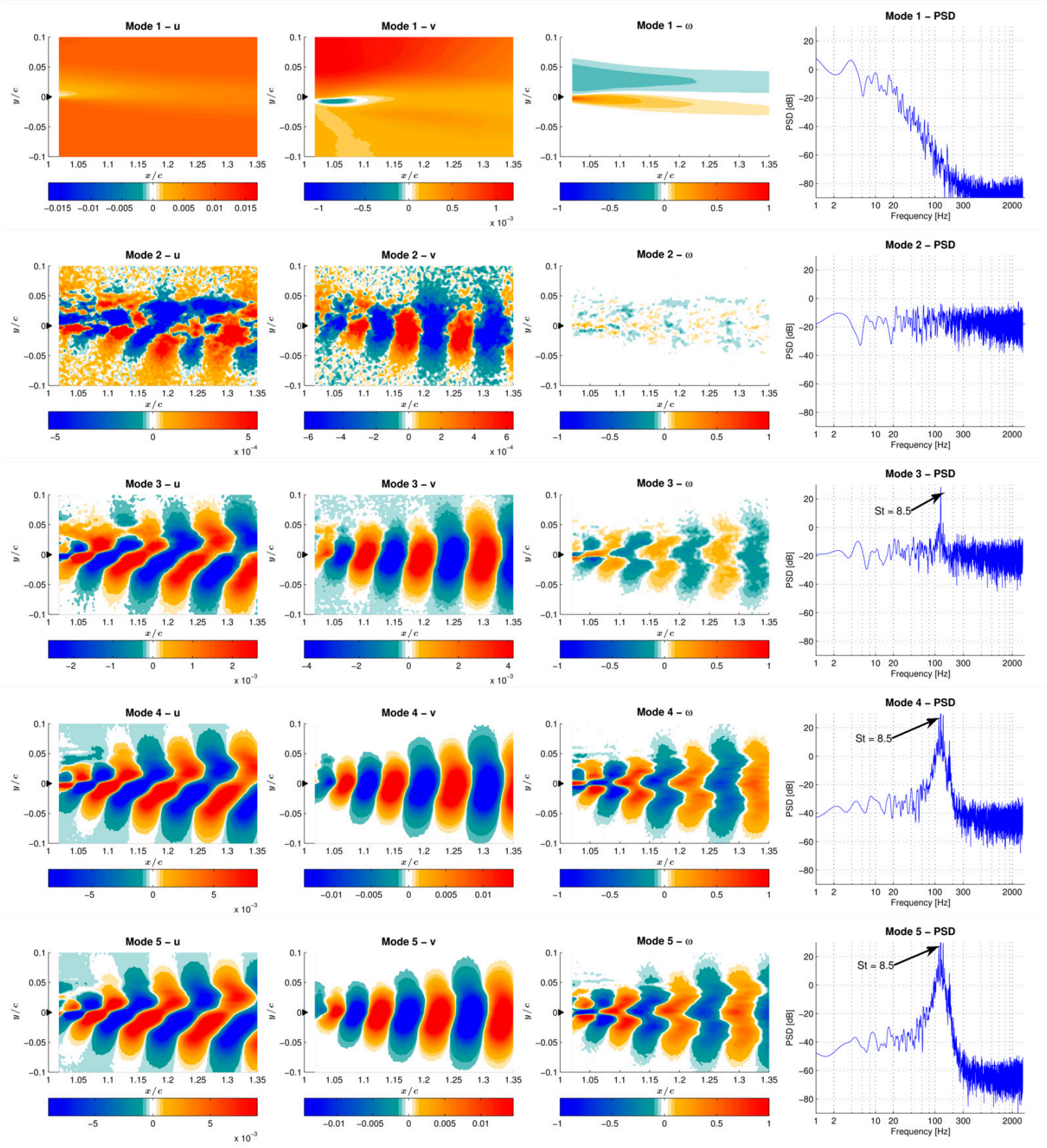

Figure 3.22: POD of the first five modes with trailing edge harmonic actuation at $f_a^* = 0.83$ $a^* = 0.09\%$ (12.5Hz 1000V). From left to right: stream-wise velocity component; crossflow velocity component; vorticity of the corresponding mode; PSD of the temporal coefficients of each POD mode.

3.6.5 Wake mechanisms, higher order modes and control strategies

This section now details some wake mechanisms and focuses on comparison between the different actuations. The control strategy described in section 3.4 is illustrated with experimental results.

1) Von Kármán vortex shedding. Regarding the static baseline, two coherent structures are also observed at $St = 8.5$ (127Hz) and at $St = 3$ (46Hz), or multiples of this latter frequency. Figure 3.23 shows an example of a mode where coherent structures at these frequencies are detected. Specifically modes where peaks at multiples of St = 3 (46Hz) are detected are #8, #9, #16, #17, #18, #19, #20, #24, #27, #34 and #35. Modes with vortex shedding phenomena at St = 8.5 (127Hz) are #12, #13 (Figure 3.25), #14, #15, #16, #17, #18, #19, #21, #22, and #24. As a consequence, there are some modes which exhibit both of these two vortical structures, respectively coupled, see Figure 3.23. It is worth noting that this coupling is found to be strongly affected by the trailing edge actuation discussed in the following. The peak at St = 3 (46Hz) can be associated with the Von Kármán instabilities. The peak at 127Hz (which will be referred to as the letter A in the next section) is a combination of Von Kármán (VK) and shear layer (SL) instabilities according to: $St_{\mathrm{A}} = St_{\mathrm{SL}} - St_{\mathrm{VK}}$.

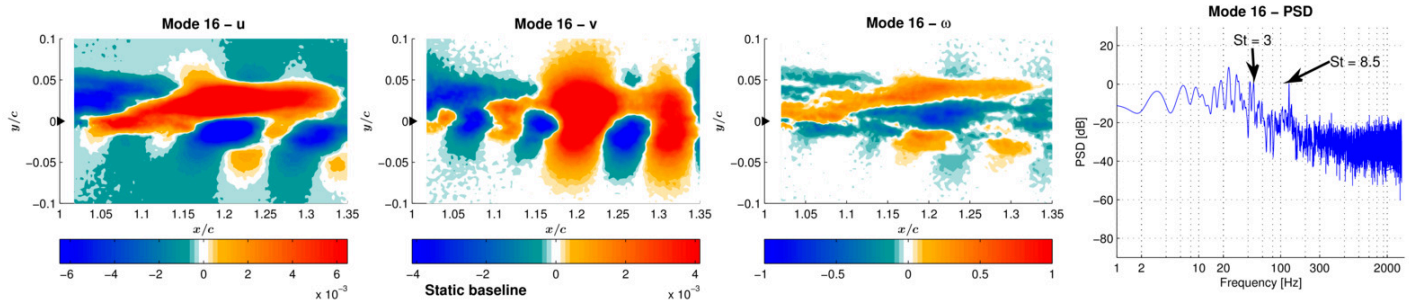

Figure 3.23: POD mode #16 for the non actuated baseline configuration. From left to right: stream-wise velocity component; crossflow velocity component; vorticity of the corresponding mode; PSD of the temporal coefficients of each POD mode.

2) Higher order mode $St = 14$**.** Figure 3.24a shows the mode #36 issued by the POD of the static case. This mode shows a special coherence and the PSD for the temporal mode corresponds to St = 14.1 (212Hz peaks referred to as B in section 3.5). The corresponding modes in case of morphing at $f_a^* = 3.7$ $a^* = 0.03\%$ (55Hz 500V) are #38 or #39, because the actuation inserts new patterns. For this reason, in the morphing case, mode #39 of the actuated case is compared to mode #36 of the static case (see Figure 3.24b). It can be seen that this mode has lost its spatial coherence, the spectrum does no more display predominant peaks and the vorticity field of this mode indicates a significant of the wake thickness, corresponding to approximatively 15%. This morphing induced effect is analogue to the re-injection of turbulence by means of higher-order POD modes studied numerically by Szubert et al. [Szu+15], enhancing an eddy-blocking effect.

It's also worth remarking that none of the 60 modes retained from the POD for all actuation cases exhibit peaks at St = 14.1 (212Hz). This confirms that these coherent structures are actually dissipated and are not moved towards larger wave numbers. This is an example of vortex breakdown.

3) Shift of modes associated to the shear layer towards higher order-lower energy modes. Both actuations at $f_a^* = 3.7$ $a^* = 0.03\%$ (55Hz, 500V) and $f_a^* = 0.83$ $a^* = 0.09\%$ (12.5Hz, 1000V) exhibit a downshift of the modes #2 and #3 compared to the static baseline. This effect is also present on the $f_a^* = 3.7$ $a^* = 0.06\%$ (55Hz, 1000V) with a higher presence of the actuation frequency in the spectra, due to a larger forcing amplitude. The cause is twofold.

Firstly, the forced flow is found to exhibit vortex shedding phenomena at super-harmonics of the actuation frequency. The two actuations at $f_a^* = 3.7$ (55Hz) have shifted the Kelvin Helmholtz shedding frequency from $St = 11.5$ to 3 times the actuation frequency $St = 11 = 3 \cdot f_a^*$. Actuation at $f_a^* = 0.83$ has shifted this frequency to 10 times the actuation frequency $St = 8.5 = 10 \cdot f_a^*$. Again the forced flow is found to exhibit vortex shedding phenomena at super-harmonics of the actuation frequency. A similar behavior was showed for instance in Refs. [Mot15a; Mot15b] on the flow response to a harmonically oscillating L-shaped Gurney flap.

Secondly, morphing introduces a new chaotic second mode - see modes #2 in Figures 3.18 and 3.22. This energy injection is the signature of the eddy blocking effect described in Section 3.4. The modes #3 and #4 of the morphing case are similar to the modes #2 and #3 of the baseline, so morphing causes the shift of these two modes to higher order. These two modes characterize the main vortex shedding of the wake lost energy. This downshift in energy is associated to vortex breakdown. Specifically, the energy distribution of this morphing case ($f_a^* = 3.7$ $a^* = 0.03\%$) shows that the chaotic mode #2 is 3% more energetic than the coherent mode #3 - see Figure 3.17. This decrease in energy reaches the value of 23% between mode #2 and #3 for the $f_a^* = 0.83$ $a^* = 0.09\%$ morphing case -

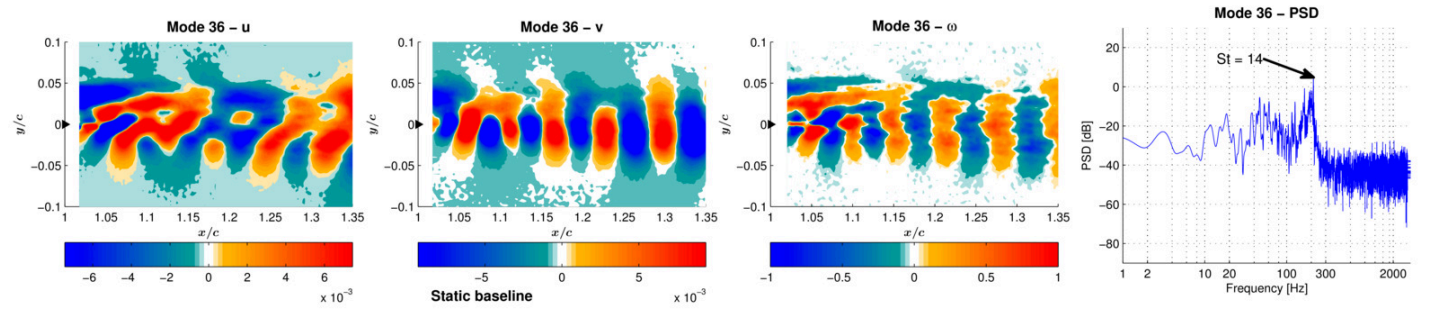

(a) mode #36 for the non-actuated baseline

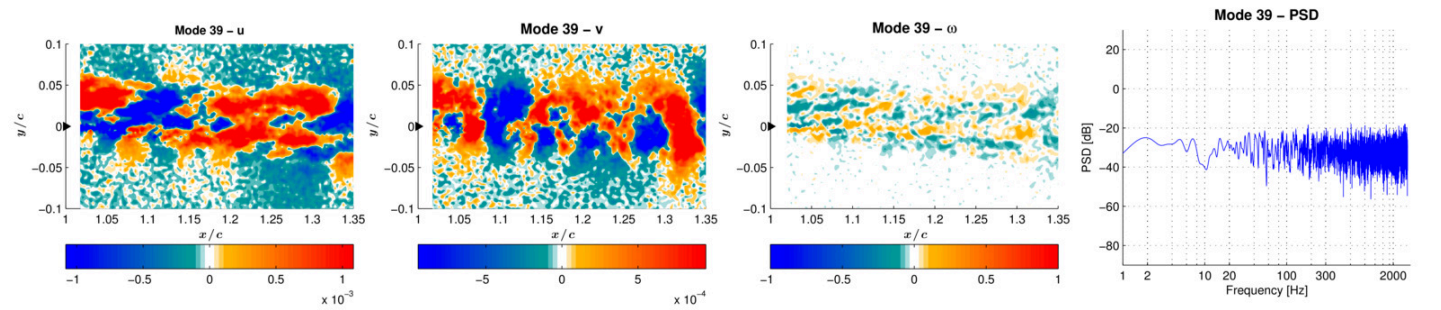

(b) mode #39 for the $f_a^* = 3.7$ $a^* = 0.03\%$ morphing case

Figure 3.24: Comparison of two POD modes. From left to right: stream-wise velocity component; crossflow velocity component; vorticity of the corresponding mode; PSD of the temporal coefficients of each POD mode.

see Figure 3.21. Further shifts in the flow modes with respect to the static case are observed when actuating at $f_a^* = 3.7$ $a^* = 0.03\%$ (55Hz, 500V). Namely coherent structures observed for mode #16 of the static configuration are found on mode #32, not reported here for brevity purposes.

4) Shear layer thinning. Morphing effects on wake thickness are visible on higher POD modes. For instance, the mode #13 of the static baseline (Figure 3.25) indicates wake expansion. The actuated case at frequency $f_a^* = 3.7$ $a^* = 0.06\%$ (55Hz, 1000V) illustrates the eddy blocking effect. The POD mode #22 (Figure 3.26) corresponds to the baseline mode #13, because there are similarities in the spatial mode distribution and their temporal coefficients show the same peak at Strouhal of 8.5; besides, actuation frequency is present in the spectrum of the morphing case (Figure 3.26d). The v component of the mode indicates a thinner wake which decreases in the wake expansion, after $x/c = 1.25$. The wake thickness, indicated by arrows on Figures 3.25c, 3.26c is reduced by approximately 22% at $x/c = 1.35$, thanks to the actuation. One can also remark that – due to the morphing – the magnitude of the characteristic peak at Strouhal of 8.5 has decreased by 10 dB, which means the power density divided by 10.

5) Downshift of the higher energy chaotic modes. Now considering the modes #4 and #5 of the static baseline (Figure 3.16 or Figure 3.27a), similarities can be found with modes #57 of the case $f_a^* = 3.7 - a^* = 0.03\%$ (Figure 3.27b) and the mode #40 of the case $f_a^* = 0.83$ $a^* = 0.09\%$ (Figure 3.27c). These modes have comparable spatial energy distribution. Modes #4 and #5 of the baseline are chaotic but with high energy. The corresponding morphing modes have thinner wakes, due to the eddy blocking effect. Spectra of morphing modes #40 and #57 present peaks that are not present in the static modes; these peaks correspond to harmonic of the actuation frequencies: the Strouhal of 9.2 corresponds to 11 times the actuation frequency ($9.2 \simeq 11 \cdot 0.83$) for the mode #40 whereas the Strouhal of 11 corresponds to 3 times the actuation frequency for the mode #57 ($11 \simeq 3 \cdot 3.7$). It is worth noting that these two morphing cases, both different in amplitude and frequency generate equivalent effects.

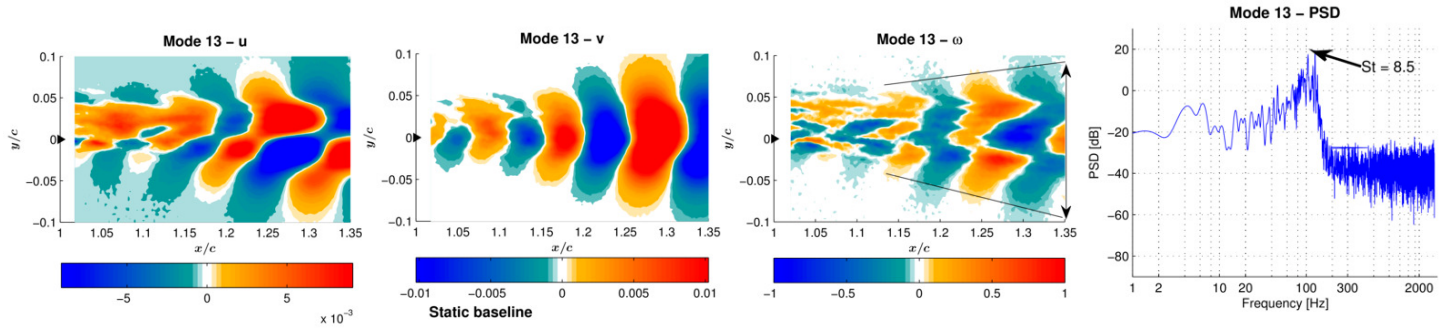

(a) (b) (c) (d)

Figure 3.25: POD mode #13 for the non actuated baseline configuration. From left to right: stream-wise velocity component; crossflow velocity component; vorticity of the corresponding mode; PSD of the temporal coefficients of each POD mode.

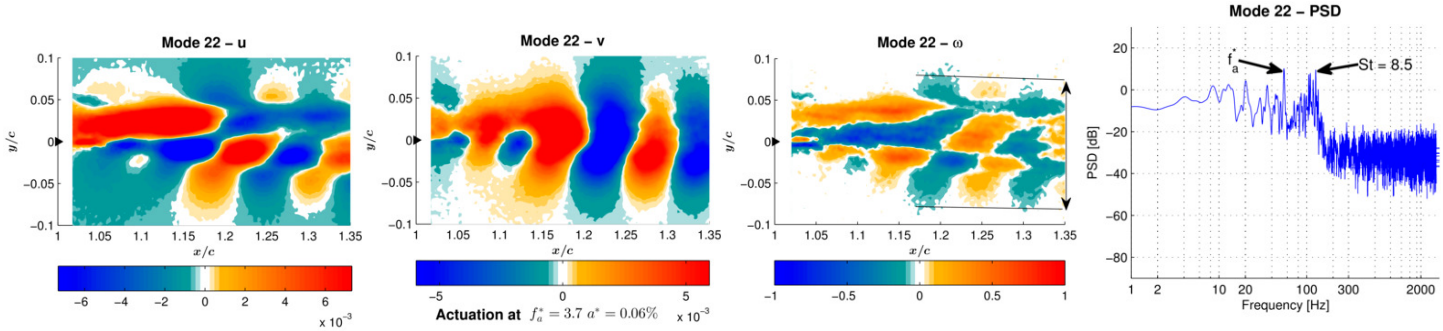

(a) (b) (c) (d)

Figure 3.26: POD of mode #22 with trailing edge harmonic actuation at $f_a^* = 3.7$ $a^* = 0.06\%$ (55Hz 1000V). From left to right: stream-wise velocity component; crossflow velocity component; vorticity of the corresponding mode; PSD of the temporal coefficients of each POD mode.

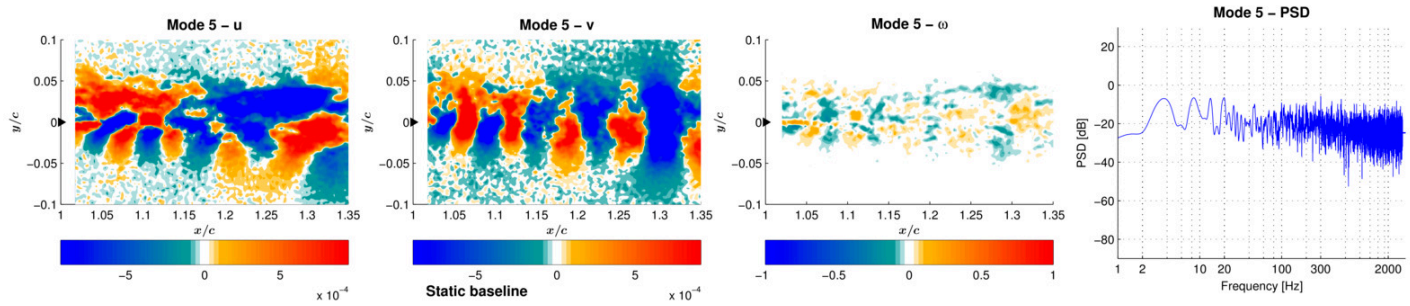

(a) POD mode #5 for the non actuated baseline configuration. From left to right: stream-wise velocity component; crossflow velocity component; vorticity of the corresponding mode; PSD of the temporal coefficients of each POD mode.

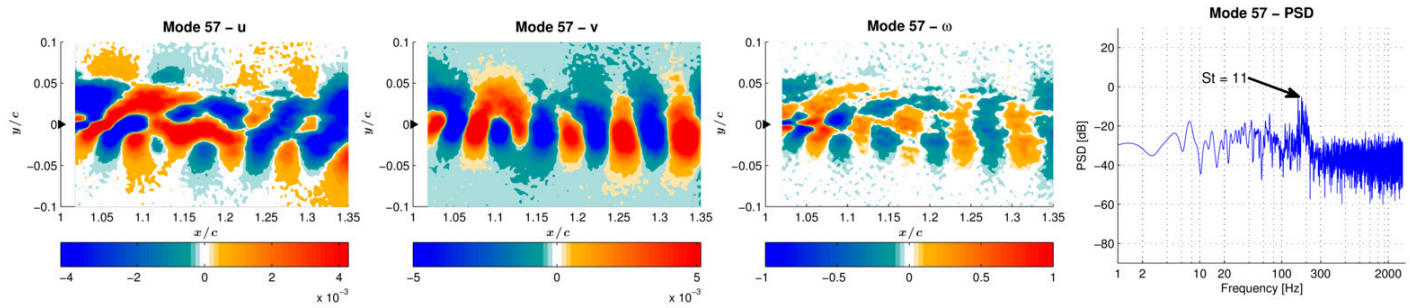

(b) POD mode #57 with trailing edge harmonic actuation at 55 Hz and 500 V. From left to right: stream-wise velocity component; crossflow velocity component; vorticity of the corresponding mode; PSD of the temporal mode for the velocity magnitude.

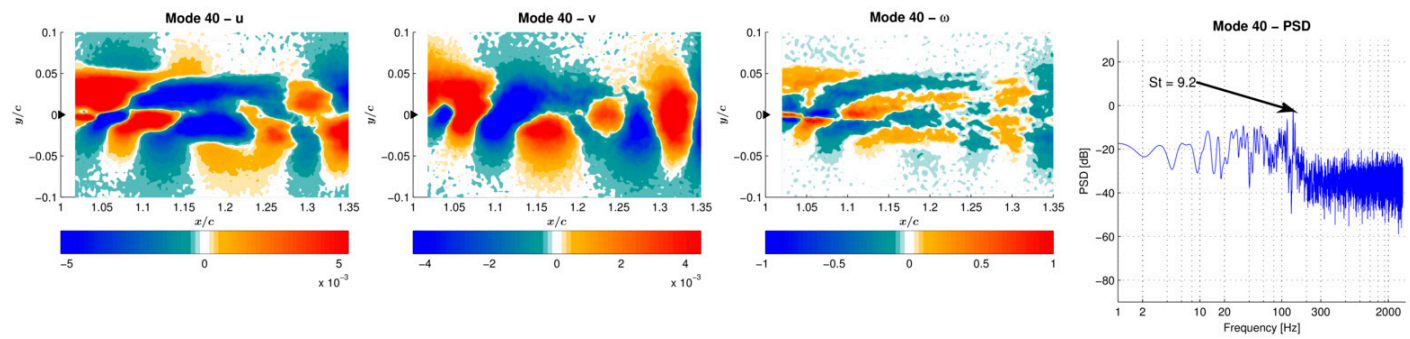

(c) POD mode #40 with trailing edge harmonic actuation at 12.5 Hz and 1000 V. From left to right: stream-wise velocity component; crossflow velocity component; vorticity of the corresponding mode; PSD of the temporal mode for the velocity magnitude.

Figure 3.27: POD modes related to the downshift of higher energy chaotic modes.

3.6.6 General remarks on the POD results

The proper orthogonal decomposition is carried out on the wake velocity field measured by PIV surveys. The first 60 modes issued by POD are investigated in terms of velocity and vorticity fields. The PSD of the temporal mode is also analyzed. It appears that the vortical structures observed at certain frequencies on the unforced flow are shifted to the actuation frequencies or to their higher harmonics. This effect occurs equally for the two actuation amplitudes here considered. With this regard it appears that for the excitation frequency of $f_a^* = 3.7$ (55Hz), actuating at $a^* = 0.03\%$ (500V) is more favorable compared to $a^* = 0.06\%$ (1000V), where a significant increase in the energy of mode #2 relative to the static case is observed. In general comparing the unforced and the forced flow, this latter features a slightly higher level of energy. The fact that the same vortical structures are observed on higher order modes relative to the static case is an indication that a proper vortex breakdown –limited to the larger coherent structures– is occurring. The turbulent fluctuation dynamics shows significant modifications due to the morphing:

- shift of the non-actuated modes 2 and 3 (Figure 3.16) associated to Kelvin-Helmholtz towards the higher order modes 4 and 5 (Figure 3.22) for actuated case;
- disappearance of coherent higher frequency modes: St = 14 for instance, shift of modes associated to the shear layer towards higher-order lower-energy modes;
- shear layer thinning at x/c=1.35 of order 22% (Figures 3.25c and 3.26c); and
- decrease of spectral amplitude of the peak at St=8.5, Figures 3.25d and and 3.26d.

Furthermore, the flow response to wake forcing is similar to that reported in Ref. [Szu+15] for transonic flow conditions. This confirms the potential suitability of high frequency actuation both for subsonic flow conditions here investigated typical of descent flight, and for cruise speeds.

3.7 Spectral analysis of flow velocity

The crossflow velocity component is extracted for 8 points from the TR-PIV measurements. These points are located in the wake close to the trailing edge and downstream, below and above the trailing edge. The center of Figure 3.28 presents the time average stream-wise velocity field of the non-activated baseline flow. The 8 points are numbered on the field. The trailing edge is visible on the left. The different Power Spectral Densities (PSD) of the crossflow velocities are presented in the spectra around the central velocity field. The PSDs are again computed using the Welch's weighted overlapped segment averaging estimator [Wel67]. To maximize the accuracy of the estimator, temporal signals of the three experiment repetitions are concatenated to obtain 33 s signals. Periodogram estimations use 4 s Hamming windows with 64% overlap (minimum variance) and zero padding.

According to the POD results, the flow energy is mainly dominated by the shear layer (SL) coherent instabilities. This corresponds to the SL arrows pointing to the frequency peaks. The shear layer instability is more concentrated in the lower flow, as the SL peaks of points 1 to 4 are over -130dB and the second harmonics are visible (2SL peaks). The points 1, 2, 5 and 6 which are located close to the trailing edge show the frequency signature of the Von Kármán vortices – presented by VK and VK/2 arrows. Coherent structures highlighted by POD analysis at Strouhal of 14.1 appear as B peaks. These peaks are absent from points 6 and 8 corresponding to the flow coming from the suction side. The Von Kármán Strouhal number is evaluated to 3. This is again comparable to CFD simulations of Ref. [Szu+15] with a Strouhal of 2.4 (computed relatively to the chord with the frequency 2630Hz). Peaks A, present on each of the considered points, correspond to the coupling of the Von Kármán and the shear layer structures. Indeed the Strouhal of the peak A is linked to these structures by the relation $St_A = St_{SL} - St_{VK}$. Physically, this can be interpreted as Kelvin Helmholtz amplitude modulation due to the Von Kármán instabilities. This peak identification not only allows for the understanding of the phenomena but also allows identifying spectral signatures in the flow. These signatures can be detected by pressure transducers (see section 3.8). In addition, the flow is significantly affected by the actuation and its effects are clearly visible on the reported spectra.

The crossflow velocity component is extracted for the actuated configurations. Globally the peaks described above are still visible, but some modifications are noticeable. As some spectra are similar, only signals from points 4, 5 and 8 are compared.

Figure 3.29 shows a comparison in PSD of point 4 between the baseline and the $f_a^* = 0.83$ (12.5Hz) actuation. The frequency range is focused on Strouhal from 7.5 to 15. Actuation harmonic frequencies from 9 to 18 are presented on the x-axis.

Peaks of baseline flow named A, SL and B are withdrawn by the actuation. In exchange the actuation gives rise to other peaks. Most of them have lower amplitude and others are harmonics of the actuation frequency. Black arrows indicate peaks corresponding to harmonics of the actuated flow. This phenomenon tends to *spread the peak energies* over actuation harmonics and over other frequencies. This could be interpreted as a vortex breakdown of the largest coherent structures.

Concerning the other points in the wake and the other actuation cases, table 3.1 deals with the Root Mean Square (RMS) values of fluctuating crossflow velocity $\overline{v^2}$ of the 8 extracted points. Variations compared to the non actuated baseline are calculated in percentage. The turbulent energy is decreased by 5 to 7% everywhere for the $f_a^* = 0.83$ (12.5Hz) actuation. The $f_a^* = 6.7$ (55Hz) actuations decrease energy close to the trailing edge by more than 8% but slightly increase it downstream. This effect is more visible for the higher amplitudes for the $a^* = 0.06\%$ (1kV) actuation compared to the $a^* = 0.03\%$ (0.5kV). This result confirms the previous remarks.

Table 3.1: Variations of crossflow velocity RMS at extracted points compared to the baseline configuration.

Point number	1	2	3	4	5	6	7	8
Baseline	0.0%	0.0%	0.0%	0.0%	0.0%	0.0%	0.0%	0.0%
12.5[Hz] 1[kV]	-7.9%	-6.7%	-7.1%	-7.1%	-2.4%	-3.3%	-4.9%	1.0%
55[Hz] 500[V]	-8.7%	-5.8%	-0.1%	4.1%	0.3%	-4.0%	5.4%	6.5%
55[Hz] 1[kV]	-10.0%	-6.7%	0.4%	7.7%	1.5%	-2.1%	8.2%	9.7%

Table 3.2: Variations of crossflow velocity PSD at some noticeable frequencies, at the extracted points 4, 5 and 8. Values are relative to the baseline configuration. Points are ranked by position starting from the trailing edge (point 5) and moving downstream (point 8). Crosses (×) indicate non visible peaks.

	VK ($St = 3$)			A=SL-VK ($St = 8.5$)			B ($St = 14$)		
Fa A^*	pt 5	pt 4	pt 8	pt 5	pt 4	pt 8	pt 5	pt 4	pt 8
12.5[Hz] 1[kV]	-3 dB	0 dB	-11 dB	+7 dB	+13 dB	+9 dB	-3 dB	-3 dB	×
55[Hz] 500[V]	-2 dB	×	-14 dB	+1 dB	+8 dB	+4 dB	-5 dB	-5 dB	×
55[Hz] 1[kV]	-2 dB	×	-14 dB	0 dB	+1 dB	0 dB	×	-7 dB	×
	SL ($St = 11.5$)			2SL ($St = 23$)					
	pt 5	pt 4	pt 8	pt 5	pt 4	pt 8			
12.5[Hz] 1[kV]	-17 dB	-18 dB	-16 dB	+37 dB	-13 dB	×			
55[Hz] 500[V]	-5 dB	-5 dB	-4 dB	×	+4 dB	×			
55[Hz] 1[kV]	-5 dB	-4 dB	-4 dB	+1 dB	-3 dB	×			

Table 3.2 sums up the effects of morphing on remarkable peaks of the spectra. It is remarkable that a few thousandth of chord fraction vibration amplitude is capable to reduce the large wake vortices power by nearly 99.9% (30 dB). It appears on one hand that both $f_a^* = 6.7$ (55 Hz) and $f_a^* = 0.83$ (12.5 Hz) morphing increase the A peaks, related to the interaction of Von Kármán and shear layer instabilities. On the other the signatures VK linked to the Von Kármán vortical structures are significantly reduced. A noticeable result is that actuation at $f_a^* = 0.83$ (12.5 Hz) deletes the most energetic peaks SL but increases the harmonic peak 2SL in the region close to the trailing edge. In comparison to this actuation, the two morphing cases $f_a^* = 6.7$ (55 Hz) yield smaller reductions and risings of the PSD peaks. Another important result is that the impact of the amplitude at $f_a^* = 6.7$ (55 Hz) is low compared to the impact of the frequency: a larger actuation amplitude increases a bit more the effects on higher frequencies B and 2SL as well as the coupling A between SL and VK. Apart from the effects on the main frequency peaks of the baseline static wing, the actuation generates other frequency peaks. Most of these peaks are actuation harmonics. Harmonic 3 of the $f_a^* = 6.7$ (55 Hz) $a^* = 0.03\%$ (500 V) actuation presents an important PSD level everywhere which increases by 3 dB for the $a^* = 0.06\%$ (1 kV) actuation.

Finally, despite the creation of coherent structures due to the actuation, the HFVTE can be beneficial as it decreases the Von Kármán and Kelvin Helmholtz vortex energies. The actuation amplitude has to be set as a compromise between vortex breakdown effect and energy introduced in the wake.

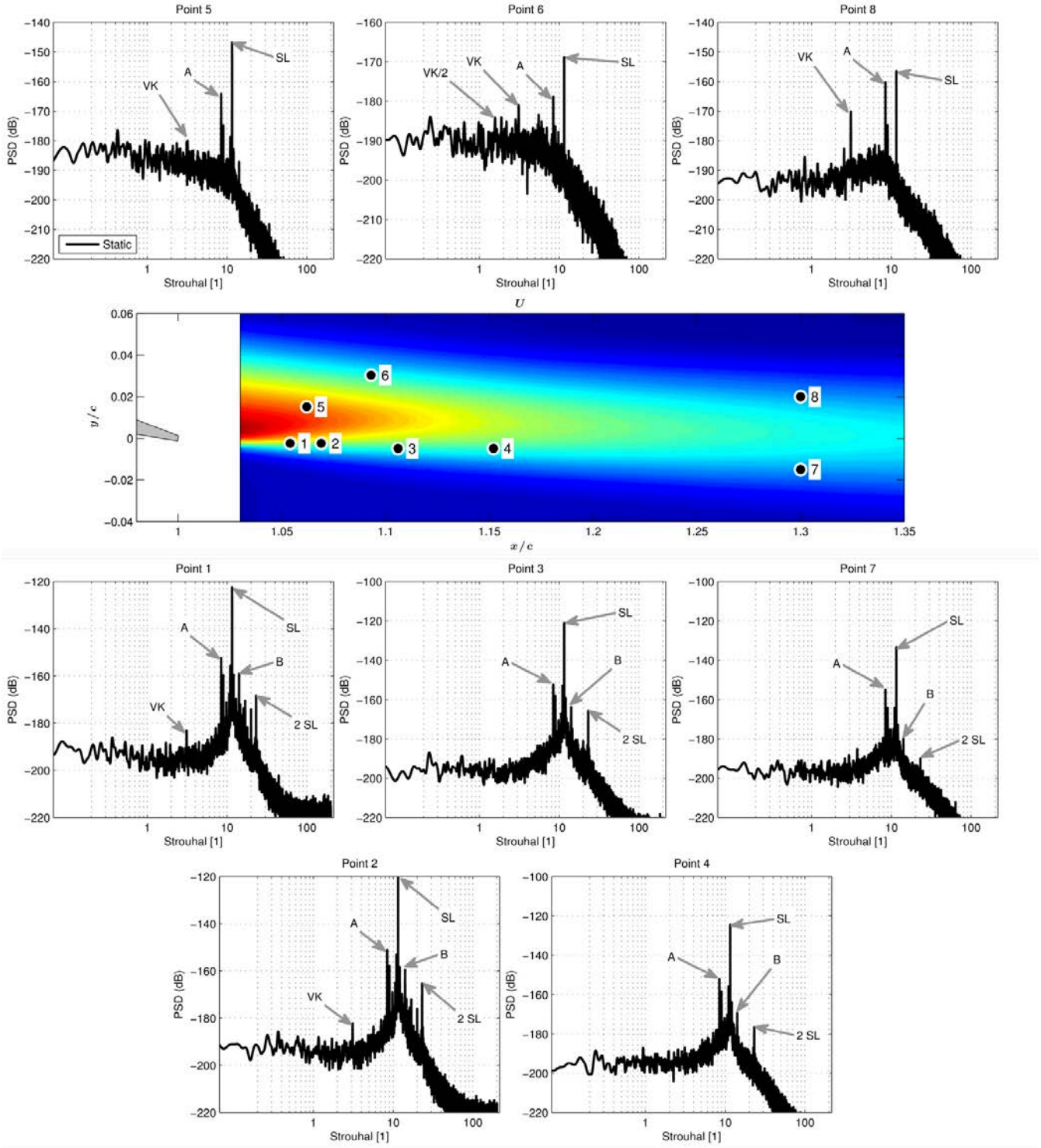

Figure 3.28: PSD of the crossflow velocity on the 8 extracted points, from the baseline configuration. The center figure presents the positions of the extracted points within the time average stream-wise velocity.

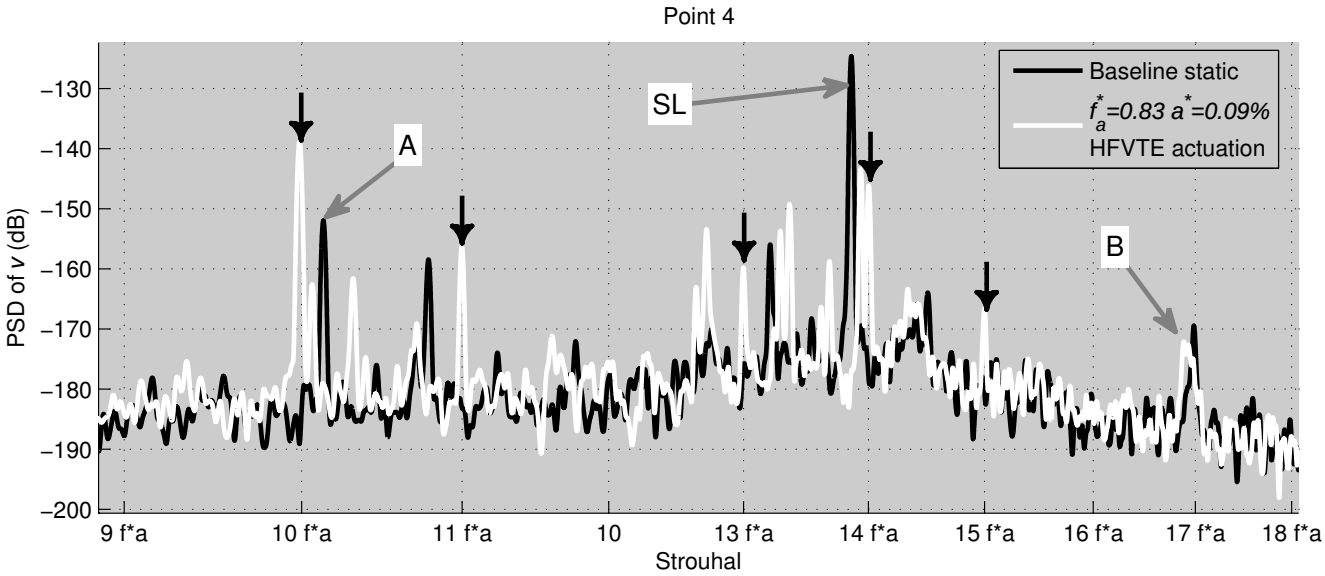

Figure 3.29: PSD magnification of point 4 of the crossflow velocity. Baseline is compared to 12.5Hz actuation. Black arrows indicate peaks at multiples of the actuation frequency f^*a that appear thanks to morphing.

3.8 Effect of high frequency actuation on aerodynamic loads

A second test campaign is carried out in order to investigate the effects of higher frequency actuation on local and resulting airloads over the wing section model. Measurements are performed at Reynolds number $\mathrm{Re} = 10^6$ and angle of attack of $10°$.

Lift and drag are measured with an aerodynamic balance, whereas pressure is acquired by means of a microphone located at the 90% of the chord and in the middle of the model span. To ensure the statistical convergence of measurements an acquisition time of 40 s is employed for each run. For this time lapse all the main statistical indicators have found to converge, both for force and pressure measurements. Flow visualizations are not reported as the limited acquisition time of 6.5 s of the PIV camera memory does not allow reaching the statistical convergence of the measured phenomena for this Reynolds number.

Sinusoidal harmonic inputs are provided to the piezo-actuators, with frequencies in the range $f_a^* \in [3.2, 14.6]$ ($F_a \in [100, 450]$Hz) and amplitude 1000V. The actuation amplitude a^* (or A) is not maintained constant. As mechanical resonance can occur in the range $f_a^* \in [4.9, 7.2]$ ($F_a \in [150, 220]$Hz), the results of the HFVTE actuation in this section depend on both coupled frequency and amplitude. With the aim to check the repeatability of measurements, several acquisitions are performed by alternating actuated with non-actuated runs. For each run, the measure is launched 20 s after the switch of the control input (on/off and vice versa), to allow for the settling of the permanent regime in the flow dynamics, as indicated in A.2. The maximum percentage difference in drag between runs is 0.5%. This confirms the reliability of the measured quantities. With regard to the non actuated configuration, differences between repeated runs are below 10^{-4}% for both lift and drag.

Figure 3.30 displays the percent gain in terms of drag and lift obtained with the trailing edge actuation at a specific frequency referred to as f_a^* and maximum amplitude 1000 V, relative to the non-actuated case. Positive values indicate that the actuation increases the measured quantity, whereas the opposite is meant for negative gains. For each of the actuation frequencies, positive gains in lift and negative gains in drag are obtained. Therefore high frequency trailing edge actuation appears beneficial in improving the overall sectional aerodynamic performance. It can be noticed that the flow at Reynolds number of 1 million undergoes a strong unsteady behavior with modifications of the forces, being this case likely to be close to a bifurcation. The vibration of the trailing edge increases the turbulence intensity in the boundary layer and the transition to turbulence goes more up-

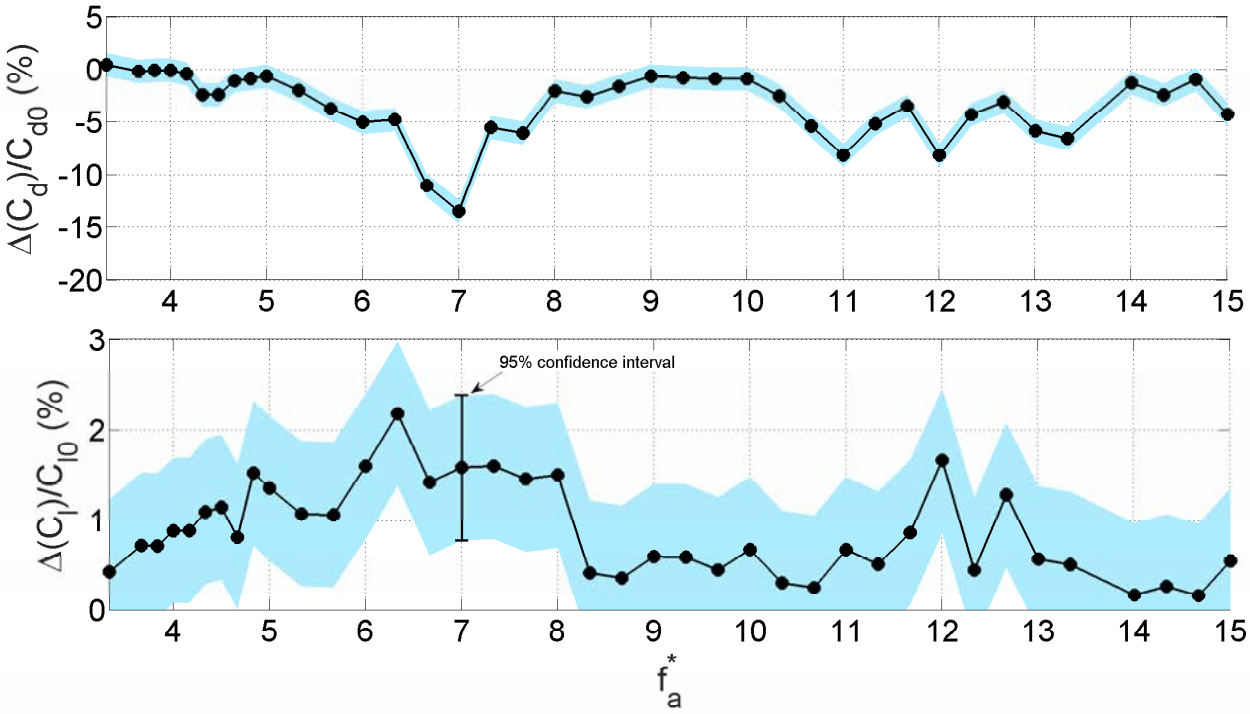

Figure 3.30: Percent gain of mean drag (top) and lift (bottom) coefficients obtained with HFVTE, relative to the non-actuated case. Experiments are done at $Re = 1$ M

stream. Therefore, the flow regime becomes critical. These critical aspects may yield a high sensitivity of the measured drag to the initial conditions and to the perturbations induced by the patch vibrations.

Therefore the eddy blocking effects, observed on in terms of velocity field, appear to yield the expected drag reduction. At $f_a^* = 7$ (210 Hz) the largest drag reduction is obtained. The specific percent gains in drag and lift are:

$$\begin{aligned} \Delta D &= -13,48 +/- 1.8\% \text{ (with incertitude : } 3\sigma) \\ \Delta L &= +1.58 +/- 1.12\% \text{ (with incertitude : } 3\sigma), \end{aligned}$$

being σ the standard deviation of the measures (not the measurement accuracy). At $St = 6.3$ 190Hz the largest lift augmentation is obtained. The corresponding percent gains read:

$$\begin{aligned} \Delta D &= -4.80 +/- 1.08\% \text{ (with incertitude : } 3\sigma) \\ \Delta L &= +2.17 +/- 0.65\% \text{ (with incertitude : } 3\sigma), \end{aligned}$$

Significant effects of piezo-actuation are found both on lift and on drag coefficient. By the way high frequency–low amplitude trailing edge actuation was first conceived specifically to reduce drag within the framework of the present research project. Therefore details on drag behavior are provided by analyzing the results achieved in terms of pressure measurements in the following. Specifically the actuation at $f_a^* = 7$ (210 Hz), where the maximum gain in drag is found, is considered. Pressure measurements – especially if performed on the trailing edge – provide a good indication of the phenomena occurring in the wake, as flow perturbations propagate in each direction, being the Mach number much smaller than the unity everywhere in the domain. In order to check the reliability of pressure measurements the same approach adopted for the balance acquisitions is followed. Namely, for each excitation frequency, several measurements are carried out alternating non-actuated and actuated runs. The maximum difference in terms of measured mean values is 1% among all the runs, for any of the considered excitation frequencies. The statistical stability of measurements without actuation is verified in the same manner. In this case differences between runs are below 10^{-4}%.

Figure 3.31 shows the power spectral density (PSD) of the pressure fluctuations measured with trailing edge actuation at $St = 7$ (210 Hz) (HFVTE activated) and without actuation (MFC OFF), respectively. The plot on the bottom is a blowing up of the top counterpart on the area surrounded by the rectangle. The trailing edge actuation provides a shift of the flow modes, compared to the non-actuated case. Namely, peaks at the actuation frequency, as well as at the corresponding super-harmonics and sub-harmonics are observed. At the same time the peak at $St = 9.5$ (285 Hz), clearly visible on the PSD of the non-actuated case (observed on loads spectra as well), has diminished by 17% compared to the mean spectral level when actuating at $f_a^* = 7$ (210 Hz). In fact actuation adds new peaks in the power spectral density, but the corresponding flow modes result less detrimental for drag, relative to the natural peak at $St = 9.5$ (285 Hz). It's worth remarking that the peak at $St = 9.5$ (285 Hz) highlighting Kelvin Helmholtz instabilities is consistent – in terms of Strouhal number – to the results reported in the previous section for a smaller Reynolds number, as well as to the estimations of Ref. [Szu+15] for transonic flow conditions.

Good indications of the flow instabilities are also provided by the statistical moments of the measured pressure [Nor11]. The variance, the third order (skewness), and the fourth order moments (flatness) are computed on the time histories of pressure measures for excitations at $f_a^* = 7$ (210Hz), and for the static configuration. The percent differences between the actuated and the non-actuated cases are reported in Table 3.3:

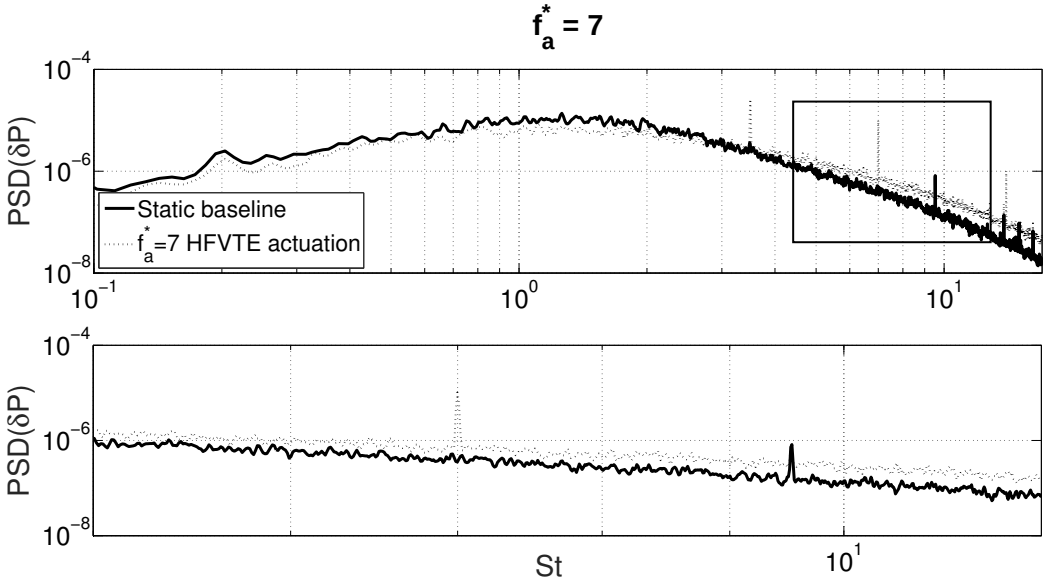

Figure 3.31: PSD of pressure fluctuations measured on the wing section with actuation at $f_a^* = 7$ (210 Hz) and without actuation. On the bottom the same plot is blown up around $f_a^* = 7$ (210 Hz).

Quantity	Percent difference between actuated and non-actuated
Variance (RMS)	-7.66%
Skewness	-36.25%
Flatness	13.03%

Table 3.3: Percent difference in statistical moments between the measures at $f_a^* = 7$ (210Hz) and those of the static configuration.

The actuation at $f_a^* = 7$ (210 Hz) leads to a smaller variance with respect to the baseline configuration. This is consistent with the results obtained in terms of drag. Indeed a reduction in the flow instabilities related to large vortical structures, i.e., in the pressure variance, yields a decrease in pressure drag. The skewness is related to instabilities in flow statistics. For a more stable wake, with less intense shedding phenomena, a smaller skewness (to be meant with sign) is expected. Actuating at $f_a^* = 7$ (210 Hz) provides a reduction in skewness with respect to the static configuration, accordingly to the measured drag downturn. The increase in flatness encountered for the actuated case is also in agreement with the observed drag reduction. Indeed flatness is larger for more regular flows, where weaker shedding phenomena are encountered. This actuation provides a vortex breakdown for the largest coherent structures and yields an upscale in the turbulent cascade from smaller scales towards larger ones.

Similar results on forces can be found at lower velocities. Figure 3.32 presents lift measurements from an accurate balance at Reynolds number $Re = 500$ k. Depending on the actuation frequency, lift improvement above 2% is measured. Each of the measured points in Figure 3.32 comes from two different runs. The sequences of the tested actuation frequencies have been randomly generated to avoid any dependence from a measure to another. Lift measurement accuracy has been evaluated to $+/-$ 0.3% for this experiment.

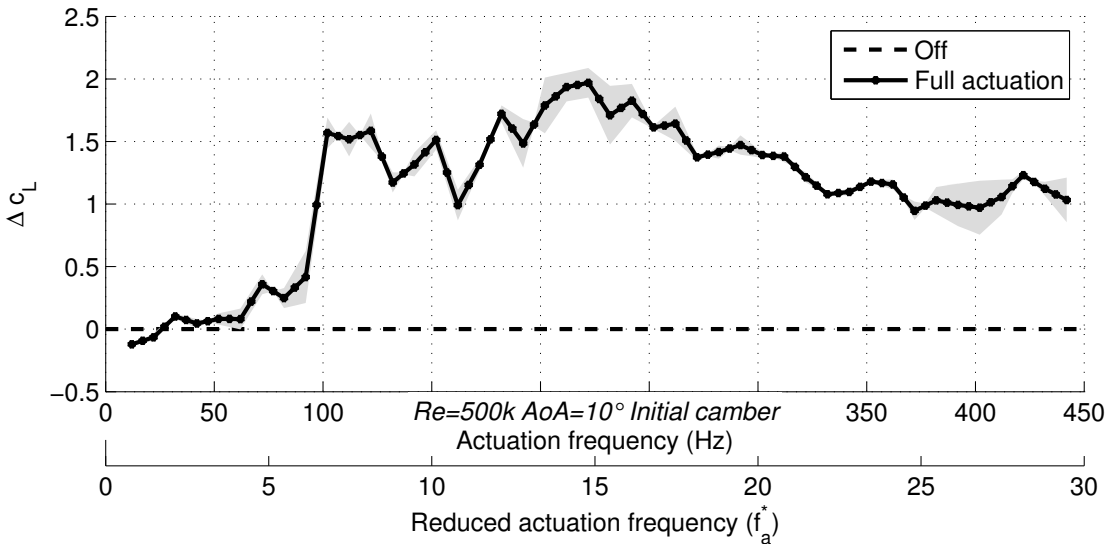

Figure 3.32: Percent gain of mean lift coefficients obtained with maximal HFVTE amplitude actuation, relative to the non-actuated case. Experiments are done at $Re = 500$ k

3.9 Conclusion

This chapter presents an experimental study of the electroactive morphing effects on the aerodynamics and time-dependent flow structures in the wake of an Airbus A320 aerofoil with piezo-actuated vibrating trailing edge. Camber control has been achieved using Shape Memory Alloys. Therefore, high frequency-low amplitude trailing edge actuation has been performed by wind tunnel tests. The angle of attack was set to 10°. Velocity measurements have been carried out at $\mathrm{Re} = 0.5 \cdot 10^6$ in the near-wake region by TR-PIV. A detailed investigation of the mechanisms modifying the eddy structure due to morphing has been done by means of the averaged velocity fields, Proper Orthogonal Decomposition and by spectral analysis. The aerodynamic forces and wall pressures on selected points have been measured by means of an aerodynamic balance and pressure transducers, respectively. A specific range of cambers and trailing edge vibrations have been depicted yielding a significant increase of lift in the order of 27%, where 4% are achieved thanks to the small amplitude vibrations. Concerning the neutral configuration (clean wing), the piezo-actuated Higher Frequency Vibrating Trailing Edge significantly affects the flow response. Namely:

- a vortex breakdown is observed for the largest coherent structures;
- an upscale energy transfer from smaller scales towards larger coherent eddies occurs. A significant reduction of large scale instabilities is obtained – approximately 20 dB power reduction (99.9%) of the predominant frequency peak is obtained.
- a reduction in pressure drag and an increase in lift are observed. Approximately 5% of drag reduction and a 2% lift enhancement is measured in optimal conditions. *Beyond this study, such macroscopic changes are linked significant changes in wake dynamics. Important reduction in wake's width together with effects upstream the actuation are visible on PIV measures of Figure 3.14.*

A wise choice in amplitude and actuation frequency has to be made to ensure the benefits without creating unwanted actuation-induced vortices. The present chapter substantiates the potential feasibility of hybrid morphing actuation as a novel means of improving aerodynamic performance by manipulating the near wake turbulence.

In a next step, the coupling between the camber control and the vibrating trailing edge is to be investigated in more detailed. Finally a closed loop control based on the best actuation frequency is currently studied.

Acknowledgements

The authors are grateful to Airbus and RTRA-STAE Foundation as well as the Direction Generale de l'Armement - DGA that provided funding for this research. The authors are also grateful to Dominique HARRIBEY, Karl Joseph RIZZO, Robert LARROCHE, Sébastien CAZIN, Moïse MARSHALL, Christophe KORBULY, Gilles HARRAN and Philippe MOUYON for their useful advice and help.

CHAPTER 4

Design through optimization: true scale cambered control flap

"Everything should be made as simple as possible, but not simpler."
Albert Einstein

This chapter is written like an article and will be soon submitted.

Figure 4.1: Word cloud of this chapter content (`www.wordclouds.com`).

Abstract Morphing requires a structure flexible enough to be easily deformed whilst being stiff enough to withstand the aerodynamic loads. This paradox leads to current issues in skin and actuator design. This cahpter presents a multi-criteria optimization process that considers the wing as a system doing different functions. Each function is addressed through different technological solutions. Different solutions for articulations, agonist-antagonistic shape memory alloy actuators, skin or feathers are described in the chapter. Taking into account industrial constraints, the optimization results in a feasible, low weight, low power consumption morphing wing design. Finally the optimal wing is designed based on the feasible optimized result.

4.1 Introduction

This work takes place within the design of the Large Scale Prototype of the ongoing European project SMS[1]*, as detailed in the outlooks of this manuscript 4.7.*

Limiting energy consumption has become a central concern for reducing the aircraft operational costs. Improving aerodynamic performance is a way to reduce the fuel consumption during flight.

Current airfoil shapes are generally optimized for one working point, corresponding to nominal cruise conditions. During flight, the altitude, the weight and the speed are continuously changing. Hence this design is suboptimal for the whole aircraft mission. Traditional solutions to control and adapt the wing shape (like slats and flaps) exhibit limited performance ranges [Bar+11]. Changing the shape of the wing during a mission can save several percents of fuel for a regional passenger aircraft [LM15]. The concept of real time shape adaptation enabling multipoint optimization is called morphing.

Within the framework of aircraft aerodynamic performance, morphing has been known for decades [Bar+11]. It was demonstrated that camber control of the trailing edge of a wing is very efficient to improve airliners performance by Lyu et al. [LM15]. It is also shown that morphing applied to a limited part of the airfoil chord may feature effectiveness comparable to that of entirely morphed airfoils. Additionally, the required deformations result in a change of camber by about 2% of the wing chord length, which corresponds to 7% of the flap chord length.

Despite the fact morphing wings have been used for military fighting aircrafts, research concerning industrial passenger aircrafts has not led to commercial appli-

[1] `http://smartwing.org/SMS`

cations. One can explain this as technology is not mature enough, the potential gains are known but reliability, maintenance, mass and power consumption of the added devices deteriorate the assessment. The skin or the interface between the structure and the outside airflow is the current technological bottle neck. Some studies simply do not deal with this issue (experiments at low velocity do not exhibit issue with elastomeric skins), others propose a degraded skin (i.e. corrugated skin for example that cause turbulent transition). As the skin is a part of the morphing system, it has to be taken into account. Thill et al. [Thi+08] draw review of morphing skin and its challenges. With this regard relatively high Technology Readiness Level (TRL) projects, targeting current industrial airliners at true scale, were undertaken. The European research program SARISTU[2] focuses on operating cost reductions as well as on improving the aerodynamic performance. One work package of SARISTU deals with a morphing wing trailing edge [Dim+16]. The device is based on servomotors driving an articulated structure. The European research program CleanSky[3] works in this direction as well. It focuses on a flap with twofold actuation, provided by servomotors and redactors respectively [PAM16]. The dual actuation allows for camber control during the different flight phases/assets. Another trailing edge morphing concept, called Adaptive Compliant Trailing Edge, was developed by NASA in cooperation with FlexSys Inc.[4]. This concept features an adjustable structure which can be actively deformed. Endurance flight tests for this concept were performed and described in Ref. [KFC16]. This solution was proved to yield aerodynamic benefits and its effectiveness and airworthiness are being ultimately assessed.

However these new adaptive structures are actuated through conventional actuators like electromechanical or hydraulic servomotors. Recent advances in the field of smart materials show the potential to overcome difficulties to make a wing both stiff enough to withstand the loads, and flexible enough to be easily deformed [Bar+14]. The related research focuses mainly on low TRL, mainly applied to low scale Micro Air Vehicles. Among electroactive materials, Shape Memory Alloys (SMAs) are the most frequently used. SMAs are characterized by thermomechanical behaviors, and most applications use an electrical resistor or the resistance of the SMAs themselves to activate the transformation. Different morphing concepts were developed, an overview of which is presented by Barbarino et al. in [Bar+11]. A counter example of the low TRL research is a recent industrial application of the SMAs within the Boeing CLEEN research program. A topic of the program consists in a flap actuated by a SMA twist tube, [CM16]. Safety issues have been solved using a redundant hydraulic actuator. It also provides brake

[2]http://www.saristu.eu
[3]http://www.cleansky.eu/
[4]http://www.flxsys.com/

and damping functions to maintain a deflected flap without requiring actuation energy. A flight test campaign has been successfully done, reaching TRL 7.

In the works previously mentioned the desired operation is generally accomplished using one specific smart material. But a combination of different smart material leading to a synergy is possible. As the SMAs can achieve large deformation at low speed, and as piezoelectric material can achieve small deformation at higher speeds, a combination of both material can enhance the global performance of the actuation. This is the proposed approach of the *synergistic smart morphing aileron* [PFI15]: the combination of a SMA actuated hinge followed by a flexible piezoelectric driven trailing edge. Another approach is an airflow point of view. Lift and large flow instabilities can be controlled through camber control whereas smaller instabilities responsible for drag and noise can be modified through active turbulence control of the trailing edge wake's shear layers. For ten years of collaborative effort from two laboratories (LAPLACE and IMFT) this approach has been leaded to the *electro-active hybrid morphing* concept: a low frequency (< 1 Hz) camber control ($\sim$10% of the chord) thanks to SMAs and a higher frequency vibrating trailing edge (fractions of millimeters up to 400 Hz). It was demonstrated that the flow dynamics are significantly affected by the trailing edge actuation. The wing's wake energy was reduced, leading to an improvement in aerodynamic performance, according to Sheller et al. in [Sch+15].

Based on an Airbus commercial aircraft, this chapter deals with a morphing flap design. After firstly describing the morphing flap concept with design requirements; different used technologies for actuator, skin and hinges are modeled. Thirdly, the optimization problem is described before presenting important results. Finally the chosen design is followed by a conclusion.

4.2 Morphing wing concept and modeling

The proposed morphing concept is applied to a flap but the assumptions are valid for a whole morphing wing. The function assessed by the proposed morphing is to adapt the wing shape configuration. This allow to change the shape that correspond to lower drag for every flight step. The high lift function is not addressed so that safety is not critical for this function. The morphing flap is based on an articulated ribs where Shape Memory Alloy actuators control the rotations of the elements around the hinges. This concept is firstly described. Then input geometry and loading are defined before the modeling of the whole camber controlled flap.

4.2.1 Articulated concept

The proposed concept, presented in Figure 4.2, is decomposed fourfold:

- *articulated ribs* define the geometry and carry the other components. They have to withstand the internal and external (i.e. aerodynamic) forces, whilst being low weight.
- *hinges* allow the rotation of the articulated ribs. Parts of forces are transmitted through these components without generating much parasite force (or torque) when rotated.
- *actuators* are devices that transmit mechanical energy to the structure. The actuators are responsible for the shape control and have to counteract aerodynamic forces as well as some internal forces coming from the other components.
- *skins* or covering devices guarantee the airtightness of the wing, transmit the aerodynamic forces to the structure and ensure a smooth shape during morphing. The skin must endure deformation without unexpected displacements like bumps or wrinkles.

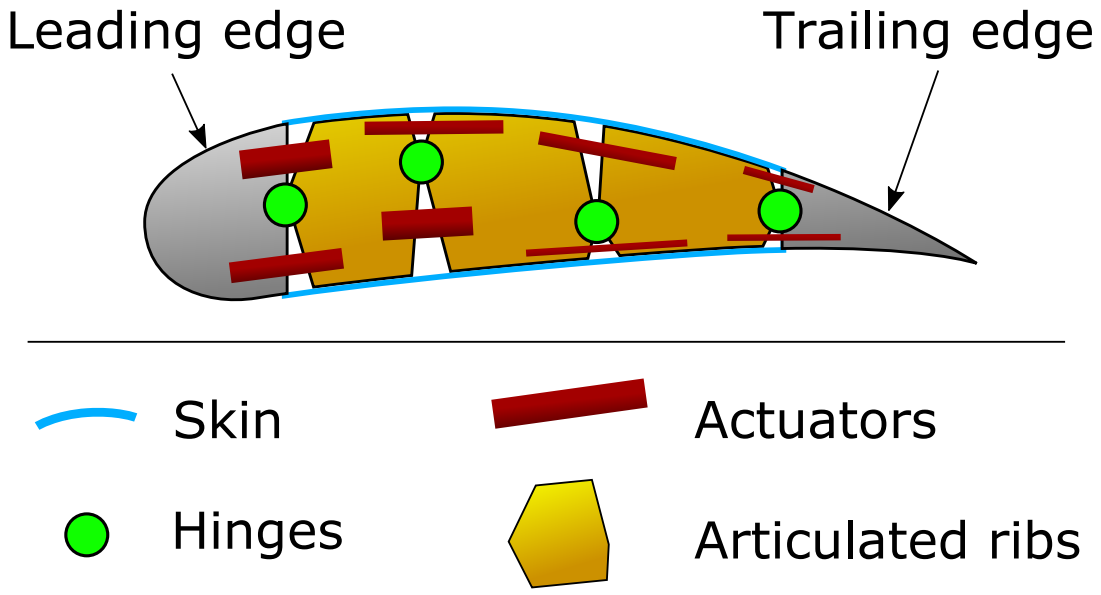

Figure 4.2: 2D illustrative sketch of the proposed concept. Articulated ribs are placed between fix leading edge and trailing edge. Actuators and specific skins are located within the morphing flap.

Additionally, mechanical stops are provided to limit the rotations of the articulations, thus preventing overloads in actuators. The internal structures represented by the articulated ribs actually consist in an engineered mechanical structure composed of ribs and spars. The fine design of this structure is outside the scope of this study, it is accepted that the lower the force in the structure, the lighter the structure. The proposed actuators consist in cylinder like actuators. Composed of shape memory alloy wires, they are able to pull on the articulated ribs, thus imposing the rotations. More detailed are presented in 4.3. One can notice the presented concept is not breakthrough, but the original purpose of this study is the comparison of the different technologies that can be applied.

4.2.2 Requirement and objectives

The previous concept performance assessment is based on a representative flap of an industrial passenger aircraft. To simplify the design, the flap's aspect ratio is assumed rectangular, with 1 m chord by 2 m span. The airfoil profile is presented in Figure 4.3. The morphing region targeted in the present chapter extends from 15% to 75% of the chord length. The trailing edge is committed to the integration of a Higher Frequency Vibrating Trailing Edge, corresponding to an actuation concept that manipulate the turbulence to enhance aerodynamic performance, developed in other studies of the authors, [Sch+15] and [Sch15]. The specified load is also presented in Figure 4.3. This vertical surface force distribution is assumed vertical and constant along the wing span. Globally, the resulting aerodynamic force on the 2 m span flap is about 1 ton force. One can notice that the higher force density are located at the trailing edge, thus the rear part of the wing carries lighter forces; this is beneficial for actuation requirements. This force specification is representative of nominal working points of the flap during all flight conditions where actuation is needed.

Regarding the objective, a flap design must perform the camber control function. Two objectives shapes are defined. Starting from the neutral initial shape, the flap can reach a low cambered shape (corresponding to upward displacement of the trailing edge tip) or also a high cambered shape (corresponding to a downward displacement of the trailing edge). The two objective shapes are presented in Figure 4.4, on the top two red airfoil profiles. According to the optimized shapes from [LM15] as well as Airbus specification, a vertical trailing edge tip displacement by about 7% of the flap chord is enough to optimally increase the cruise performance – 10% is selected for the design of a proof of concept. The profiles' deformations have been interpolated by polynomial; then the polynomials are applied to current flap profile to obtain the high and specified low cambered shapes. Finally, the optimized designed flap has to respect the morphing shape while being as lightweight

and low-energy consumer as possible – the objective formulations are detailed in the following.

4.2.3 Model

As the morphing concept and its objective and specifications are defined, the optimization model is now defined.

4.2.3.1 Shape calculation

Starting from the positions and the rotation angles at every hinge, the profile is cut in sections corresponding to the different ribs sections. Then, using rotation matrices, every section is rotated. After the calculations of the new positions of the hinge centers, the rotated sections are assembled together. It results a deformed flap which is lightly faceted. To evaluate the relevance of the obtained shape, vertical position differences between the obtained shape and the objective shape are calculated for the upper and lower side of the airfoil profile. For each of the two ob-

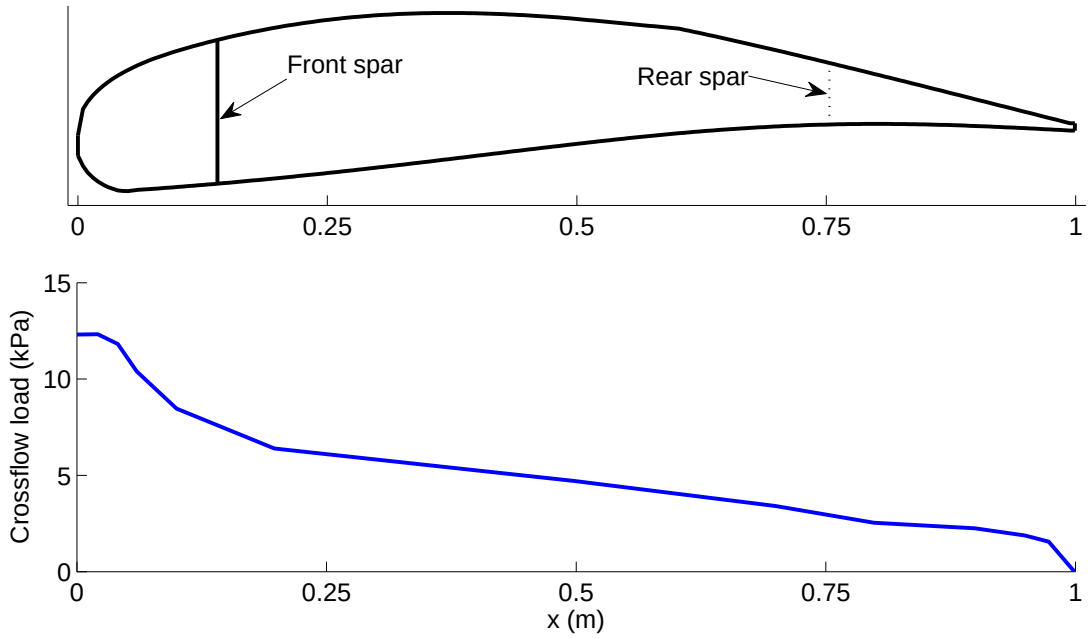

Figure 4.3: Top: Airfoil profile. Camber controlled part is located between the front spar and the rear spar. Bottom: distribution of the resultant surface vertical force loading.

jective shapes, articulation angles are found by minimizing the difference between the current articulated flap profile and the targeted profile. The function's cost is defined as the sum of the mean absolute error plus the maximum absolute error. This minimization is done thanks to a multi-variable gradient based constraint algorithm[5]. Figure 4.4 presents an optimized articulated flap with superimposed objective.

4.2.3.2 Force balance

Figure 4.5 schematically represents an articulated flap with four hinges. The leading edge is recessed in the spar. Actuators are present at every articulation, in parallel with the hinge. As the morphing displacement is slow, quasi-static assumption is done, thus the Newton's second law can be applied on a selected wing section Ω comprising a rib section and all the following ones until the trailing edge.

[5]Mathwork MATLAB *fmincon* function.

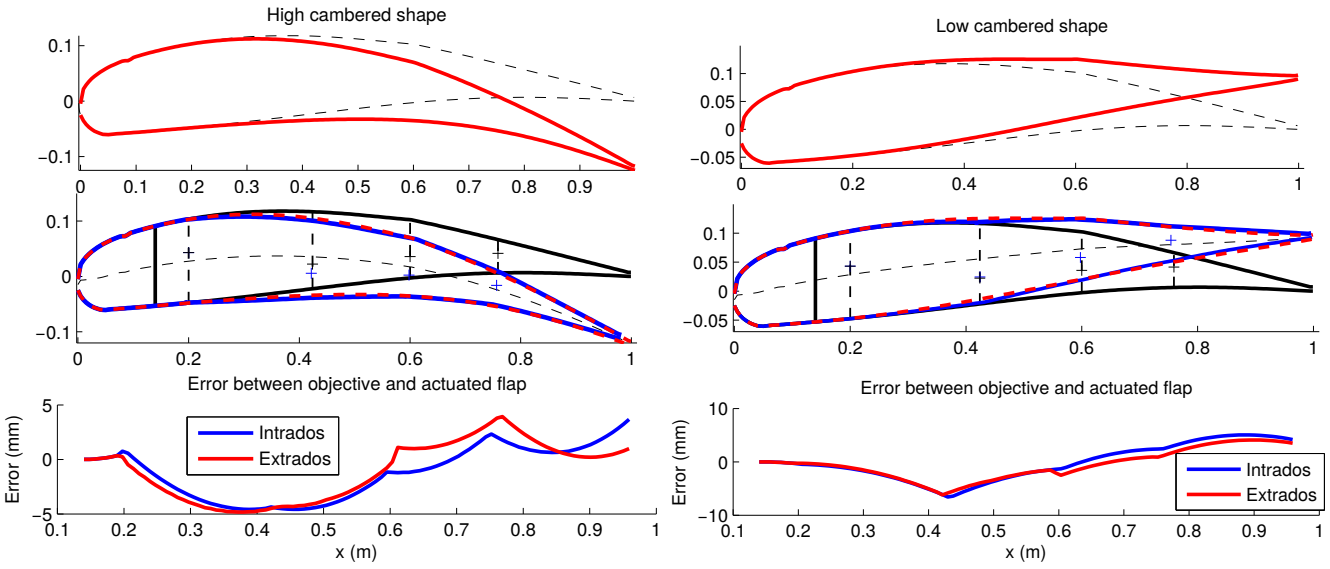

(a) (b)

Figure 4.4: From top to bottom: The two objective shapes superimposed with the original non-deformed profile; deformed shape of the articulated morphing flap fitting the objective; error between the articulated flap and the objective. (b) presents the low cambered shape with upward trailing displacement, whereas the high cambered shape characterized by downward trailing edge displacement is presented in (a).

An example of the selection is blue highlighted in Figure 4.5. The resulting forces and moments expressed at the hinge location are:

- *Actuators*' participations: Force $F_{act} = \Sigma F_{act_i}$ and $M_{act} = \Sigma F_{act_i} \cdot l_i$, where l_i are the lever arms. The actuators inside the selected wing section Ω.

- *Hinge*'s participations: Parasite moment due to elasticity or friction in the hinge M_{hinge} and F_{hinge} the resulting force transmitted to the previous rib through the articulation.

- *Aerodynamic forces*: Resulting force $F_{aero} = \int_\Omega P(x) \cdot dx$ and resulting moment $M_{aero} = \int_\Omega P(x) \cdot x \cdot dx$

The force balance is presented in equation 4.1.

$$\begin{aligned} F_{hinge} &= -(F_{act} + F_{aero}) \\ M_{act} &= -(M_{hinge} + M_{aero}) \end{aligned} \tag{4.1}$$

Two important results sum up this balance: 1- the force transmitted to the previous ribs F_{hinge} allow the sizing of the hinge; 2- the resulting moment allow for the sizing of the actuator moment M_{act}, where the actuators' forces and lever arms are design variables.

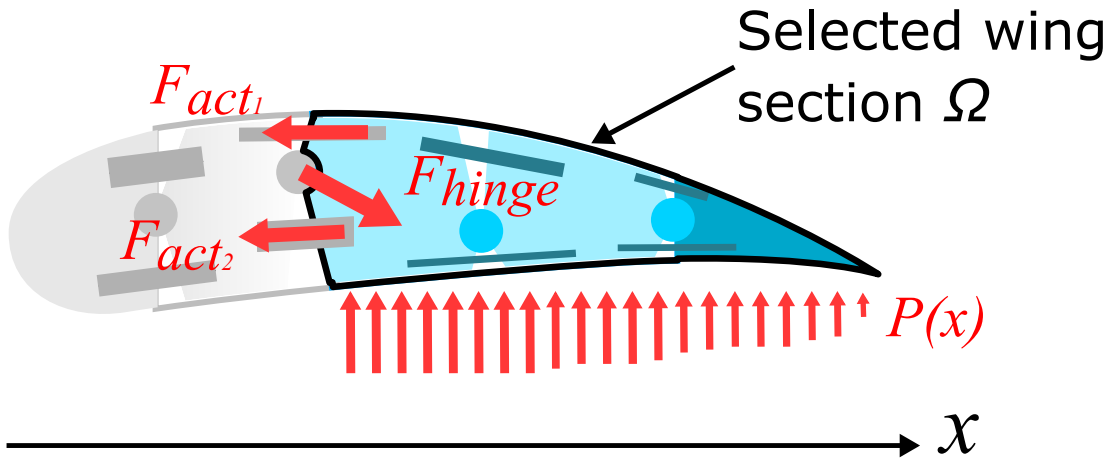

Figure 4.5: Sketch of the flap's force balance model. Among the 4 articulations of this design, the force balance is presented for the 2^{nd} one. The parasite hinge moment is not represented for greater clarity.

4.2.3.3 Hinge technologies

Various technologies realize mechanical articulations between two parts at low rotation angles. The specifications of the articulations are to transmit the forces with minimal movement in every direction and rotation. Excepted for the rotation axes where the parasite torque has to be minimum. The articulations have to be as light as possible and fit with the available room. Then two technological families exist. The first one is based on deformable parts, i.e. metallic bending beams or elastomer links. The behavior of such hinges can be modeled as elastic links, thus the parasite moment is linked to the rotation angle and the stiffness of the hinge. This stiffness is determined by the sizing that depends on the transmitted forces. The second family is based on gliding bearings. As the rotation angle and velocity ranges are small, ball bearings are not suitable. The parasite torque is due to friction, which is linked to the transmitted forces.

These different hinge technologies have been compared regarding the morphing flap sizing. For brevity purpose, the models are not detailed. For gliding bearings and elastomer links, routines have been coded to automatically select a hinge within a subcontractor catalog that fits the requirements. For the metallic bending beams, the beams must be as flexible as possible whilst withstanding the load with no buckling. To avoid large translations, the beams have to be as shorter as possible, but thin enough to stay slim. A routine has been coded to size the elastic beams while respecting the constraints. All these routines are parts of the sizing code described in this chapter.

4.3 Actuator modeling

The proposed morphing concept relies on actuators using Shape Memory Alloy (SMA). This section first shows that SMAs are suitable for the actuators. Then actuators are modeled and actuation topologies are described. It is important to notice that non linearity like material hysteresis, slake SMA wires or dependencies between actuators are not discussed in this chapter. Those specific issues are assumed to be addressed by suitable controllers.

4.3.1 Shape Memory Alloy behavior

Amongst smart materials, SMA are metallic alloys that exhibit an impressive thermo-mechanical coupling, due to crystallographic phase changes at microscopic scale. They have been studied for decades, Lexcellent draws a complete handbook about SMAs, [Lex13]. The most common are based on Nickel-Titanium alloys

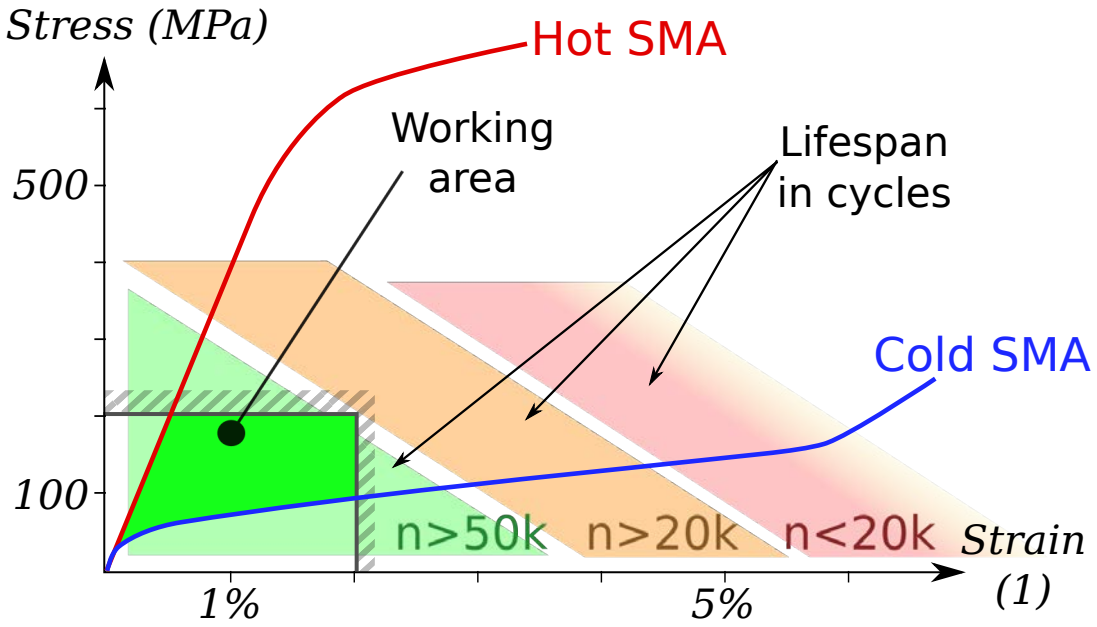

Figure 4.6: Tensile test of SMA wires at two temperature. Areas $n < 20$k, $n > 20$k and $n > 50$k respectively indicate that for actuators working in these areas, less than $20,000$, more than $20,000$ and more than $50,000$ cycles can be expected. Below the 200 MPa and 2% limits lies the specified working area.

with small amount of chemical additives to tailor thermo-mechanical properties. Basically, cold SMA is martensitic which exhibits low stiffness and pseudo-plastic behavior. Hot SMA is austenitic, characterized by a higher stiffness and super-elastic behavior. This two-material in one withstands strain levels up to 7% and stress level up to 600 MPa, as presented by hot and cold stress-strain characteristics in Figure 4.6. Its high specific actuation energy (about 1 kJ/kg), stainless property and growing maturity make this material of interest for aeronautic applications. SMA actuators are not designed in respect with the maximum stress and strain, but in respect with fatigue. A cycle life up to one million actuation cycles have been shown on small diameter SMA wires at limited stress and strain, [Jan+14]. Generally, the lower the diameter and strain-stress loading, the longer the cycle life. Areas drawn on Figure 4.6 indicate the expected maximum number of cycles. Therefore, a reliable design relies on a specification area where the working points are included. To ensure about 100,000 cycles with 1.5 mm diameter for the first demonstrator, limits are set at $\sigma_{SMA\ max} = 150$ MPa stress and $\epsilon_{SMA\ max} = 2\%$ strain. This choice allow a wire section large enough that limit the number of

wires to be integrated; this eases the prototype assembly.

4.3.2 Actuator model

The previously described SMA are integrated in actuators. Based on back and forth wires to increase the force, the proposed actuator concept is like a cylinder that pull only – as the wires can only work in tension. This actuator is clamped on two following ribs that are articulated. The active length (i.e. relaxed SMA length) L as well as the lever arm h have to be within feasible limits ($L \leq L_{max}$, $h_{min} \leq h \leq h_{max}$) that depends on geometry and manufacturing possibilities. Figure 4.7a illustrates a hinge with one actuator at neutral position; geometric parameters are indicated. The actuator's forces applied on the anchors are presented as F_{act} and the moment at hinge axis due to the actuator applied from rib 2 to 1 is named $M_{act\ 2/1} = F_{act} \cdot h$. Figures 4.7b and 4.7c present the two extreme rotated shapes. The small angles assumption is made. If $h/L \ll 1$, it can be reasonably assumed that: lever arm h is independent from the hinge rotation, and actuator's stroke s is defined by $s = h \cdot \theta$.

The sizing of an actuator starts with the specification of:

- the actuator torque $M_{act\ 2/1}$ – detailed in global sizing algorithm, section 4.5.3,
- the angle range $\theta = \theta_u + \theta_d$ – from section 4.2.3.1,
- the geometric limits L_{max}, L_{min}, h_{max}, h_{min}.

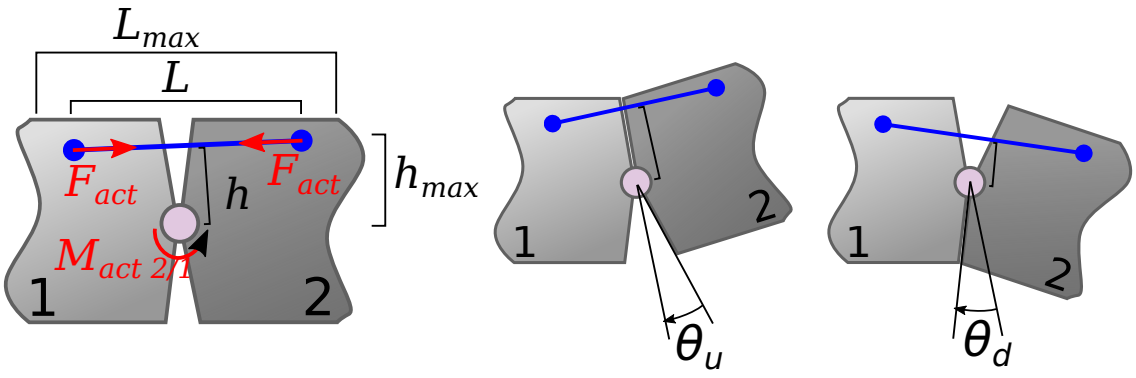

(a) (b) (c)

Figure 4.7: (a) Parametrized sketch of an actuated articulation. (b) Rotation when actuated, the maximum rotation angle is θ_u. (c) Rotation when non-actuated, the mainimum rotation angle is θ_d.

The sizing Algorithm 1 describes the calculation of the lever arm h, the force F_{act} and other properties like the mass of the design actuator. A flag giving information about the successful design is output. It is used to penalize a flap with non feasible actuators, without crashing the computation. The total mass of the actuator is evaluated, as well as the power consumption. This is done with results from a thermal analysis of the actuator, non presented here for brevity purpose. Assuming a cylinder like actuator, with a passive cooling and a cooling time of 60 s in nominal conditions, the insulation cover thickness and the power consumption are evaluated. It can be shown that independently of the exact shape or topology, a good approximation of power consumption per kilogram of SMA during heating is 960 W/kg whilst 295 W/kg seems enough to maintain the maximum temperature at minimum ambient temperature.

Algorithm 1 Actuator sizing algorithm

procedure ACTUATOR SIZING($M_{act\ 2/1}, \theta$, Geometric limits, SMA limits)
  $L = L_{max}$ ▷ First, try with maximum available length
  $h = \epsilon_{SMA\ max} \cdot L_{max}/\theta$ ▷ corresponding lever arm
  Flag = ok ▷ A priori there is no design issue.
  if $h < h_{min}$ **then** ▷ Design within limits?
    $h = h_{min}$
    Flag = Aging issue ▷ We do not respect SMA limits
  else if $h > h_{max}$ **then** ▷ There is too much length available
    $h = h_{max}$ ▷ Limits the lever arm, then calculate the new length
    $L = h \cdot \theta/\epsilon_{SMA\ max}$
    if $L > L_{max}$ **then** ▷ New design over limits?
      $L = L_{max}$
      Flag = Aging issue ▷ We do not respect SMA limits
  $F_{act} = M_{act\ 2/1}/h$ ▷ Evaluate force
  $\epsilon_{act} = h \cdot \theta/L$ ▷ Effective strain
  $S_{SMA} = F_{act}/\sigma_{SMA\ max}$ ▷ actuator's SMA section
  Evaluate mass and power consumption with amount of SMA, anchors' masses depend on force, case's mass depends on dimensions.
  return L, h, masses, Flag

4.3.3 Antagonistic actuation concept

This subsection deals with the actuation topology. As the SMA actuators can only pull, a device has to be implemented to recover the initial shape. Additionally the aerodynamic forces are not always present so they cannot be the only way

to be used to recover the non-actuated shape. Two solutions are compared: a passive counter-spring and an antagonist SMA actuator. To chose between the two technologies, the representative comparison cases are presented in Figure 4.8.

A first approach is a simple analytical modeling. For the counter spring concept, respectively the antagonist concept; it is assumed the forces applied on articulated ribs are the actuator (force F_{act}) and the counter spring (force F_{sp}) or respectively the antagonist actuator (force F_{ant}). Force moments are calculated at hinge's center. The lever arms are noted h_1 and h_2. The usable output torque is M_u. SMA actuator minimum force is $F_{act\ cold}$ and maximum force is $F_{act\ hot}$. The counter spring is assumed as a linear spring, with its stiffness K_{sp} and its relaxed length L_{sp0}.

Considering the counter spring solution, the spring moment at hinge center is expressed in equation 4.2, where δL is the spring pre-strain.

$$\begin{aligned} M_{sp} &= h_2 \cdot K_{sp} \cdot (h_2 \cdot \theta) + M_{sp\ 0} \\ M_{sp\ 0} &= h_2 \cdot K_{sp} \cdot \delta L \end{aligned} \tag{4.2}$$

The counter spring aims to counter act the cold SMA force from the actuator to recover the initial shape. The counter spring pre-strain must apply a minimum moment equal to the opposite of the cold SMA moment. In order to limit the exceed in this force, the stiffness K_{sp} have to be minimize, this is possible by selecting a low stiffness spring with a high pre-strain. For integration reason, the pre-strain is reasonably limited to 70% of the actuator length L_{SMA} ($\delta L = 70\% L_{SMA}$). The torque balance gives the expression of the output moment in equation 4.3. This equation also contain the resulting force F_X in the hinge.

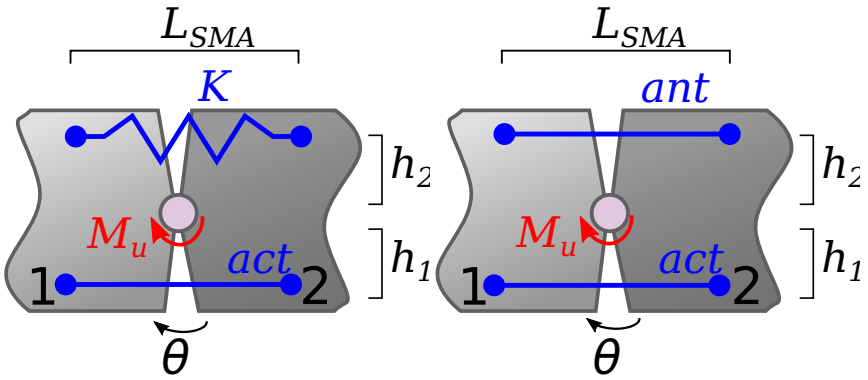

(a) Counter spring concept. (b) Agonist-antagonist concept.

Figure 4.8: Sketch of the two compared solutions.

$$\begin{aligned} \text{Maximum actuation: } M_u &= F_{act\ hot} \cdot h_1 - F_{act\ cold} \cdot h_1 \cdot (1 + \frac{h1 \cdot \theta}{\delta L}) \\ \text{Minimum actuation: } M_u &= -F_{act\ cold} \cdot h_1 \cdot \frac{h1 \cdot \theta}{\delta L} \\ F_X &= F_{act} + F_{act\ cold} \frac{h_1}{h_2} (1 + \frac{h_1 \cdot \theta}{\delta L}) \end{aligned} \tag{4.3}$$

Regarding the agonist-antagonist concept, the representation on Figure 4.8b distinguishes the actuator F_{act} and the antagonist actuator F_{ant} which is design to be actuated to counter act the cold actuator. The torque balance as well as the resulting hinge force are presented in equation 4.4.

$$\begin{aligned} \text{Maximum actuation: } M_u &= F_{act\ hot} \cdot h_1 - F_{ant\ cold} \cdot h_2 \\ \text{Minimum actuation: } M_u &= F_{act\ cold} \cdot h_1 - F_{ant\ hot} \cdot h_2 \\ F_X &= F_{act} + F_{ant} \end{aligned} \tag{4.4}$$

We can see that the output torque of the spring solution depends on the rotation angle. With a more accurate model, the antagonist actuator also depends on the rotation angle but in a smaller way. To compare the two concepts, standard values are taken: $h_1 = h_2 = 50$ mm, $L_{SMA} = 150$ mm, for a SMA strain of 1.5% the maximum angle is $\theta_{max} = 2.6°$. Actuator forces are $F_{act\ hot} = 8,700$N and $F_{act\ cold} = 2,000$N. Results are summed up in table 4.1.

This simple example shows that internal forces are lower for the antagonist concept and the output torque is 43% higher than the counter spring concept, with the same SMA actuator. The fact that antagonists actuators can be "switched off" compared to counter spring that always applies the restoring torque explains the large efficiency difference.

The previous models do not take articulation parasite torque into account. The sizing algorithm has been applied to an articulated hinge for a range of output torques. The performance of the technologies are presented in Figure 4.9. The

Table 4.1: Force comparison of counter spring VS antagonist solutions.

Technology	actuated $M_u(\theta_{max})$	actuated $M_u(\theta = 0)$	$\max(F_X)$	Spring/antago force
Counter spring	557 N.m	565 N.m	$28,830$ N	$F_{sp}(\theta_{max}) = 8,830$ N
Antagonist actuator	811 N.m	811 N.m	$16,220$ N	$F_{ant\ hot} = F_{ant\ cold}$, $F_{ant\ cold} = 3,780$ N

total estimated mass of the actuators and hinges, the hinge force and the amount of SMA are drawn depending on the output torque. Computations of non-functional system without antagonist actuator nor spring is represented as "No return system" for comparison. Some jumps due to a change in hinge references are visible. The conclusion is significant: counter spring solution add forces that need larger total SMA amount and larger hinges.

Finally, despite the need of a more sophisticated control system, the agonist-antagonist actuator concept is more efficient than a counter spring. The solution is lighter, requires lower SMA amount with lower forces in the structure. According to integration point of view, the counter spring can be materialized by an elastic skin, as presented in the next Section 4.4. An analogy with biologic articulations can be made, a simplified vision is that elbows are actuated by two antagonist muscles (biceps and triceps). This natural solution is preferred than one large muscle with a counter spring materialized by tendons. Thus the agonist-antagonist actuator topology is selected for the morphing wing design.

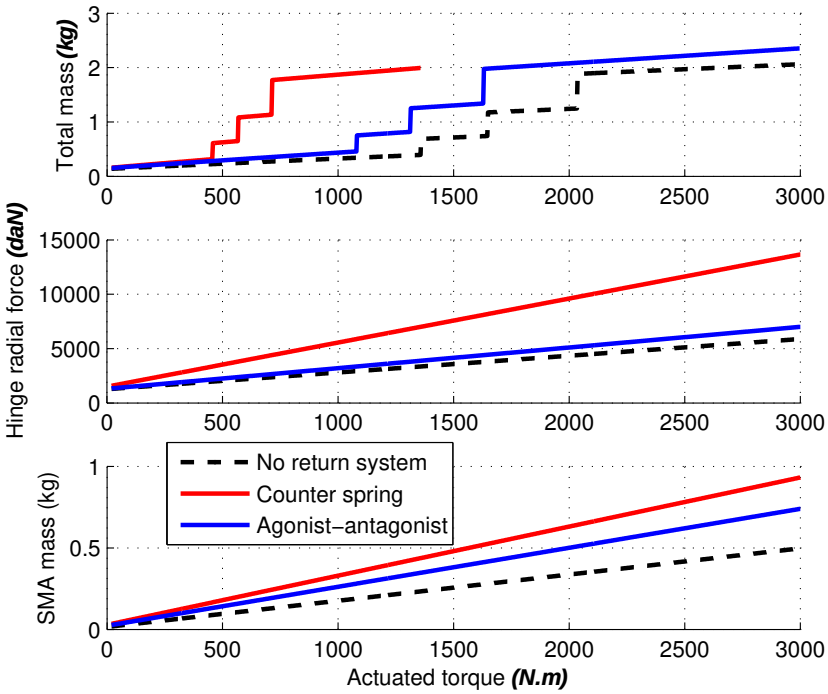

Figure 4.9: Performance of the counter spring and the antagonist solutions compared to the no return system.

4.4 Skin technologies and modeling

The skin is the device that covers the whole wing and defines the interface with the airflow. The skin for morphing wing is considered as the most demanding function. Thill et al. [Thi+08] draw a review of morphing skins within complete morphing systems. It is concluded that the combination of stiffness and flexibility is a major bottleneck. Indeed, the skin has to keep the airfoil profile fitting the required shape regardless to the deformations nor aerodynamic loading. Whilst carrying the pressure, the skin must be airtight, lightweight and consumes low energy. Some industrial specifications like temperature and environment compatibility, abrasion resistance or electric conduction are required.
Two different technologies are optimized and compared for the articulated flap: an elastic skin that covers the flap with some hung or free parts 4.4.1, and a promising innovative bio-inspired skin based on feathers 4.4.2. For both technologies, the specifications are to withstand the aerodynamic pressure with less than 1 mm deformation.

4.4.1 Elastic skin

The elastic skin concept consists in a taut membrane that is hung on the articulated ribs. The skin is free between the ribs at articulations levels, as presented in Figure 4.10. The free skin elements can be elongated when the articulations moves while the dynamic pressure tends to deform it.

To model the skin, one free element is focused on the detailed view in Figure 4.10. The free length is note L, T is the skin tension force (considering a span length $Span$) and H is the normal deformation due the pressure P (supposed constant on the free length). The skin is modeled as a membrane; but reduced to

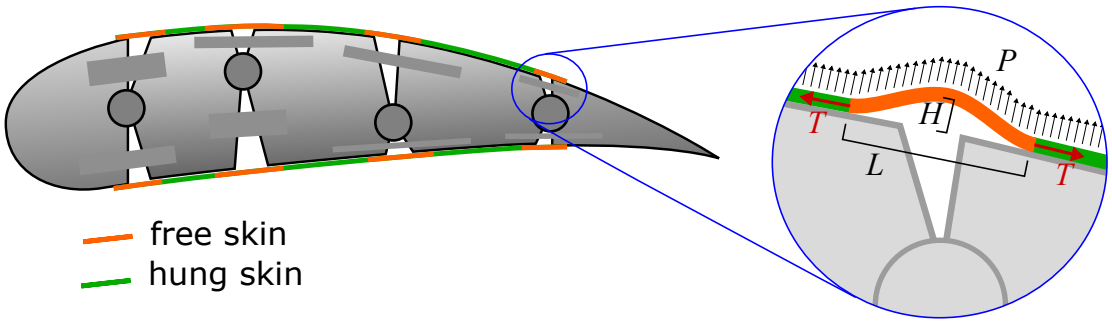

Figure 4.10: Morphing flap with elastic skin. Skin is hung when represented in green, whereas it is free and taut when represented in orange. The right part presents a detailed view of a parametrized taut skin element.

two dimensions, the skin is assumed to be modeled like a taut cable. The relation between the normal deformation and the other parameters is depict in equation 4.5. In a case corresponding to constant length L, a choice of the couple length, tension (L, T) is made to ensure a small normal deformation $H < H_{max} = 1$ mm. But due to the movements of the articulations, the skin length changes. Additionally the elasticity of the skin cause changes in the tension.

$$H = \frac{P \cdot Span \cdot L^2}{8 \cdot T} \tag{4.5}$$

Therefore, equation 4.6 models the skin as a pre-stressed elastic material; where t is the skin thickness, $\mathbb{E}$ its Young modulus and δL the skin extension due to articulation movements.

$$T = T_{pre} + \mathbb{E} \cdot t \cdot \frac{\delta L}{L} \tag{4.6}$$

The skin pre-stress T_{pre} corresponds to the minimum tension in skin when morphing movement impose minimum skin length. This tension is calculated from equation 4.5 to ensure a small normal skin deformation. When stretch, elastic force increase the skin tension thus ensuring small normal deformation. The dependence of T_{pre} as a function of the free skin length L is drawn in Figure 4.11. During morphing deformations, the skin's maximum extension δL add an important tension in the skin, inversely proportional to the free skin length L. The dependence of the elastic force is also drawn in Figure 4.11.

Therefore, the total maximum tension – drawn in Figure 4.11 – exhibits an optimum free length L that minimize the maximum tension. It is reminded that the lower the forces, the lighter the structure and the actuators. The formula of this optimal length L_{opt} with the corresponding maximal tension are written in equation 4.7.

$$\begin{aligned} L_{opt} &= \sqrt[3]{\frac{4\mathbb{E} \cdot t \cdot \delta L \cdot H_{max}}{P}} \\ T_{max} &= \frac{P \cdot Span}{8H_{max}} L_{opt}^2 + \mathbb{E} \cdot t \cdot Span \frac{\delta L}{L_{opt}} \end{aligned} \tag{4.7}$$

Finally, these equations are integrated in the design algorithm. This routine takes the skin displacement and the available room as inputs. It computes the free skin lengths and pre-stresses that fit the available room – optimum length are selected if possible. Outputs are the tensions that are transmitted by the hinges, and the maximum torques that actuators have to counter act, due to skin elastic forces when stretched during morphing.

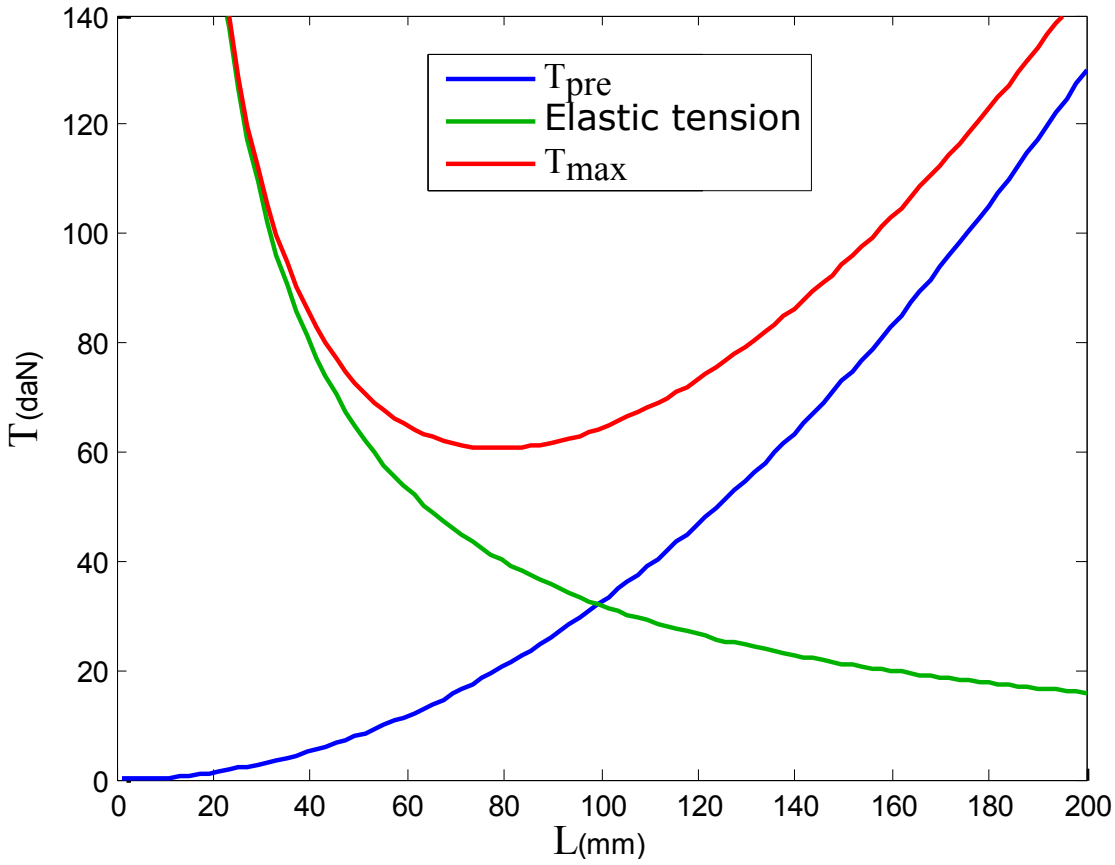

Figure 4.11: Illustration of skin tensions. The considered skin is an elastomeric coated fabric from Pennel & Flipo. The considered stretch is $\delta L = 8.5$ mm, for a 5 cm span.

An early result – detailed in section 4.6 – is that elastic skins require high tensions (about 3 tons for a 2 m span flap) that are transmitted through the structures and the hinge. These forces are much larger than aerodynamic forces, thus very heavy design is mandatory to carry these loads. Additionally, the skin stiffness consumes 60% of the actuator output energy so actuators have to be oversized to fulfill their functions. This early result confirms that the skin technology is a bottleneck for morphing purpose.

Figure 4.12 illustrates possible skin materials. The skin is a fabric based flexible composite that contains different layers dedicated to different requirements like stiffness and environment resistance.

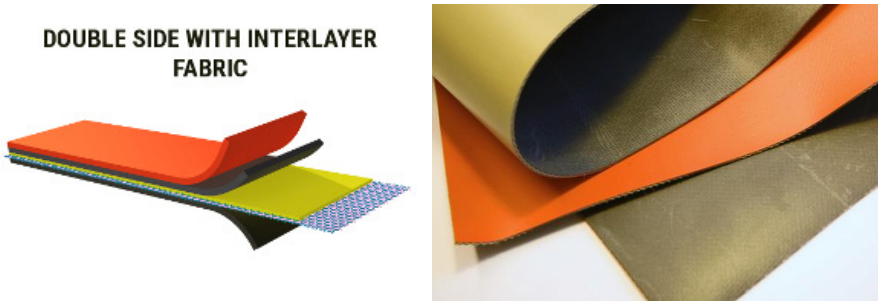

Figure 4.12: Illustration of ORCA products made by Pennel & Flipo.

4.4.2 Innovative feather and skin concept

The proposed innovative concept is bio-inspired from birds. Birds' bodies are covered by heterogeneous feathers. When a bird moves its wings, the wing profiles stay smooth, as the feathers glide on each others. If the feathers ensure the aerodynamic profile, birds have skin under the feathers to protect their bodies from the external environment. Inspired from this function decoupling, the proposed concept consists in an internal airtight skin and external gliding devices. The internal skin has no shape specification, but must be airtight to prevent internal airflow going outside and must carry the average aerodynamic loads. The external gliding devices, like artificial feathers, slide on the external profile and are thin enough to respect the 1 mm shape accuracy. Figure 4.13 presents the concept applied on one articulation.

The sizing of the internal skin do not require it to be extended so the forces due to the internal skin are neglected. Particular attention is paid to ensure there is enough room between the feathers and the actuators. The sizing of the feathers is decomposed threefold: geometric constraints, friction induced parasite torque , pressure induced deformation.

Geometric constraints concern the feather thickness t that must be under 1 mm, ($t < 1$ mm). The feather length L must be larger than the gliding length ($L > h \cdot (\theta_d + \theta_{op}$, where h is the articulation lever arm, θ_d and θ_{op} the extremal rotation angles). This second condition ensures the airfoil profile is always closed.

The friction induced torque comes from the calculation of the force exerted between the feather and the rib. Due to the rotation, the feather tip displacement y is evaluated. Assuming the feather is a cantilever beam in aluminum, the length have to be higher than a minimum value depending on the elasticity modulus $\mathbb{E}$ and elasticity limit σ_{max}. The maximum displacement y allows for calculating the contact force F_y with the rib (I stands for the second moment area of the feather cross section). Then, in the worth case corresponding to maximum deformation and force, the parasite friction torque M_{frot} is evaluated, depending on the friction

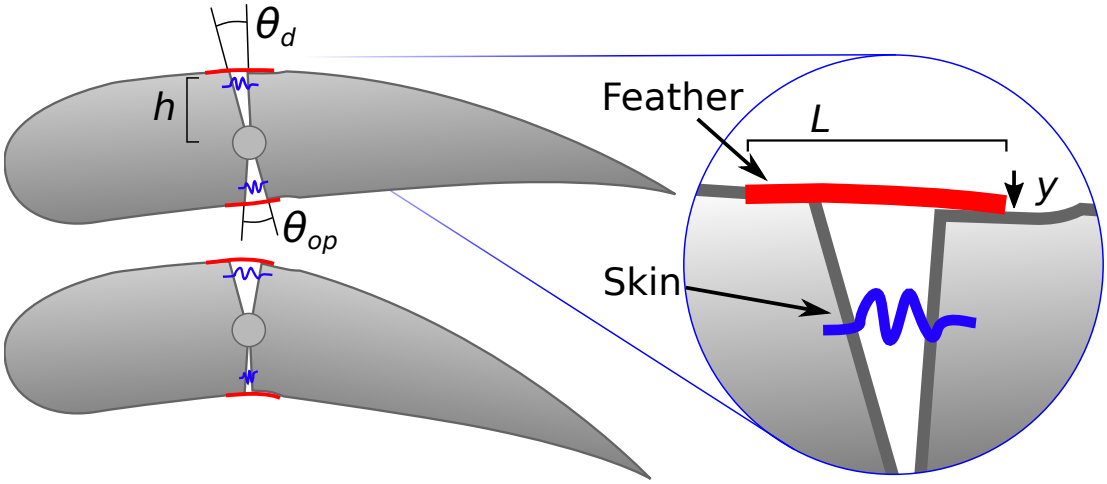

Figure 4.13: Skin and feather concept applied on one articulation. The flap is drawn for two rotation angles. A parametrized detailed view is also presented on right.

coefficient ν. Equations are detailed in equation 4.8.

$$\begin{aligned} y_p &= h \cdot tan^2(\theta_p) \\ L &> \sqrt{\frac{3y \cdot t \cdot \mathbb{E}}{2\sigma_{max}}} \\ F_y &= \frac{3y \cdot \mathbb{E} \cdot I}{L^3} \\ M_{frot} &= h \cdot \nu \cdot F_y \end{aligned} \tag{4.8}$$

The pressure induced deformations are static and dynamic. The feather tip deformation is calculated assuming the aerodynamic pressure is applied on only one side of the feather. This assumption is conservative because as the feathers are not airtight, the mean pressure between the feather and the skin is close to the outside mean pressure. The tip calculated displacement is very low (about 50 μm, for $L = 15$ mm, $t = 0.5$ mm), even within the conservative assumption. The dynamics aspects are important, feather flutter must not happen. Therefore, the first resonance frequency f_1 of the feathers are evaluated, thanks to equation 4.9 (cantilever beam, S is the cross section, ρ is the density). This frequency has to be high enough to avoid fluid-mechanic resonance; this condition is respected for every feather.

$$f_1 \approx \frac{1.875^2}{2\pi \cdot L^2}\sqrt{\frac{\mathbb{E} \cdot I}{\rho \cdot S}} \tag{4.9}$$

Despite of the different constraints, the skin and feather solution seems effective. Early results present feather of 0.5 mm thick, the longest ones are about 20 mm while the average length is approximately 6 mm. The parasite torques due to friction are always under 0.5 N.m, which represent less than 1% of the aerodynamic loads. First resonance frequencies of the feathers are above 2 kHz that is found to be acceptable. Finally, the algorithm's routine that size skins and feather only computes the needed length, as force or resonance constraints are always observed.

4.5 Optimization problem

Now that components are modeled, this section deals with a global flap sizing algorithm. The study aims designing a feasible and realistic flap, not the development of new optimization algorithm. Thus the computations are based on the genetic optimization algorithm from Mathworks' Matlab software.

4.5.1 Design variable

Previous sections 4.3.2 and 4.4 present methods that optimally size the actuators and the skin according to a given articulated geometry and forces. Then, actuators' lever arms, strokes and length, as well as skins' pre-tensions and free length or feathers' sizes are not design variables to be globally optimized. Nevertheless, hinges' locations as well as ribs where actuators are hold have to be selected. But to guaranty the controllability of each articulation angle, one actuator and one antagonist actuator are set between each consecutive articulated rib.

Thus the hinge locations remain to be optimized. The horizontal position (normed by the chord length) of the i-th hinge is named h_{Xi} while h_{Yi} is its relative vertical position (in % normed to the profile thickness). Hinge positions are limited within feasible making constraints, as summed up in equation 4.10, where N is the number of articulations.

$$\begin{aligned} \forall i \in [1:N], \text{Front spar} < h_{Xi} < \text{Rear spar} \\ \forall i \in [1:N], 30\% < h_{Yi} < 70\% \\ \forall i \in [1:N-1], h_{Xi} < h_{Xi} + 3 \text{ cm} \end{aligned} \tag{4.10}$$

Concerning the number of articulation N, shape optimizations with 2 to 7 hinges have been performed. Approximation errors – calculated in section 4.2.3.1 – due to the faceted profiles severely decrease up to 4 hinges. The gap between a 4 hinge flap profile and a 5 hinge flap profile has been found insignificant compared to the added implementation complexity.

As the internal structure is not precisely modeled in the sizing algorithm, the number of actuators spread along the span direction of the wing is not an important matter. A realistic compromise between force distribution and complexity is 4 actuators in the span. The optimization is then based on 50 cm span wingboxes, forming the 2 m span flap.

4.5.2 Cost and objective formulations

The sizing algorithm computes weights, power consumptions, shape approximation error, lifespan and penalization:

- The total weight W_{total} is the sum weight from the agonist actuators, the antagonist actuators, the hinges and an assumed simplified rib structure.

- The power consumption comes from the SMA activation, as explained in section 4.3.2. The maximum power is computed when heating all the actuators and antagonist actuators. The maintaining power P_{SMA} corresponds to the average power needed to maintain all the agonist and antagonist actuators at maximum temperature.

- The shape approximation errors are assessed like in section 4.2.3.1. S_{AV} is the average absolute error whereas S_{max} is the maximum absolute error.

- The lifespan concerns the actuators. The system expected lifespan is limited by the actuator with the lowest lifespan, noted L_{min}.

- Penalizations can be added, when sizing difficulties are encountered. Penalties are calculated when dimensions of dedicated actuator place are lower than the minimum lever arm, when there are not enough places for hinges and when the design is not converged. Additionally the number of different penalties is taken into account for the total penalty cost P_{enalty}.

To allow the optimization towards one optimal design, a unique cost must be defined from the different costs. A normalization is necessary. Costs like weight and power consumption are normalized to a representative value. The normalized shape cost is evaluated from the square of the averaged and maximum absolute approximation error. Cost related to the cycle life is proportional to the inverse of the expect number of cycles. Both shape and cycle life costs have a upper bound to prevent the optimization being piloted by these two costs only. The formulas corresponding to the cost normalization are summarized in equation 4.11, where

$.^n$ exponents are related to normalized costs.

$$\begin{aligned} W_{total}^n &= \frac{W_{total}}{5 \text{ kg})} \\ P_{SMA}^n &= \frac{P_{SMA}}{1.3 \text{ kW}} \\ S^n &= (S_{AV}/2.3 \text{ mm})^2 + 100 \cdot (1 - e^{(-S_{max}/100 \text{ mm})}) \\ L_{min}^n &= 100 \cdot (1 - e^{(-10^6/L_{min})}) \end{aligned} \tag{4.11}$$

Finally, the definition of unique cost uses mixing ratios. The choice of the mixing ratios does not come from sound scientific criteria but from empiric criteria leading to a balance flap between the effective weight, shape approximations, power consumption and lifespan.

4.5.3 Cost function: sizing algorithm

The sizing algorithm that uses the previously modeled components is described in Algorithm 2. This algorithm corresponds to the cost function of the optimization problem.

Starting from a hinge distribution and sizing rules (i.e. SMA limits and geometrical parameters), the algorithm firstly computes the optimized rotation angles that best fit the specified shapes for both up and down morphing. The design is placed in the worth case regarding the position, so only the maximum rotation angle θ_i – defined in the present algorithm – are used. Then aerodynamic forces and skins are evaluated. Therefore the sizing of the different actuators and hinges starts. The specified actuator torques $M_{act\ i}$ correspond here to the actuator torques $M_{act\ 2/1}$ of the model presented in Section 4.3.2. The first sizing iteration considers unknown forces as zero, so the first design of the actuator does not take into account the cold antagonist actuators nor the hinge parasitic torque. Then the antagonist actuators are computed based on the cold actuator forces; and finally the hinges are computed knowing the forces of all the actuators and antagonist actuators. This first loop is followed by other sizing loops. Taking the previous antagonist actuators and hinge to size the actuators, several iterations are done until the modifications in the hinge parasitic torque or the force from the cold antagonist actuators do not change by more than 5%. It results a sized system where the actuators, the antagonist actuators and the hinges can work together. If the design does not converge within 13 iterations, the sizing algorithm stop with a penalty cost. The final step of the algorithm is the computation of all the costs, defined in the previous section.

Algorithm 2 Actuator sizing algorithm

procedure GLOBAL FLAP SIZING(h_{Xi}, h_{Yi})

Compute rotation angles θ_{Ui} from *optimized shape*, *Up morphing*

Compute rotation angles θ_{Di} from *optimized shape*, *Down morphing*

$\theta_i = \max(\theta_{Ui}, \theta_{Di}, \theta_{Ui} - \theta_{Di})$ ▷ Angle ranges

Compute aerodynamic forces on hinges $F_{aero\ i}, M_{aero\ i}$

Compute forces and parasite torque of skin $F_{skin\ i}, M_{skin\ i}$

$M_{act\ OLD\ i} = 0$, $M_{ant\ OLD\ i} = 0$, $M_{hinge\ OLD\ i} = 0$ ▷ Initialization

▷ Actuator sizing

$M_{act\ i} = M_{aero\ i} + M_{skin\ i} + M_{hinge\ OLD\ i} + M_{ant\ OLD\ i}$

Compute $F_{act\ i}$ from *actuator sizing*($M_{act\ i}, \theta_i$, Sizing rules)

▷ Antagonist actuator sizing

$M_{ant\ i} = M_{act\ i} + M_{skin\ i} + M_{hinge\ OLD\ i}$

Compute $F_{ant\ i}$ form *actuator sizing*($M_{ant\ i}, \theta_i$, Sizing rules)

▷ Hinge sizing

$F_{hinge\ i} = F_{act\ i} + F_{aero\ i} + F_{skin\ i} + F_{ant\ i}$

Get $M_{hinge\ i}$ from *hinge selection*($F_{hinge\ i}, \theta_i$, Sizing rules)

do ▷ Iterative design loop

$M_{act\ OLD\ i} = M_{act\ i}$

$M_{ant\ OLD\ i} = M_{ant\ i}$

$M_{hinge\ OLD\ i} = M_{hinge\ i}$ ▷ Aging specifications

▷ Actuator sizing

$M_{act\ i} = M_{aero\ i} + M_{skin\ i} + M_{hinge\ OLD\ i} + M_{ant\ OLD\ i}$

Compute $F_{act\ i}$ from *actuator sizing*($M_{act\ i}, \theta_i$, Sizing rules)

▷ Antagonist actuator sizing

$M_{ant\ i} = M_{act\ i} + M_{skin\ i} + M_{hinge\ OLD\ i}$

Compute $F_{ant\ i}$ form *actuator sizing*($M_{ant\ i}, \theta_i$, Sizing rules)

▷ Hinge sizing

$F_{hinge\ i} = F_{act\ i} + F_{aero\ i} + F_{skin\ i} + F_{ant\ i}$

Get $M_{hinge\ i}$ from *hinge selection*($F_{hinge\ i}, \theta_i$, Sizing rules)

while $(|\frac{M_{hinge\ i} - M_{hinge\ OLD\ i}}{\frac{1}{2}\cdot(M_{hinge\ i} + M_{hinge\ OLD\ i})}| > 5\%$ and $|\frac{F_{ant\ i} - F_{ant\ OLD\ i}}{\frac{1}{2}\cdot(F_{ant\ i} + F_{ant\ OLD\ i})}| > 5\%)$ or number of iterations below maximum

▷ Sizing design end

Compute costs and penalties

return costs

4.6 Optimization results

Based on the modeled concept, actuators, skin and optimization problem, several tests have been performed. Different cost parameterizations and different hinge and skin technologies have been assessed. The cost function evaluation – i.e. computation of a completely sized flap with specified shape, actuators, antagonist actuators and skin – takes about 0.6 s on a laptop with 8 core CPU at 2.3 GHz. Different genetic algorithm parameters are tried. Finally, a population of $N = 150$ individuals (initially randomly generated) with a cross over fraction of 0.9, computed in parallel using migration has been selected. Each optimization lasts about 10 min and is processed many times with small variations in cost weightings to ensure the suitability of the results.

The optimization is used first to determine the best technologies. Then the locus of the hinge locations is determined for a multi-objective optimization using Pareto fronts.

4.6.1 Technological impacts on objectives

This section compares the results from two technological choices: elastic skins with elastic beam hinges and feathered skins with gliding hinges.

4.6.1.1 Flap with elastic skin with elastic beam hinges

The considered flap uses the elastic skins modeled in Section 4.4.1, with beams between the articulated ribs. These beams are bend when the ribs rotate. An algorithm calculates the dimensions of these flexible beams made of titanium, but is not detailed for brevity purpose.

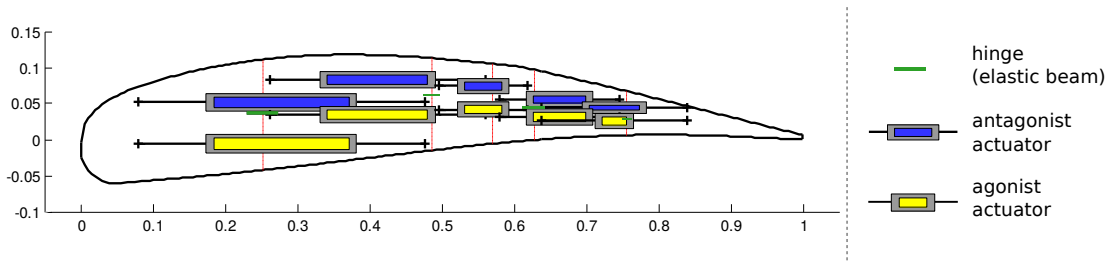

Figure 4.14: Sketch of the flap profile with the actuators and the flexible articulations. The sizes of the actuators represent the amount of SMA, assuming a square section. Actuators are drawn horizontal with maximum length between anchors, but this can be adapted in a final design step.

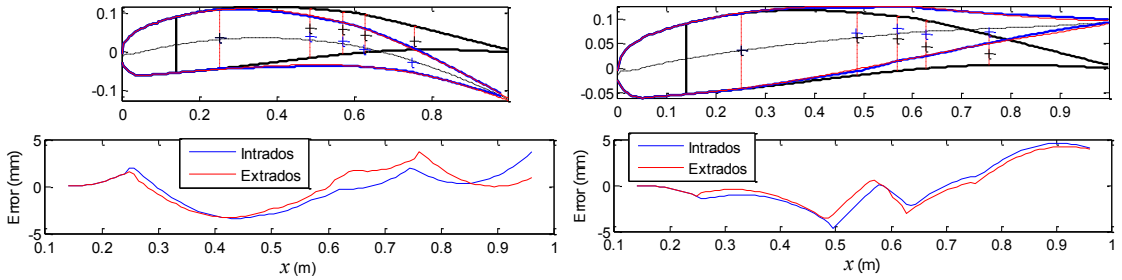

Figure 4.15: Optimized shape for both down and up morphing, with the corresponding approximation errors, as explained in 4.2.3.1.

Figure 4.14 schematically presents the flap with the actuators and the flexible beam articulations. The shape approximation performance is presented in Figure 4.15. The result of the optimization is detailed in Appendix B.1. For the 0.5 m span flap section, the total mass is estimated to 4.9 kg and a maximum heating power of 8 kW. The internal forces are quite large, for example, the first agonist actuator is designed to apply a force equivalent to 4.3 tons. This high force in the actuator is not only due to the aerodynamic forces, as visible in table 4.2. More than half the actuator specified torque is dedicated to counter act the skin elasticity. The part required by the hinge elasticity is below 5 %. This indicates that the actuators can be downsized by a factor 2 if the skin is removed.

Another important result regarding the technological choice is design of the flexible beams. The forces and available spaces (mostly in span direction) restrict the design of the flexible hinges to bad aspect ratios. The beams are not slim, which may conduct to unexpected behaviors. This is detected in the sizing algorithm that generates penalties. This result finally indicates that despite their relatively low parasite torque due to elasticity, the flexible beams are not suitable for the proposed morphing flap.

Table 4.2: Design moments for the actuators at hinge locations (without the torques from agonist and antagonist actuators)

	Design moment	Aero part	Skin elastic part	Hinge parasite part
Hinge #1	845.3 Nm	48.4%	49.2%	2.4%
Hinge #2	317.4 Nm	50.4%	47.4%	2.2%
Hinge #3	178.2 Nm	59.0%	40.7%	0.3%
Hinge #4	206.3 Nm	34.1%	61.2%	4.4%
Hinge #5	91.9 Nm	29.1%	78.6%	2.3%

4.6.1.2 Flap with feathered skin and gliding hinges

The considered flap uses the skin and feather concept modeled in Section 4.4.2. Instead of flexible beams, the articulations are realized using gliding bearings. These two selected technologies introduce friction but are not elasticity.

Figure 4.16 schematically presents the flap with the actuators and the gliding hinges. The shape approximation performance is presented in Figure 4.17. The result of the optimization is detailed in Appendix B.2. For the 0.5 m span flap section, the total mass is estimated to 2.6 kg and a maximum heating power of 2 kW. The internal forces are lower than the solution with elastic skins. For example, the first agonist actuator is designed to apply a force equivalent to 2.0 tons. This force in the actuator is mainly due to the aerodynamic forces, as visible in table 4.3. The part required by the friction from hinges and feathers is below 1.3 %.

The proposed solution with gliding bearings and feathers is efficient because parasitic forces are very low. Then the actuators are designed to only actuated against the aerodynamic forces and the antagonist actuators. The gliding bearings are selected as the best articulation technology, as their little dimensions, their very low parasite torques and their integration easiness are better than the other technologies. The feathers demonstrate here their suitability regarding a low power consumption morphing flap; thus this technology is selected.

4.6.2 Multi-objective optimum

Previous optimization results provides interesting results but are highly depends on cost weightings. These weightings are empirically tailored and the impacts from the skin accuracy or the actuator integration are not distinguished. To discriminate

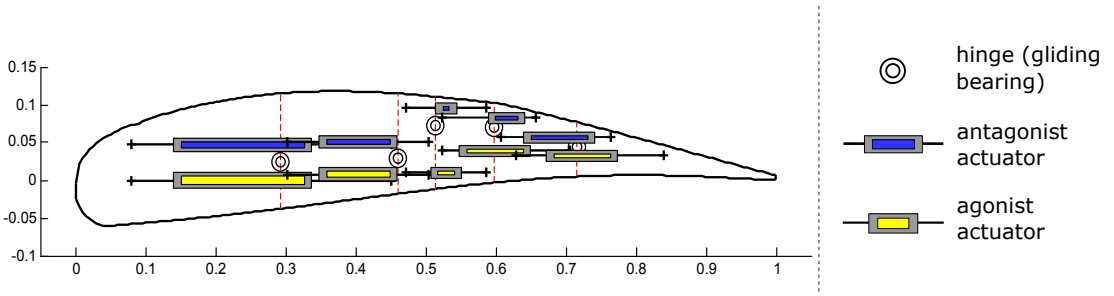

Figure 4.16: Sketch of the flap profile with the actuators and the gliding bearings. The sizes of the actuators represent the amount of SMA, assuming a square section. Actuators are drawn horizontal with maximum length between anchors, but this can be adapted in a final design step.

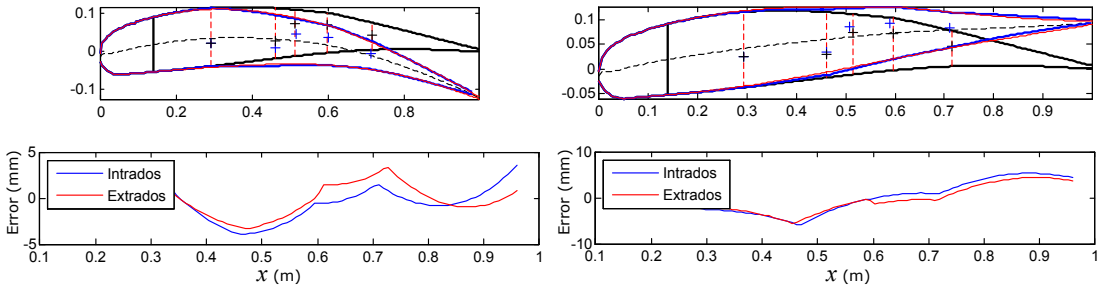

Figure 4.17: Optimized shape for both down and up morphing, with the corresponding approximation errors, as explained in 4.2.3.1.

Table 4.3: Design moments for the actuators at hinge locations (without the torques from agonist and antagonist actuators)

	Design moment	Aero part	Feather friction part	Hinge parasite part
Hinge #1	368.1Nm	98.7%	0.0% (0.07Nm)	1.3% (4.7Nm)
Hinge #2	184.5Nm	99.7%	0.0% (0.02Nm)	0.3% (0.6Nm)
Hinge #3	142.3Nm	100.0%	0.0% (0.01Nm)	0.0% (0.0Nm)
Hinge #4	90.2Nm	99.8%	0.0% (0.02Nm)	0.2% (0.2Nm)
Hinge #5	39.6Nm	98.6%	0.4% (0.16Nm)	1.0% (0.4Nm)

the impact of the different costs, a multi-objective approach based on Pareto front is used in the following.

Considering a population of N flaps, named $X_i, i \in [\![1, N]\!]$.The costs $C_{sha}(X_i)$ (respectively $C_{int}(X_i)$) is related to the shape (respectively is related to the integration of actuators). The flap X_j is Pareto optimal if there is no flap with one better cost, i.e. $\forall i \in [\![1, N]\!], C_{sha}(X_i) > C_{sha}(X_j)$ OR $C_{int}(X_i) > C_{int}(X_j)$.

The cost definitions for this multi-objective optimization are written in Equation4.12. It is remembered that: $S_{maxUP}/S_{maxDOWN}$ are the maximum skin error between the reference and the effective deformed shape for UP and DOWN deformation; k is the hinge/actuator/antagonist actuator number of the considered flap, $M_{aero\ k}$ is the aerodynamic torque on the k^{th} hinge; $\theta_{max\ k}$ is the angle range of the k^{th} hinge, $h_{max\ k}$ and $L_{max\ k}$ are the maximum available lever arm and length of the considered agonist/antagonist actuator.

$$\begin{aligned} C_{sha}(X_i) &= S_{maxUP}(X_i) + S_{maxDOWN}(X_i) \\ C_{int}(X_i) &= \sum_k M_{aero\ k} \frac{\theta_{max\ k} \cdot h_{max\ k}}{L_{max\ k}} \end{aligned} \tag{4.12}$$

To justify the integration cost, consider the k^{th} actuator is designed with the lowest force. To apply the required torque at lowest force, the lever arm must be maximum (h_{max_k}). Then the stroke of an actuator is $\theta_{max\ k} \cdot h_{max\ k}$. The actuator length is assumed maximum, the relation between the stroke, the length is $L_{max\ k} = \theta_{max\ k} \cdot h_{max\ k}/\epsilon_{SMA}$. Depending on the geometric parameters, the SMA strain ϵ_{SMA} can be expressed by $\epsilon_{SMA} = \frac{\theta_{max\ k} \cdot h_{max\ k}}{L_{max\ k}}$. The actuator is feasible if the SMA strain is low enough to ensure the expected fatigue life. So the minimization of cost $C_{int}(X_i)$ tends to minimize the forces in the structure, whilst maximizing the space for actuator integration.

Considering these two costs, a genetic algorithm has spread the population of the flap on the Pareto front presented in Figure 4.18. Two main areas of the Pareto front are identified: an area where the shape approximation costs are low (< 8 mm) for a wide range of integration costs, and an area where the integration costs decreases with the increase of the shape costs. At the extremity of these two areas are the best shape approximation flap and the best actuator integration capability flap. These two designs are respectively drawn on the figure with red highlighted drawbacks. For the first one the integration is not performed for one actuator; respectively for the other one, the shape approximation is very bad in the highlighted area. This observation indicates that a optimized flap which has both the best shape approximation and the best actuator integration capability does not exist. A compromise must be done.

Corresponding to the Pareto front flaps, the locus of the hinge positions is represented on Figure 4.19. The locus of hinges #5 does not move, locus for hinges #1, #3 and #4 are quite continuous whereas the positions of hinges #2 are spread on two spots. The Figures 4.19b and 4.19c indicates that the best hinge positions corresponding to the best shape approximation or the best actuator integrability are not identical. A compromise must be done.

This compromise is selected where the previously described two main areas cross each other. This crossing area corresponds also as a compromise between the different hinge positions. The Pareto front of Figure 4.20 presents the two compromise flap designs. The costs here are normalized, so that the costs are between 0 and 1. Both designs present a good shape approximation and a good actuator integration ability. Considering the worst shape approximation flap – also the one with the best integrability – (bottom right part of the figure), an improvement of 55% of the shape approximation costs only 8% of the integrability costs. On the other corner, the best shape approximation flap – also the one with the worst integration capability – (top left part of the figure), an improvement of 70% of the integration costs a 30% decrease in shape approximation. Additionally the compromise flap with the best actuator integration capability presents actuators larger by 5%, thereby corresponding to a heavier design consuming more energy.

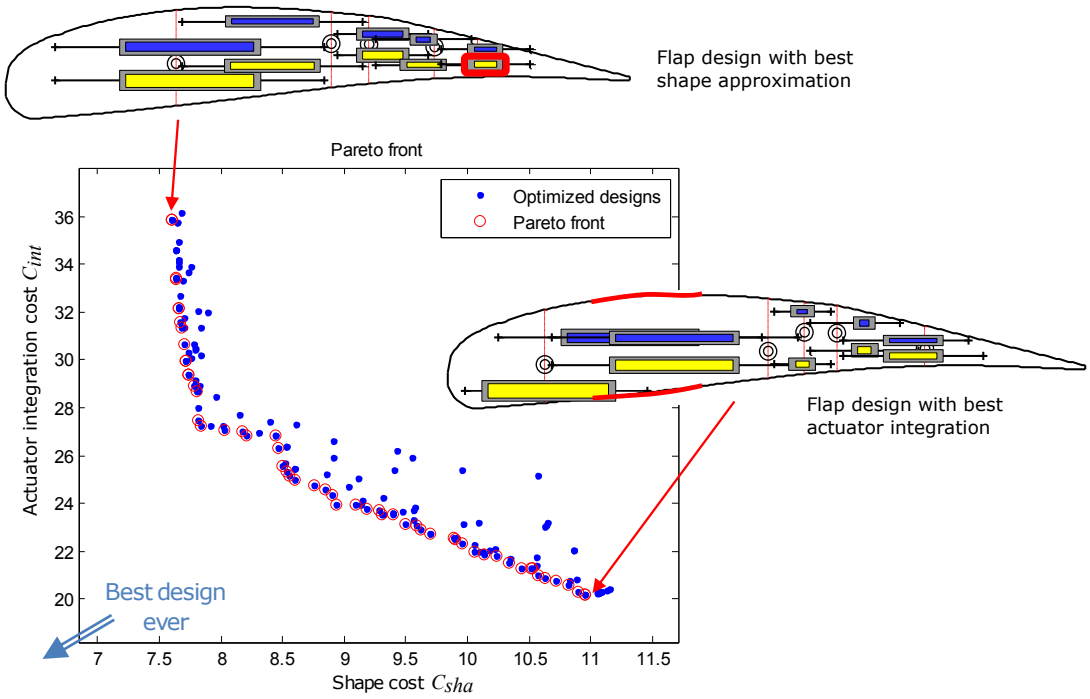

Figure 4.18: Pareto front Shape cost VS Integration cost. The population is represented by blue points and the Pareto optimal individuals are presented by red circles. The two extreme flaps are represented with red highlighted drawbacks: large integration issue for the last actuator or large error in shape approximation.

Finally, the choice of the ultimate flap design is the flap with the best shape approximation, to ensure a feasible flap. The articulation positions corresponding to the final choice are indicated on Figure 4.19.

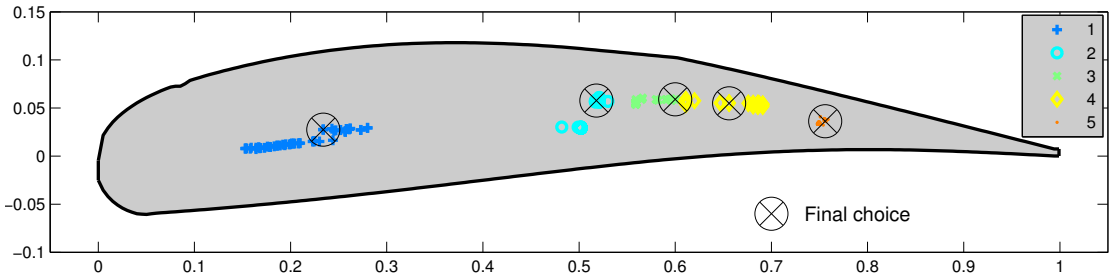

(a) Hinge locus ranked by hinge number.

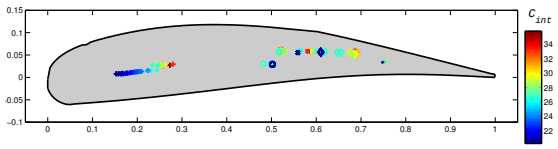

(b) Hinge locus ranked by C_{int} cost.

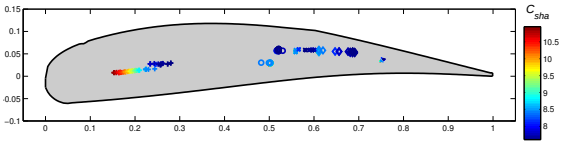

(c) Hinge locus ranked by C_{sha} cost.

Figure 4.19: Hinge locus. The positions of the hinges of the Pareto front's flaps are plotted threefold: 4.19a color shades represent the hinge number, 4.19b color shades represent the actuator integration cost and 4.19c color shades represent the shape approximation cost.

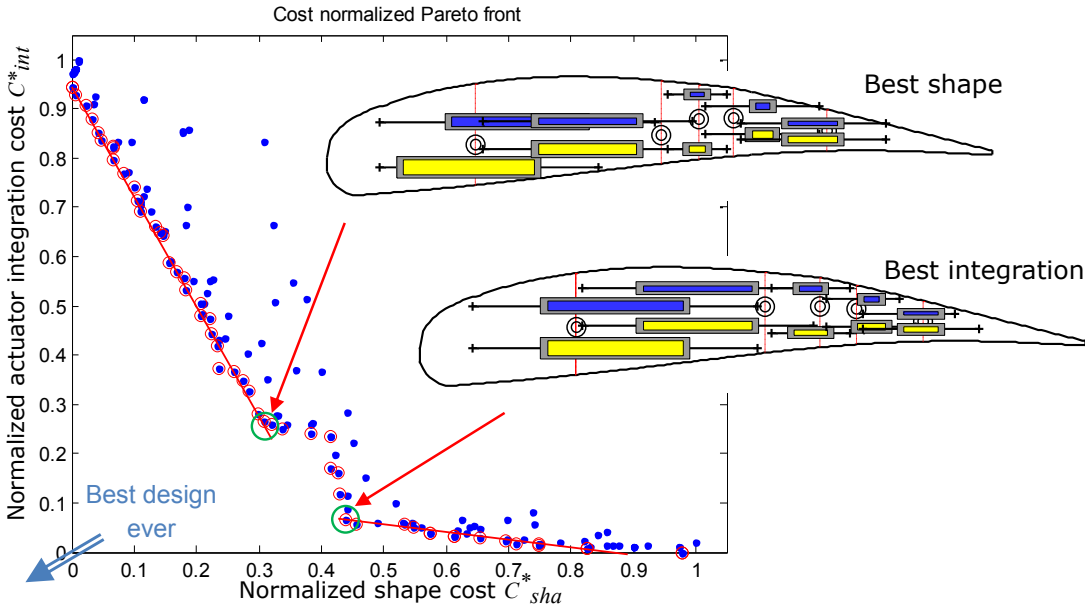

Figure 4.20: Normalized Pareto front Shape cost VS Integration cost. Here the costs have been affine transformed to be between 0 and 1. The population is represented by blue points and the Pareto optimal individuals are presented by red circles. The two possible compromise flaps are represented on the right.

4.6.3 Design choice

The justification of the selected design is presented in the previous Section 4.6.2. The hinge positions are presented in Figure 4.19. The design estimates a 9 kg flap section with an average consumption of 0.515 kW, as it is developed in B.3. One can notice that the expected fatigue life is limited to 40,000 cycles, which is very low. This estimation comes from the lever arm limitation in the thin rear part of the wing. This issue is alleviated during detailed design by inclining the actuators – a new calculation of the active lengths and lever arms is performed for such inclined actuators.

Additionally, all the actuators have been inclined to increase the lever arm and then to decrease the forces in the structure. Taking into account the available space in the span direction, the different actuators are spread in the span. It results a macro-actuator composed of the different actuators, the articulated ribs and the hinges. The flap is then made by the assembly of four macro-actuators plus spars, stiffeners, skin and feathers. The detailed design of the such optimized flap prototype is not detailed anymore in this chapter. Figure 4.21 presents a view of the manufacturing CAD model of the macro actuator.

4.7 Conclusion and outlooks

The present chapter deals with morphing wing design through optimization. The target is a true scale flap of a regional industrial aircraft. A camber control concept based on articulated ribs is proposed. This concept can be used with different hinge technologies and different skin technologies. The actuators, based on innovative smart materials like shape memory alloys, are also investigated. Comparing different actuation topologies, it has been shown that in terms of weight and internal forces, the agonist/antagonist topology is better than a solution with one actuator and a counter spring. Based on industrial specifications and constraints, genetic optimizations have been performed comparing the different technological choices. As a result, the elastic skin causes large issues according to the internal forces in the structures and is responsible for over-sizing by more than 50% the actuator forces. Then an innovative bio-inspired skin and feather concept has been selected, taking advantage of the specifications and constraints. As the optimization objectives are related to the weight, the shape approximation, the energy consumption and the fatigue life of actuators, a multi-objective optimization based on Pareto front is used to choose the ultimate flap design.

Finally, the resulting design is feasible and a detailed design has been done. Future works will focus on the design, integration, and control of the macro-actuators

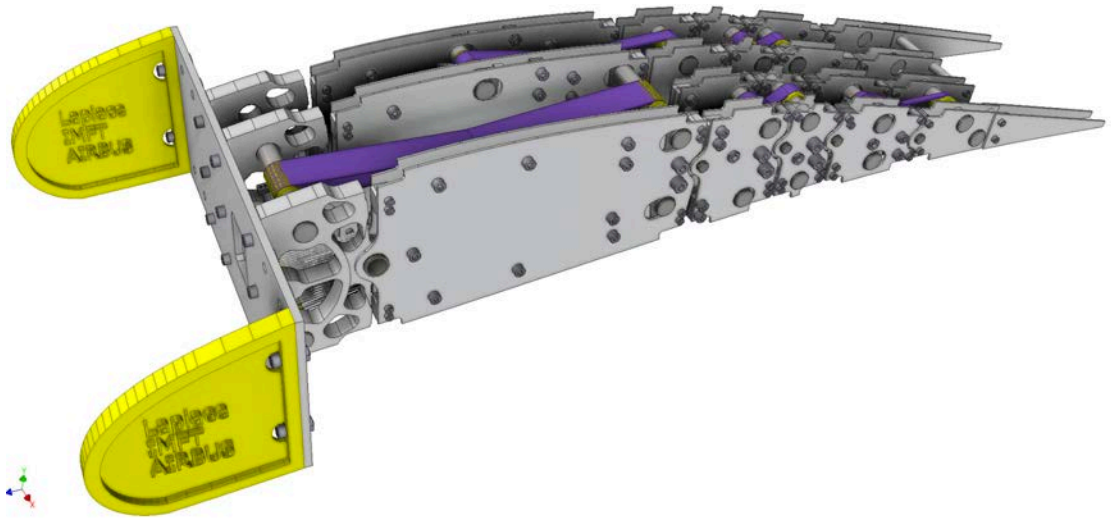

(a) 3D CAD view of the detailed design of the macro-actuator of the flap.

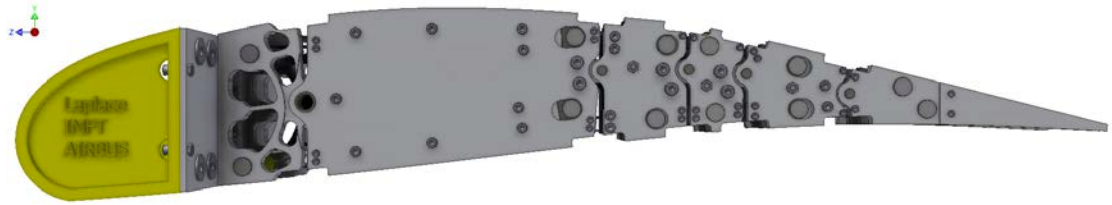

(b) Side view of the detailed design of the macro-actuator of the flap.

Figure 4.21: Detailed design views of the macro-actuator of the flap.

in a true scale flap prototype. Then electromechanical and aerodynamic characterizations will be performed on dedicated static test bench and in wind-tunnel.

Acknowledgements

The authors are grateful to Airbus and RTRA-STAE Foundation that provided funding for this research. The authors would also like to thank Dominique HARRIBEY, Oussama FILALI and Maxime RUFFEL for their useful advice and help within this work.

Conclusion

This thesis has investigated electroactive hybrid morphing, with a calling towards real scale application for Airbus A320.

Morphing wings have potential to increase aerodynamic performance but actuators, structures and aerodynamics have to be studied together. Within the framework of the LAPLACE and IMFT laboratories, the originality of the proposed approach is to combine different smart material actuators to both adapt the wing shape by large deformation and manipulate the airflow turbulence.

In this multidisciplinary study in cooperation with Airbus, a reduce model of an electroactive hybrid morphing wing has been made. Wind tunnel experiments have been performed. The morphing impacts on lift and drag is measured and wake dynamics with morphing mechanisms are described. To apply the developed concept on a true scale wing, a first step consisting in sizing and designing a A320 morphing flap is dealt with.

- In more details, the first part of the work consisted in making a 700 mm chord hybrid morphing wing. Models have been developed for design purpose and for control purpose. Validations were performed on previous mock-up (Scheller's NACA4412 model) or specifically made test bench (actuated plate). Models are in agreement with experiments but analytical models exhibit limits for complex structures. Plus, finite element analysis highlighted the sensibility to pre-strain applied to actuators, this informing the care to be given during making. Electrodynamic characterization has been performed: a notable result is the choice of controller settings can reduce the power consumption by 20%.

- The second contribution regards the experimental aerodynamic characterization. The wing prototype has been instrumented with pressure transducers and a home made balance. The sensors' accuracies and reliabilities have been characterized and the experiments have been programmed to be automatically processed in order to maximize the reliability and the independence of the different morphing configuration. For the first time, the force changes due to camber control, trailing edge vibration and their combination have been acquired in a large database. Lift enhancement by 27% (23% due to

camber + 4% due to small trailing edge vibrations) has been measured. The measured decrease of 13% in drag at Reynolds number of 10^6 has been seen only once. The measurement set up has been update to perform accurate measures at lower velocities at initial cambers, where the reproducibility is observed with gains of 2% at optimal frequency. High speed time resolved particle image velocimetry (HS TR-PIV) measurements have been performed in the trailing edge wake region. The flow dynamics has been studied by means of time average fields, spectra and Proper Orthogonal Decomposition. Vortices have been identified and a theory based on models from Hunt is used to explain eddy blocking effect and vortex breakdown. A morphing induced reduction of 99.9% of coherent vortices power density has been observed.

- The optimal design of a true scale morphing flap is the third contribution of the manuscript. From Airbus data and specifications, the transition towards true scale actuators for camber control is investigated. The technology gap implies that the developed solutions for a reduced scale are not applicable. Based on a simple parametrized articulated structure, analytic models for shape evaluation, force balance, actuators, skin technologies and hinges are developed. These models are parts of the sizing algorithm, codded to optimize the flap design according to shape approximation error, weight, power consumption and life span. It is showed that agonist-antagonist actuator is better than a single one way actuator with a counter spring. Also skin has to be pre-stressed to carry the aerodynamic loads with limited airfoil profile deformation. This leads to very high internal forces that over size the structure and the actuators. Consequently, an innovative solution bio-inspired with feathers and internal skin appears to be a good alternative. A multi-objective optimization based on Pareto front helped to choose the final choice: a 10 kg and 1 m length macro actuator carry 250 kg of aerodynamic force while deforming the trailing edge by 20 cm with a maximum average power consumption of 0.5 kW. The result is now the basis for designing a true scale demonstrator but the analytic model with static assumption is limited; the dynamic fluid-structure behavior has to be addressed.

The works presented in this manuscript is part of the basis of the European project *Smart Morphing and Sensing*[6]. This project is coordinated by Marianna BRAZA. It started in May 2017 and will end in April 2020. It will include part of activities developed in the reduced scale prototype (Chapter 2) with further testing of close-loop control as well as innovative electromagnetic actuators. The large scale prototype of this project will result from the continuation of the designed morphing flap presented in Chapter 4.

[6] smartwing.org/SMS

Outlooks

This work answered some questions and some elements have to be continued or enhanced. Two main points are discussed here:

- The understanding of the physics phenomena due to hybrid morphing are not well understood yet. Better force measurements are needed and a new update of the sensors can be proposed. This is already difficult because the measurement specifications are very demanding. Eventually, a new wing prototype, lighter with upgraded actuators could be designed for this purpose. Regarding the PIV measurements, the actuations selected in the manuscript correspond to points with small effects. New measures – of the wake and of the flow over the trailing edge – at vibrations leading to significant changes in lift have already been investigated and are know being post-processed; an example is provided in Figure 3.14. The SMS project could answer the questions raised by the present thesis. Notably, a closed loop controller of the turbulence is investigated. Innovative optical pressure sensors are used to sense the turbulence in order to control the morphing actuators.

- The wing demonstrator at true scale is not done yet. The technologies are selected, the camber control actuator is sized. The design is in progress and a validation test of the macro-actuator is planed soon. Also, a further investigation of the design by optimization can be addressed. Convergence criteria or cost definition can be improved; deterministic optimization algorithms may be used instead of genetic algorithm. It will take place in the already made fixed leading edge visible on Figure 4.22 Dynamics study of the fluid-structure-actuator interaction is currently being assessed. Then, the mechanical structure has to be designed before the final making.

- All of the work related in the Chapter 4 is dedicated to camber control only; the vibrating trailing edge has to be designed too. Due to the increased velocities, forces and amplitudes for the subsonic and transonic flights, the technology transfer can not be a homothety of the small scale vibrating actuator. Magnetic actuators – with conventional electro-mechanical devices or innovative magnetic shape memory alloys for instance – will be investigated in the framework of the SMS project.

- Bio-inspiration can go further. The manta ray uses traveling waves on its fins to efficiently propel itself. This is done with a smart interaction with generated vortices. This idea can be transposed to the trailing vibrations, to generate spanwise traveling waves. These transverse mechanical waves

interact with the 3D secondary vortices, with potential drag and noise reductions.

The following section presents a list of my contributions: publications, co-supervising, scientific popularization.

Related publications and contributions

Within the current framework of PIV measurements, experiments discussed in Chapter 3 were used to evaluate and buy new cameras and lasers by Sébastien Cazin and Moïse Marchal from the technical support of IMFT. These experiments were processed on the MPI cluster EOS of Calmip team, using the software CPIV developed by Pierre Elyakim. Also, the presented work has been participating to the Smart Wing platform[7]. The electroactive hybrid morphing wing prototype realized for the purpose of this thesis will be used for further investigations in the context of the SMS European project.

Scientific popularization:

- "Aéronautique : des chercheurs toulousains travaillent sur la mise au point des ailes du futur", a video report in 4 episodes on regional TV (France 3), 2014 [8]
- "Royal Society Summer Science Exhibition", "Smart Wing Design through turbulence control: Science imitating nature", London, United Kingdom, July 2014. [9]
- "Fête de la science", visit of the LAPLACE laboratory, Toulouse, France, October 2015.
- "The Wings of the Future" , video report by CNRS, 2015 [10]
- `"Ma Thèse en 180 secondes (MT180)", French national competition, selected for regional final, 2016 [11]

[7] http://smartwing.org/

[8] http://france3-regions.francetvinfo.fr/occitanie/haute-garonne/toulouse/aeronautique-des-chercheurs-toulousains-travaillent-sur-la-mise-au-point-des-ailes-du-futur-544498.html

[9] http://sse.royalsociety.org/2014

[10] https://news.cnrs.fr/videos/the-wings-of-the-future

[11] http://www.dailymotion.com/video/x4cdfb4

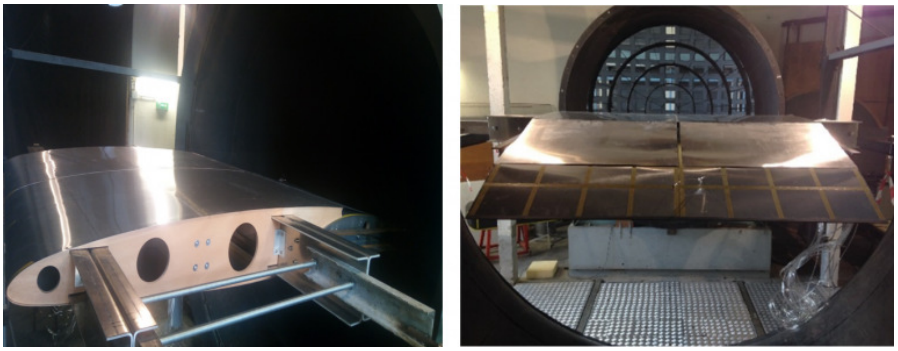

(a)

Figure 4.22: (a) Pictures of the Large Scale prototype in the S1 wind tunnel of IMFT laboratory. This prototype is part of the SMS project. This project has received funding from the European Union's H2020 program for research, technological development and demonstration under grant agreement no 723402.

- "Le biomimétisme : la nouvelle innovation qui s'inspire de la nature", 5min video report on the most watched national TV news (France 2), 2016 [12]

- "Fête de la science, bio-inspiration & aérodynamique", at Aeroscopia museum, Toulouse, France, October 2016. [13]

Supervised and co-supervised trainees:

- Dimirti Behary-Laul-Sirder, *Conception et réalisation d'un convertisseur statique multi voies sinus haute tension pour charge capacitive*, 2^{nd} year internship, ENSEEIHT engineering school (M1), 2015.

- Maxime Ruffel, *Conception d'un banc d'essai statique pour aile déformable*, 4^{th} year internship, INSA Toulouse engineering school (M1), 2016.

[12] http://www.francetvinfo.fr/decouverte/le-biomimetisme-la-nouvelle-innovation-qui-s-inspire-de-la-nature_1512499.html

[13] http://www.musee-aeroscopia.fr/fr/actualites/fete-de-la-science-au-mus%C3%A9e-les-8-9-octobre

- Oussama Filali, *Évaluation, comparaison et caractérisation de systèmes d'actionnement destinés au morphing de surfaces portantes de grandes envergures*, final year project of ENIT engineering school (M2), 2016.

- Vanilla Temtching Temou, *Simulation numérique en aéroélasticité des interactions fluide-structure et participation à la conception de la maquette d'une aile de type Airbus A320 en morphing électroactif hybride dans une échelle proche de 1*, final year project of SUPAERO engineering school (M2), 2016.

- Yannick Bmegaptche Tekap, *Conception d'un prototype d'une aile d'Airbus A320 d'échelle proche de 1 avec volet en morphing électroactif hybride*, final project of M2 research in mechanical engineering specialized in structures and materials, 2016.

- Mateus Carvalho, *Contribution á l'étude du morphing d'une aile d'avion de type Airbus A320 en échelle intermédiaire et échelle 1*, final year project of INSA engineering school (M2), 2017

- Martin Laroche, *Mise en oeuvre expèrimentale de dispositifs de caractérisation d'alliages á mémoire de formes thermiques et magnétiques*, 2^{nd} year internship, ENSEEIHT engineering school (M1), 2017.

Award and distinction:

- Best presentation award at the GEET day, annual meeting of the doctoral school, 2017.

- Best paper award – student travel grant award; for the paper: G. Jodin, J. Scheller, J.F. Rouchon, M. Braza. "On the multidisciplinary control and sensing of a smart hybrid morphing wing, *2017 IEEE International Workshop ofElectronics, Control, Measurement, Signals and their Application to Mechatronics (ECMSM)*, `https://doi.org/10.1109/ECMSM.2017.7945866`

Related publications

Peer-review publications:

1. J. Scheller, G. Jodin, K. J. Rizzo, E. Duhayon, J. F. Rouchon, M. Triantafyllou, M. Braza. "A Combined Smart-Materials Approach for Next-Generation Airfoils", *Solid State Phenomena*, Volume 251 Pages 106-112, 2016, `doi.org/10.4028/www.scientific.net/SSP.251.106`

2. G. Jodin, J. Scheller, E. Duhayon, J. F. Rouchon, M. Triantafyllou, M. Braza. "An Experimental Platform for Surface Embedded SMAs in Morphing Applications", *Solid State Phenomena*, Volume 260, pages 69-76, 2017, doi.org/10.4028/www.scientific.net/SSP.260.69

3. G. Jodin, J. Scheller, E. Duhayon, J. F. Rouchon, M. Braza. "Implementation of a Hybrid Electro-Active Actuated Morphing Wing in Wind Tunnel", *Solid State Phenomena*, Volume 260, pages 85-91, 2017, doi.org/10.4028/www.scientific.net/SSP.260.85

4. G. Jodin, V. Motta, J. Scheller, E. Duhayon, C. Döll, J.F. Rouchon, M. Braza. "Dynamics of a hybrid morphing wing with active open loop vibrating trailing edge by Time-Resolved PIV and force measures", Journal of Fluid and Structures, 2017, doi.org/10.1016/j.jfluidstructs.2017.06.015

International conferences:

1. G. Jodin, J. Scheller, J.F. Rouchon, M. Braza. "On the multidisciplinary control and sensing of a smart hybrid morphing wing, *2017 IEEE International Workshop ofElectronics, Control, Measurement, Signals and their Application to Mechatronics (ECMSM)*, https://doi.org/10.1109/ECMSM.2017.7945866

2. G. Jodin, N. Simiriotis, V. Temtching, D. Szubert, Y. Hoarau, J. Scheller, J.F. Rouchon, M. Braza. "Electroactive morphing of a supercritical wing for increasing the aerodynamic performance", *52nd 3AF International Conference on Applied Aerodynamics* , International Conference on Applied Aerodynamics, 27 – 29 March 2017, Lyon – France

3. G. Jodin, J. Scheller, K.J. Rizzo, E. Duhayon, J.F. Rouchon, M. Braza. "On the hybridization of electro-active materials to enhance aircraft aerodynamic performance", *More Electric Aircraft MEA2017*, 1 – 2 February 2017, Bordeaux – France

4. G. Jodin, J. Scheller, J.F. Rouchon, M. Braza. "Experimental investigation of the dynamics of a hybrid morphing wing: time resolved particle image velocimetry and force measures", *APS DFD 2016 - The 69textrmth Annual Meeting of The American Physical Society – Division of Fluid Dynamics*, November 2016, Portland, Oregon, USA

5. G. Jodin, J. Scheller, E. Duhayon, J.F. Rouchon, M. Braza. "Implementation of a hybrid electro-active actuated morphing wing in wind tunnel", *MSM 2016 - 12textrmth International Conference Mechatronic Systems and Materials*, July 2016, Bialystok, Poland

6. G. Jodin, J. Scheller, E. Duhayon, J.F. Rouchon, M. Triantafyllou, M. Braza. "An experimental platform for surface embedded SMAs in morphing applications", *MSM 2016 - 12textrmth International Conference Mechatronic Systems and Materials*, July 2016, Bialystok, Poland

7. J. Scheller, K.J. Rizzo, G. Jodin, S. Cazin, M. Marchal, E. Duhayon, J.F. Rouchon, M. Braza. "PIV measurements of a high-frequency vibrating trailing edge morphing NACA4412 airfoil", *NIM 2015 - Workshop on Non-intrusive Measurements for unsteady flow and aerodynamics*, October 2015, Poitier, France

8. K.J. Rizzo, J. Scheller, G. Jodin, E. Duhayon, J.F. Rouchon, M. Braza. "Écoulement en bord de fuite d'un profil NACA 4412 morphé par un actionnement hybride", *CFM 2015 - 22ème Congrès Français de Mécanique*, August 2015, Lyon, France

9. J. Scheller, K.J. Rizzo, G. Jodin, E. Duhayon, J.F. Rouchon, M. Braza. "A hybrid morphing NACA4412 airfoil concept", *ICIT 2015 - 2015 IEEE International Conference on Industrial Technology*, March 2015, Sevilla, Spain

10. J. Scheller, K.J. Rizzo, G. Jodin, E. Duhayon, J.F. Rouchon, G. Harran, M. Braza. "Time-resolved PIV measurements of a hybrid morphing NACA4412 airfoil", *IFASD - International Forum on Aeroelasticity and Structural Dynamics*, July 2015, Saint Petersburg, Russia

11. J. Scheller, K.J. Rizzo, G. Jodin, E. Duhayon, J.F. Rouchon, M. Braza. "A Combined Smart-Materials Approach for Next-Generation Airfoils", *MSM 2015 - 11th International Conference Mechatronic Systems and Materials*, July 2015, Kaunas, Lithuania

12. G. Jodin, Johannes Scheller, Karl Joseph Rizzo, Eric Duhayon, Jean-François Rouchon, Marianna Braza. "Dimensionnement d'une maquette pour l'investigation du morphing électroactif hybride en soufflerie subsonique", *CFM 2015 - 22textrmme Congrès Français de Mécanique*, August 2015, Lyon, France

13. G. Jodin, J. Scheller, K. J. Rizzo, E. Duhayon, J. F. Rouchon, M. Braza. "Models for dimensioning hybrid morphing airfoil actuating system", *MEA 2015 More Electric Aircraft , International conference*, February 2015, Toulouse, France

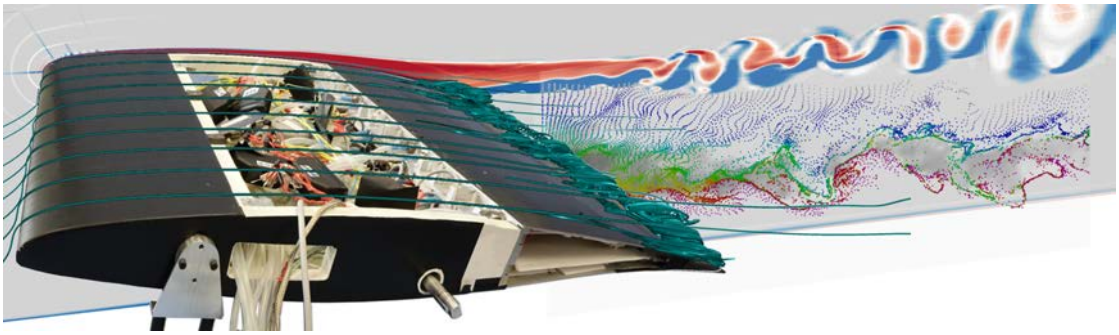

Figure 4.23: Artist view of electroactive morphing. Photomontage from a picture of the small wing prototype, streak-lines from PIV measures and numerical simulations made by IMFT. Image made for 3AF, 2017.

APPENDIX A

Wind tunnel experiment appendices

A.1 Experimental result validation: statistical convergence of the PIV

As the airflow is chaotic and characterized by coherent structures and random structures, statistic tools are used. Before making physical interpretation on statistical results, the statistical convergence is checked. To perform the convergence calculation, the same 8 points as 3.7 are selected. Points 1 to 4 are placed in the more energetic part of the wake. Points 5 and 6 are in the upper and middle part of the wake, behind the trailing edge. The points 7 and 8 are placed far downstream. For these points, the time averages depending on the experiment time is presented in figure below. The first order quantities (the mean stream-wise and crossflow velocities) converge quickly, then the second order (the Reynolds tensor components) reasonably converge at few per cent of the final value. For example Figure A.1 presents the convergence for baseline experiment. All quantities are within an interval of +/-2% before 8 s, so the experiment has reasonably converged. The convergence has been checked for all the morphing experiments. Therefore we can conclude that the 10 s experiments are statistically converged.

A.2 Experimental result validation: statistical convergence of the balance

For the same reasons as presented in A.1, convergence analysis of the balance measurements is performed. Figure A.2 presents the convergence of the average then the variance of lift and drag, for a selection of 80 different experiments at

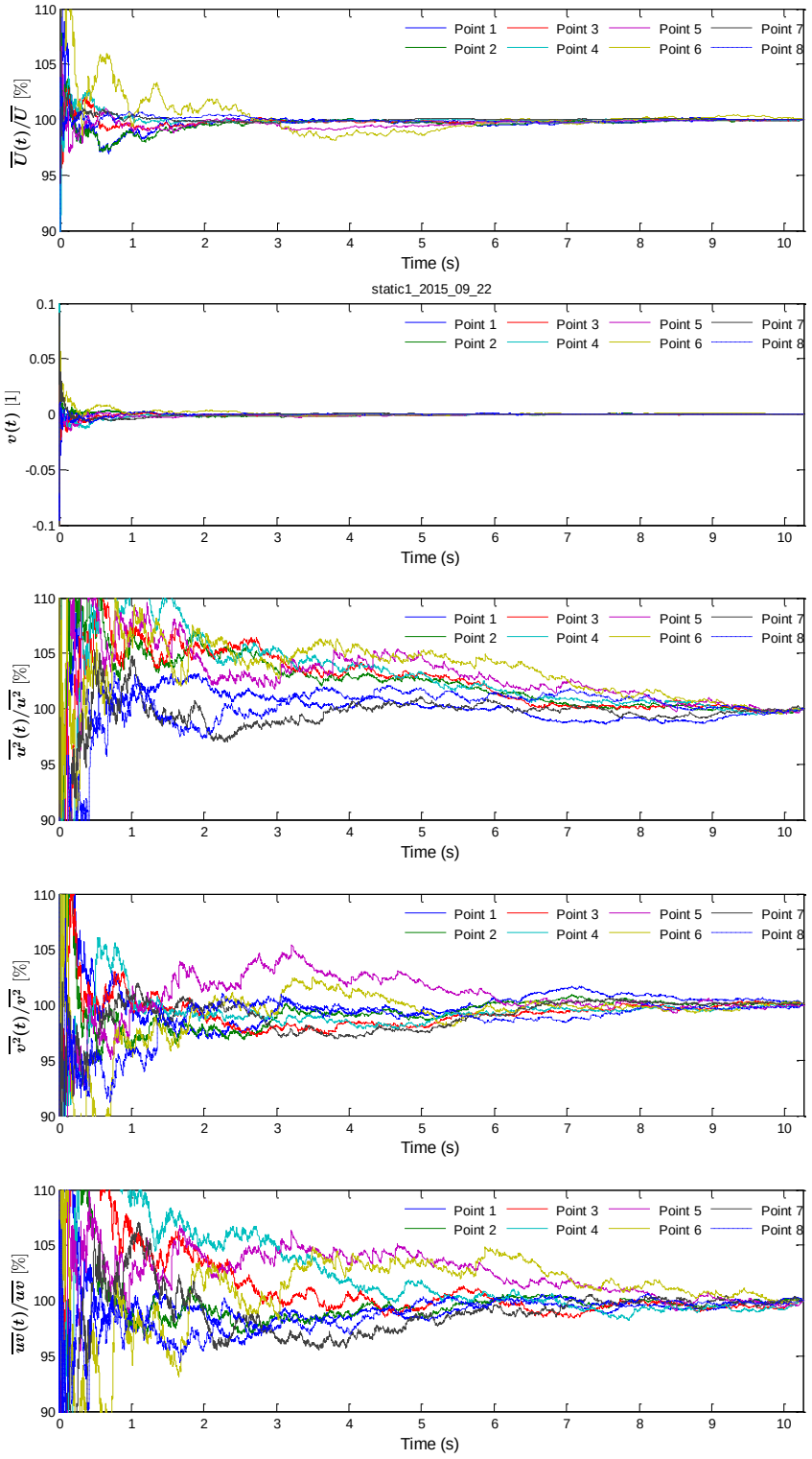

Figure A.1: Convergence of $\overline{U}$, $\overline{v}$, $\overline{u^2}$, $\overline{v^2}$ and $\overline{uv}$ quantities for the baseline configuration.

$Re = 10^6$. The average values are converged under 1% in less than 2 s; the variance values require more than 13 s. This ensure the right interpretation of the results, but not their accuracies. The accuracies and repeatability of the measured values are checked using calibrated weights hold on the balance's arms through pulleys and ropes.

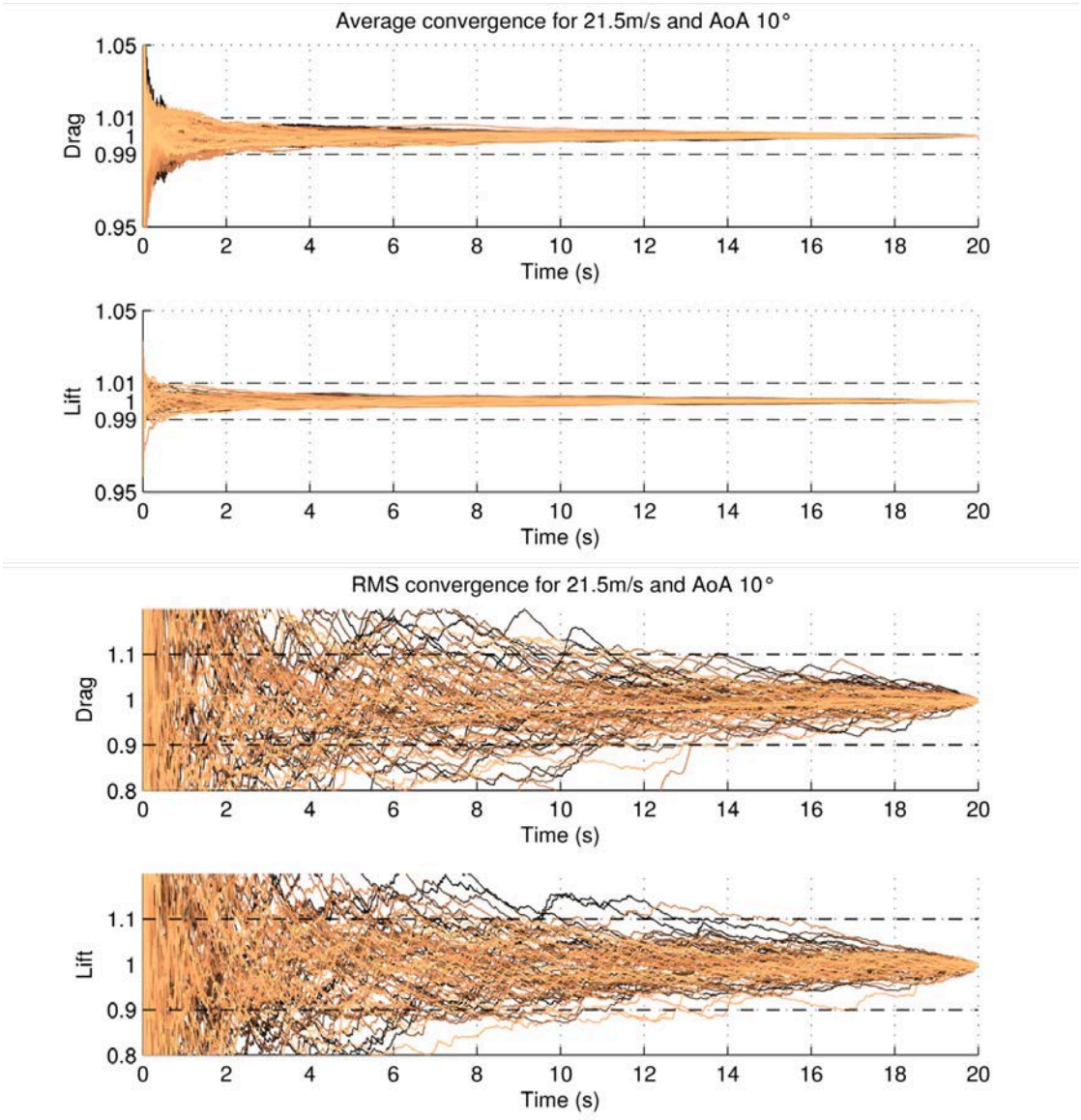

Figure A.2: Convergence of lift ($L/\overline{L}$) and drag ($D/\overline{D}$) for 80 actuation cases including baseline configuration.

A.3 Parasite drag effect

The aspect ratio and the wind tunnel's walls cause perturbation in the force measurements. Effects on lift and parasite drag have been studied and it is possible to estimate correction coefficients that are applied on the aerodynamic coefficients. An example about the corrected lift coefficient $C_{Lcorrected}$ follows: $C_{Lcorrected} = \alpha \cdot C_{Lmeasured}$, where α is a correction coefficient that depends on the dimensions of the wing model and wind tunnel, as well as flow conditions (i.e. free stream velocity). In the present study, we focus on the comparison of the actuated cases to the static baseline case. As flow conditions and geometries do not change during morphing, the value of α remains constant. Hence the calculation of the relative morphing effect ΔC_L does not depend on the correction coefficient: $\Delta C_{Lmeasured} = \frac{C^{morphing}_{Lmeasured} - C^{baseline}_{Lmeasured}}{C^{baseline}_{Lmeasured}} = \frac{\alpha \cdot C^{morphing}_{Lmeasured} - \alpha \cdot C^{baseline}_{Lmeasured}}{\alpha \cdot C^{baseline}_{Lmeasured}} = \frac{C^{morphing}_{Lcorrected} - C^{baseline}_{Lcorrected}}{C^{baseline}_{Lcorrected}} = \Delta C_{Lcorrected}$.

The correction factor α may depend on the $C_{Lmeasured}$ but the morphing effects on flow are non significant enough to cause a change in the correction factor. Thus the previous statement is valid. As a conclusion, the relative morphing effects calculated throughout the paper are valid regardless of the common wind tunnel compensation.

APPENDIX B

True scale cambered control flap appendices

B.1 Optimization results of the flap with elastic skin and elastic beam hinges

Normalized costs:

mass: 0.97	energy: 0.40	cycle life: 8.04
shape: 1.66	penality: 11.23	Sum: 22.30

General parameters

Span = 0.500 m

SMA set: design to 2% strain and 150 MPa

Optimization results

Number of rib section:	#1	#2	#3	#4	#5
Hinge positions (x/C)	25.2%	48.6%	57.1%	62.9%	75.7%
Hinge height position	42.5%	57.4%	57.5%	45.5%	41.8%

Rotation angles:

Rib section:	#1	#2	#3	#4	#5
	+7.5°	+6.6°	-3.5°	+7.7°	+6.5°

Skin strain:

	Up bending	Down bending
Intrados skin:	-1.3%	1.8%
Extrados skin:	2.0%	-1.4%

Rib report

One rib mass: 1.722kg

Force report

Force repartition

	Design moment	Aero part	Skin elastic part
Hinge #1	845.3 Nm	49.6%	50.4%
Hinge #2	317.4 Nm	51.5%	48.5%
Hinge #3	178.2 Nm	59.2%	40.8%
Hinge #4	206.3 Nm	36.0%	64.0%
Hinge #5	91.9 Nm	29.8%	70.2%

Actuators report

	mass	Force	Strain	Lever arm	Angle	Active Length	Stress
Act.#1	0.547 kg	4269 daN	2.0%	0.029 m	7.46°	0.188 m	150 MPa
Act.#2	0.253 kg	2546 daN	2.0%	0.024 m	6.56°	0.139 m	150 MPa
Act.#3	0.085 kg	1927 daN	2.0%	0.017 m	3.50°	0.051 m	150 MPa
Act.#4	0.152 kg	2625 daN	2.2%	0.012 m	7.73°	0.073 m	150 MPa
Act.#5	0.130 kg	2211 daN	2.0%	0.006 m	6.48°	0.033 m	150 MPa

Total actuator mass: 1.168 kg
Total SMA mass only: 0.881 kg
Antagonist actuators:

	mass	Force	Strain	Lever arm	Angle	Active Length	Stress
Act.#1	0.359 kg	2759 daN	2.0%	0.029 m	7.46°	0.188 m	150 MPa
Act.#2	0.260 kg	2617 daN	2.0%	0.024 m	6.56°	0.139 m	150 MPa
Act.#3	0.082 kg	1852 daN	2.0%	0.017 m	3.50°	0.051 m	150 MPa
Act.#4	0.105 kg	1797 daN	2.2%	0.012 m	7.73°	0.073 m	150 MPa
Act.#5	0.044 kg	628 daN	2.0%	0.012 m	6.48°	0.068 m	150 MPa

Total actuator mass: 0.850kg
Total SMA mass only: 0.668kg

Skin elongation requirements
Elongation due to rotations in mm

Number of rib section:	#1	#2	#3	#4	#5
Up skin:	9.7	5.9	2.8	7.1	4.2
Down skin:	10.3	8.7	4.0	6.0	2.6
Optimal skin free-length : (mm)					
Up skin:	97.1	82.5	72.0	98.1	82.6
Down skin:	111.2	94.5	82.5	112.3	94.5
Optimal skin force : (daN)					
Max up skin:	742.8	536.5	291.9	541.8	383.7
Max down skin:	744.3	681.7	358.4	460.7	270.6
Min up skin:	247.6	178.8	97.3	180.6	127.9
Min down skin:	216.3	156.2	85.0	157.8	111.7

Estimated average power consumption
Total maintaining power: 0.453 kW
Total heating power: 2.001 kW
Actuators energy distribution:

#1	#2	#3	#4	#5	antago	#1	#2	#3	#4	#5
26.4%	11.6%	3.2%	6.3%	2.4%		26.4%	11.6%	3.2%	6.3%	2.4%

Life span estimation
Minimum life cycle: 1e+05 cycles
Actuator estimated life:

#1	#2	#3	#4	#5	antago	#1	#2	#3	#4	#5
2E+05	2E+05	2E+05	1E+05	2E+05		2E+05	2E+05	2E+05	1E+05	2E+05

Hinge report

	mass	b	h	L	max resitivie torque	Radial force
Hinge.#1	0.53kg	499mm	4mm	44mm	20.4Nm	8021.6daN
Hinge.#2	0.20kg	497mm	3mm	24mm	7.2Nm	6024.3daN
Hinge.#3	0.02kg	449mm	1mm	4mm	0.5Nm	4235.6daN
Hinge.#4	0.28kg	498mm	3mm	31mm	9.5Nm	5122.2daN
Hinge.#5	0.07kg	481mm	2mm	13mm	2.2Nm	3333.8daN

Total hinge mass: 1.099kg

Mass distribution

Total	Actuator	Rib structure	Elastic hinges
4.839kg	2.018kg	1.722kg	1.099kg
100.0%	41.7%	35.6%	22.7%

Overall flap

Total mass: 19.356 kg

Total average power: 8.004 kW

B.2 Optimization results of the flap with feathers and gliding bearings

Normalized costs:

mass: 0.52 energy: 0.10 cycle life: 6.73
shape: 2.29 penality: 39.13 Sum: 48.77

General parameters

Span = 0.500 m
SMA set: design to 2% strain and 150 MPa

Optimization results

Number of rib section:	#1	#2	#3	#4	#5
Hinge positions (x/C)	29.3%	46.1%	51.4%	59.8%	71.7%
Hinge height position	40.0%	35.4%	68.9%	69.2%	55.0%

Rotation angles:

Rib section:	#1	#2	#3	#4	#5
Up bending:	+6.7°	-1.1°	+0.1°	+2.8°	+4.6°
Down bending: -1.9°	-5.9°	+0.5°	-0.2°	-3.5°	

Rib report

One rib mass: 1.804kg

Force report

Force repartition

	Design moment	Aero part	Feather friction part
Hinge #1	363.4Nm	100.0%	0.0% (0.07Nm)
Hinge #2	183.9Nm	100.0%	0.0% (0.02Nm)
Hinge #3	142.3Nm	100.0%	0.0% (0.01Nm)
Hinge #4	90.0Nm	100.0%	0.0% (0.02Nm)
Hinge #5	39.2Nm	99.6%	0.4% (0.16Nm)

Actuators report

	mass	Force	Strain	Lever arm	Angle	Active Length	Stress
Act.#1	0.246kg	1989daN	2.0%	0.024m	8.52°	0.176m	150MPa
Act.#2	0.078kg	1093daN	2.0%	0.022m	4.82°	0.091m	150MPa
Act.#3	0.012kg	289daN	2.0%	0.063m	0.46°	0.025m	150MPa
Act.#4	0.026kg	371daN	2.0%	0.031m	2.99°	0.081m	150MPa
Act.#5	0.029kg	422daN	2.1%	0.012m	8.02°	0.081m	150MPa

Total actuator mass: 0.391 kg
Total SMA mass only: 0.301 kg
Antagonist actuators:

	mass	Force	Strain	Lever arm	Angle	Active Length	Stress
Act.#1	0.119kg	928daN	2.0%	0.024m	8.52°	0.176m	150MPa
Act.#2	0.038kg	510daN	2.0%	0.022m	4.82°	0.091m	150MPa
Act.#3	0.014kg	370daN	2.0%	0.023m	0.46°	0.009m	150MPa
Act.#4	0.025kg	444daN	2.0%	0.012m	2.99°	0.032m	150MPa
Act.#5	0.015kg	198daN	2.1%	0.012m	8.02°	0.081m	150MPa

Total actuator mass: 0.211 kg
Total SMA mass only: 0.141 kg

Feathers length (mm):

Rib section:	#1	#2	#3	#4	#5
Extrados feathers	10.7	13.5	3.4	4.5	3.6
Intrados feathers	8.1	8.8	3.8	6.4	3.7

Feather deformation (mm):

Rib section:	#1	#2	#3	#4	#5
Extrados feathers	1.252	0.032	0.000	0.079	0.205
Intrados feathers	0.065	0.506	0.007	0.001	0.145

Estimated average power consumption
Total maintaining power: 0.129 kW
Total heating power: 0.571 kW
Actuators energy distribution:

#1	#2	#3	#4	#5	antago	#1	#2	#3	#4	#5
45.8%	13.0%	0.9%	3.9%	4.5%		21.4%	6.1%	0.4%	1.8%	2.1%

Life span estimation
Minimum life cycle: 1e+05 cycles
Actuator estimated life:

#1	#2	#3	#4	#5	antago	#1	#2	#3	#4	#5
2E+05	2E+05	2E+05	2E+05	1E+05		2E+05	2E+05	2E+05	2E+05	1E+05

Hinge report

	mass	b	h	L	max resitivie torque	Radial force
Hinge.#1	0.16kg	471mm	2mm	25mm	4.7Nm	2919.9daN
Hinge.#2	0.02kg	141mm	1mm	10mm	0.6Nm	1605.1daN
Hinge.#3	0.00kg	3mm	4mm	10mm	0.0Nm	662.5daN
Hinge.#4	0.00kg	25mm	2mm	10mm	0.2Nm	816.7daN
Hinge.#5	0.02kg	207mm	1mm	10mm	0.4Nm	621.2daN

Total hinge mass: 0.200kg

Mass distribution

Total	Actuator	Rib structure	Elastic hinges
2.605kg	0.602kg	1.804kg	0.200kg
100.0%	23.1%	69.2%	7.7%

Overall flap
Total mass: 10.421 kg
Total average power: 0.518 kW

B.3 Optimization results of the final chosen flap design

Normalized costs:

mass: 0.48	energy: 0.10	cycle life: 22.80
shape: 1.76	penality: 47.24	Sum: 72.39

General parameters
Span = 0.500 m
SMA set: design to 2% strain and 150 MPa

Optimization results

Number of rib section:	#1	#2	#3	#4	#5
Hinge positions (x/C)	23.4%	51.8%	60.2%	65.7%	75.6%
Hinge height position	46.9%	57.0%	58.8%	60.4%	49.1%

Rotation angles:

Rib section:	#1	#2	#3	#4	#5
Up bending:	+4.8°	+1.5°	+1.5°	+2.2°	+3.4°
Down bending:	-2.5°	-5.3°	+0.1°	+0.4°	-4.1°

Rib report
Rib report One rib mass: 1.707kg

Force report
Force repartition

	Design moment	Aero part	Feather friction part
Hinge #1	445.4Nm	100.0%	0.0% (0.16Nm)
Hinge #2	132.5Nm	100.0%	0.0% (0.06Nm)
Hinge #3	87.4Nm	100.0%	0.0% (0.02Nm)
Hinge #4	61.1Nm	100.0%	0.0% (0.01Nm)
Hinge #5	27.6Nm	99.3%	0.7% (0.20Nm)

Actuators report

Agonist actuators:

	mass	Force	Strain	Lever arm	Angle	Active Length	Stress
Act.#1	0.265kg	1818daN	2.0%	0.031m	7.62°	0.209m	150MPa
Act.#2	0.071kg	571daN	2.0%	0.030m	6.33°	0.164m	150MPa
Act.#3	0.019kg	444daN	2.0%	0.025m	2.03°	0.044m	150MPa
Act.#4	0.014kg	291daN	2.0%	0.027m	1.17°	0.027m	150MPa
Act.#5	0.015kg	297daN	3.1%	0.012m	7.56°	0.051m	150MPa

Total actuator mass: 0.383 kg

Total SMA mass only: 0.300 kg

Antagonist actuators:

	mass	Force	Strain	Lever arm	Angle	Active Length	Stress
Act.#1	0.129kg	849daN	2.0%	0.031m	7.62°	0.209m	150MPa
Act.#2	0.035kg	267daN	2.0%	0.030m	6.33°	0.164m	150MPa
Act.#3	0.009kg	207daN	2.0%	0.025m	2.03°	0.044m	150MPa
Act.#4	0.011kg	258daN	2.0%	0.014m	1.17°	0.014m	150MPa
Act.#5	0.007kg	140daN	3.1%	0.012m	7.56°	0.051m	150MPa

Total actuator mass: 0.192 kg

Total SMA mass only: 0.140 kg

Feathers length (mm):

Rib section:	#1	#2	#3	#4	#5
Extrados feathers	6.4	6.3	3.4	4.7	3.0
Intrados feathers	6.0	7.4	3.6	5.6	3.0

Feather deformation (mm):

Rib section:	#1	#2	#3	#4	#5
Extrados feathers	0.624	0.027	0.022	0.042	0.135
Intrados feathers	0.149	0.526	0.010	0.011	0.131

Estimated average power consumption

Total maintaining power: 0.129 kW

Total heating power: 0.568 kW

Actuators energy distribution:

#1	#2	#3	#4	#5	antago	#1	#2	#3	#4	#5
50.1%	12.4%	2.6%	1.0%	2.0%		23.4%	5.8%	1.2%	0.5%	0.9%

Life span estimation

Minimum life cycle: 4e+04 cycles

#1	#2	#3	#4	#5	antago	#1	#2	#3	#4	#5
2E+05	2E+05	2E+05	2E+05	4E+04		2E+05	2E+05	2E+05	2E+05	4E+04

Hinge report

	mass	b	h	L	max resitivie torque	Radial force
Hinge.#1	0.09kg	469mm	2mm	17mm	2.6Nm	2671.0daN
Hinge.#2	0.02kg	148mm	1mm	10mm	0.4Nm	841.0daN
Hinge.#3	0.00kg	10mm	3mm	10mm	0.1Nm	654.0daN
Hinge.#4	0.00kg	4mm	3mm	10mm	0.0Nm	550.9daN
Hinge.#5	0.01kg	124mm	1mm	10mm	0.3Nm	438.9daN

Total hinge mass: 0.120kg

Mass distribution

Total	Actuator	Rib structure	Elastic hinges
2.402kg	0.575kg	1.707kg	0.120kg
100.0%	23.9%	71.1%	5.0%

Overall flap

Total mass: 9.609 kg

Total average power: 0.515 kW

Bibliography

[88] *IEEE standard on piezoelectricity, ANSI IEEE 1987-176*. 1988. DOI: 10.1109/IEEESTD.1988.79638.

[Ald+16] M.A. Aldheeb et al. "A review on aerodynamics of non-flapping bird wings". In: *Journal of Aerospace Technology and Management* 8.1 (2016), pages 7–17.

[And10] J.D. Anderson Jr. *Fundamentals of aerodynamics*. Tata McGraw-Hill Education, 2010.

[Av49] I.H. Abbott and A.E. von Doenhoff. *Theory of Wing sections*. New York, NY: Dover Publication, Inc., 1949.

[Bal07] Rüdiger G Ballas. *Piezoelectric multilayer beam bending actuators: Static and dynamic behavior and aspects of sensor integration*. Springer Science & Business Media, 2007.

[Bar+11] S. Barbarino et al. "A review of morphing aircraft". In: *Journal of Intelligent Material Systems and Structures* 22.9 (2011), pages 823–877.

[Bar+14] S. Barbarino et al. "A review on shape memory alloys with applications to morphing aircraft". In: *Smart Materials and Structures* 23.6 (2014), page 063001. URL: http://stacks.iop.org/0964-1726/23/i=6/a=063001.

[Bar04] Yoseph Bar-Cohen. *Electroactive polymer (EAP) actuators as artificial muscles: reality, potential, and challenges*. Volume 136. SPIE press, 2004.

[BCM86] M. Braza, P.H.H.M. Chassaing, and H.H. Minh. "Numerical study and physical analysis of the pressure and velocity fields in the near wake of a circular cylinder". In: *Journal of fluid mechanics* 165 (1986), pages 79–130.

[Ber11] Berkooz, G. and Holmes, P. and Lumley, J.L. "The proper orthogonal decomposition in the analysis of turbulent flows". In: *Annual Review of Fluid Mechanics* 25.1 (2011), pages 539–575.

[BF93] R.E. Brown and M.R. Fedde. “Airflow sensors in the avian wing”. In: *Journal of experimental biology* 179.1 (1993), pages 13–30.

[BFP01] M. BRAZA, D. Faghani, and H. Persillon. “Successive stages and the role of natural vortex dislocations in three-dimensional wake transition”. In: *Journal of Fluid Mechanics* 439 (2001), pages 1–41.

[Bil+10] O. Bilgen et al. “Macro-fiber composite actuated simply supported thin airfoils”. In: *Smart Materials and Structures* 19.5 (2010), page 055010.

[Bil05] Onur Bilgen. “Aerodynamic and Electromechanical Design, Modeling and Implementation of Piezocomposite Airfoils”. PhD thesis. Virginia Polytechnic Institue and State University, 2005.

[BL07] M. Behl and A. Lendlein. “Shape-memory polymers”. In: *Materials today* 10.4 (2007), pages 20–28.

[Bou+08] R. Bourguet et al. “Anisotropic Organised Eddy Simulation for the prediction of non-equilibrium turbulent flows around bodies”. In: *Journal of Fluids and Structures* 24.8 (2008), pages 1240–1251.

[Bri07] Michel Brissaud. *Matériaux piézoélectriques: caractérisation, modélisation et vibration*. PPUR presses polytechniques, 2007.

[Bub+10] E.A. Bubert et al. “Design and fabrication of a passive 1D morphing aircraft skin”. In: *Journal of Intelligent Material Systems and Structures* 21.17 (2010), pages 1699–1717.

[Bur+15] D. Burdette et al. “Aerostructural design optimization of an adaptive morphing trailing edge wing”. In: *Proceedings of the AIAA Science and Technology Forum and Exposition (SciTech), Kissimmee, FL*. 2015, pages 2015–1129.

[Cat+03] L. Cattafesta et al. “Review of active control of flow-induced cavity resonance”. In: *AIAA paper* 3567 (2003), page 2003.

[CCP16] A. Cornogolub, P.J. Cottinet, and L. Petit. “Hybrid energy harvesting systems, using piezoelectric elements and dielectric polymers”. In: *Smart Materials and Structures* 25.9 (2016), page 095048.

[CCS96] J.D. Carlson, D.M. Catanzarite, and K.A. St. Clair. “Commercial magneto-rheological fluid devices”. In: *International Journal of Modern Physics B* 10.23n24 (1996), pages 2857–2865.

[Chi+14] M. Chinaud et al. “Trailing-edge dynamics and morphing of a deformable flat plate at high Reynolds number by time-resolved {PIV}”. In: *Journal of Fluids and Structures* 47 (2014). Special Issue on Unsteady Separation in Fluid-Structure Interaction-l, pages 41–54. ISSN: 0889-9746. DOI: http://dx.doi.org/10.1016/j.jfluidstructs.2014.02.007. URL: http://www.sciencedirect.com/science/article/pii/S0889974614000231.

[CLM03] F. Claeyssen, N. Lhermet, and T. Maillard. “Magnetostrictive actuators compared to piezoelectric actuators”. In: *Proc. SPIE*. Volume 4763. 2003, pages 194–199.

[CM16] F.T. Calkins and J.H. Mabe. “Flight Test of a Shape Memory Alloy Actuated Adaptive Trailing Edge Flap”. In: *ASME 2016 Conference on Smart Materials, Adaptive Structures and Intelligent Systems*. American Society of Mechanical Engineers. 2016, V001T04A007–V001T04A007.

[Col+04] S.S. Collis et al. “Issues in active flow control: theory, control, simulation, and experiment”. In: *Progress in Aerospace Sciences* 40.4 (2004), pages 237–289.

[CP15] C.J. Clark and R.O. Prum. “Aeroelastic flutter of feathers, flight and the evolution of non-vocal communication in birds”. In: *Journal of Experimental Biology* 218.21 (2015), pages 3520–3527.

[Cum+16] St.B. Cumming et al. “Aerodynamic Flight-Test Results for the Adaptive Compliant Trailing Edge”. In: (2016).

[Deb+13] M. Debiasi et al. “Deformation of the upper and lower surfaces of an airfoil by macro fiber composite actuators”. In: *31st AIAA applied aerodynamics conference*. 2013, pages 24–27.

[Dim+16] I. Dimino et al. “Smart Intelligent Aircraft Structures (SARISTU): Proceedings of the Final Project Conference”. In: edited by Christof Piet Wölcken and Michael Papadopoulos. Cham: Springer International Publishing, 2016. Chapter Distributed Actuation and Control of a Morphing Wing Trailing Edge, pages 171–186. ISBN: 978-3-319-22413-8. DOI: 10.1007/978-3-319-22413-8_9. URL: http://dx.doi.org//10.1007//978-3-319-22413-8_9.

[Dob10] Werner Dobrzynski. “Almost 40 years of airframe noise research: what did we achieve?” In: *Journal of aircraft* 47.2 (2010), pages 353–367.

[Duv05] Jé rôme Duval. “Conception et mise en oeuvre d’un système d’actionneurs AMF ré partis pour le contrôle de forme é lectroactif de voilures aéronautiques”. PhD thesis. Institut National Polytechnique de Toulouse, 2005.

[Ela04] Mohammad Elahinia. “Effect of system dynamics on shape memory alloy behavior and control”. PhD thesis. Virginia Tech, 2004.

[Ert+08] A. Erturk et al. “Piezoelectric energy harvesting from macro-fiber composites with an application to morphing-wing aircrafts”. In: *Proceedings of the 19th International Conference on Adaptive Structures and Technologies, Ascona, Switzerland, Oct.* 2008, pages 6–9.

[ESW03] D.M. Elzey, A.Y.N. Sofla, and H.N.G. Wadley. “A bio-inspired high-authority actuator for shape morphing structures”. In: *Smart Structures and Materials 2003* 5053 (2003), pages 92–100.

[FL95] Rong F.H. and Chih L.L. “Vortex Shedding and Shear-Layer Instability of Wing at Low-Reynolds Numbers”. In: *AIAA Journal* 33.8 (1995), pages 1398–1403. DOI: http://dx.doi.org/10.2514/3.12561.

[FNM16] A.D.B.L. Ferreira, P.R.O. Novoa, and A.T. Marques. “Multifunctional material systems: a state-of-the-art review”. In: *Composite Structures* 151 (2016), pages 3–35.

[FT06] R. Featherstone and Y. Teh. “Improving the speed of shape memory alloy actuators by faster electrical heating”. In: *Experimental Robotics IX* (2006), pages 67–76.

[GH97] D. Grant and V. Hayward. “Variable structure control of shape memory alloy actuators”. In: *IEEE Control Systems Magazine* 17.3 (1997), pages 80–88.

[Gid+11] P. F Giddings et al. “Modelling of piezoelectrically actuated bistable composites”. In: *Materials Letters* 65.9 (2011), pages 1261–1263.

[GK15] N. Gabdullin and S.H. Khan. “Review of properties of magnetic shape memory (MSM) alloys and MSM actuator designs”. In: *Journal of Physics: Conference Series*. Volume 588. 1. IOP Publishing. 2015, page 012052.

[Gre95] S.I. Green. *Fluid Vortices: Fluid Mechanics and its Applications*. Volume 30. New York, NY: Springer, 1995.

[Gri] Grigorie, L. and Botez, M.R. and Popov, A.V. “Self-adaptive morphing wing model, smart actuated and controlled by using a multi-loop controller based on a laminar flow real time optimizer”. In: *24th AIAA/AHS Adaptive Structures Conference, San Diego CA, USA, 4–8 January 2016*.

[Hai+14] C.S. Haines et al. “Artificial muscles from fishing line and sewing thread”. In: *science* 343.6173 (2014), pages 868–872.

[HBP16] C.J.C. Heath, I.P. Bond, and K.D. Potter. “Variable stiffness sandwich panels using electrostatic interlocking core”. In: *SPIE Smart Structures and Materials+ Nondestructive Evaluation and Health Monitoring*. International Society for Optics and Photonics. 2016, 97992A.

[HEW08] J.C.R. Hunt, I. Eames, and J. Westerweel. “Vortical Interactions with Interfacial Shear Layers”. In: *IUTAM Symposium on Computational Physics and New Perspectives in Turbulence: Proceedings of the IUTAM Symposium on Computational Physics and New Perspectives in Turbulence, Nagoya University, Nagoya, Japan, September, 11-14, 2006*. Edited by Yukio Kaneda. Dordrecht: Springer Netherlands, 2008, pages 331–338. ISBN: 978-1-4020-6472-2. DOI: 10.1007/978-1-4020-6472-2_50. URL: http://dx.doi.org/10.1007/978-1-4020-6472-2_50.

[HFA97] J.E. Huber, N.A. Fleck, and M.F. Ashby. “The selection of mechanical actuators based on performance indices”. In: *Proceedings of the Royal Society of London A: Mathematical, Physical and Engineering Sciences*. Volume 453. 1965. The Royal Society. 1997, pages 2185–2205.

[HL95] R.F. Huang and C.L. Lin. “Vortex shedding and shear-layer instability of wing at low-Reynolds numbers”. In: *AIAA journal* 33.8 (1995), pages 1398–1403.

[Hoa+03] Y. Hoarau et al. “Organized modes and the three-dimensional transition to turbulence in the incompressible flow around a NACA0012 wing”. In: *Journal of Fluid Mechanics* 496 (December 2003), pages 63–72. DOI: 10.1017/S0022112003006530. URL: https://www.cambridge.org/core/article/organized-modes-and-the-three-dimensional-transition-to-turbulence-in-the-incompressible-flow-around-a-naca0012-wing/4D03E354E6CD728DCBA13B3D2A1FF963.

[Hun+16] J. Hunt et al. “Turbulence Near Interfaces—Modelling and Simulations”. In: *Advances in Fluid-Structure Interaction*. Edited by Marianna Braza, Alessandro Bottaro, and Mark Thompson. Volume 133. Notes on Numerical Fluid Mechanics and Multidisciplinary Design. Updated contributions reflecting new findings presented at the ERCOFTAC Symposium on Unsteady Separation in Fluid-Structure Interaction, 17-21 June 2013, St John Resort, Mykonos, Greece. Springer International Publishing Switzerland, April 2016, pages 283–292. DOI: 10.1007/978-3-319-27386-0_17. URL: http://icube-publis.unistra.fr/1-HISA16.

[Ina+15] K. Inaoka et al. “Feedback flow control of a low-Re airfoil by flap actuators”. In: *Journal of Fluids and Structures* 58 (2015), pages 319–330. ISSN: 0889-9746. DOI: http://dx.doi.org/10.1016/j.jfluidstructs.2015.08.011. URL: http://www.sciencedirect.com/science/article/pii/S0889974615002108.

[Jan+06] P. Janker et al. “New actuators for aircraft and space applications”. In: *Proc Actuator*. 2006, pages 325–330.

[Jan+14] J.M. Jani et al. “A review of shape memory alloy research, applications and opportunities”. In: *Materials & Design* 56 (2014), pages 1078–1113.

[Jay+05] J. Jayender et al. “Modelling and gain scheduled control of shape memory alloy actuators”. In: *Control Applications, 2005. CCA 2005. Proceedings of 2005 IEEE Conference on*. IEEE. 2005, pages 767–772.

[Jay+08] J. Jayender et al. “Modeling and control of shape memory alloy actuators”. In: *IEEE transactions on control systems technology* 16.2 (2008), pages 279–287.

[Jod] Jodin, G. and Scheller, J. and Rizzo, K.J. and Duhayon, E. and Rouchon, J.F. and Braza M. “Dimensionnement d’une maquette pour l’investigation du morphing électroactif hybride en soufflerie subsonique”. In: *Congrès Français de Mécanique, Online AFM, Association Française de Mécanique, 2015.*

[Jod+17] G. Jodin et al. “Implementation of a hybrid electro-active actuated morphing wing in wind tunnel”. In: *{To appear in} Solid State Phenomena* (2017).

[K+14] A. Koreanschi, O. Sugar-Gabor, R.M. Botez, et al. “New numerical study of boundary layer behavior on a morphing wing-with-aileron system”. In: *American Institute of Aeronautics and Astronautics AIAA 32nd Applied Aerodynamics Conference, Atlanta, GA, USA*. 2014, pages 16–20.

[KB12] S. Kunze and C. Brücker. “Control of vortex shedding on a circular cylinder using self-adaptive hairy-flaps”. In: *Comptes Rendus Mécanique* 340.1-2 (2012), pages 41–56.

[KBR14] S.H. Ko, J.S. Bae, and J.H. Rho. “Development of a morphing flap using shape memory alloy actuators: the aerodynamic characteristics of a morphing flap”. In: *Smart Materials and Structures* 23.7 (2014), page 074015.

[KFC16] S. Kota, P. Flick, and F. Collier. “Flight Testing of the FlexFloil TM Adaptive Compliant Trailing Edge”. In: *54th AIAA Aerospace Sciences Meeting*. 2016, page 0036.

[KH08] S. Kota and J.A. Hetrick. *Adaptive compliant wing and rotor system*. US Patent 7,384,016. June 2008.

[Kim+12] H. Kim et al. “Sensorless displacement estimation of a shape memory alloy coil spring actuator using inductance”. In: *Smart Materials and Structures* 22.2 (2012), page 025001.

[Kim16] Wonhee Kim. “Model-based Design Framework for Shape Memory Alloy Wire Actuation Devices”. PhD thesis. Mechanical engineering department of the University of Michigan, 2016.

[Kin+16] M. Kintscher et al. “Assessment of the SARISTU enhanced adaptive droop nose”. In: *Smart Intelligent Aircraft Structures (SARISTU)*. Springer, 2016, pages 113–140.

[KN14] U.K. Kaul and N.T. Nguyen. “Drag Optimization Study of Variable Camber Continuous Trailing Edge Flap (VCCTEF) Using OVERFLOW”. In: *AIAA Paper* 2444 (2014), page 2014.

[Lee+15] J. Lee S.and Kim et al. “The function of the alula in avian flight.” In: *Scientific reports* 5 (2015), pages 9914–9914.

[Lex13] Christian Lexcellent. *Shape-memory alloys handbook*. John Wiley & Sons, 2013.

[Li+15] C. Li et al. “Passive vibration control of flexible hydrofoils using piezoelectric material”. In: *Fourth International Symposium on Marine Propulsors, Austin, TX, June*. 2015.

[LI14] B.W. LaCroix and P.G. Ifju. “Macro fiber composites and substrate materials for MAV wing morphing”. In: *Experimental Mechanics of Composite, Hybrid, and Multifunctional Materials, Volume 6*. Springer, 2014, pages 89–101.

[Lil98] G.M. Lilley. “A study of the silent flight of the owl”. In: *AIAA paper* 2340.1998 (1998), pages l–6.

[Lin02] J.C. Lin. “Review of research on low-profile vortex generators to control boundary-layer separation”. In: *Progress in Aerospace Sciences* 38.4 (2002), pages 389–420.

[LM15] Z. Lyu and J.R.R.A. Martins. “Aerodynamic Shape Optimization of an Adaptive Morphing Trailing Edge Wing”. In: *Journal of Aircraft* 52 (November 2015), 1951–1970. DOI: 10.2514/1.C033116.

[Mad+16] F. B Madsen et al. “The Current State of Silicone-Based Dielectric Elastomer Transducers”. In: *Macromolecular rapid communications* 37.5 (2016), pages 378–413.

[Mil+16] E.J. Miller et al. “Evaluation of the Hinge Moment and Normal Force Aerodynamic Loads from a Seamless Adaptive Compliant Trailing Edge Flap in Flight”. In: *54th AIAA Aerospace Sciences Meeting*. 2016.

[MMD16] V. Motta, P. Mouyon, and C. Döll. “Discrete Time Open-Loop and Closed-Loop Flow Control Based on Van der Pol Modeling”. In: *8th AIAA Flow Control Conference*. 2016, page 3256.

[Mot15a] Motta, V. and Quaranta, G. “Linear Reduced-Order Model for Unsteady Aerodynamics of an L-Shaped Gurney Flap”. In: *Journal of Aircraft* 52 (2015), pages 1887–1904. DOI: {10.2514/1.C033099}.

[Mot15b] V. Motta. “Computational fluid dynamic analysis of a L-shaped Gurney flap for vibration control”. PhD thesis. Milano, ITALY: Politecnico di Milano, 2015.

[MSL04] N. Ma, G. Song, and H.J. Lee. “Position control of shape memory alloy actuators with internal electrical resistance feedback using neural networks”. In: *Smart materials and structures* 13.4 (2004), page 777.

[Mus01] A. Musolff. “Adaptiver Tragflügel mit Formgedächtnisaktuatoren”. In: *Konstruktion* 5 (2001), pages 72–77.

[NA09] D. Neal and H. Asada. “Nonlinear, large-strain PZT actuators using controlled structural buckling”. In: *Robotics and Automation, 2009. ICRA’09. IEEE International Conference on*. IEEE. 2009, pages 170–175.

[Nag+16] C. Nagel et al. “Seamless Morphing Concepts for Smart Aircraft Wing Tip”. In: *Smart Intelligent Aircraft Structures (SARISTU)*. Springer, 2016, pages 275–291.

[Nor11] Norman, A.K. and McKeon, B.J. “Unsteady force measurements in sphere flow from subcritical to supercritical Reynolds numbers”. In: *Experiments in fluids* 51 (2011), pages 1439–1453.

[Oha+12] O.J. Ohanian et al. “Piezoelectric morphing versus servo-actuated MAV control surfaces”. In: *AIAA Paper* 1512 (2012), pages 23–26.

[Orn13] Cornell Lab of Ornithology. *All About Feathers. All About Bird Biology*. Cornell Lab of Ornithology, Ithaca, New York. 2013. URL: https://academy.allaboutbirds.org/feathers-article/ (visited on July 9, 2017).

[PAM16] R. Pecora, F. Amoroso, and M. Magnifico. “Toward the bi-modal camber morphing of large aircraft wing flaps: the CleanSky experience”. In: volume 9801. 2016, pages 980106–98018. DOI: 10.1117/12.2218415. URL: http://dx.doi.org/10.1117/12.2218415.

[PB98] H. Persillon and M. Braza. “Physical analysis of the transition to turbulence in the wake of a circular cylinder by three-dimensional Navier–Stokes simulation”. In: *Journal of Fluid Mechanics* 365 (1998), pages 23–88.

[PDW02] D.M. Pitt, J.P. Dunne, and E.V. White. “SAMPSON smart inlet design overview and wind tunnel test Part I-Design overview”. In: *Proc. SPIE*. Volume 4698. 2002, page 13.

[Per05] R. Perrin. “Analyse physique et modélisation d’écoulements incompressibles instationnaires turbulents autour d’un cylindre circulaire à grand nombre de Reynolds”. PhD thesis. 2005.

[PFI15] A.M. Pankonien, C.T. Faria, and D.J. Inman. “Synergistic smart morphing aileron: Experimental quasi-static performance characterization”. In: *Journal of Intelligent Material Systems and Structures* 26.10 (2015), pages 1179–1190.

[PML14] N. Precup, M. Mor, and E. Livne. “Design, Construction, and Tests of an Aeroelastic Wind Tunnel Model of a Variable Camber Continuous Trailing Edge Flap (VCCTEF) Concept Wing”. In: *AIAA Paper* 2442 (2014).

[Ram+05] D.S. Ramrakhyani et al. “Aircraft structural morphing using tendon-actuated compliant cellular trusses”. In: *Journal of aircraft* 42.6 (2005), pages 1615–1621.

[Red+02] O.K. Rediniotis et al. “Development of a shape-memory-alloy actuated biomimetic hydrofoil”. In: *Journal of Intelligent Material Systems and Structures* 13.1 (2002), pages 35–49.

[Rou+11] J.F. Rouchon et al. “Activation d’une voilure déformable par des câbles d’AMF répartis en surface”. In: *20ème Congrès Français de Mécanique, 28 août/2 sept. 2011-25044 Besançon, France (FR)* (2011).

[Rou+13] J.F. Rouchon et al. “Assembling and testing of quasi-static hybrid piezoelectric motor based on electroactive lubrication principle”. In: *Archives of Electrical Engineering* 62.2 (2013), pages 237–250.

[RSE14] K.S. Ramadan, D. Sameoto, and S. Evoy. “A review of piezoelectric polymers as functional materials for electromechanical transducers”. In: *Smart Materials and Structures* 23.3 (2014), page 033001.

[SCB03] G. Song, V. Chaudhry, and C. Batur. “Precision tracking control of shape memory alloy actuators using neural networks and a sliding-mode based robust controller”. In: *Smart materials and structures* 12.2 (2003), page 223.

[Sch] Scheller, J. and Rizzo, K. and Duhayon, E. and Rouchon, J.F. and Braza, M. “A hybrid morphing NACA4412 airfoil concept”. In: *IEEE International Conference on Industrial Technology (ICIT), 17–19 March 2015, Seville, Spain*, pages 1974–1978. DOI: 10.1109/ICIT.2015.7125385.

[Sch+15] J. Scheller et al. “Trailing-edge dynamics of a morphing {NACA0012} aileron at high Reynolds number by high-speed {PIV}”. In: *Journal of Fluids and Structures* 55 (2015), pages 42–51. ISSN: 0889-9746. DOI: http://dx.doi.org/10.1016/j.jfluidstructs.2014.12.012. URL: http://www.sciencedirect.com/science/article/pii/S0889974615000158.

[Sch+16] J. Scheller et al. “A Combined Smart-materials Approach for Next-generation Airfoils.” In: *Solid State Phenomena* 251 (2016).

[Sch15] Johannes Scheller. “Electroactive morphing for the aerodynamic performance improvement of next generation airvehicles”. PhD thesis. Institut Narional Polytechnique de Toulouse, 2015.

[SF05] C. Scherer and Antonio M. Figueiredo N. “Ferrofluids: properties and applications”. In: *Brazilian Journal of Physics* 35.3A (2005), pages 718–727.

[SK01] M. Shahinpoor and K.J. Kim. “Ionic polymer-metal composites: I. Fundamentals”. In: *Smart materials and structures* 10.4 (2001), page 819.

[SLY08] A.K. Seow, Y. Liu, and W.K. Yeo. “Shape memory alloy as actuator to deflect a wing flap”. In: *AIAA Paper* 1704 (2008).

[Szu+15] D. Szubert et al. “Shock-vortex shear-layer interaction in the transonic flow around a supercritical airfoil at high Reynolds number in buffet conditions”. In: *Journal of Fluids and Structures* 55 (2015), pages 276–302. ISSN: 0889-9746. DOI: http://dx.doi.org/10.1016/j.jfluidstructs.2015.03.005. URL: http://www.sciencedirect.com/science/article/pii/S0889974615000602.

[Szu+16] D. Szubert et al. “Numerical study of the turbulent transonic interaction and transition location effect involving optimisation around a supercritical aerofoil”. In: *European Journal of Mechanics-B/Fluids* 55 (2016), pages 380–393.

[Szu15] Damien Szubert. “Physics and modelling of unsteady turbulent flows around aerodynamic and hydrodynamic structures at high Reynold number by numerical simulation”. PhD thesis. Institut Narional Polytechnique de Toulouse, 2015.

[Thi+08] C. Thill et al. “Morphing skins”. In: *The Aeronautical Journal* 112.1129 (2008), pages 117–139.

[Urs+07] N. Ursache et al. “Morphing winglets for aircraft multi-phase improvement”. In: *7th AIAA ATIO Conf, 2nd CEIAT Int'l Conf on Innov and Integr in Aero Sciences, 17th LTA Systems Tech Conf; followed by 2nd TEOS Forum*. 2007, page 7813.

[WBF14] B.K.S. Woods, O. Bilgen, and M.I. Friswell. “Wind tunnel testing of the fish bone active camber morphing concept”. In: *Journal of Intelligent Material Systems and Structures* 25.7 (2014), pages 772–785.

[Wel67] P.D. Welch. “The use of fast Fourier transform for the estimation of power spectra: A method based on time averaging over short, modified periodograms”. In: *IEEE Transactions on audio and electroacoustics* 15.2 (1967), pages 70–73.

[Wu+17] R. Wu et al. “A morphing aerofoil with highly controllable aerodynamic performance”. In: *The Aeronautical Journal* 121.1235 (2017), pages 54–72.

[YSK06] S. Yarusevych, P.E. Sullivan, and J.G. Kawall. “Coherent structures in an airfoil boundary layer and wake at low Reynolds numbers”. In: *Physics of Fluids* 18.4, 044101 (2006). DOI: http://dx.doi.org/10.1063/1.2187069. URL: http://scitation.aip.org/content/aip/journal/pof2/18/4/10.1063/1.2187069.

Résumé :

Le Morphisme Electroactif est un axe multidisciplinaire, associant l'aérodynamique, les matériaux innovants et la mécatronique. Ce concept consiste en l'amélioration des performances aérodynamiques par l'utilisation d'actionneurs déformant la surface portante d'un aéronef en temps réel.

Soutenue par Airbus, la modélisation, conception et réalisation d'un démonstrateur petite échelle est une première étape. Basée sur un profil d'aile A320, il est équipé d'actionnements pour le morphisme électroactif hybride : de grandes déformations à faibles vitesses par des Alliages à Mémoire de Forme sont associés à l'intégration au bord de fuite d'actionneurs piézoélectriques permettant de hautes fréquences d'actionnement à amplitude moindre.

Une seconde étape de la thèse est dédiés aux essais en soufflerie. La mesure de forces et la vélocimétrie d'images de particules permettent de comprendre la physique de l'écoulement et de la turbulence. L'étude de ce couplage fluide-structure-actionneurs présente les effets du morphisme par actionnement indépendant ; puis le couplage non linéaire de l'actionnement hybride.

La troisième étape consiste au passage vers une échelle réaliste des actionneurs, par la conception d'un volet « électro-morphé ». Une approche de dimensionnement par optimisation est proposée. Basé sur des technologies nouvelles d'actionnement, un prototype d'un tel macro-actionneur est alors conçu pour être testé.

Mots clés :

morphisme de structure, matériaux électroactifs, aéronautique, soufflerie, turbulence

Abstract:

Electroactive Morphing is a multidisciplinary axis, combining aerodynamics, innovative materials and mechatronics. This concept consists in improving the aerodynamic performance by the use of actuators deforming the airfoil of an aircraft in real time.

Supported by Airbus, the modeling, design and implementation of a small scale demonstrator is a first step. Based on an A320 wing profile, it is equipped with actuators for hybrid electroactive morphing: large deformations at low speeds by Shape Memory Alloys are associated with the integration at the trailing edge of piezoelectric actuators allowing high operating frequencies at lower amplitude.

A second step of the thesis is dedicated to wind tunnel tests. The measurement of forces and the Particle Image Velocimetries allow for the understanding of the flow and turbulence physics. The study of this fluid-structure-actuator coupling presents the effects of the morphism by independent actuation; then the nonlinear coupling of the hybrid actuation.

The third step is the transition to a realistic scale of actuators, by designing an "electro-morphed" macro-actuator. An optimization sizing approach is proposed. Based on new actuation technologies, a prototype of such a macro-actuator is then designed to be tested.

Keywords:

structure morphing, electroactive materials, aeronautics, true scale, turbulence